SAN DIEGO STATE UNIVERSITY
and
UNIVERSITY OF CALIFORNIA, IRVINE

Analysis, Computation, and Design of Innovative High Gain Feed-Reflector and Beam Steering Antenna Solutions

DISSERTATION

submitted in partial satisfaction of the requirements
for the degree of

DOCTOR OF PHILOSOPHY

in Computational Science

by

Ghanshyam Mishra

Dissertation Committee:
Professor Satish K. Sharma, Chair
Professor Filippo Capolino, Co-Chair
Professor A. Lee Swindlehurst
Professor Gustaaf Jacobs
Professor Faryar Jabbari

2020

DEDICATION

To

All children for whom the right to education and health are inaccessible

TABLE OF CONTENTS

Page

LIST OF FIGURES

Page

LIST OF TABLES

ACKNOWLEDGEMENTS

First, I would like to thank my parents for believing in me and teaching me the true meaning of '*Tough times do not last, but tough people do*!'. I could not have done this without their unconditional love and support. Next, I would like to thank my high school teacher and a lifelong mentor, Mr. Yadunandan Pathak, for inspiring me to face the challenges and for consistently encouraging me during difficult times.

I would like to sincerely thank my advisor, Professor Satish K. Sharma, for giving me the opportunity to do research under his mentorship. I am grateful for his support and guidance during my entire Ph.D. journey since Fall 2014. Without his generous help and continuous support at different phases, I could not have finished this journey. Numerous long hours of technical discussions with him have helped in achieving the research goals, and I highly appreciate him for spending his valuable time. I also thank him for offering me unlimited access to research resources in the Antenna and Microwave Laboratory (AML) and financial support from his research funds and nominating me for different fellowships and awards from San Diego State University (SDSU) and IEEE Antennas and Propagation Society and USNC-URSI Commission B. I also thank him for his generosity in connecting me to his research collaborators with whom I have had research interactions and published several coauthored research papers that were in addition to my dissertation research.

I would like to thank and express my sincere gratitude to Professor Filippo Capolino, Professor A. Lee Swindlehurst, Professor Gustaaf Jacobs, and Professor Faryar Jabbari for their time and efforts as part of my dissertation committee members. I would like to thank Professor Jose Castillo, the program director of the Computational Science Research Center at SDSU, for his support during the completion of my Ph.D. I would also like to thank the computational science joint doctoral program JDP staff, Ms. Parisa Plant from SDSU, and Ms. Jean Bennett from University of California, Irvine (UCI) for their timely assistance.

I would like to thank the funding agencies without whose support my research would not have been possible. I would like to thank the college of engineering, SDSU, for providing funding in the form of Teaching Associate for AY 2014-15. I am grateful to San Diego State University for the University Graduate Fellowship (UGF, AY 2018-19). I would thank the Office of Naval Research (ONR) grant numbers N00014-16-1-2166 and 11970207, PI: Professor Satish K. Sharma. I would also like to thank the Naval Information Warfare Center Pacific (NIWC-PAC) grants # N66001-15-D-0099/N6600118F0996 and N6600115D0099/N6600120F0356, PI: Professor Satish K. Sharma. Finally, I would also like to thank Analog Devices Inc. for providing the beamforming board for the *Ka*-band beamforming measurements.

I would also like to thank Dr. Jia-Chi S. Chieh with the NIWC-PAC for his valuable technical support and discussions. He has always encouraged and appreciated me at each stage of the research, which was a morale booster during challenging times. I sincerely thank him for his appreciation of my research ethics, which brought out the best in me and helped me keep a positive attitude.

I also thank all my current and former colleagues in the research group especially Dr. Behrouz Babakhani, Dr. Nathan Labadie, Dr. Kumud Jha, Tavis Hall, Rafid Damman, Alejandro Castro, Roshin Rose George, Mohana Komandla, Sandhya Krishna, Hao-Lung Chu, Dr. Xinhua Yu, Ila

Agnihotri, Ningning Luo, Sherry Wagner, Sonika Biswal, Tommy Khoury, Philip Nguyen, and Connor Laffey for being supportive and encouraging during my entire stay with them. I especially want to thank Dr. Babakhani for treating me like a younger brother and being there for me from my very first day in the United States. I will always be indebted to him for his support and advice.

I want to express my special thanks to Mark Bruno, SDSU Electrical and Computer Engineering Department's Equipment/Systems Specialist, for his excitement and love to help students all the time. I am grateful to him for assisting in the fabrication of various antennas for my research.

Finally, I want to thank my brother and sisters, my friends, and my students back in India for their love and support.

Chapter 3 of this dissertation, in part, is a reprint of the material as it appears in G. Mishra, S. K. Sharma and J. S. Chieh, "A Circular Polarized Feed Horn With Inbuilt Polarizer for Offset Reflector Antenna for W -Band CubeSat Applications," in *IEEE Transactions on Antennas and Propagation*, vol. 67, no. 3, pp. 1904-1909, March 2019 and G. Mishra, S. K. Sharma and J. S. Chieh, "Analysis and Design of a W-Band Circular Polarized Feed Horn with Inbuilt Polarizer for Low *f*/*D* Offset Reflector Antenna," *2019 URSI International Symposium on Electromagnetic Theory (EMTS)*, San Diego, CA, USA, 2019, pp. 1-4. The co-authors listed in this publication directed and supervised research which forms the basis for the dissertation.

Chapter 4 of this dissertation, in part, is a reprint of the material as it appears in G. Mishra, S. K. Sharma and J. S. Chieh, "A High Gain Series-fed Circularly Polarized Traveling-Wave Antenna at W-band using a New Butterfly Radiating Element," in *IEEE Transactions on Antennas and Propagation*, 2020 and G. Mishra, S. K. Sharma and J. S. Chieh, "A W-Band Butterfly Shaped Series-Fed Circular Polarized Phased Array Antenna for CubeSats," *2019 IEEE International Symposium on Phased Array System & Technology (PAST)*, Waltham, MA, USA, 2019, pp. 1-8. The co-authors listed in this publication directed and supervised research which forms the basis for the dissertation.

Chapter 5 of this dissertation is a reprint of the material as it appears in G. Mishra, S. K. Sharma, J. S. Chieh and R. B. Olsen, "Ku-Band Dual Linear-Polarized 1-D Beam Steering Antenna Using Parabolic-Cylindrical Reflector Fed by a Phased Array Antenna," in *IEEE Open Journal of Antennas and Propagation*, vol. 1, pp. 57-70, 2020. The co-authors listed in this publication directed and supervised research which forms the basis for the dissertation.

Chapter 6 of this dissertation has been submitted and is currently under review and may appear as G. Mishra and S. K. Sharma, "A Multi-Functional Full-Polarization Reconfigurable 28 GHz Staggered Butterfly 1D-Beam Steering Antenna," in *IEEE Transactions on Antennas and Propagation*. The co-author listed in this publication directed and supervised research which forms the basis for the dissertation.

VITA

Ghanshyam Mishra

2011	Bachelors in Electronics and Telecommunication Engineering, University of Mumbai, India
2013	Masters in Electronics and Electrical Communication Engineering, Indian Institute of Technology IIT, Kharagpur, India
2020	Joint Ph.D. in Computational Science, San Diego State University and University of California, Irvine

RELATED REFEREED PUBLICATIONS

G. Mishra and S. K. Sharma, "A Multi-Functional Full-Polarization Reconfigurable 28 GHz Staggered Butterfly 1D-Beam Steering Antenna," in *IEEE Transactions on Antennas and Propagation* (under review).

G. Mishra, S. K. Sharma, and J. S. Chieh, "A High Gain Series-fed Circularly Polarized Traveling-Wave Antenna at *W*-band using a New Butterfly Radiating Element," in *IEEE Transactions on Antennas and Propagation*, vol. 68, 2020.

G. Mishra, S. K. Sharma, J. S. Chieh and R. B. Olsen, "Ku-Band Dual Linear-Polarized 1-D Beam Steering Antenna Using Parabolic-Cylindrical Reflector Fed by a Phased Array Antenna," in *IEEE Open Journal of Antennas and Propagation*, vol. 1, pp. 57-70, 2020.

G. Mishra, S. K. Sharma and J. S. Chieh "Analysis and Design of a W-Band Circular Polarized Feed Horn with Inbuilt Polarizer for Low f/D Offset Reflector Antenna," *Radio Science Bulletin*, (Invited extended paper as Young Scientist Award in URSI EMTS 2019).

G. Mishra, S. K. Sharma, and J. S. Chieh, "A Circular Polarized Feed Horn with Inbuilt Polarizer for Offset Reflector Antenna for *W*-Band CubeSat Applications," in *IEEE Transactions on Antennas and Propagation*, vol. 67, no. 3, pp. 1904-1909, March 2019.

G. Mishra and S. K. Sharma, "*Ka*-band Full Polarization Reconfigurable 1D Beam Steering Staggered Butterfly Phased Array Antenna," *2020 IEEE International Symposium on Antennas and Propagation & USNC/URSI National Radio Science Meeting*, Montreal, Canada, 2020.

G. Mishra, S. K. Sharma, J. S. Chieh, R. Olsen, and P. Nguyen, "Ku-Band Dual Linear Polarized Parabolic-Cylindrical Reflector Antenna with Beam Steering Performance," *International Applied Computational Electromagnetics Society Symposium (ACES)*, Monterey, CA 2020.

G. Mishra, S. K. Sharma and J. S. Chieh, "Finite Metal Wall Effects of W-Band Circular Polarized Horn Antenna with Inbuilt Polarizer," 2019 *IEEE International Symposium on Antennas and Propagation and USNC-URSI Radio Science Meeting*, Atlanta, GA, USA, 2019, pp. 971-972.

G. Mishra, S. K. Sharma and J-C. S. Chieh, " A W-Band Butterfly Shaped Series-Fed Circular Polarized Phased Array Antenna for CubeSats," presented at the *IEEE International Symposium on Phased Array Systems and Technology (PAST)*, Waltham, MA, Oct. 15-18, 2019.

G. Mishra, S. K. Sharma and J. S. Chieh, "Analysis and Design of a W-Band Circular Polarized Feed Horn with Inbuilt Polarizer for Low *f*/*D* Offset Reflector Antenna," 2019 *URSI International Symposium on Electromagnetic Theory (EMTS)*, San Diego, CA, USA, 2019, pp. 1-4.

G. Mishra, S. K. Sharma and J. S. Chieh, "A New Butterfly Radiating Element for Circular Polarized Series Fed Phased Array with Wide Axial Ratio Beamwidth at Millimeter Wave Band," *2018 IEEE International Symposium on Antennas and Propagation & USNC/URSI National Radio Science Meeting*, Boston, MA, 2018, pp. 1909-1910.

G. Mishra, A. T. Castro, S. K. Sharma and J. C. S. Chieh, "W-band feed horn with polarizer structure for an offset reflector antenna for cubesat applications," *2017 IEEE International Symposium on Antennas and Propagation & USNC/URSI National Radio Science Meeting*, San Diego, CA, USA, 2017, pp. 557-558.

G. Mishra, S. K. Sharma, J. C. S. Chieh and J. Rowland, "W-band circular polarized series fed single plane beamsteering array antenna with 4-bit phase shifter for cubesat applications," *2017 IEEE International Symposium on Antennas and Propagation & USNC/URSI National Radio Science Meeting*, San Diego, CA, USA, 2017, pp. 2555-2556.

AWARDS AND HONORS

Honorable Mention Paper Award, Student Paper Competition: 2020
IEEE International Symposium on Antennas and Propagation Society AP-S

Student Paper Competition Finalist: 2020
International Applied Computational Electromagnetics Society (ACES) Symposium

IEEE Antennas and Propagation Society Doctoral Research Grant Fellowship 2019

Student Paper Competition Finalist: 2019
IEEE International Symposium on Phased Array Systems and Technology

Young Scientist Award: 2019
International Union of Radio Science (URSI Commission B)

2nd Place: All California State University (CSU) Student Research Competition 2019

ESET Award: Computational Science Research Center 2019
Applied Computational Science and Engineering Student Support (ACSESS)

USNC-URSI Travel Grant Fellowship: 2019
National Radio Science Meeting

President Award: Student Research Symposium 2019
San Diego State University

University Graduate Fellowship: 2018
San Diego State University

Tioga Research Award: Computational Science Research Center 2018
Applied Computational Science and Engineering Student Support (ACSESS)

Director's Award: Computational Science Research Center 2017
Applied Computational Science and Engineering Student Support (ACSESS)

Junior Research Fellowship 2012
National Eligibility Test (NET) by the CSIR with an All India Rank-22.

ABSTRACT OF THE DISSERTATION

Analysis, Computation, and Design of Innovative High Gain Feed-Reflector and Beam Steering Antenna Solutions

by

Ghanshyam Mishra

Doctor of Philosophy in Computational Science

San Diego State University, 2020
and
University of California, Irvine, 2020

Professor Satish K. Sharma, Chair

Wireless communication is ubiquitous as we are in the cusp of intelligent connectivity (e.g., fifth-generation (5G) and internet of things (IoT)), autonomous devices, advance satellite communications, millimeter-wave communications, and augmented reality. The technology demands exploration in cost-effective and energy-efficient antenna technologies to facilitate the transformation of these innovations. This dissertation is the collection of research on novel high gain feed-reflector and beam steering antenna solutions to meet these futuristic demands in satellite and wireless communications.

As part of the dissertation, following significant antenna research contributions have been made to facilitate the high data throughput for satellite and wireless communication networks: (1) *W*-band (79 – 88 GHz) novel circularly polarized feed horn antenna feeding an offset parabolic reflector for CubeSats; (2) *W*-band (86 GHz) fixed-beam novel circularly polarized series-fed novel Butterfly antenna and 1D-beam steering phased array antenna for CubeSats; (3) *Ku*-band (12 – 14 GHz) dual-linear polarized 1D-beam steering parabolic-cylindrical reflector fed by a

silicon RFIC transceiver based flat panel phased array antenna; (4) Multi-functional *Ka*-band (28 GHz) staggered Butterfly array antenna for 5G communications with key features of full-polarization reconfigurability, flexible radiation pattern, and wide-angle 1D-beam steering performance; and (5) Investigation on the *Ka*-band (26.5 – 29.5 GHz) 3D metal printed dual circularly polarized feed-horn feeding a spherical reflector for high gain multiple-beam switching applications.

The relevant computational methods used in the research are computational electromagnetics, physical optics (PO), linear algebra, Monte-Carlo statistical analysis, and beam synthesis algorithm. Discussion about the proposed antennas include detailed theoretical analysis, numerical simulation, optimizations, beam synthesis algorithms, fabrication of the antennas and its control/beamforming feed networks, and finally, its characterization of impedance matching, gain, and radiation patterns.

Chapter 1

Introduction

1.1 Objective

There is an increasing demand for high gain antennas for satellite and wireless communication applications. The objective of the dissertation is to present fundamental insights into several innovative antenna designs along with their analyses and characterizations. The research is a collection of innovative feed-reflector antennas and planar 1D-beam steering array antennas providing high gain, cost-effective, and energy-efficient solutions for satellite and wireless applications.

First, two different novel antenna solutions are proposed for high data rate CubeSat application in the millimeter-wave *W*-band. One of the designs is an innovative inbuilt polarizer that provides symmetric and stable radiation pattern with high circular polarization (CP) purity. This polarizer is then fed to an offset reflector to provide high gain. The alternative solution is proposed using a novel series-fed Butterfly antenna array for high gain and 1D-beam steering performance for the CubeSat application at *W*-band (86 GHz).

Next, a hybrid reflector-phased array antenna technology is introduced to provide a cost-effective and energy-efficient solution for high data rate wireless application at *Ku*-band (12 – 14 GHz). The reflector is parabolic-cylindrical, and the phased array is a dual-linear polarized feed source placed along the focal line of the reflector to provide wide 1D-beam steering and high gain.

In line with the Butterfly radiating element, a modified staggered Butterfly array is proposed for the multi-functional application at 28 GHz fifth-generation (5G) band. The proposed staggered array is capable of full-polarization reconfiguration (right-hand circular polarization

(RHCP), left-hand circular polarization (LHCP), Linear-X, and Linear-Y polarization) with wide-angle 1D-beam steering and flexible radiation patterns of varying 3 dB gain-beamwidth.

Finally, a dual circularly polarized 3D metal printed feed horn is proposed for the 5G *Ka*-band high gain applications. A collection of such dual CP feed horns will be placed along the focal arc of the spherical reflector to provide high gain wide-angle beam switching.

1.2 Motivation and Background

1.2.1 *W*-band high gain circularly polarized antenna for CubeSat application

Although the prospect of high data rates is attractive at the millimeter-wave frequencies, the reality is that at these frequencies the wavelength is much smaller, and the associated free space path loss and propagation loss is much higher. Therefore, the characterization of the propagating channel between 75 – 110 GHz is critical, and using a CubeSat to do this is ideal. The benefit of operation in this band is that given a limited volume, the gain of the antenna is much higher.

CubeSats have evolved from an educational platform allowing universities to develop cost-effective flight-ready spacecraft to standard platforms that allow for advanced technology demonstrations [1]. Most CubeSats are used for earth science observation, including optical, infrared, and microwave imaging for things such as atmospheric properties including clouds and precipitation, land topography and soil moisture, ocean surface salinity and temperature, snow and ice cover, and gravity and magnetic field monitoring. CubeSats occupy the low earth orbit (LEO) at 500 km above the earth, with the ceiling at 2180 km. All these remote sensing applications generate large amounts of data, which require a satellite communication (SATCOM) downlink with high data rates. Although wideband SATCOM links do exist currently, spectrum demand is

only increasing. Many researchers have proposed using the millimeter-wave frequency band for SATCOM because it is relatively uncrowded and allows for high fractional bandwidths.

The *W*-band frequency spectrum is advantageous because of its wide swath of available bandwidth, which is uncrowded, and more importantly, there is an O_2 absorption window between 80 to 100 GHz, which allows for low atmospheric attenuation [2], as shown in Fig. 1.1. Fig. 1.2 shows some of the underlying assumptions that were used in the link budget calculations. We approximated the distance between the ground station and the CubeSat at the zenith to be 500km. At 60˚ away, the distance increases to 1000km. Table 1.1 shows the link budget calculations for a LEO downlink using *W*-Band. Calculations are for clear sky links, which do not include the effects of heavy clouds and rain. The Transmit antenna size was constrained to 1U diameter of 10 cm and

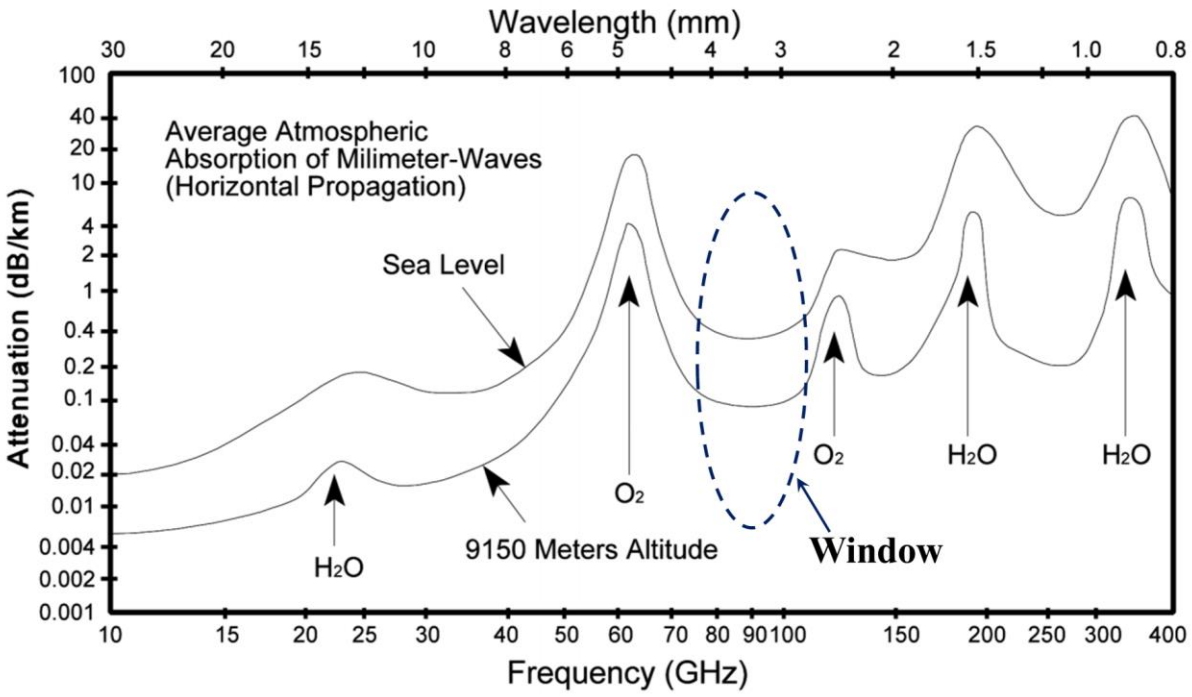

Figure 1.1 Atmospheric attenuation vs. frequency [2].

the propagation loss was calculated based on O_2 and H_2O absorption curves. Propagation loss in the millimeter-wave regime is often said to be severe, this is true, albeit only for terrestrial radio links. For SATCOM applications, the effective atmosphere extends only about 8 km, and so the propagation loss due to atmospheric absorption is minimal. In practice, a 10 dB link margin is probably realistic. From the available literature, CubeSats typically occupy LEO, usually in a circular orbit at an altitude of 500 km. As can be seen, a 200 Mbps link can be obtained in the *W*-Band at 86 GHz with a modest link margin of 12.2 dB at 500 km.

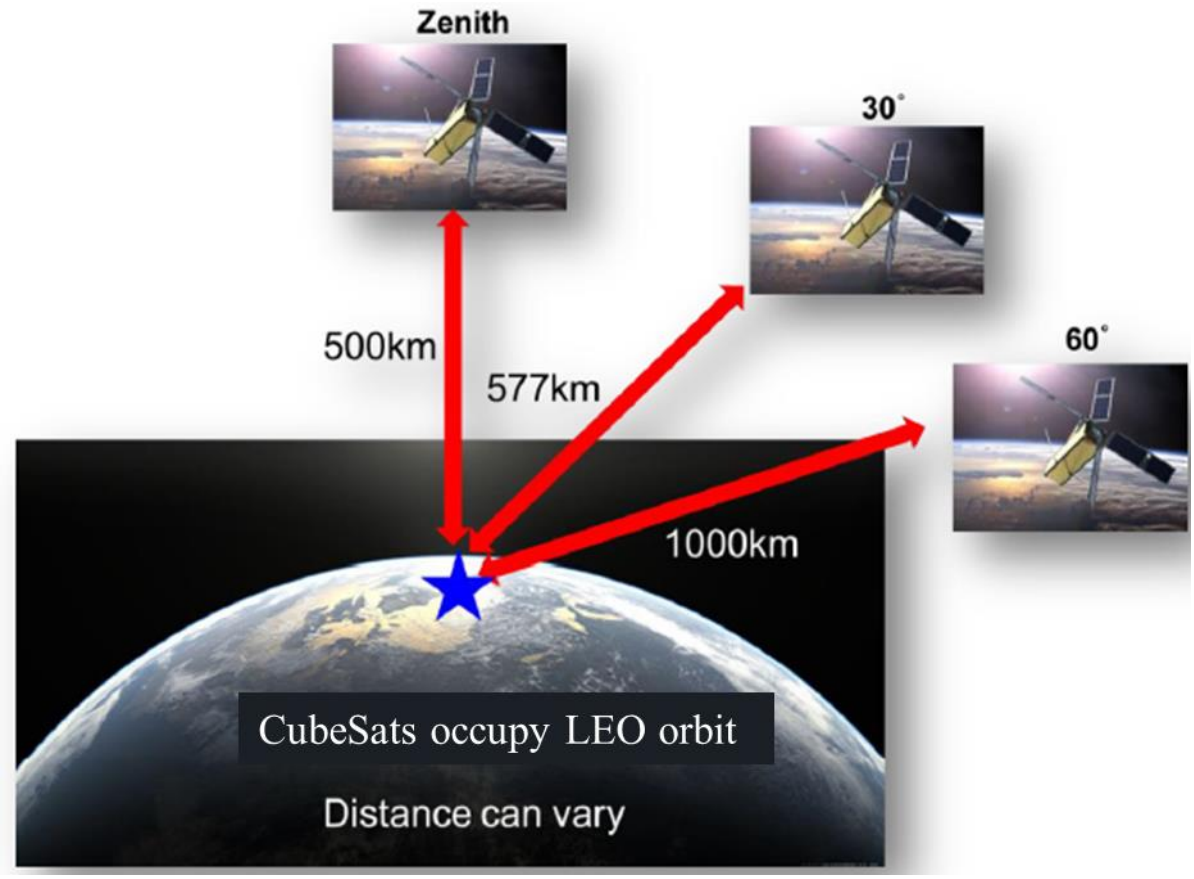

Figure 1.2 Assumptions for link budget calculations.

Table 1.1 Downlink budget for *W*-Band for various distances

LINK BUDGET ANALYSIS		
Parameters	***W*-band (86 GHz)**	**Unit**
Satellite Transmitter Power	0.6	W
Satellite Transmitter Power	28	dBm
Tx Losses	-3	dB
Tx Implementation Loss (Phase Noise)	-2	dB
Tx Antenna Gain (10 cm dish)	34	dBic
Tx EIRP	**57**	**dBm**
Path Loss (1000 km)	-191.1	dB
Polarization Loss	-0.5	dB
Antenna Misalignment Loss	-1	dB
Other Misc. Losses (Atmosphere ITU Rec 676-9)	-3	dB
Isotropic Signal Level receive Station	-138.6	dBm
Rx Antenna Gain (2 m dish)	65	dBic
Rx Signal Level	**-73.6**	**dBm**
Rx Noise Temperature	627	K
Rx Noise Figure	5	dB
Channel Bandwidth	100	MHz
Rx Noise power	-90.63	dBm
Rx C/No	17.03	dBHz
Rx Eb/No (FEC 0.75, 8 PSK)	14	dB
Required Rx Eb/No (8 PSK BER 10E-6)	7.9	dB
Data Rate	**200**	**Mbps**
Link Margin (2000 km)	**0.1**	**dB**
Link Margin (1000 km)	**6.2**	**dB**
Link Margin (500 km)	**12.2**	**dB**

There are several resources available related to feed-reflector and phased array antenna. A variety of feed horn antennas and the reflector assembly is presented in [3], [4]. In Fig. 1.3(a), a dual CP feed polarizer is designed using an array of metallic pins as delay structure to achieve the desired phase shift for the generation of CP [5]. The losses of the pins, along with the fabrication challenges, limit the use of this method at millimeter-wave frequencies. In Fig. 1.3(b), a linear polarization to circular polarization conversion is achieved at sub-mm-wave frequencies by

exploiting differential dispersion in hexagonal waveguides [6]. Fig.1.4 shows a configuration of offset parabolic reflector fed by a feed horn antenna [7].

(a)

(b)

Figure 1.3 Literature examples of circularly polarized feed horn antennas (a) *Ka*-band dual CP horn antenna with arrays of pins [5], and (b) Sub-millimeter hexagonal waveguide-based CP horn antenna [6].

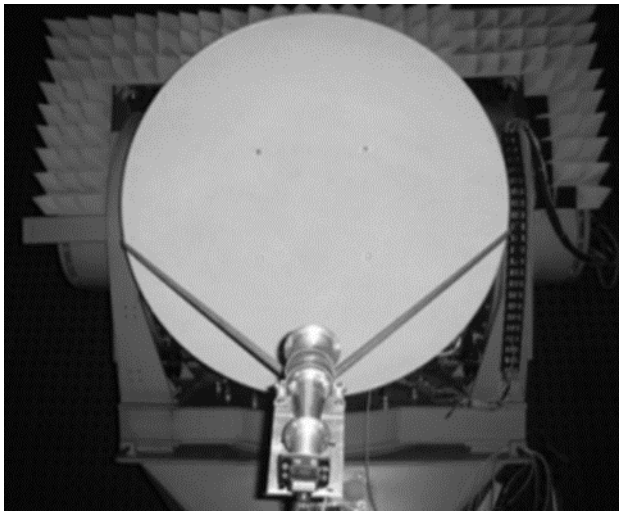

Figure 1.4 Offset parabolic reflector fed by horn antenna [7].

1.2.2 *Ku*-band hybrid reflector-phased array for naval high data rate wireless applications

An ever-increasing demand for high data rate wireless communication has augmented the interest in the design of energy-efficient and cost-effective antenna systems. Naval ships traditionally use satellite communications and other maritime radios for ship-to-ship and ship-to-shore communications. However, such communications are restricted by delays and limited bandwidth. High data rate wireless networks can enable rapid deployability of the ships in adverse situations, quick adaptation to a dynamic environment, and improved interoperability with a high probability of interception of friendly or enemy vessels. The antennas enabling high data rate wireless networks require a broad impedance bandwidth, a stable radiation pattern, high gain, and beam steering characteristics.

We propose a hybrid reflector-phased array antenna system with an integrated beamforming network for high gain 1D-beam steering solution at *Ku*-band (12 – 14 GHz). The hybrid reflector-phased array antenna system uses a phased array antenna as the feed source to illuminate the parabolic-cylindrical reflector. The parabolic-cylindrical reflector provides wide-angle beam steering at low *f*/*D* compared to a conventional parabolic reflector [8] - [9]. The phased array, when used as a feed source for the reflector, will require 75% fewer antenna elements and active RF components as compared to a stand-alone phased array antenna. Thus, the power requirement and the cost of the system is reduced by one-fourth. The proposed antenna will attain four primary objectives: (1) wideband dual-polarized antenna for transmit and receive communications; (2) stable radiation pattern with low cross-polarization; (3) high antenna gain of at least 25 dBi; and (4) beam steering of at least ±30°.

In [8], a dual-band *Ku*- and *Ka*-band array-fed offset parabolic-cylindrical reflector antenna is reported for advanced precipitation radar. The cross-section of the array-fed reflector is shown

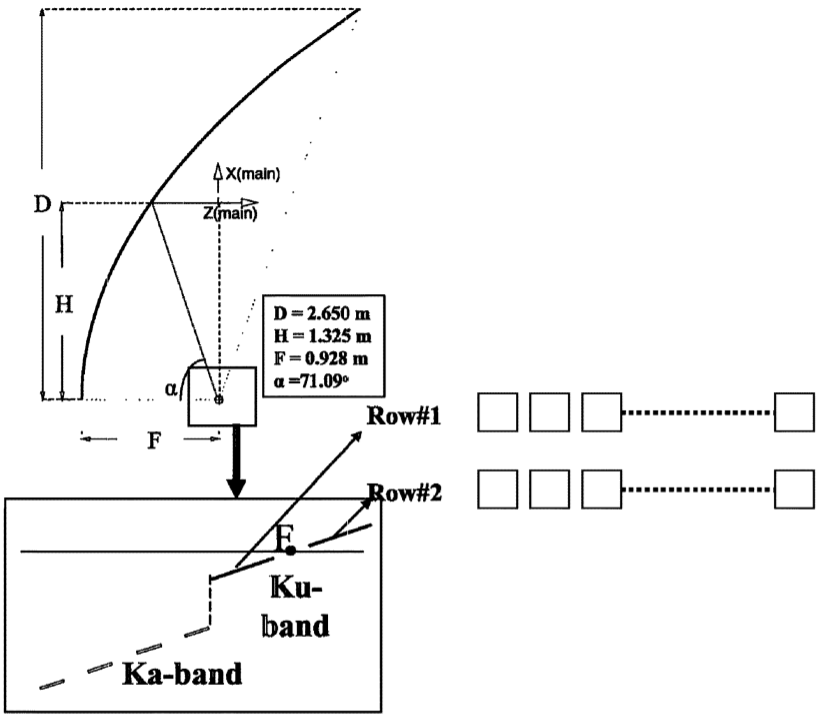

(a)

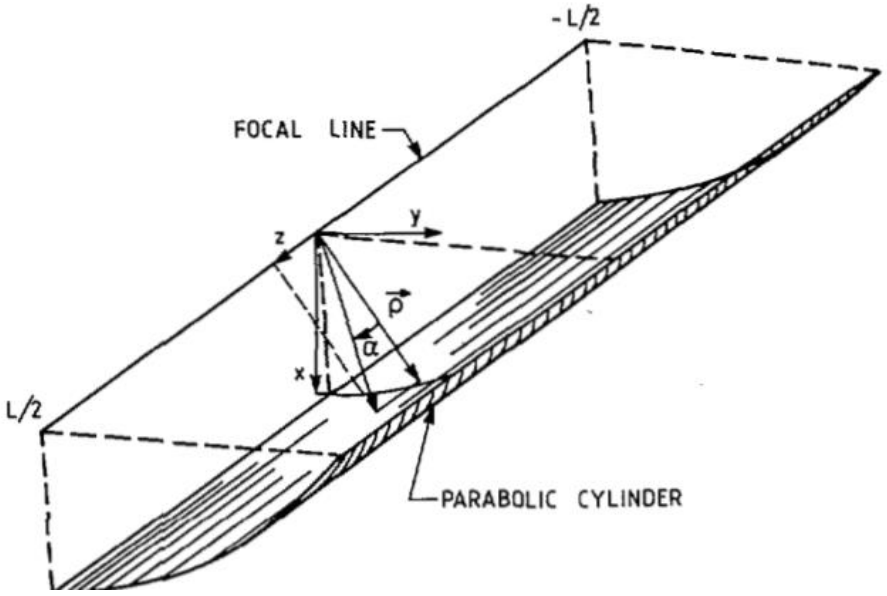

(b)

Figure 1.5 Literature examples of parabolic-cylindrical reflector antenna (a) Cross-section of array-fed offset cylindrical reflector [8], and (b) Coordinates for radiation analysis of cylindrical reflector [10].

in Fig. 1.5(a). In [8], a passive array design is implemented without the real implementation of active beamforming. A comprehensive analysis of the parabolic-cylindrical reflector antenna is discussed in [10]. Fig. 1.5(b) shows the parabolic-cylindrical reflector coordinates used in the radiation analysis.

1.2.3 Multi-functional beam steering antenna application at *Ka*-band

The fifth-generation (5G) demands the utilization of efficient antennas, which can cater to multiple users and, at the same time, be cost-effective. A multi-functional antenna is an ideal candidate for such challenging applications as they can achieve full-polarization reconfiguration (RHCP, LHCP, Linear-X, and Linear-Y) along with wide-angle 1D-beam steering and flexible radiation patterns.

As modern wireless communication systems develop, polarization reconfigurable antennas have received increasing attention. They have desirable advantages for wireless communication applications, such as avoiding fading loss caused by multipath effects in wireless networks, realizing frequency reuse to expand the capability in satellite communication systems, and being a good candidate in massive multiple-input–multiple-output (Massive-MIMO) systems to improve the system capacity by dynamic polarization reconfiguration of the antenna along with beam steering.

In addition to polarization reconfiguration, a wide-angle beam steering array antenna can further enhance multi-functionality by providing connectivity with the mobile communication device. Another feature of a multi-functional antenna is flexible radiation patterns to provide varying 3 dB gain-beamwidth. Flexible patterns can be used to optimize the transmit power of the

5G base station in the dynamic environment for a user with diverse cell range, angle, and gain requirements.

In [11], a multifunctional circular microstrip patch antenna with simultaneous polarization reconfiguration (linear horizontal, linear vertical, LHCP, and RHCP polarization) is reported, as shown in Fig. 1.6(a). Fig. 1.6(b) indicates previously published work on the multi-functional antenna, which is a 1 × 4 phased array antenna between 1.5 – 2.4 GHz, capable of achieving full-polarization reconfiguration and 1D-beam steering [12]. In [13], a 28 GHz series-fed linear polarized array is presented, as shown in Fig. 1.6(c). The array is capable of 1D-beam steering and flexible radiation pattern with varying 3 dB gain-beamwidth.

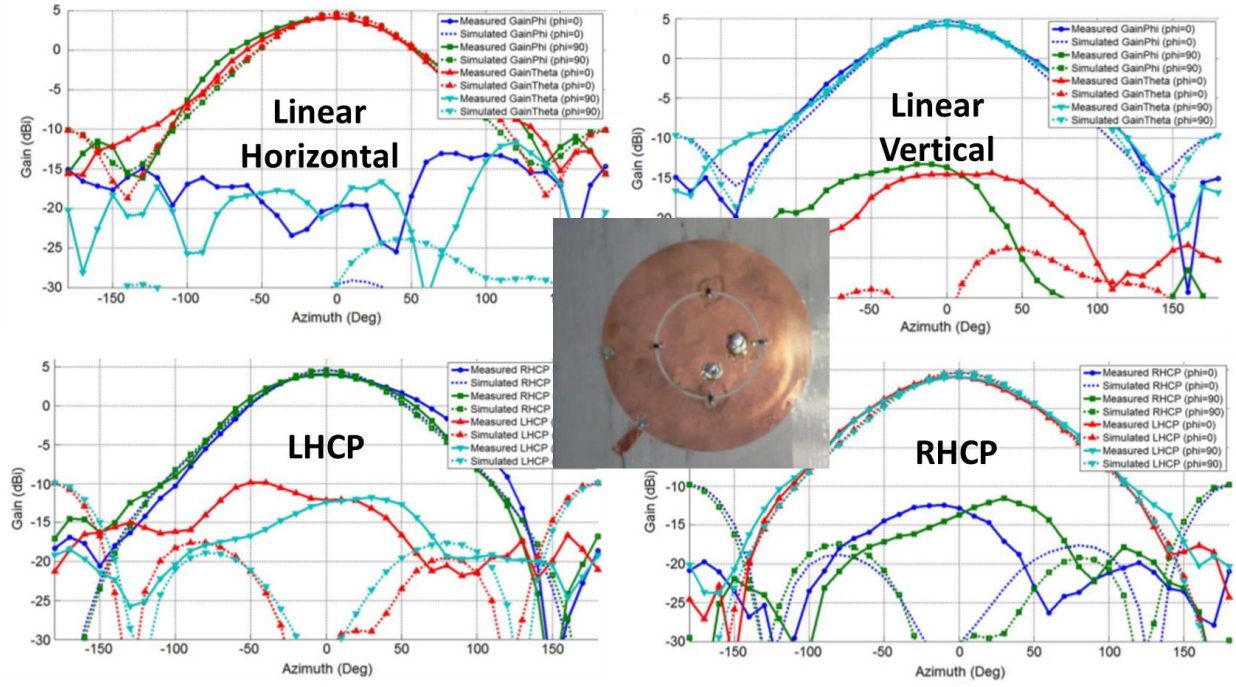

(a)

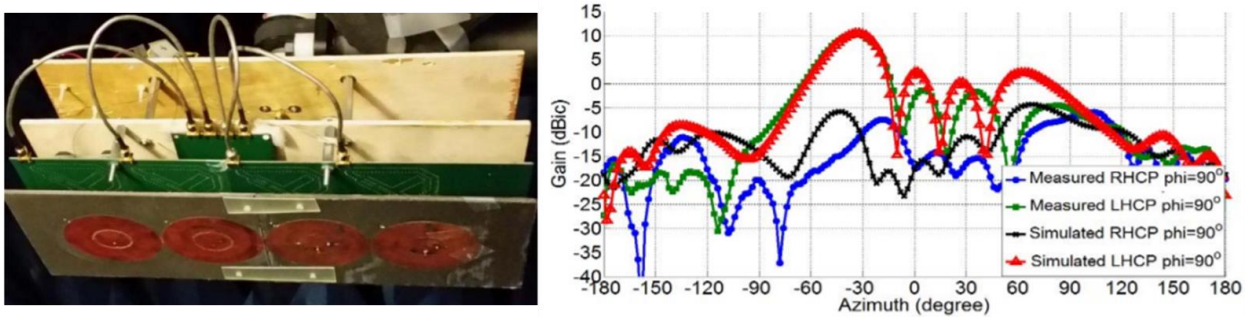

(b)

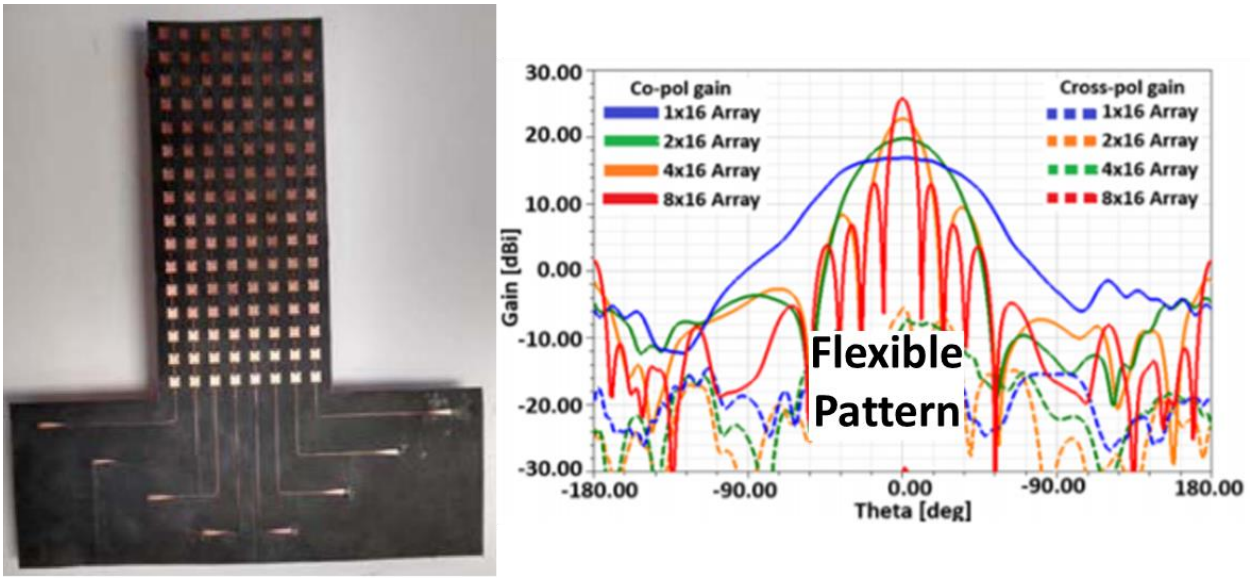

(c)

Figure 1.6 Literature examples of multi-functional antenna (a) Polarization reconfigurable patterns [11], (b) 1 × 4 multi-functional phased array antenna geometry with integrated beamforming network [12], and (c) 28 GHz series-fed multi-functional antenna array [13].

1.2.4 *Ka*-band 3D metal printed dual circular polarized feed horn antenna

A dual CP horn antenna with high inter-port isolation is highly desired for increasing the system capacity of the wireless communication. In the *Ka*-band due to higher path loss, high gain antennas are required. Thus, the dual-CP feed horn antenna is used as a feed source to a spherical

reflector to provide high gain. Also, multiple horns placed along the focal arc of the spherical reflector can provide multiple-switched beams to cater to different users at various locations.

The metal 3D printing technique can be advantageous because of its lower cost, lighter weight, and faster prototyping. Another critical factor is that the 3D printing process can produce the proposed antenna in a single piece, which can reduce the assembly error. Figs. 1.7(a) and 1.7(b) show the literature on the 3D metal printed CP horn antenna at *Ka*-band and *V*-band, respectively [14], [15]. In [14], the inbuilt polarizer consists of radially opposite grooves inside a circular waveguide and excited using a coaxial probe. In [15], the inbuilt polarizer includes a mono-groove inside the circular waveguide and excited using waveguide ports. A wide-angle scanning offset reflector antenna using multiple-displaced feed source is presented in [16], as shown in Fig. 1.8.

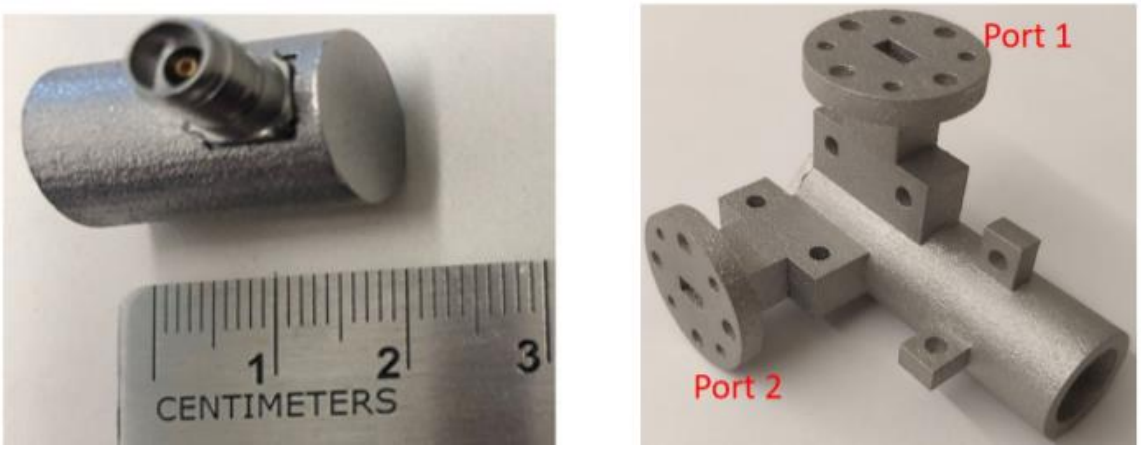

(a) (b)

Figure 1.7 Literature examples of 3D metal printed CP horn antenna (a) *Ka*-band CP horn antenna [14], and (b) *V*-band dual CP horn antenna [15].

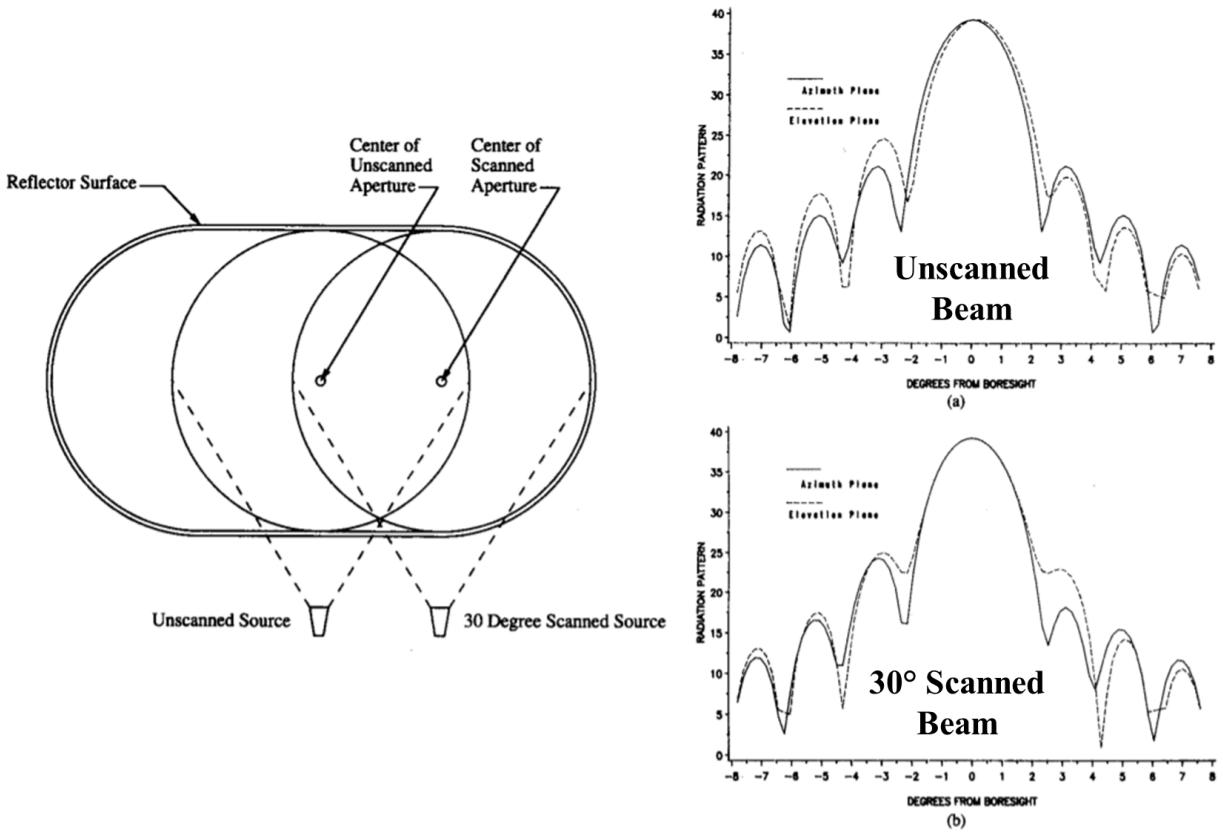

Figure 1.8 Wide-angle scanned reflector beams with the displacement of feed source [16].

1.3 Literature Review

Detailed literature reviews of each of the research topics are included in the respective chapters 3 to 7.

1.4 Research Resources

The research begins with the analysis to provide insights into the proposed designs. The mathematical analysis is followed with numerical simulations to achieve the desired objectives. The results are finally verified with the fabrication and measurement of the prototypes. This process requires the utilization of extensive software and hardware resources. A brief description

of these simulation, fabrication, and measurement tools used in the completion of the research is outlined below.

1.4.1 Simulation and Analysis Tools

The Antenna and Microwave Laboratory (AML) at San Diego State University has most of the required resources to accomplish the research goals from analysis to measurement. The AML laboratory is equipped with powerful work stations which have all the necessary software such as Ansys high frequency structural simulator (HFSS) which is a commercial finite element method based Maxwell solver for electromagnetic structures, TICRA GRASP for reflector analysis, NI AWR microwave office and Keysight ADS for circuit analysis, MATLAB for numerical analysis and post-processing of the results, and Altium Designer for multilayer PCB designing.

1.4.2 Fabrication Tools

The Protomat LPKF S62 milling machine is available for fabrication of the planar microwave printed circuit board PCB, as shown in Fig. 1.9. The finest milling drill bit of S62 is the universal cutter with a diameter of 0.15 mm. The soldering of the connectors and other passive and active RF components are then performed at the soldering station shown in Fig. 1.10.

Figure 1.9 LPKF Protomat PCB milling machine S62.

Figure 1.10 Surface mount soldering station.

1.4.3 Measurement Tools

The scattering parameters of the designs are measured using the Anritsu 37269D vector network analyzer (VNA) covering 40 MHz to 40 GHz, as shown in Fig. 1.11(a), and Keysight E5063A covering 100 kHz to 18 GHz, as shown in Fig. 1.11(b). There are two anechoic chambers at AML for the antenna radiation pattern measurement installed by Microwave Vision Group (MVG) ORBIT FR. The first anechoic chamber shown in Fig.1.12 is capable of both the spherical near-field and far-field radiation measurements. It can cover the frequency range from 800 MHz

(a)

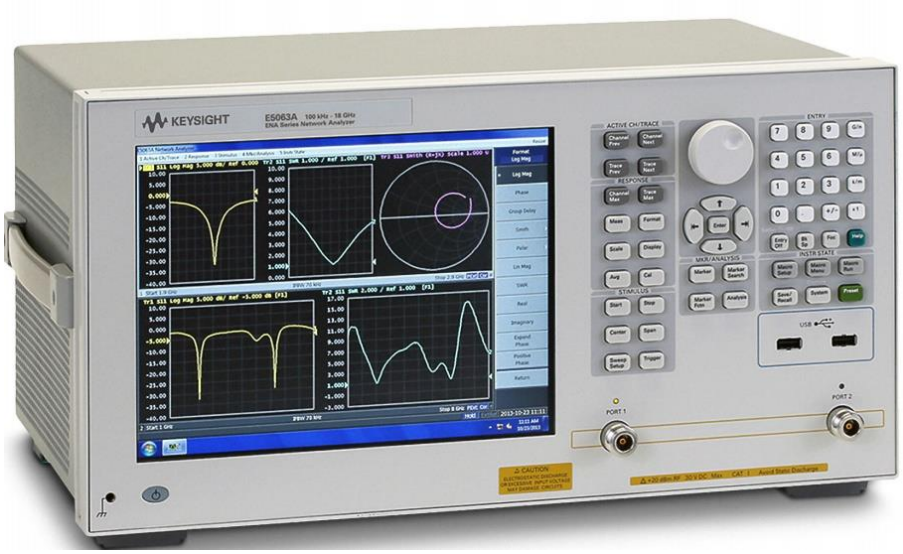

(b)

Figure 1.11 Vector network analyzer (VNA) used for measurement of antenna scattering parameter (a) Anritsu 37269D and (b) Keysight E5063A.

to 40 GHz with the ORBIT/FR 959 acquisition measurement software and provide measurement results for 2D/3D radiation pattern, realized gain, and polarization with sense of rotation.

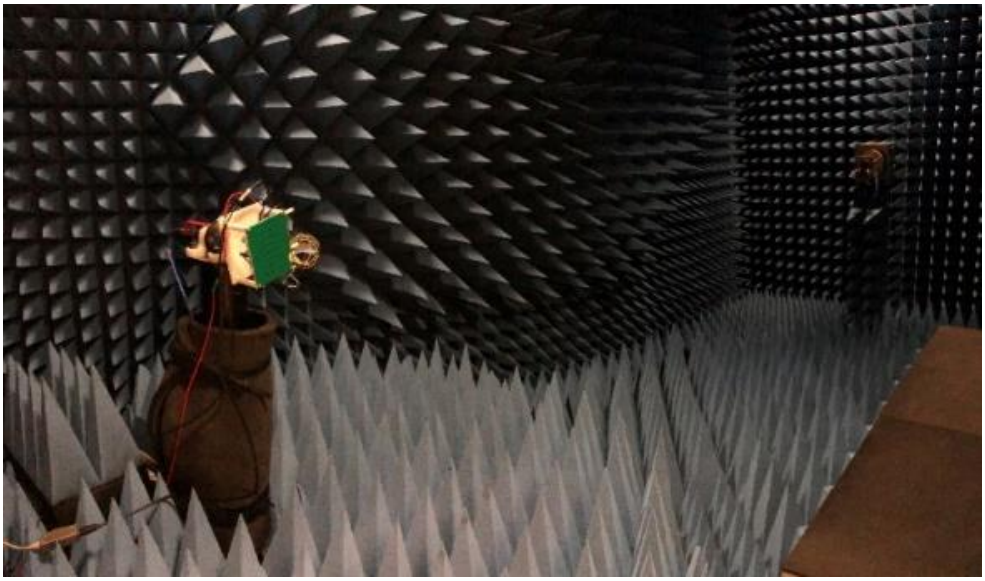

Figure 1.12 Antenna testing in anechoic chamber at Antenna and Microwave Laboratory, San Diego State University.

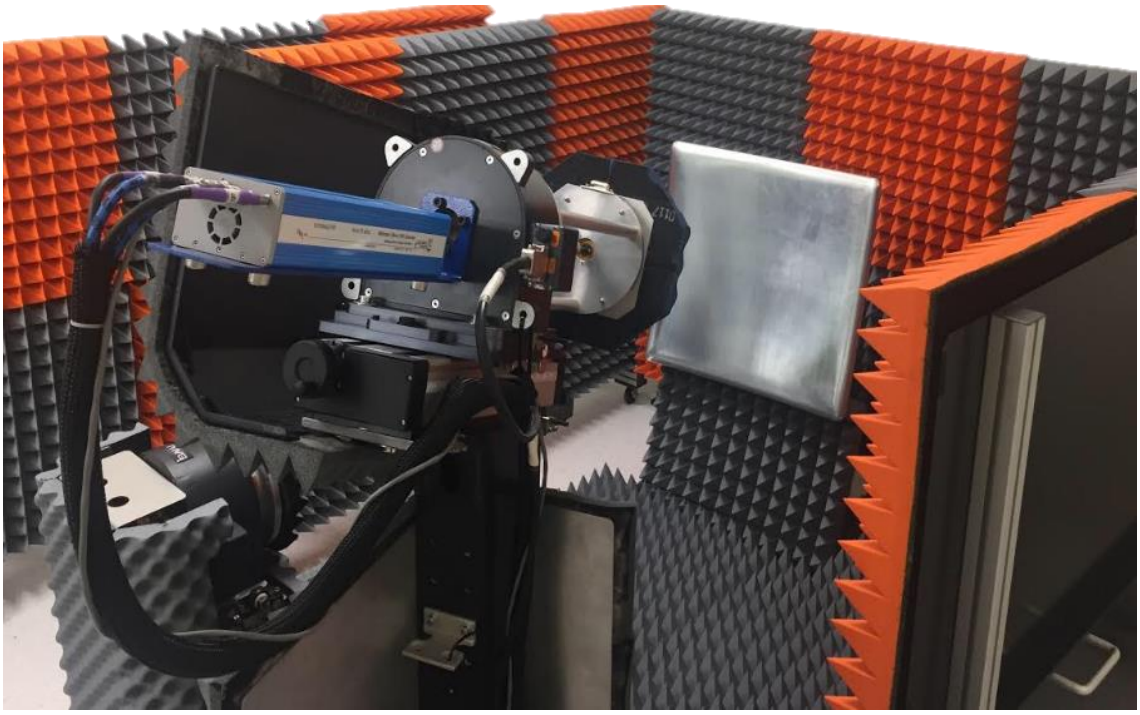

Figure 1.13 Mini-Compact Antenna Test Range (M-CATR) system at Antenna and Microwave Laboratory, San Diego State University.

The second anechoic chamber is a Mini-Compact Antenna Test Range (M-CATR) from Microwave Vision Group (MVG) for millimeter-wave antenna measurements up to 110 GHz, as shown in Fig. 1.13. It is connected with the Keysight N5225A Power Network Analyzer (PNA) that ranges from 10 MHz to 50 GHz and can be extended up to 110 GHz using external frequency extenders. The extenders available are for two spectrums, namely, *V*-band (50 GHz-75 GHz) and *W*-band (75 GHz-110 GHz). The mini-compact chamber is capable of measuring realized gain, 2D and 3D radiation patterns, and polarization of the antenna with the sense of rotation using the ORBIT/FR 959 acquisition measurement software.

1.5 Dissertation Overview

The organization and overview of the dissertation are as follows. Chapter 2 describes the theory of phased array antenna, circular waveguide, leaky-wave antenna, and computational electromagnetic theory relevant to the research.

Chapter 3 is focused on the analysis and design of circularly polarized high gain *W*-band feed reflector antennas for CubeSat applications. The inbuilt polarizer section of the horn consists of nine pairs of circular cavities to generate circular polarization, eliminating the need for an external orthomode transducer or a complex septum. The polarizer is analyzed using the differential dispersion effect from the cavities along the length of the waveguide. The antenna has impedance matching ($|S_{11}| < -15$ dB) and axial ratio (AR) below 1.2 dB from 79.5 GHz to 88 GHz. The horn antenna is then used as a feed source to illuminate an offset parabolic reflector of 10 cm diameter and low $f/D = 0.25$. The feed-reflector assembly is also integrated inside a 1U volume of a 6U-CubeSat chassis, and the radiation performance is analyzed using the multilevel fast multipole method (MLFMM) along with the method of moments (MoM) in TICRA GRASP. The measurement of the prototyped feed horn and the offset parabolic reflector antenna validates the analysis and simulation results.

Chapter 4 is based on the analysis, design, and optimization of a novel series-fed CP traveling-wave antenna called Butterfly antenna, at millimeter-wave (*W*-band). The Butterfly unit-cell consists of a sequentially rotated series-fed linear array of four microstrip patch antennas. The proposed circularly polarized Butterfly structure offers low cross-polarization radiation and wide axial ratio beamwidth. A periodic leaky-wave antenna (LWA) analysis provides insights into the radiation characteristics of the Butterfly series-fed linear array antenna, which is validated by the full-wave electromagnetic simulations. The open-stopband (OSB) is suppressed in the broadside

direction due to the cancellation of the internal reflections within each cell of the sequential-phase fed linear array. The measured and the simulated axial ratio, radiation patterns, and gain are presented for the broadside radiation of the parallel-series fed 8 × 24 and 32 × 24 planar array antennas at 86 GHz. The average measured 3 dB gain beamwidths are 9.5° and 2.9° along the ϕ = 0° plane of the 8 × 24 and 32 × 24 planar array antennas, respectively. The simulation of 1D-beam steering performance is also achieved using appropriate beamforming algorithms; however, it could not be experimentally verified due to fabrication issues.

In chapter 5, we have proposed a 1D-beam steering high gain hybrid reflector-phased array antenna system for wireless communication at *Ku*-band (12 - 14 GHz). The proposed hybrid antenna system consists of a D = 50 cm offset parabolic-cylindrical reflector with f/D = 0.4 fed by an 8 × 4 dual linear-polarized stacked patch phased array antenna placed along the focal line of the reflector. The parabolic-cylindrical reflector has the property of a wide-angle beam steering along the cylindrical axis as compared to a conventional parabolic reflector. A complete implementation of the dual linear-polarized phased array antenna with the silicon RFIC chipset-based beamforming network and integrated with aluminum offset parabolic-cylindrical reflector is reported. Cavity model and physical optics approximations are used to analyze the radiation characteristics of the phased array and the induced currents on the parabolic-cylindrical reflector surface, respectively. Furthermore, the multilevel fast multipole method (MLFMM) is used along with the method of moments (MoM) in TICRA GRASP for a comprehensive analysis of the proposed hybrid reflector system. The peak directivity of the reflector pattern is around 27 dBi for both the X-polarization and Y-polarization, and a beam scanning of ±30° is achieved along the cylindrical axis of the reflector for 3 dB reduction in the gain. The analytical and computed results of the proposed hybrid reflector-phased array antenna system are experimentally verified.

In chapter 6, a novel multi-functional staggered 8 × 12 Butterfly phased array antenna is proposed at *Ka*-band (28 GHz) for 5G communications with key features of full-polarization reconfigurability, flexible radiation pattern, and wide-angle 1D beam steering performance. The unit-cell of the proposed array is two Butterfly radiating antennas separated by $2\lambda g$ (λg = effective wavelength) with two-ports, where each Butterfly is a sequentially-rotated series-fed microstrip patch antennas. Full-polarization reconfiguration (RHCP, LHCP, Linear-X, and Linear-Y polarization) is achieved by suitable excitation of the ports to realize increased system capacity. Flexible radiation pattern with dynamic 3 dB gain-beamwidth from 16° to 90° is achieved to realize a variable cellular range, angle, and gain requirements. The proposed staggered planar array configuration reduces the spacing between the adjacent series-fed linear array to $0.45\lambda_0$, where λ_0 is the free-space wavelength at 28 GHz. This reduced spacing enables a larger beam steering angle up to ±84° without any grating lobes. An analytical study using a periodic leaky-wave antenna (LWA) theory is included to provide insights into the radiation characteristics of the Butterfly series-fed linear array antenna. The beam steering characteristics are verified using measured patterns of the individual branches and by applying the computed array factor. The full-polarization reconfiguration and flexible radiation patterns with sidelobe reduction are implemented and experimentally verified with a 16-channel Analog Devices ADMV4821 RFIC *Ka*-band beamformer.

Chapter 7 discusses the analysis, optimization, and development of a *Ka*-band dual circularly polarized feed-reflector antenna for 5G applications. A spherical reflector is used with five dual-CP feed sources to achieve high gain multiple-beam switching. Finally, conclusions and future studies are included in chapter 8.

Chapter 2

Computational Electromagnetics and Relevant Antenna Theory

2.1 Computational Electromagnetics

2.1.1 Finite Element Method

Finite Element Method (FEM) is a computational tool for engineers and physicists, utilizing rapid computations to solve large problems insoluble by analytical, closed-form expressions [17]. The "Finite Element Method" involves subdividing a large problem into individually simple constituent units, which are each soluble via direct analytical methods, then reassembling the solution for the entire problem space as a matrix of simultaneous equations. The model is subdivided into tetrahedral elements and basis function, W_n is defined per tetrahedral. W_n define conditions between nodal locations in the overall mesh of tetrahedra, based on the problem inputs. The functions are simple and non-zero only within the tetrahedra. These basis functions are then multiplied by field equation.

Ansys HFSS uses FEM based numerical solver to solve for the radiation fields. The following are the steps in the Ansys HFSS FEM solution process.

HFSS solves field equation derived from Maxwell's equations as (2.1) [18]:

$$\nabla \times \left(\frac{1}{\mu_r} \nabla \times \vec{E} \right) - k_o^2 \varepsilon_r \vec{E} = 0 \tag{2.1}$$

Integrating the result over volume, we get (2.2) [18]:

$$\int_V \left[W_n \cdot \nabla \times \left(\frac{1}{\mu_r} \nabla \times \vec{E} \right) - k_o^2 \varepsilon_r W_n \vec{E} \right] dV = 0 \tag{2.2}$$

Integration is replicated in thousands of equations for n =1, 2 ...N. Intent is to obtain N equations with N unknowns for the solution.

The equation is rewritten, using Green's and Divergence theorem, and set equal to excitation/boundary terms as (2.3) [18]:

$$\int_V \left[(\nabla \times W_n) \bullet \left(\frac{1}{\mu_r} \nabla \times \vec{E} \right) - k_o^2 \varepsilon_r W_n \vec{E} \right] dV = \int_S (boundary\, term) dS \tag{2.3}$$

The E-field is written as a summation of unknowns, x_m, times same basis functions used in generating the initial series of equations $\vec{E} = \sum_{m=1}^{N} x_m W_m$

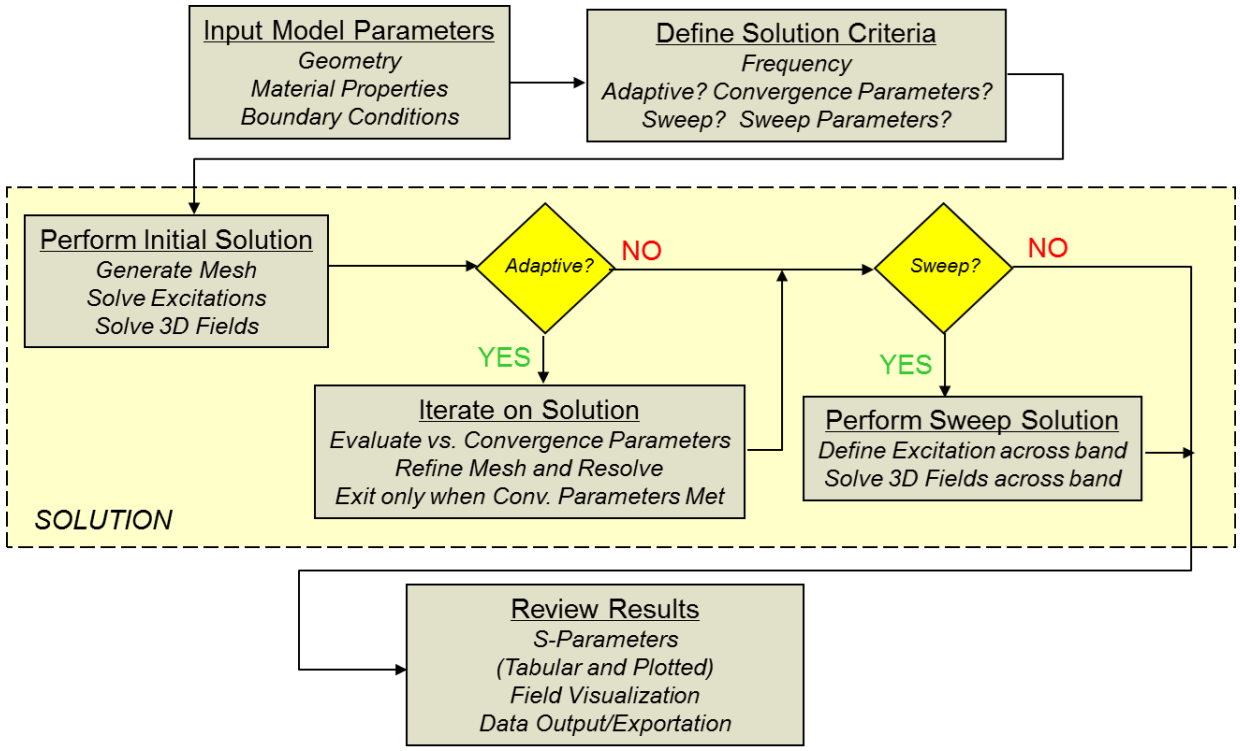

Figure 2.1 Flowchart of the general design process in Ansys HFSS full-wave numerical analysis tool [18].

Resulting equations allow the solution of unknowns, x_m, to find E as given by (2.4) [18]:

$$\sum_{m=1}^{N} x_m \cdot \left(\int_V \left[(\nabla \times W_n) \bullet \left(\frac{1}{\mu_r} \nabla \times W_m \right) - k_o^2 \varepsilon_r W_n W_m \right] dV \right) = \int_S (boundary\ term) dS \tag{2.4}$$

Note: Equation has the basic form $Ax = B$, where A is the basis functions and field equation, in a known $N \times N$ matrix, 'x' is the unknown to be solved for, and B is the excitation.

Due to its sparse and banded nature, the matrix can be solved using mathematical matrix decomposition techniques. HFSS uses an iterative *Multifrontal Matrix Solver*. Matrix equations are thus formulated to solve electromagnetic field behavior. The flowchart of the general design process in Ansys HFSS is illustrated in Fig. 2.1 [18].

Reflector analyses are based on asymptotic high-frequency expansions of Maxwell's equations. These are high-frequency methods that are only accurate when the dimensions of the objects being analyzing are large compared to the wavelength of the field. The asymptotic techniques briefly introduced in the following sections include physical optics, geometrical optics, and multilevel fast multipole methods.

2.1.2 Current Distribution Method: Physical optics (PO)

Physical optics (PO) assumes that the incident field from the feed is known and that it excites surface currents ($\mathbf{J_s}$) on the reflector's surface as $\mathbf{J_s} = 2\hat{\mathbf{n}} \times \mathbf{H}^i$. Once the induced surface currents $\mathbf{J_s}$ are found on the reflector's surface, the magnetic vector potential $\mathbf{A}$ and the far-zone field can be calculated [19].

In practice, the electric far-field is calculated directly from $\mathbf{J}s$ by (2.5) [19]:

$$\mathbf{E}^{far} = -j\omega\mu \frac{e^{-j\beta r}}{4\pi r} \iint_{S_r} \left[\mathbf{J_s} - (\mathbf{J_s} \cdot \hat{\mathbf{r}}) \hat{\mathbf{r}} \right] e^{j\beta \hat{r} \cdot r'} ds' \tag{2.5}$$

This equation follows directly from the relation between the far-zone electric field and the magnetic vector potential **A**, given as (2.6) [19]:

$$\mathbf{E}^{far} = -j\omega\mathbf{A}_{\perp} \tag{2.6}$$

which can be written formally as (2.7) [19]:

$$\mathbf{E}^{far} = -j\omega\mathbf{A} - \left(-j\omega\mathbf{A}\cdot\hat{\mathbf{r}}\right)\hat{\mathbf{r}} = -j\omega\left(A_{\theta}\hat{\theta} + A_{\phi}\hat{\phi}\right) \tag{2.7}$$

This approach is also known as Rusch's method [19]. TICRA GRASP can be used to evaluate the PO based field patterns for any aperture shape and any aperture current distribution.

2.1.3 Aperture Distribution Analysis: Geometric Optics (GO)

With the *aperture distribution method,* the electric field is first determined over a plane, which is normal to the reflector's axis, and lies at the focal point (the *antenna aperture*). GO (ray tracing) is used to determine the electric field. Equivalent sources are formed over the aperture plane. It is assumed that the equivalent sources are zero outside the reflector's aperture. The radiation pattern is then computed from the electric field on the focal-plane aperture [20].

Ticra Grasp tool is used to perform the GO analysis of the reflector. The following provides a brief overview of the reflector radiation pattern when a feed with a rotationally symmetric pattern is placed at the focal point, which has its axis inclined at an angle ψ relative to the axis of the reflector.

If the feed is made from coaxial circular waveguides excited by TE_{1m} and TM_{1m} modes, it will have a radiation pattern of the form, given by (2.8) [20]:

$$\mathbf{E}_f = \frac{e^{-jk_0 r}}{r}\left[\mathbf{a}_{\theta_0} e_1(\theta_0)\sin(\phi_0) + \mathbf{a}_{\phi_0} e_2(\theta_0)\cos(\phi_0)\right] \tag{2.8}$$

For a circular symmetric pattern with no cross-polarization $e_1(\theta_0) = e_2(\theta_0) = e(\theta_0)$

The reflected pattern at the reflector surface is given by (2.9) [20]:

$$\mathbf{E}_r = -\mathbf{E}_f + 2(\mathbf{n}\cdot\mathbf{E}_f)\mathbf{n} \tag{2.9}$$

The focal-plane aperture fields are given by (2.10) – (2.12) [20]:

$$E_{ax} = \frac{4fe^{-j2k_0 f}e(\theta_0)}{(4f^2+\rho^2)\left[4f^2+\rho^2-4fy\sin\psi+(4f^2-\rho^2)\cos\psi\right]}\times\left[2xy(1-\cos\psi)-4fx\sin\psi\right] \tag{2.10}$$

$$E_{ay} = \frac{4fe^{-j2k_0 f}e(\theta_0)\times\left[(4f^2+\rho^2-2x^2)+(4f^2-\rho^2+2x^2)\cos\psi-4fy\sin\psi\right]}{(4f^2+\rho^2)\left[4f^2+\rho^2-4fy\sin\psi+(4f^2-\rho^2)\cos\psi\right]} \tag{2.11}$$

$$E_{az} = 0 \tag{2.12}$$

where, $\rho^2 = x^2 + y^2$ and $\theta_0 = \cos^{-1}\left(\frac{4f^2-\rho^2}{4f^2+\rho^2}\cos\psi - \frac{4fy}{4f^2+\rho^2}\sin\psi\right)$

Both the GO and the PO methods produce accurate results for the main beam and first sidelobe. The far-off angle pattern from the main beam can be accurately predicted by including diffraction effects (scattering) from the reflector's rim. It is done by augmenting GO with the use of the geometrical theory of diffraction (GTD), or by augmenting the PO method with the physical theory of diffraction (PTD). Appendix A shows the MATLAB code for GO analysis for a linear polarized feed source for an offset reflector.

2.1.4 Multilevel Fast Multipole Method (MLFMM)

The effect of CubeSat chassis on the integrated feed reflector assembly is analyzed in Ticra ESTEAM. The multilevel fast multipole method (MLFMM) is used along with the method of moment (MoM), which formulates the linear partial differential equation to an integral equation

for electrically large objects. MLFMM is faster for large objects than MoM alone, and there is no loss of accuracy. This method is an alternative to MoM and applies to electrically larger structures like radar cross-section (RCS) analysis, reflector antenna design, finite-size antenna arrays, antenna integration on large structures, etc., making full-wave current-based solutions of such structures a possibility.

The MLFMM reduces the memory complexity from N^2 to $N\log N$, and the solving complexity from N^3 to $N_{iter}N\log N$ as compared to MoM method, where N and N_{iter} are the number of unknowns and the number of iterations in the solver. The MLFMM method subdivides the boundary element mesh into different clusters, and if two clusters are in each other's far-field, all calculations can be reduced to the midpoints of the clusters with almost no loss of accuracy. For clusters not in the far-field, the traditional boundary element mesh must be applied. That is, MLFMM introduces different levels of clustering to enhance computation speed additionally. The MLFMM implementation example in TICRA is shown in Fig. 2.2 [21].

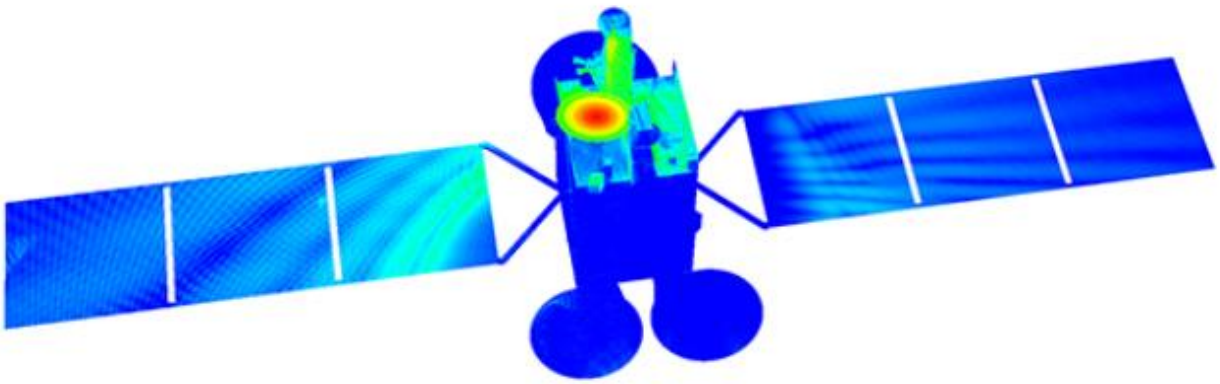

Figure 2.2 MLFMM implementation on electrically large platform [21].

2.1.5 Sequential Nonlinear Programming Optimization Method

Ansys HFSS is used to optimize the proposed designs based on the optimization method of Sequential Nonlinear Programming (SNLP). It is for the numerical solution of constrained nonlinear optimization problems of the form given by (2.13) and (2.14) [22]:

$$\text{minimize } f(x) \text{ over } x \in \mathrm{R}^{\mathrm{n}} \tag{2.13}$$

$$\text{subject to } h(x) = 0 \tag{2.14}$$

Sequential quadratic programming is an iterative procedure that models the nonlinear programming (NLP) for a given iteration x^k, by a Quadratic Programming (QP) sub-problem. It solves the QP sub-problem and then uses the solution to construct a new iteration x^{k+1}. This construction is done in such a way that the sequence (x^k) converges to a local minimum x^* of the NLP (2.13) - (2.14) as $k \rightarrow \infty$ [22].

The method has a theoretical basis that is related to

1. The solution of a set of nonlinear equations using Newton's method.
2. The derivation of simultaneous nonlinear equations using Kuhn-Tucker conditions to the Lagrangian of the constrained optimization problem.

The Lagrange function, $L(\mathbf{X}, \lambda)$, corresponding to the problem is given by (2.15) [22]:

$$L = f(\mathrm{X}) + \sum_{k=1}^{p} \lambda_k h_k(\mathrm{X}) \tag{2.15}$$

where λ_k is the Lagrange multiplier for the kth equality constraint.

The Kuhn-Tucker necessary conditions can be stated as (2.16) [22]:

$$\nabla L = 0 \text{ or } \nabla f + \sum_{k=1}^{p} \lambda_k \nabla h_k = 0$$

$$h_k(X) = 0, \quad k = 1, 2, \ldots, p \tag{2.16}$$

where [A] is an $n \times p$ matrix whose kth column denotes the gradient of the function h_k. The above equations represent a set of $n+p$ nonlinear equations in $n+p$ unknowns (x_i, $i=1,...,n$ and λ_k, $k=1,...,p$). Thus, we obtain (2.17) [22]:

$$\begin{bmatrix} [\nabla^2 L] & [H] \\ [H]^T & [\varnothing] \end{bmatrix}_j \begin{Bmatrix} \Delta X \\ \Delta\lambda \end{Bmatrix}_j = -\begin{Bmatrix} \nabla L \\ h \end{Bmatrix}_j \quad \text{with} \quad \begin{matrix} \Delta X_j = X_{j+1} - X_j \\ \Delta\lambda_j = \lambda_{j+1} - \lambda_j \end{matrix} \tag{2.17}$$

The above equation can be solved to find the change in the design vector $\Delta\mathbf{X_j}$ and the new values of the Lagrange multipliers λ_{j+1}. The iterative process indicated by the above equation can be continued until convergence is achieved.

2.2 Reflector Antennas

Reflector antennas are widely used in satellite communications, radio-astronomy, high-resolution radars, etc., owing to its simple design and very high gain. The simplest reflector antenna consists of two components: a reflecting surface and a feed antenna at the reflector's focal point. Three types of reflectors, namely, offset parabolic reflector, parabolic-cylindrical reflector, and spherical reflector, are studied as part of different research, and brief description of them are outlined below.

2.2.1 Offset parabolic Reflector Antenna

A paraboloid reflector transforms a spherical wave radiated by the feed located at its focus into a plane wave. Fig 2.3 presents the geometry of the offset-fed parabolic reflector. The equations for the reflector surface are given by (2.18) and (2.19) [23]:

$$\text{Rectangular coordinates } r^2 = 4\left(f + z\right) \tag{2.18}$$

$$\text{Polar coordinates } \rho = \frac{f}{\cos^2(\psi/2)} \tag{2.19}$$

where f is the focal length, D is the diameter, ρ the distance from the focus to the reflector, and ψ is the angle made by the feed at the reflector from the horizontal axis.

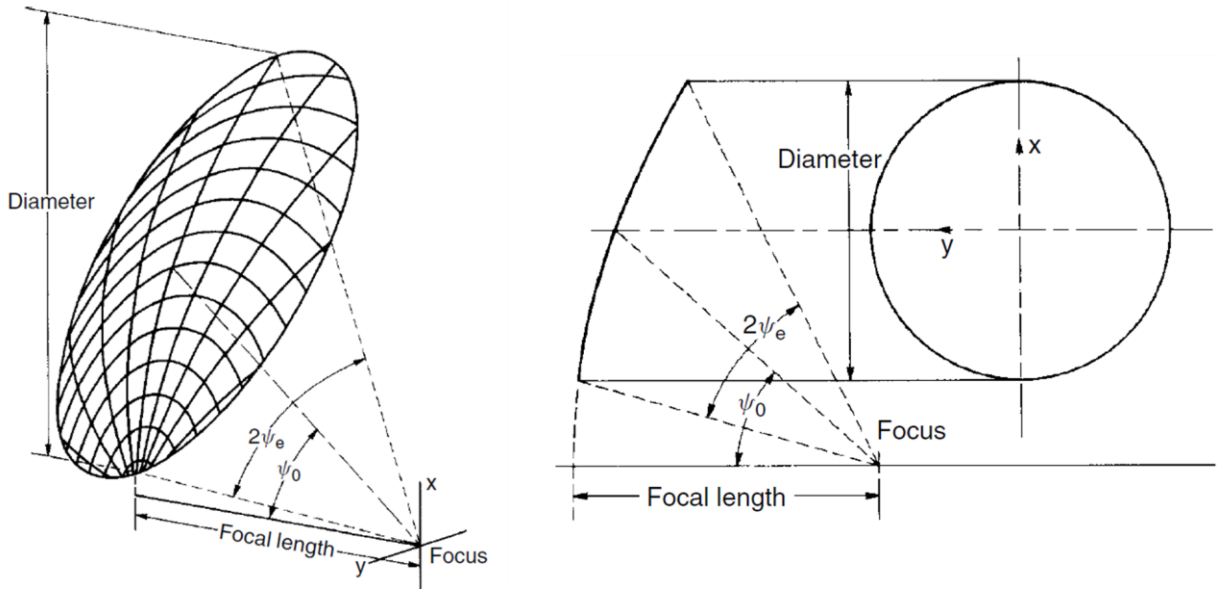

(a) (b)

Figure 2.3 Offset-fed parabolic reflector geometry (a) Perspective, and (b) Orthographic view [23].

The phase center of the feed needs to be at the focus of the reflector to eliminate any phase error losses in the aperture plane because it would have a constant phase. However, the feed phase center cannot always be placed at the focus. The phase-center location will change with frequency, which is called as axial defocusing. The axial defocusing phase error loss can be estimated by approximating the distribution with a quadratic aperture phase distribution. Given z as the axial defocusing, the maximum phase deviation S can be combined with the quadratic phase error loss of the circular Gaussian distribution to estimate the phase error loss, where S is given as (2.20) [23]:

$$S = \frac{z}{\lambda}\left[1 - \cos\left(2\tan^{-1}\frac{1}{4f/D}\right)\right] \tag{2.20}$$

In offset reflector, the feed is moved out of the aperture and thus reduces the blockage loss compared to the symmetric reflector. The feed is pointed toward the center of the reflector to reduce the spillover, but the feed phase center is still located at the focus of the reflector. The projection of the offset reflector is a circle, but the rim of the reflector is elliptical. The angle from the axis of the parabola to the center of the cone of the reflector is ψ_0 and the reflector subtends an angle $2\psi_e$ about this centerline.

The relevant angles for the offset reflector are given by (2.21) – (2.22) [23]:

$$\psi_0 = \tan^{-1}\frac{16fH}{16f^2 + D^2 - 4H^2} \tag{2.21}$$

$$\psi_e = \tan^{-1}\frac{8fD}{16f^2 + 4H^2 - D^2} \tag{2.22}$$

One disadvantage of the parabolic reflector antenna is limited beam scanning by laterally moving the phase center of the feed off-axis. The secondary beam degrades when the feed is moved at a larger distance from the focus point. The sidelobes show the effect of coma lobes, where the sidelobes on the boresight side grow, and the sidelobes on the other side decrease.

To achieve, wide-angle beam scanning, the alternative reflector geometries like parabolic-cylindrical reflector and spherical reflector are used.

2.2.2 Parabolic-Cylindrical Reflector Antenna

The parabolic-cylindrical reflector is cylindrically shaped with a parabolic cross-section. Due to the cylindrical shape, this reflector has a focal line instead of a single focal point as with

the parabolic reflector. The parabolic-cylindrical reflector provides a wide-angle beam steering along the cylindrical axis (1D-beam steering) compared to a conventional parabolic reflector. The feed source is a line source or a planar source along the focal line of the reflector.

The geometry and the coordinate system of the parabolic-cylindrical reflector fed by the line feed source antenna are shown in Fig. 2.4.

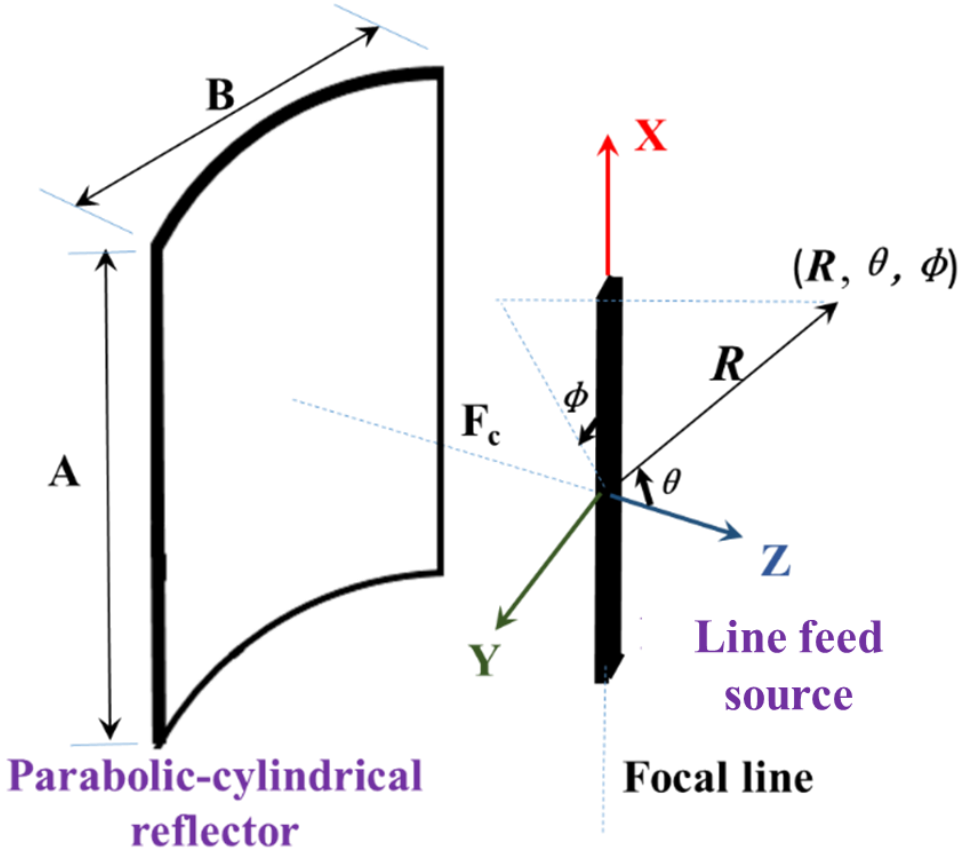

Figure 2.4 Geometry and coordinate system of parabolic-cylindrical reflector fed by a line source.

The reflector geometry is defined using (2.23) and (2.24) as [24]:

$$z(y) = \frac{y^2}{4F_c} - F_c \tag{2.23}$$

$$\hat{n} = \hat{y}\cos\phi_n + \hat{z}\sin\phi_n \text{ and } \phi_n = \tan^{-1}\left(-\frac{2F_c}{y}\right) \tag{2.24}$$

where $\hat{n}$ is the unit normal vector of the reflector surface and F_c is the focal length of the parabolic cross-section of the reflector.

The physical optics (PO) approximate method is used to find the induced current on the reflector surface. The PO analysis assumes that the incident field from the feed is known and that it excites surface currents ($\mathbf{J_s}$) on the reflector's surface given by (2.25) [24]:

$$\mathbf{J_s} = 2\hat{\mathbf{n}} \times \mathbf{H}^i \tag{2.25}$$

where, $\mathbf{H}^i = H_\theta^T \hat{\theta} + H_\phi^T \hat{\phi}$ is the incident magnetic field on the reflector surface.

Once the induced surface currents $\mathbf{J_s}$ are found on the reflector's surface, the magnetic vector potential **A** and the far-zone field can be calculated. In practice, the electric far-field is calculated directly from $\mathbf{J}_S$ by (2.26) [24]:

$$\mathbf{E}^{far} = -j\omega\mu\frac{e^{-jk_0R}}{4\pi R}\iint_{S_r}\left[\mathbf{J_s} - \left(\mathbf{J_s}\cdot\hat{a}_R\right)\hat{a}_R\right]e^{jk_0\vec{r}\cdot\hat{a}_R}ds \tag{2.26}$$

Thus, for the parabolic-cylindrical reflector antenna, the electric field can also be expressed as (2.27) [24]:

$$\mathbf{E}^{far} = \frac{j}{2}\frac{\eta_0}{\lambda}\frac{e^{-jk_0R}}{R}\int_{-A/2}^{A/2}\int_{-B/2}^{B/2}\left[\mathbf{J_s} - \left(\mathbf{J_s}\cdot\hat{a}_R\right)\hat{a}_R\right]\sqrt{1+\frac{y^2}{4F_c^2}}e^{jk_0\vec{r}\cdot\hat{a}_R}dxdy \tag{2.27}$$

The other class of antenna that can provide wide-angle beam steering is a spherical reflector where the feed sources are placed along the focal arc.

2.2.3 Spherical Reflector Antenna

For a feed-scan parabolic reflector, the pattern develops coma lobes, and the beam shape generally degrades. In a spherical reflector, however, when the feed is moved in an arc from the center of the sphere, it sees the same reflector geometry, and thus wider scanning is possible. The geometry of a spherical reflector is shown in Fig. 2.5. To cover the desired angular scanning range, the physical size of the reflector should be larger than the effectively illuminated aperture [25].

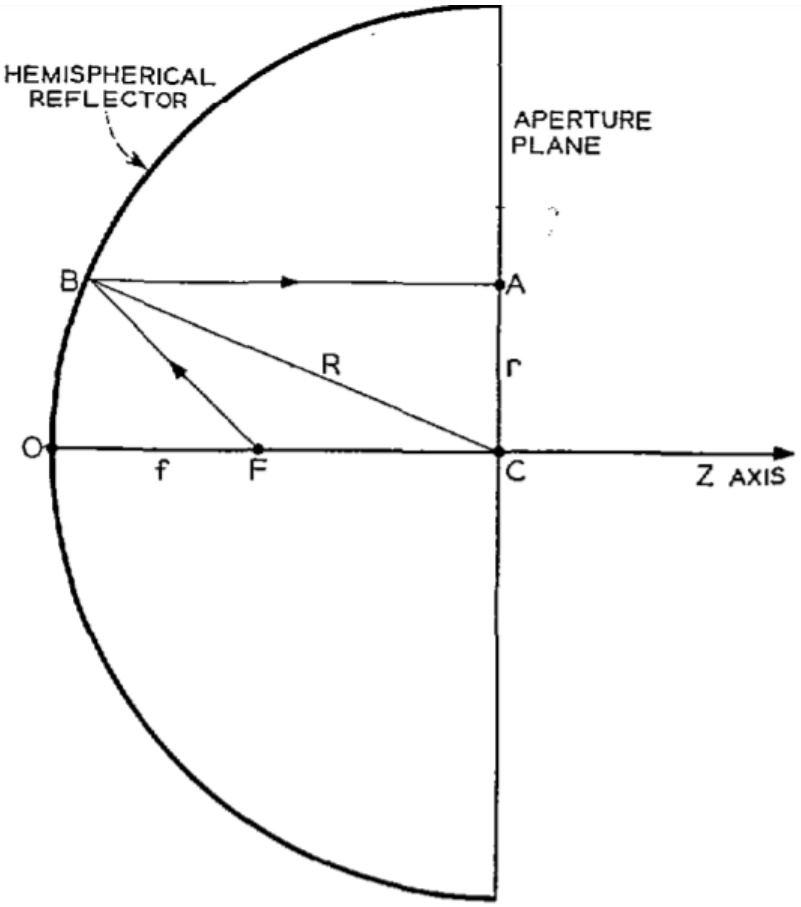

Figure 2.5 Geometry of a spherical reflector [25].

Using the geometrical properties of a sphere, for a beam scan angle of α (degrees or radians) and radius of the sphere R, the relation between the diameter of effectively illuminated aperture ($D_{ill.}$), and the diameter of the actual aperture of reflector (D) is given as (2.28) [26].

$$D = 2R\sin\left(\sin^{-1}\left(\frac{D_{ill.}}{2R}\right)+\alpha\right) \tag{2.28}$$

The total phase error over the illuminated aperture can be minimized if the feed is located at an optimal distance from the reflector apex. The optimal focal length is given by (2.29) [26]:

$$F_{op} = \frac{1}{4}\left(R+\sqrt{R^2-\left(\frac{D_{ill}}{2}\right)^2}\right) \tag{2.29}$$

The feeds for the reflector used in the research include phased array feed and circular waveguide-based feedhorn antenna. The theory for both the phased array antenna and the circular waveguide is explained next.

2.3 Phased Array Antenna and Beamforming Concept

Electronically steerable antennas, also known as phased arrays, have been a research topic for more than 70 years with the analysis of linear arrays by Schelkunoff in 1943 [27] being one of the pioneering works. In phased arrays, all the antenna elements are simultaneously excited, and the beam is steered by applying a progressive phase shift across the aperture. Thereby higher gain can be achieved than for switched-beam arrays where only a small number of the elements are turned on at a time. It remained a costly technology, employed mostly for specialized applications such as air traffic control in airports [28], [29], as well as various space-borne applications [30]. With the continued breakthroughs and cost reductions of electronic components, phased array technology is no longer prohibitively expensive. Furthermore, the development of modern-day mobile communications network and the increased demands hereof, imply that phased arrays are now of interest for many such applications, also from a commercial perspective.

Array antenna is a solution to obtain highly directive antennas from a combination of a plurality of antennas. The total radiated field of the array is the vector addition of electrically and geometrically arranged individual elements radiated fields. The directive pattern is obtained by constructive interference of fields from the elements of the array in the desired direction and cancellation in undesired directions. The geometrical configuration of the overall array (linear, circular, rectangular, and spherical, etc.), the relative displacement between the elements, the excitation amplitude, the excitation phase of the individual elements and the relative pattern of the individual elements are the influencing factors of array radiation characteristics.

Phased array is obtained by controlling the excitation phase of individual elements in an array where each succeeding element has a β progressive phase lead current excitation relative to the preceding one. The maximum radiation can be realized in any desired direction to form a scanning array by controlling the progressive phase difference between the elements.

2.3.1 Linear Array Antenna

In a linear array, antenna elements are geometrically arranged along a line, as presented in Fig. 2.6 [31]. The array factor is the resultant radiation characteristics of the geometrical arrangement of an isotropic radiator. If the actual elements are not isotropic sources, the total field is the product of array factor and the field of a single element.

Array factor (*AF*) of a linear array is given by (2.30) [32]:

$$AF = \sum_{n=1}^{N} e^{j(n-1)(kd\cos\theta+\beta)} = \sum_{n=1}^{N} e^{j(n-1)\psi} \tag{2.30}$$

where, $\psi = kd\cos\theta + \beta$, and N is the number of the elements.

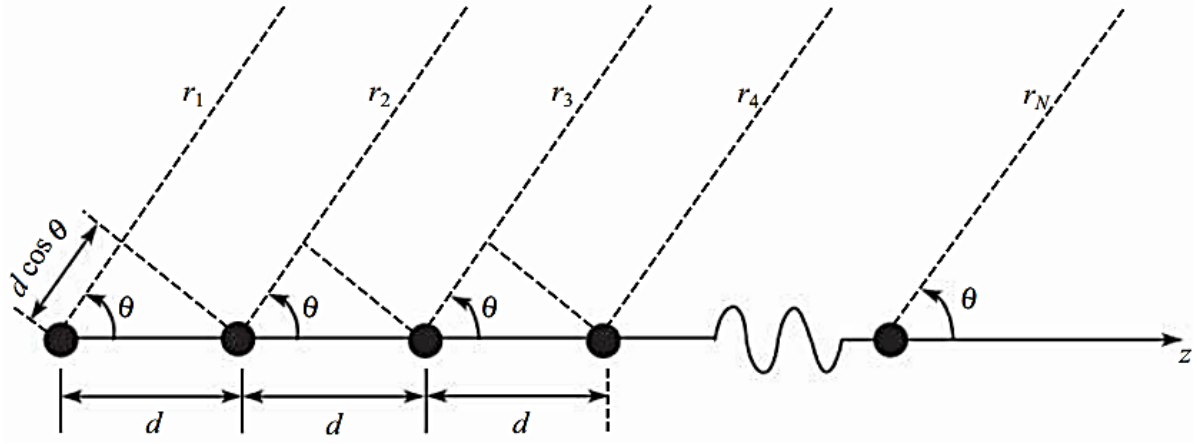

Figure 2.6 Far-field geometry of an N-element array of isotropic sources along the z-axis [31].

The *AF* can be normalized when the reference is the physical center of the array as (2.31) [32]:

$$AF = \frac{1}{N}\left[\frac{\sin\left(\frac{N}{2}\psi\right)}{\sin\left(\frac{1}{2}\psi\right)}\right] \tag{2.31}$$

If the desired direction to steer a *z*-directed linear array is at $\theta = \theta_0$, progressive phase shift β must be determined as follows (2.32) [32]:

$$\beta = -kd\cos\theta_0 \tag{2.32}$$

In broadside array, maximum radiation of the array is directed normal to the axis of the array, whereas in end-fire array maximum radiation is along the axis of the array. Fig. 2.7 shows the broadside and end-fire radiation of the linear array with *N=10*.

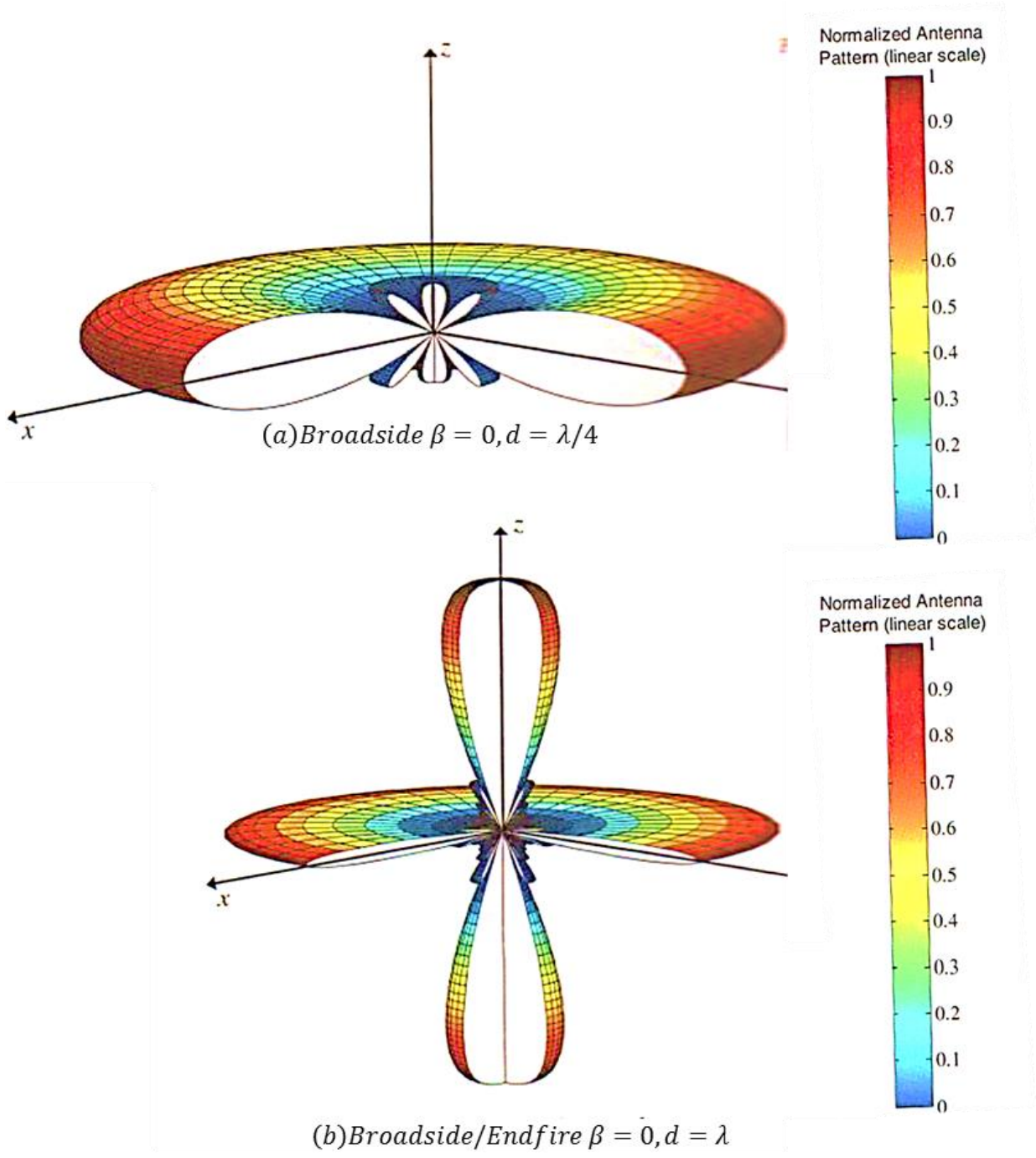

Figure 2.7 Example of broadside and end-fire radiation of the linear array [32].

2.2.2 Planar Array Antenna

In the planar array, radiators are geometrically arranged along the two dimensions, as shown in Fig. 2.8. The planar array offers control and shaping of the array in two planes as opposed to one plane in the linear array.

The normalized array factor *AF* for the planar array is given as (2.33) [32]:

$$AF = \left\{ \frac{1}{M} \frac{\sin\left(\frac{M}{2}\psi_x\right)}{\sin\left(\frac{\psi_x}{2}\right)} \right\} \left\{ \frac{1}{N} \frac{\sin\left(\frac{N}{2}\psi_y\right)}{\sin\left(\frac{\psi_y}{2}\right)} \right\} \tag{2.33}$$

where, *M* and *N* are the number of elements along *x*- and *y*-direction, respectively, and

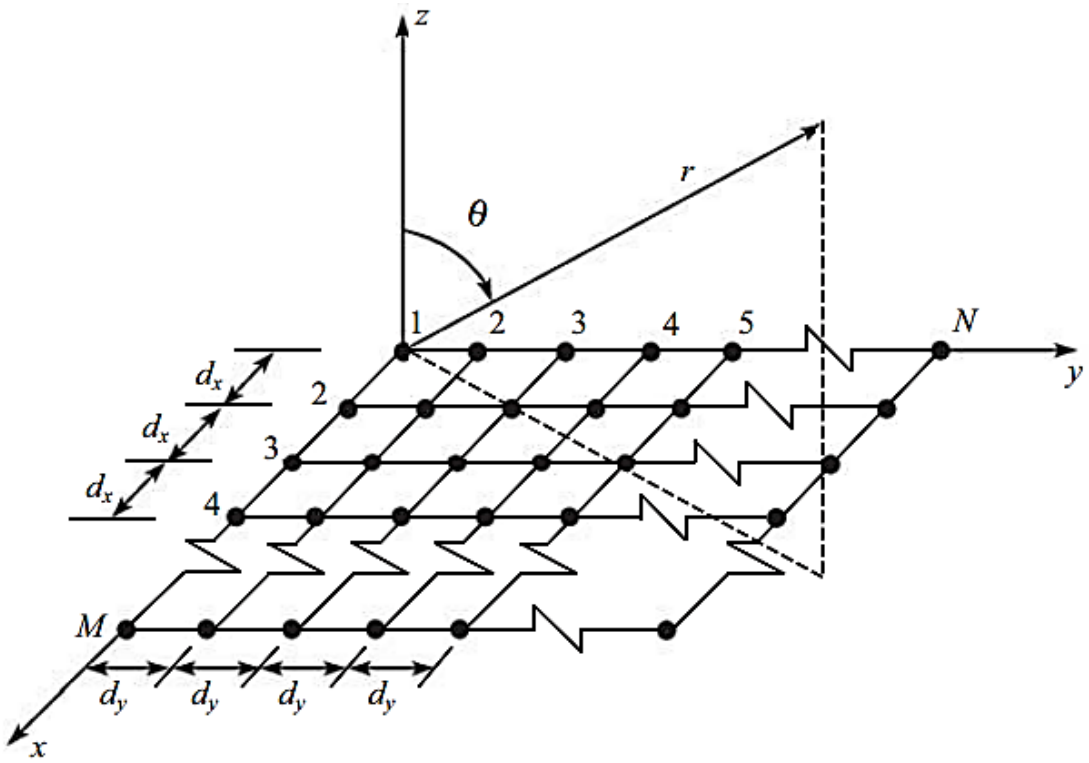

Figure 2.8 Planar array geometry [32].

$$\begin{aligned}\psi_x &= kd_x \sin\theta\cos\phi + \beta_x \\ \psi_y &= kd_y \sin\theta\sin\phi + \beta_y\end{aligned} \tag{2.34}$$

where d_x and d_y are, the inter-element spacing in the x-direction and y-direction respectively, and β_x and β_y is the progressive phase between the adjacent elements along x and y-direction, respectively. To obtain the main beam along $\theta = \theta_0$ and $\phi = \phi_0$ direction, the progressive phase shifts must be given as (2.35) [32]:

$$\begin{aligned}\beta_x &= -kd_x \sin\theta_0\cos\phi_0 \\ \beta_y &= -kd_y \sin\theta_0\sin\phi_0\end{aligned} \tag{2.35}$$

The three-dimensional 3D radiation pattern of 5 × 5 planar arrays separated with 0.5λ spacing along both x and y-direction and zero progressive phase shift is presented in Fig. 2.9.

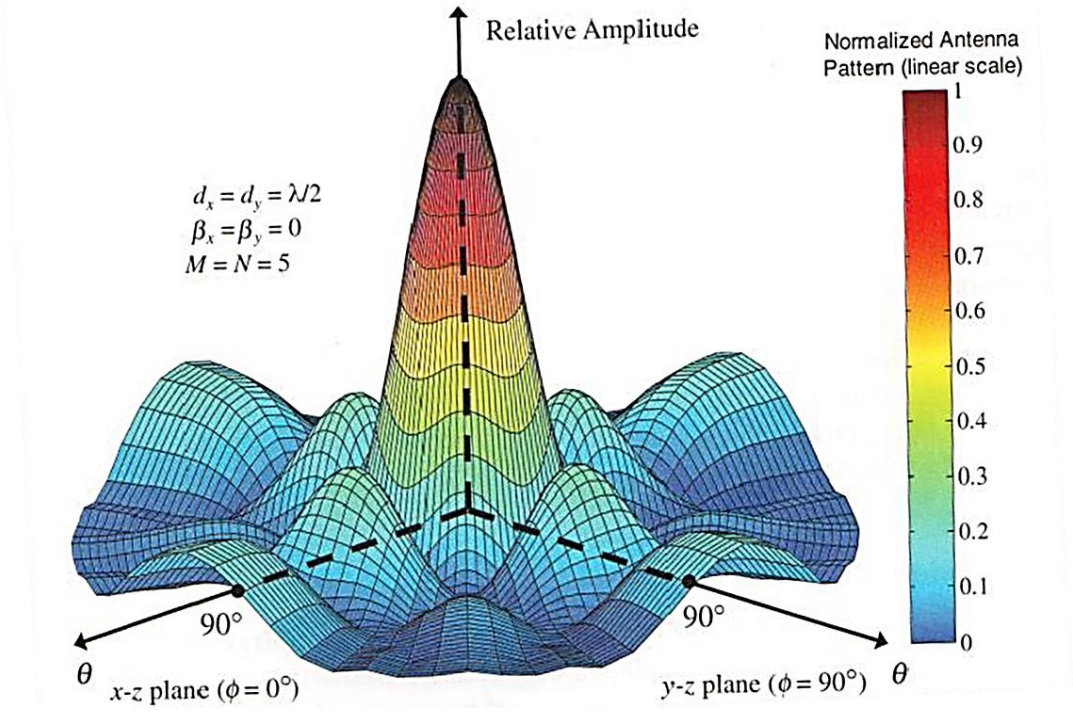

Figure 2.9 3D antenna pattern of a planar array of isotropic elements with a spacing of 0.5λ [32].

2.3.2 Grating Lobes

A grating lobe is a secondary lobe, other than the main lobe, generated by an array antenna when the inter-element spacing is large to permit the in-phase addition of radiated fields in more

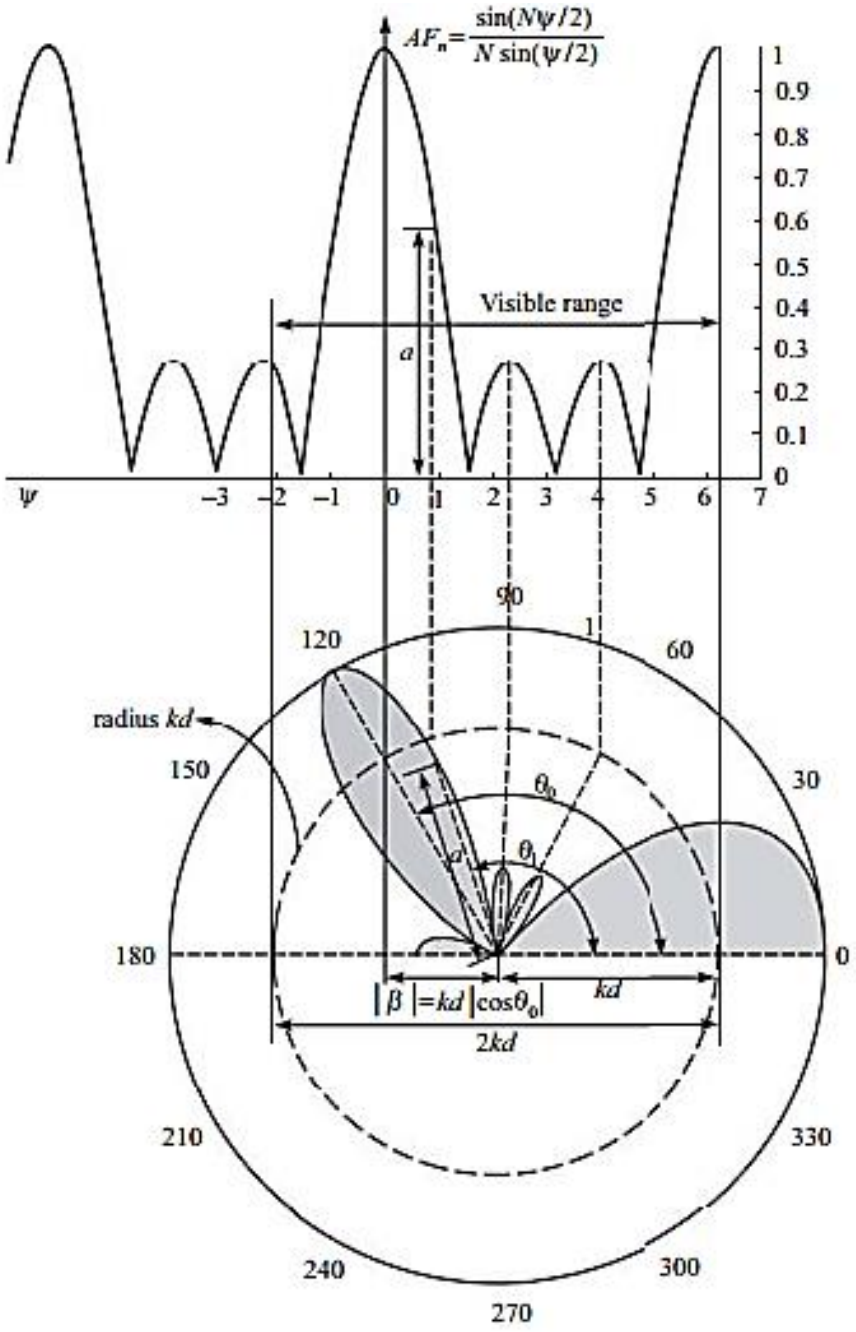

Figure 2.10 Visible range geometrical construction of polar diagram [31].

than one direction in real space. The condition to avoid grating lobes for an array placed along *z*-axis is to have the element spacing as given by (2.36) [31]:

$$d < \frac{\lambda}{1+\left|\cos\theta_0\right|} \tag{2.36}$$

The polar diagram of the array factor shown in Fig. 2.10 depicts the visible range and possible grating lobe in the far-field of the array pattern [31]. The phased array must be designed with an optimal spacing between the radiating elements to eliminate the grating lobes.

2.3.3 Beamforming network

The three main advantages of phased array of single antenna elements are:

1. Improved spatial resolution
2. Electronic steering
3. Interference suppression

Beamformer enhances the detection of signals by coherently summing signals across elements of arrays, as shown in Fig. 2.11 [33]. Beam steering is achieved by applying progressive phase shifts across the elements of the array. In addition to beam steering, sidelobe level (SLL) can be reduced by non-uniform amplitude tapering. Amplitude tapering excitation of each element of the array is controlled by variable gain amplifier (VGA), as shown in Fig. 2.11.

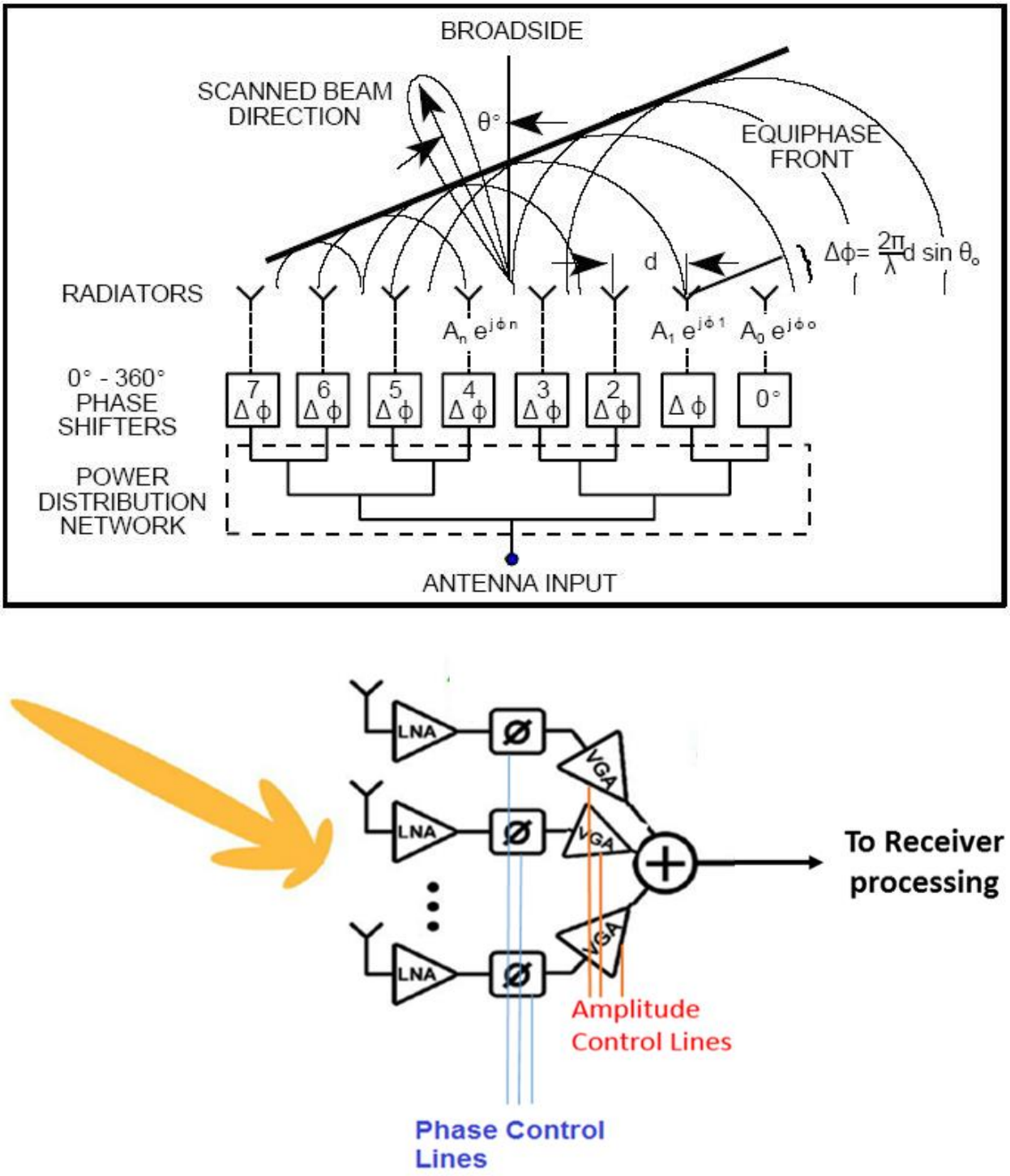

Figure 2.11 Analog beamforming mechanism using phase shifters for beam steering and VGA for side lobe level reduction [33].

2.4 Circular Waveguide Theory

The circular waveguide has a circular cross-section, and it can support transverse electric (*TE*) and transverse magnetic (*TM*) modes. Fig. 2.12 illustrates a cylindrical waveguide with a circular cross-section of radius *a*. Given the cylindrical geometry, cylindrical coordinates are most appropriate for the waveguide analysis.

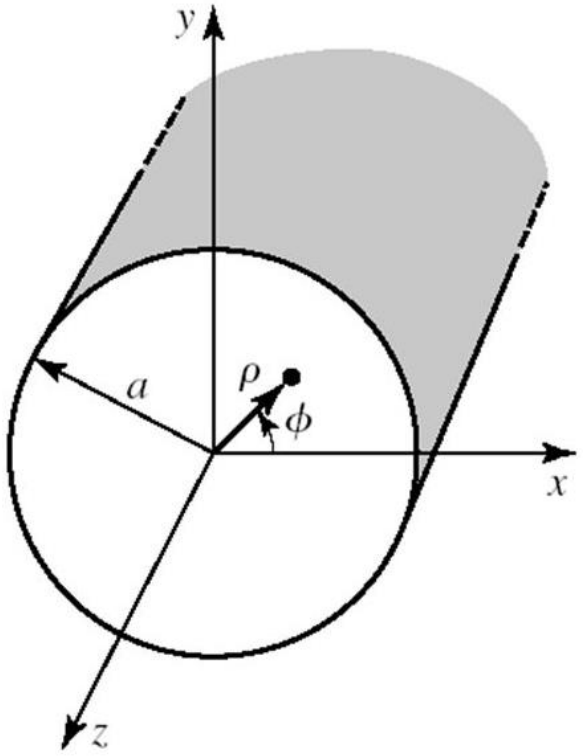

Figure 2.12 Circular waveguide geometry of radius *a* [34].

To calculate the field components, all the transverse component is evaluated using the longitudinal (E_z, H_z) components [34]. In cylindrical coordinates, the transverse field is (2.37) [34]:

$$\bar{E}_T = \hat{\rho}E_\rho + \hat{\phi}E_\phi \text{ and } \bar{H}_T = \hat{\rho}H_\rho + \hat{\phi}H_\phi \tag{2.37}$$

***TE* modes:**

For the *TE* modes, a solution of $\left(\nabla^2 + k^2\right)H_z = 0$ is satisfied to give the *E*-field as (2.38) [34]:

$$E_{\phi}(\rho,\phi,z)=\frac{j\omega\mu}{k_c^2}\left[A\sin(\nu\phi)+B\cos(\nu\phi)\right]k_c J_{\nu}^{'}(k_c\rho)e^{-j\beta z} \tag{2.38}$$

where $J_{\nu}^{'}(x)=\frac{d}{dx}J_{\nu}(x)$, A and B are the constants obtained by applying necessary boundary conditions, and $k_c=\frac{p_{\nu n}^{'}}{a}$ where $p_{\nu n}^{'}$ is the nth zero of derivative of Bessel function $J_{\nu}^{'}(x)$.

The propagation constant of the *TE* mode is given by (2.39) [34]:

$$\beta^2=k^2-\left(\frac{p_{\nu n}^{'}}{a}\right)^2 \tag{2.39}$$

The corresponding cutoff frequency of the *TE* mode is given by (2.40) [34]:

$$f_{c,\nu n}=\frac{c}{2\pi}\frac{p_{\nu n}^{'}}{a} \tag{2.40}$$

The dominant *TE* mode with the smallest non-zero value of $p_{\nu n}^{'}$ is the TE_{11} mode.

_TM_ Modes

The derivation is the same as *TE* except now it is solved for E_z given by (2.41) [34]:

$$E_z(\rho,\phi,z)=\left[A\sin(\nu\phi)+B\cos(\nu\phi)\right]J_{\nu}(k_c\rho)e^{-j\beta z} \tag{2.41}$$

Applying the boundary condition leads to $k_c=\frac{p_{\nu n}}{a}$ where $p_{\nu n}$ is the nth zero of $J_{\nu}(x)$.

The propagation constant and cutoff frequency of the *TM* mode are given by (2.42) and (2.43) [34]:

$$\beta^2=k^2-\left(\frac{p_{\nu n}}{a}\right)^2 \tag{2.42}$$

$$f_{c,\nu n}=\frac{c}{2\pi}\frac{p_{\nu n}}{a} \tag{2.43}$$

The first six modes inside the circular waveguide is shown in Fig. 2.13 [35].

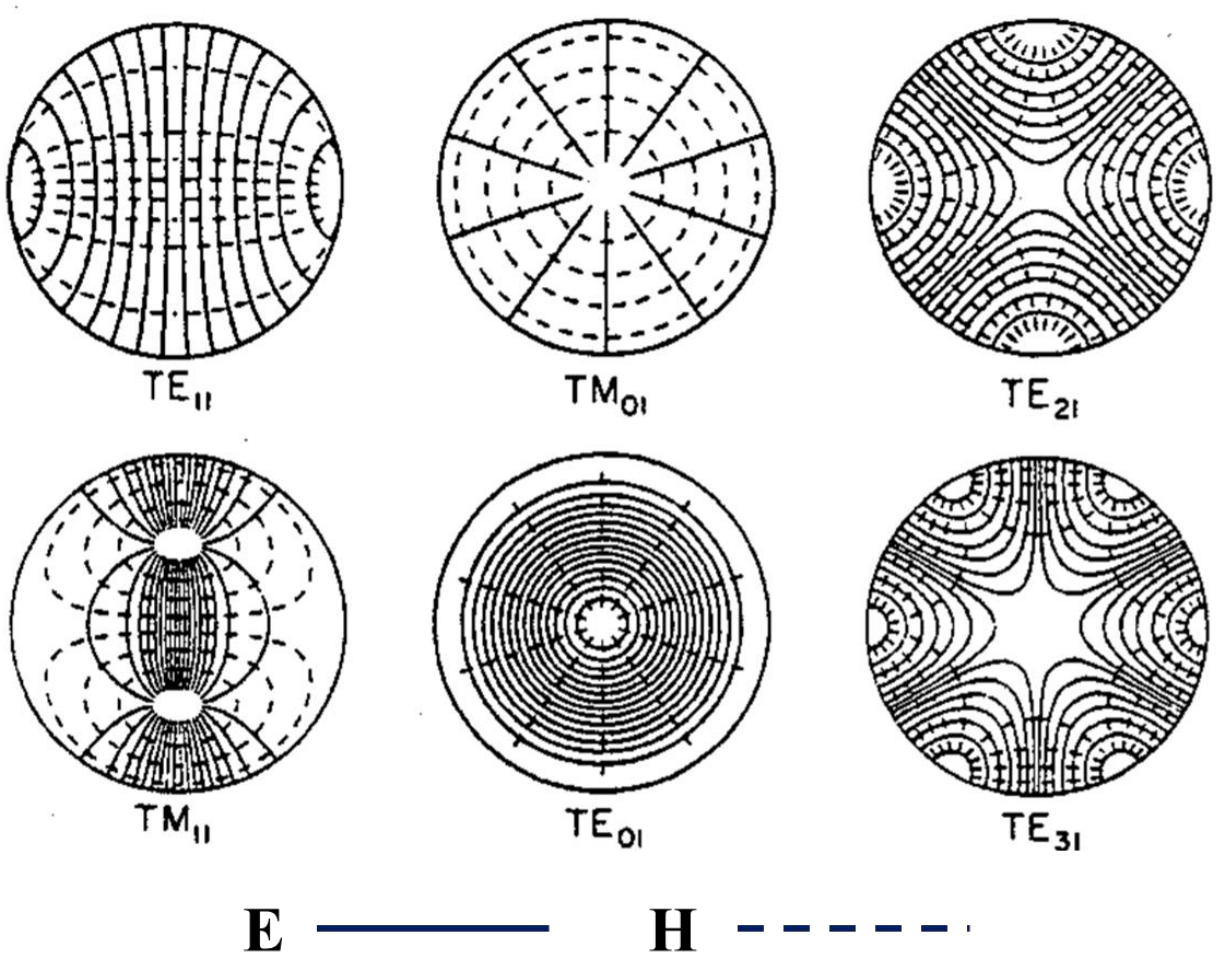

Figure 2.13 Transverse modal field distribution for a circular waveguide (first six modes) [35].

2.5 Leaky-wave Antenna Theory

A leaky-wave antenna (LWA) is a guiding structure that permits leakage all along its length [36]. Due to the leakage, the leaky antenna has a complex propagation wavenumber K_{LW}. There are two basic types of leaky-wave antennas, namely, uniform and periodic LWA, depending on whether the geometry is uniform or periodically modulated along its length. In this dissertation, we will focus on periodic LWA, where the periodicity produces the leakage. The dominant mode in a periodic LWA is a slow wave that does not radiate even though the structure is open. However,

after the introduction of the periodic perturbation along the length produces infinite space harmonics which can be fast or slow-wave. However, only the fast space harmonics will radiate. The antenna is designed so that only the first space harmonic (n = -1) is fast, i.e. $|\beta_{-1}| < k_0$. Fig. 2.14 shows an example of periodic leaky-wave structure where periodic metallic strips are placed that causes radiation [37].

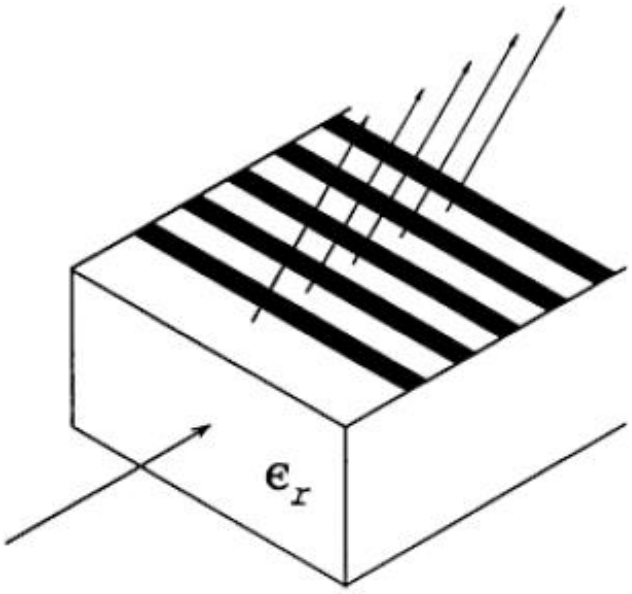

Figure 2.14 A typical example of periodic leaky wave antenna [36].

The corresponding complex leaky-wave number of a periodic LWA is $k_{LW} = \beta_{-1} - j\alpha$, and it can be extracted using the eigenvalue of the *ABCD* matrix of the structure. Most LWA exhibits an open-stopband (OSB) region where there is a significant gain degradation when the main beam points towards broadside. At OSB, when $\beta_{-1} \approx 0$, the summation of the internal reflections within the unit cells in the periodic LWA leads to the reduced radiation at broadside [38]. Several methods have been reported to suppress the OSB and realize a continuous beam scan [38], [39].

Periodic LWA can scan from the backward end-fire through broadside into part of the forward quadrant. The zero-crossing of the phase constant β_{-1} dictates the center frequency of broadside radiation. The leakage constant α is related to the beamwidth and the radiation efficiency of the LWA.

Once β_{-1} and α are known as a function of frequency, the principal features of the leaky-wave antenna can be computed. Such features include the characteristic Bloch impedance, the variation of the scan angle with frequency, the radiation efficiency, the beamwidth, and the radiation pattern [14], [17].

The Bloch impedance Z_B is the ratio of the voltage and current waves at the input terminal of the N cascaded cells of the periodic LWA and is computed using (2.44) [40]:

$$Z_B = \frac{-B}{A - e^{\gamma Nd}} \tag{2.44}$$

The beam squint angle (θ_m) of the peak gain from the broadside is given as (2.45) [36]:

$$\sin\theta_m \approx \frac{\beta_{-1}}{k_0} \tag{2.45}$$

The radiation pattern can be determined from the Fourier transform of the aperture distribution. For an infinite length antenna, the radiation power pattern of the LWA is given by (2.46) [36]:

$$R(\theta) \propto \frac{\cos^2\theta}{\left(\alpha / k_0\right)^2 + \left(\beta / k_0 - \sin\theta\right)^2} \tag{2.46}$$

The remainder of the dissertation, chapter 3 to chapter 7, is focused on the analysis, design, and characterization of the innovative feed-reflector and beam steering antenna solutions.

Chapter 3

Analysis and Design of a *W*-Band Circular Polarized Feed Horn with Inbuilt Polarizer for Low *f*/*D* Offset Reflector Antenna

3.1 Introduction

Circular polarized electromagnetic waves are preferred for space to ground satellite communications (SATCOM), owing to its resilience to scintillation and other scattering effects. Reflector antennas with circularly polarized (CP) feed sources provide high gain solutions for satellite communication systems [3], [4]. CubeSats are miniaturized satellites that typically reside in the low earth orbit (LEO) with configurations ranging from 1U – 6U sizes (1U represents a 10 cm × 10 cm × 10 cm cube). High gain CP antenna systems are necessary to maintain the reliable communication link. A CP wave is realized by combining two orthogonal linear polarized (LP) signals with 90° time-phase difference. In [5], a dual CP feed polarizer is designed using an array of metallic pins as delay structure to achieve the desired phase shift for the generation of circular polarization. The losses of the pins along with the fabrication challenge limit the use of this method at millimeter-wave frequencies. In [6], a LP-CP conversion is achieved at sub-mm -wave frequencies by exploiting differential dispersion in hexagonal waveguides. This design overcomes the need for waveguide partitions and assemblies often required for CP horns, and it is potentially less susceptible to fabrication tolerances owing to hollow waveguide structure.

In an orthomode transducer (OMT), the CP wave is generated by combining the two orthogonal linear polarized signals in the compact waveguide structure [41]-[50]. This approach requires a dual input source with hybrid or septum that increases the complexity, especially at

millimeter-wave frequencies due to smaller feature sizes. In the septum polarizer based method, the CP wave is generated from a single linear polarized signal [51]-[54]. The septum is a stepped ridge structure in the middle of the rectangular waveguide. The length and number of stepped ridges affect the axial ratio and polarization quality. The benefit of this method is that the structure is compact, offers wideband CP, and a single input is necessary. However, the septum is an asymmetric structure that leads to difficulty in the fabrication and degradation of radiation performances at millimeter-wave [3], [55].

In [56], the metallic ridges are embodied inside the rectangular waveguide to induce CP from a linear polarized wave. This method is similar to the septum method in [51] and [52]. The orthogonal signals are created from a tapered ridge waveguide; however, the construction requires the ridge waveguide to be stepped in size, and thus piecewise fabrication is needed, adding complexity. Dielectric loaded circular horn antenna and substrate integrated waveguides based OMT generated CP approaches are discussed in [57]-[64]. The dielectric-loaded waveguides offer compact design but suffer from high dielectric losses at millimeter-wave frequencies along with the fabrication challenges.

CubeSat at microwave and millimeter-wave frequencies demand compact and high gain antenna solutions. In [65]-[68], a 0.5 m deployable mesh reflector antenna with f/D = 0.5 is developed for high gain and wide matching bandwidth at *Ka*-band. The deployable mechanism becomes necessary due to the lower frequency of operation at the *Ka*-band. It requires a stowage volume of 1.5U and a complex deployment mechanism with stubs and 30 folding ribs. An alternate high gain deployable antenna solution for CubeSat is provided with the reflectarray antenna at X-band [69]. It has narrow matching bandwidth (< 5 %) and a deployed size of 33.5 cm × 59.7 cm. In [70], a 118 GHz radiometer antenna is designed for a 3U CubeSat. The radiometer payload

module is compact and embedded inside the CubeSat chassis. However, the antenna is linear polarized and has *f*/*D* ratio of 0.56.

In this research, a *W*-band left-hand circular polarized (LHCP) feed horn antenna with an inbuilt polarizer structure with single input is proposed. The proposed polarizer portion is electrically longer than the conventional polarizers, but it incorporates excellent performance with an easy fabrication process. This feed horn antenna provides impedance matching (S_{11}) below -15 dB and axial ratio (AR) below 1.2 dB from 79.5 GHz to 88 GHz, in addition to the symmetric radiation pattern. This feed horn antenna is integrated with an offset parabolic reflector of *f*/*D* = 0.25 for the CubeSat application. The proposed feed reflector antenna can fit inside the 1U volume of the CubeSat owing to the high frequency of operation at *W*–band, without a complex deployable mechanism. The prototype of the feed horn and offset reflector antenna is fabricated, and the measured results are in excellent agreement with the simulation. The measured right-hand circular polarized (RHCP) gain of the reflector antenna is above 34 dBic, and the total measured efficiency is above 60% within the desired bandwidth.

3.2 Proposed Feed Horn Requirements

The proposed horn antenna is developed as a feed for illuminating a compact offset parabolic reflector for 6U CubeSat (10 cm × 20 cm × 30 cm) application. The feed horn and reflector assembly take around 1U CubeSat volume. Fig. 3.1 illustrates the orthographic representation of the offset parabolic reflector antenna configuration. The stringent space constraint led to the selection of a small *f/D* of 0.25 to accommodate the reflector of diameter *D* = 10 cm inside the 1U block of the CubeSat. Accordingly, the clearance *H* is taken to be zero to avoid extension of the feed horn and reflector assembly beyond the allotted volume.

The above constraints on the parameter value resulted in the half cone angle subtended at the rim of the reflector ψ_e, to be 63.44°, as given in (3.1). Also, the feed source needs to be directed towards the center of the offset reflector from the focal axis by an angle ψ_f = 90°, as equated in (3.2) [23]:

$$\psi_e = \tan^{-1}\frac{2fD}{4f^2 + H(\mathrm{D}+\mathrm{H})} = 63.44^{\circ} \tag{3.1}$$

$$\psi_f = 2\tan^{-1}\frac{2H+D}{4f} = 90^{\circ} \tag{3.2}$$

As a result, the proposed feed horn antenna is designed to have a 12 dB half-edge illumination of around 64° within the desired bandwidth of 79 GHz to 88 GHz. The ray-tracing diagram of an offset parabolic reflector with these obtained values is plotted using Ticra GRASP and is shown in Fig. 3.2.

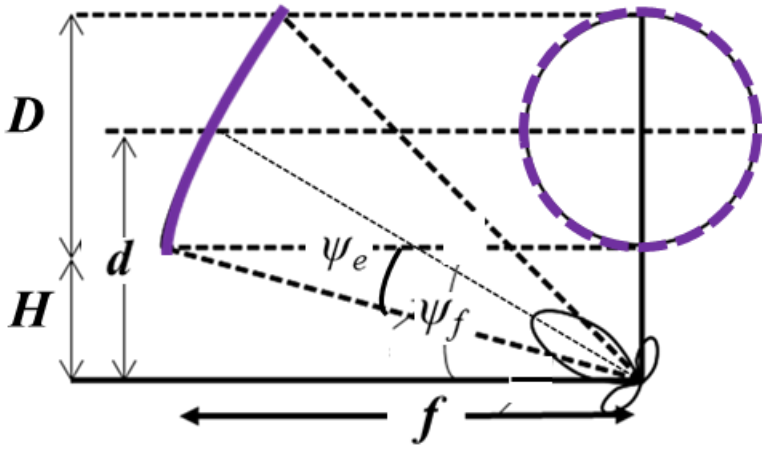

Figure 3.1 Parameters of an offset fed parabolic reflector in an orthographic representation.

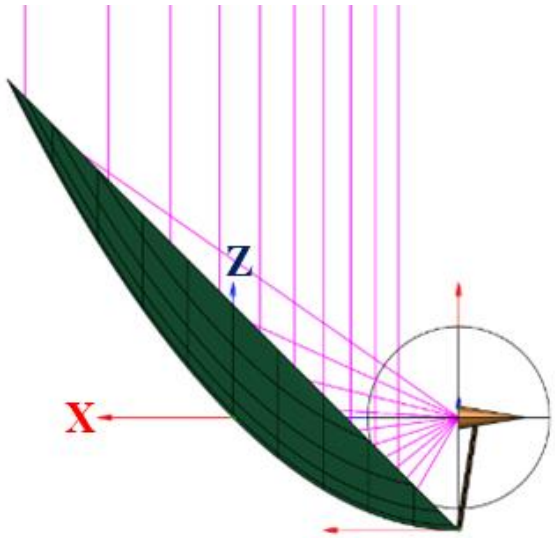

Figure 3.2 Ray tracing diagram using Ticra GRASP with $\psi_e = 63.44°$ and $\psi_f = 90°$ for an offset parabolic reflector with $f/D = 0.25$.

To study the effect of strict physical constraints on the co- and cross-polarization performance of the antenna, an ideal simulation with the Gaussian left-hand circular polarization (LHCP) feed source is carried in GRASP. Ideal Gaussian feed assumes that the cross-polarization level is below -200 dB. The peak RHCP directivity of the offset parabolic reflector illuminated by the ideal Gaussian LHCP feed is 37.5 dBic, and the cross-polarization separation is 41.5 dB within the main lobe at 86 GHz, as presented in Fig. 3.3. The 3dB beamwidth is 2.3°, and the spillover loss of the offset reflector is 0.63 dB at 86 GHz. Spillover radiation occurs at 45°, which is the angle of orientation of the reflector with respect to the boresight of the feed horn. The spillover loss could be reduced by increasing the *f/D* ratio. However, the *f/D* ratio is limited by the volume constraint of the CubeSat. Thus, significant cross-polarization is observed with the ideal feed illumination of the reflector.

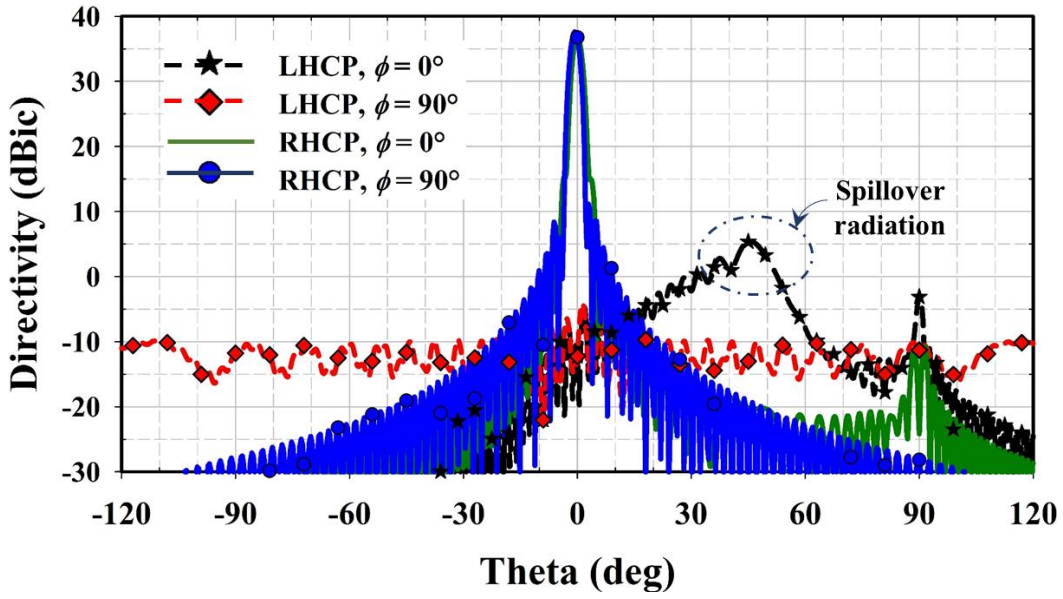

Figure 3.3 Simulated directivity pattern of an ideal Gaussian fed offset parabolic reflector with *f/D* = 0.25 in TICRA GRASP.

3.3 Inbuilt Feed Horn Polarizer

3.3.1 Proposed Feed Horn Antenna Geometry (Initial Design)

Circular polarization is achieved by incorporating a polarizing structure inside the cylindrical waveguide. Fig. 3.4(a) and Fig. 3.4(b) show the front view and the split view geometry in YZ plane of the proposed feed horn antenna. The inbuilt polarizing structure employs nine pairs of circular cavities in the cylindrical waveguide wall, as shown in Fig. 3.4(b). These cavities are at 45° with respect to the rectangular input port. The horn is designed using a circular waveguide section of 1.0 mm thick aluminum with an overall length of 26 mm, and the aperture diameter of 3.26 mm. The cavity diameter, *d* is 1.39 mm, and the spacing between the cavity, *s* is 1.7 mm.

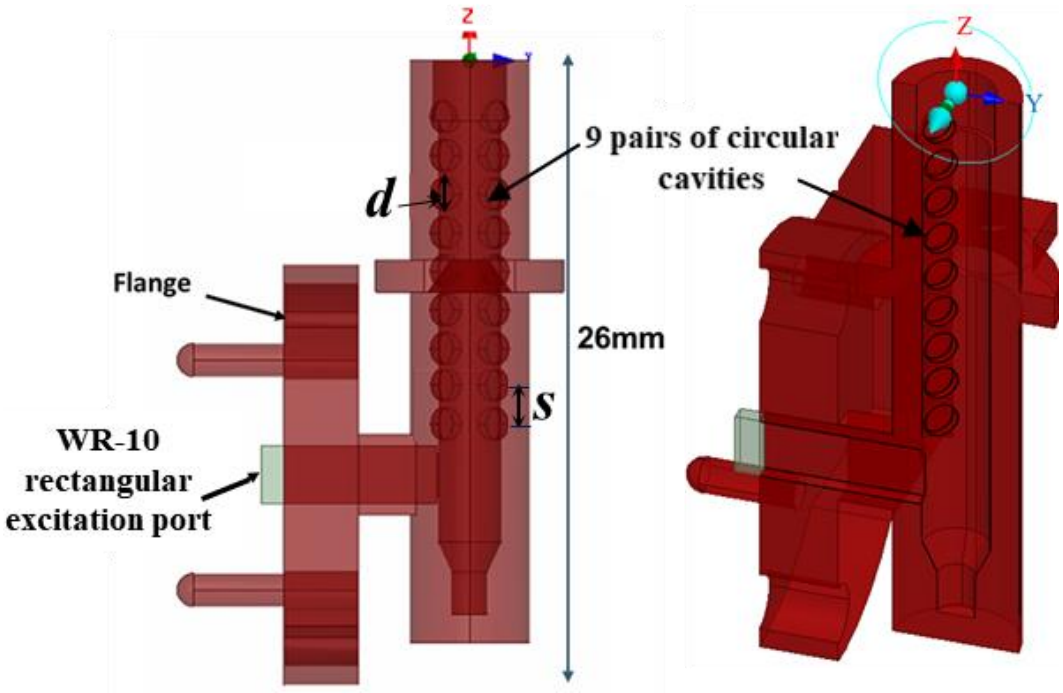

(a) (b)

Figure 3.4 Proposed LHCP feed horn antenna geometry (a) Front view, and (b) Split plane view.

The waveguide section below the polarizing structure is around λ/4 in length and helps in the suppression of any spurious modes. In addition, the tapered waveguide backshort section improves the impedance matching. The proposed inbuilt polarizer has the advantage of reducing the degradation in the antenna radiation performance from fabrication inaccuracy because the cavities are placed on the wall of the circular waveguide where the electromagnetic field is sparse as opposed to placing metallic pins [5] in the dense electromagnetic field region inside the circular waveguide. The number of cavities, the diameter of the cavities, and the spacing of the cavities are the design parameters that can be tuned to optimize the overall impedance matching and the axial ratio bandwidth.

3.3.2 Principle of Operation and Parametric Study

The principle of CP generation is explained for the inbuilt polarizer section of the proposed feed horn antenna. Fig. 3.5 shows the two-port model of the polarizer section of the feed horn. Since the input is 45° offset with respect to the cavity pairs, the input RF signal E_{inc} splits into two orthogonal degenerate TE_{11} modes. The propagation constant of these propagating modes is different due to the cavity pairs along $E_{out1,}$ as shown in Fig. 3.6. As a result, the E_{out1} field in the direction of the cavity pairs gets an additional phase delay of $\lambda/4$ relative to the orthogonal field E_{out2} at the aperture of the polarizer to generate the desired LHCP. The polarizer device can be considered as a three-port structure, even with its two physical ports. The two degenerate modes at the output circular wave-port make the polarizer as a three-port structure. The general expression for the 3 × 3 scattering matrix for the proposed polarizer is written as (3.3):

$$S = \frac{1}{2}\begin{bmatrix} 0 & -\sqrt{2}\cdot e^{-j\beta_1 L} & \sqrt{2}\cdot e^{-j\beta_2 L} \\ -\sqrt{2}\cdot e^{-j\beta_1 L} & 0 & 0 \\ \sqrt{2}\cdot e^{-j\beta_2 L} & 0 & 0 \end{bmatrix} \tag{3.3}$$

where L is the length of the circular waveguide polarizer and β_1, β_2 are the propagation constants in the polarizer.

The summation of the difference in propagation constants of the two modes $\beta_1(z_i, f)$ and $\beta_2(z_i, f)$ along the length of the polarizer gives the phase difference of 90°, as shown in (3.4) [6]:

$$\sum_{i=1}^{L/\delta z} \left(\beta_2(z_i, f) - \beta_1(z_i, f)\right)\delta z = \frac{\pi}{2} \tag{3.4}$$

where z_i (along the z-direction) is the distance from the feed point for the i^{th} discretized section in the waveguide at frequency f.

The effect of the presence of circular cavities in the polarizer section is analyzed using Ansys HFSS. Without the circular cavities, the section acts as a regular cylindrical waveguide, and the linear polarized wave is observed at the output port, as illustrated in Fig. 3.7(a). With the proposed optimized design of 9 pairs of circular cavities and cavity diameter d = 1.39 mm, the field component E_{out1} experiences an additional phase lag of 90°. Also, the amplitude of the two orthogonal field components is the same leading to the generation of LHCP wave at the output port, as shown in Fig. 3.7(b).

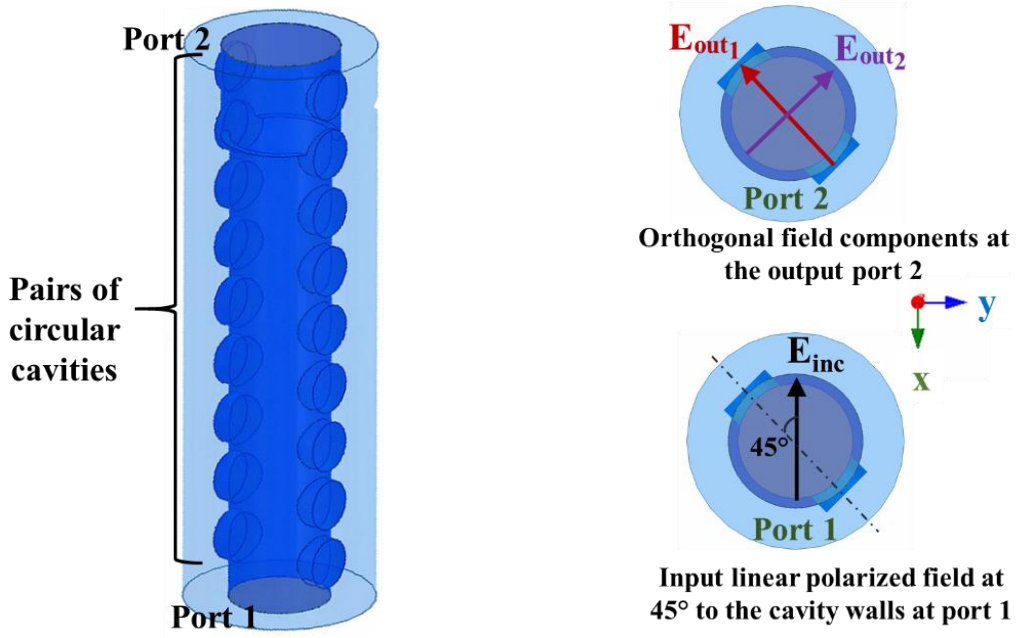

(a) (b)

Figure 3.5 Two-port model of polarizer structure of the proposed antenna (a) Front view, and (b) Top view showing input and output field components.

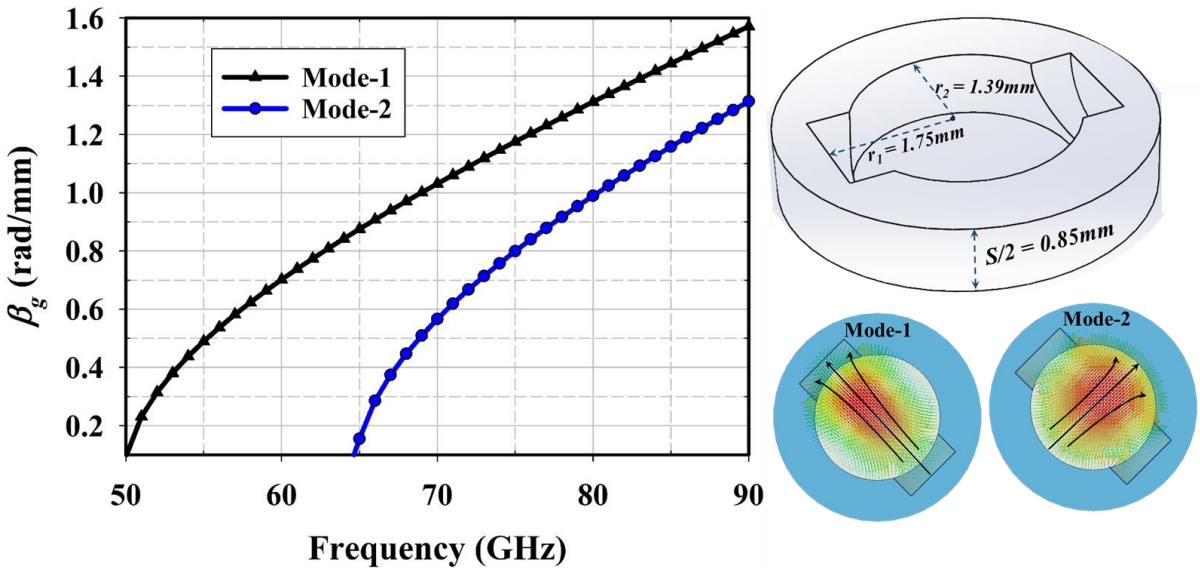

Figure 3.6 Dispersion relation graph for a section of the polarizer simulated in Ansys HFSS.

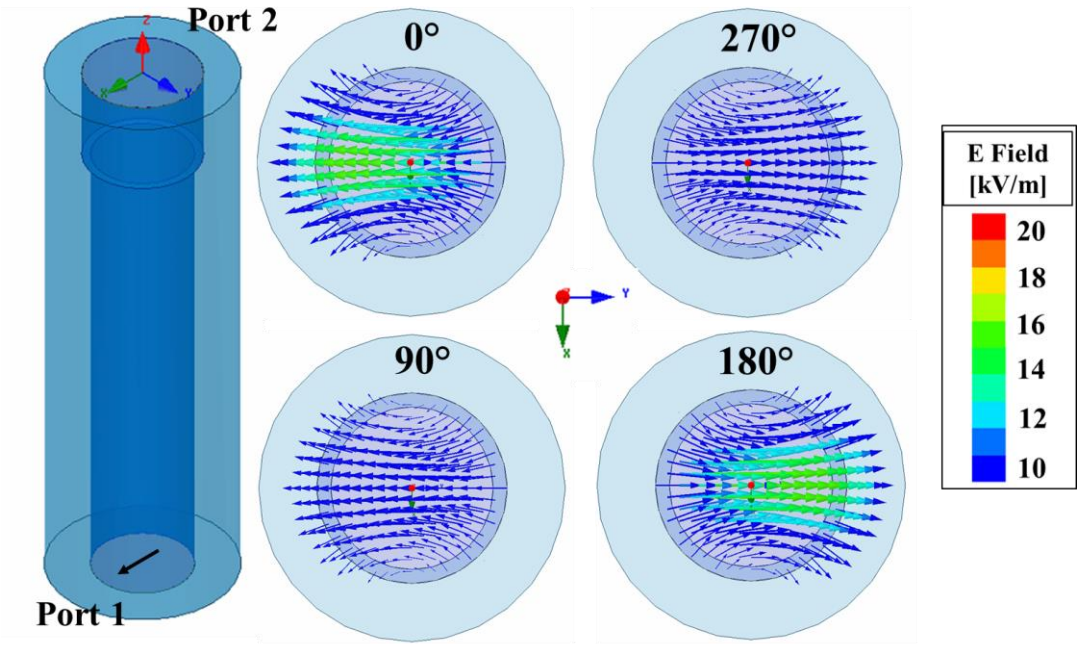

(a)

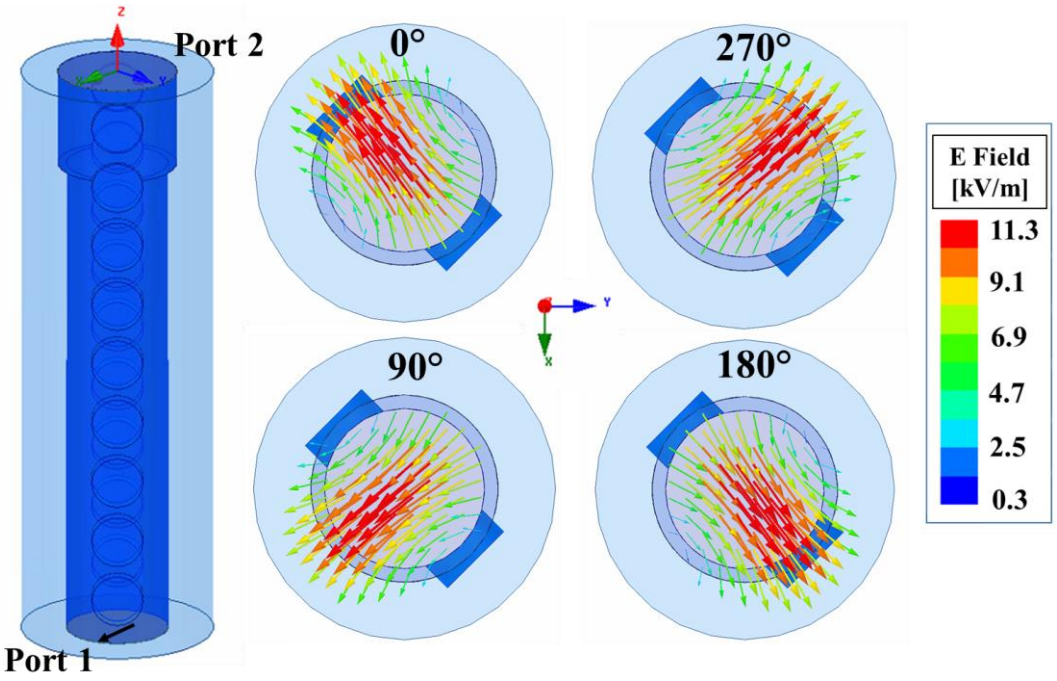

(b)

Figure 3.7 Effect of circular cavities on the *E*-fields in the polarizer section (a) No cavity pairs leading to linear polarization and (b) 9 cavity pairs leading to circular polarization.

A parametric analysis is carried out on the number of circular cavity pairs, diameter, depth, and spacing between the circular cavities keeping the length of the feed horn constant to determine the optimum value of the parametric variables. Later, based on the optimum parametric values, sequential nonlinear programming (gradient) optimization method is employed on the feed horn with the goal of AR less than 1.5 dB within the frequency range of 79 GHz to 88 GHz. The effect of the number of circular cavity pairs on the amplitude and phase difference between the two orthogonal field components is shown in Fig. 3.8. It is seen that for nine pairs of circular cavities, the phase difference between the output field components is 90° (±15°), and the maximum amplitude imbalance is 0.10 dB.

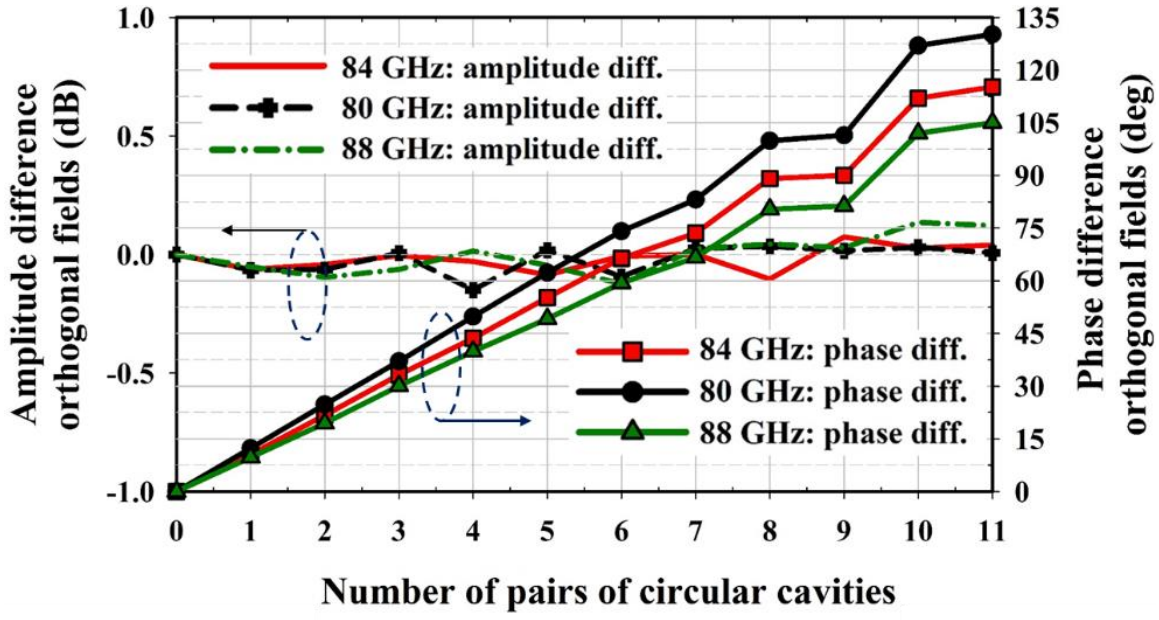

Figure 3.8 Amplitude and phase difference between the two orthogonal field components at the output port of the polarizer as a function of number of circular cavities pairs.

Fig. 3.9(a) presents the effect of varying the cavity diameter on the output phase difference between the field components as a function of frequency for nine pairs of circular cavities. For cavity diameter d = 1.39, the phase difference between the output field components is around 90°. The effect of different spacing s between the cavities on the phase difference is shown in Fig. 3.9(b). The spacing s = 1.70 mm provides the phase delay of 90° (± 10°) between the output field components.

Hexagonal, square, and triangular are the three different shapes of the cavity that are studied in addition to the circular cavity shapes, as illustrated in Fig. 3.10. The effect of different cavity shapes on the phase difference is shown in Fig. 3.11. The triangular cavity polarizer provides the least phase delay, whereas the proposed circular cavity polarizer offers the optimum phase difference to generate CP.

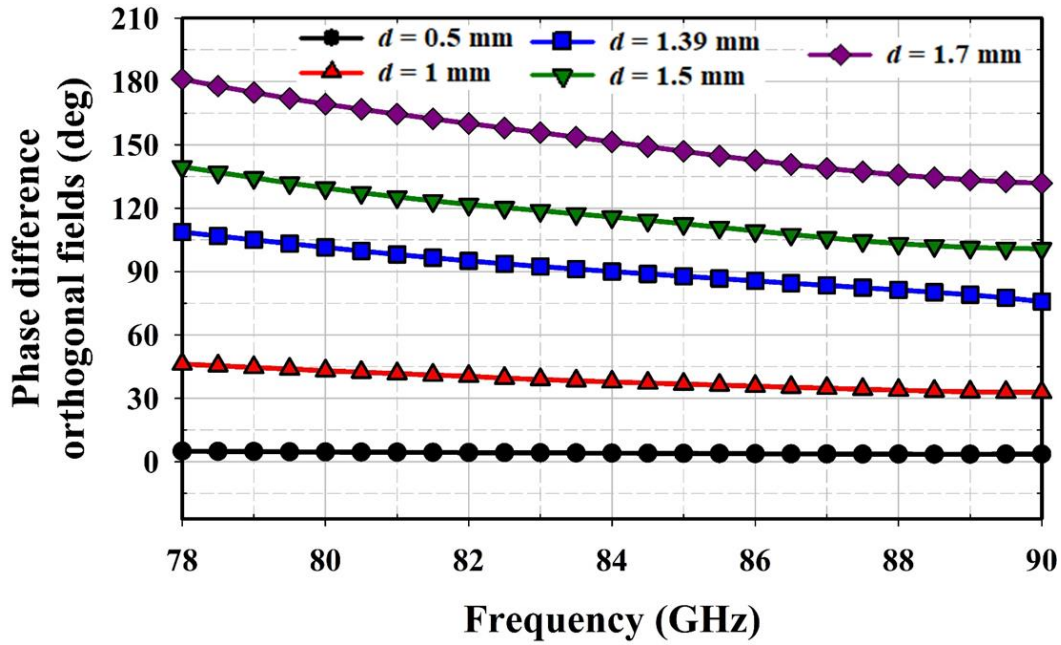

(a)

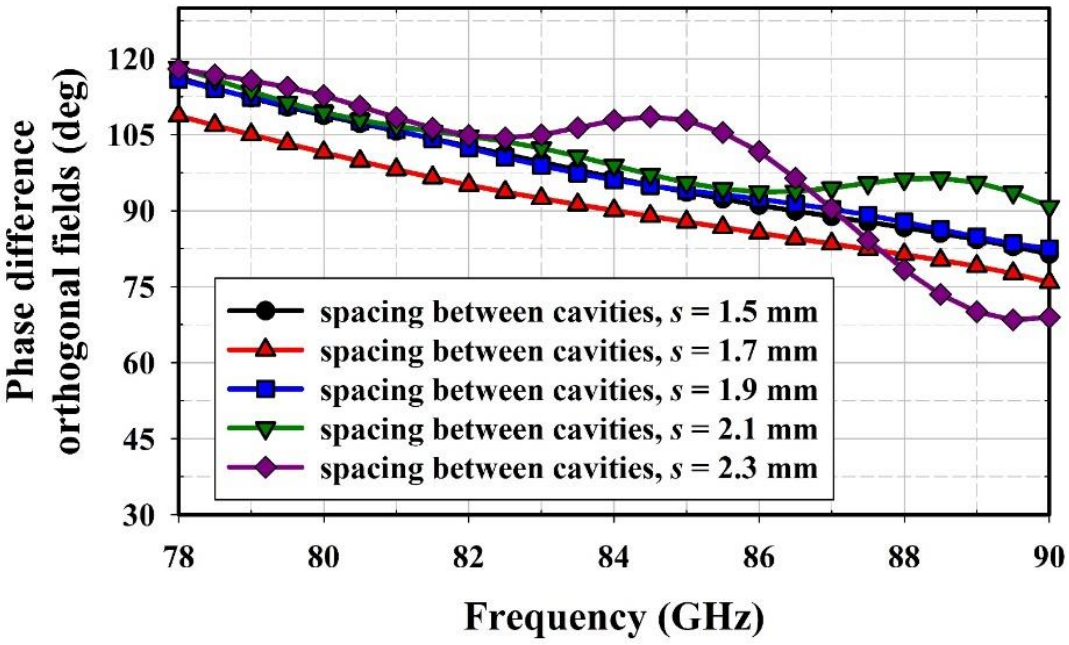

(b)

Figure 3.9 Effect of different (a) Cavity diameter =*d*, and (b) Spacing = *s* between the cavities, on the phase difference between the two orthogonal fields at the output port of the polarizer.

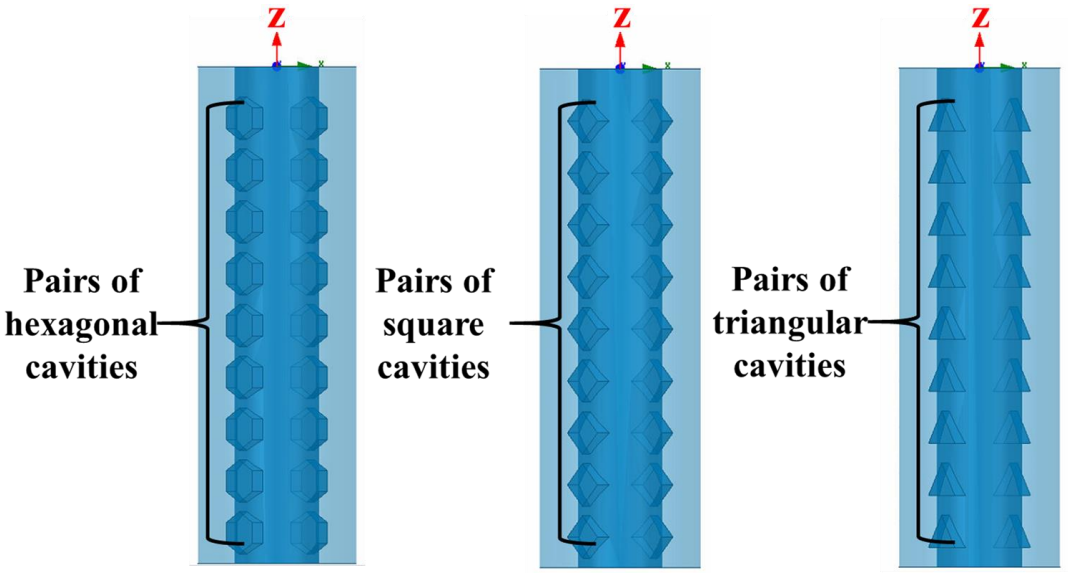

Figure 3.10 Different cavity shapes in the polarizer (a) Hexagonal, (b) Square, and (c) Triangular cavity shapes.

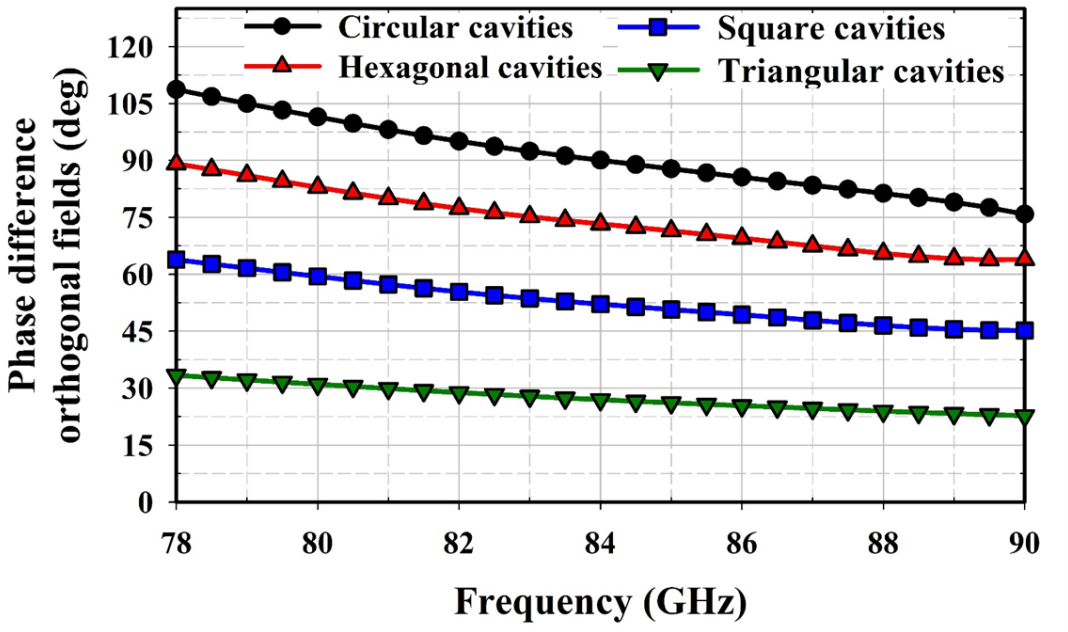

Figure 3.11 Effect of different shapes of the cavity on the phase difference between the two orthogonal fields.

3.4 Modified Designs for Ease of Fabrication

The initial proposed design of Fig. 3.1 needs to be modified for the ease of fabrication. Extra aluminum thickness is added to the walls of the initial horn antenna for structural rigidity. Two different modified designs are studied with the additional metal thickness with split plane waveguide construction, which allows in easier fabrication in machining through CNC technology.

Fig. 3.12 shows the CAD rendering of the modified design #1 with a rectangular wall around the cylindrical horn antenna. The overall thickness of the aluminum wall is 5.25 mm. The rectangular metal wall creates asymmetry in the feed aperture, which results in higher diffraction around the wall edges. A final modified design is proposed, as shown in Fig. 3.13, which includes a 1.4 mm thick circular skirt at the top of the rectangular wall to make the aperture symmetric and mitigate the diffraction current. The physical dimension of the optimized horn antenna is 26 mm × 14 mm × 5.25 mm which corresponds to the electrical dimension of 7.2λ × 3.9λ × 1.4λ at 84 GHz. The optimum cavity diameters are $d_1 = d_2 = d_9 = 1.40$ *mm*, $d_3 = d_4 = d_7 = d_8 = 1.35$ *mm, and* $d_5 = d_6 = 1.30$ *mm*. The spacing between the cavity pairs are $s_1 = s_2 = s_3 = s_5 = s_7 = s_8 = 1.70$ *mm,* $s_4 = 1.60$ *mm, and* $s_6 = 1.80$ *mm*, and the depth of the cavity is 0.36 mm.

The simulated impedance matching performances of the modified design #1 and the final optimized designs are presented in Fig. 3.14. Both the designs offer wideband matching (S_{11} below -15 dB) from 79.5 GHz to 88 GHz. The circular polarization purity is affected by the asymmetric aperture wall of the modified design #1, as observed in the AR plot of the two designs presented in Fig. 3.15. The final optimized design shows an excellent AR below 1.2 dB over the entire

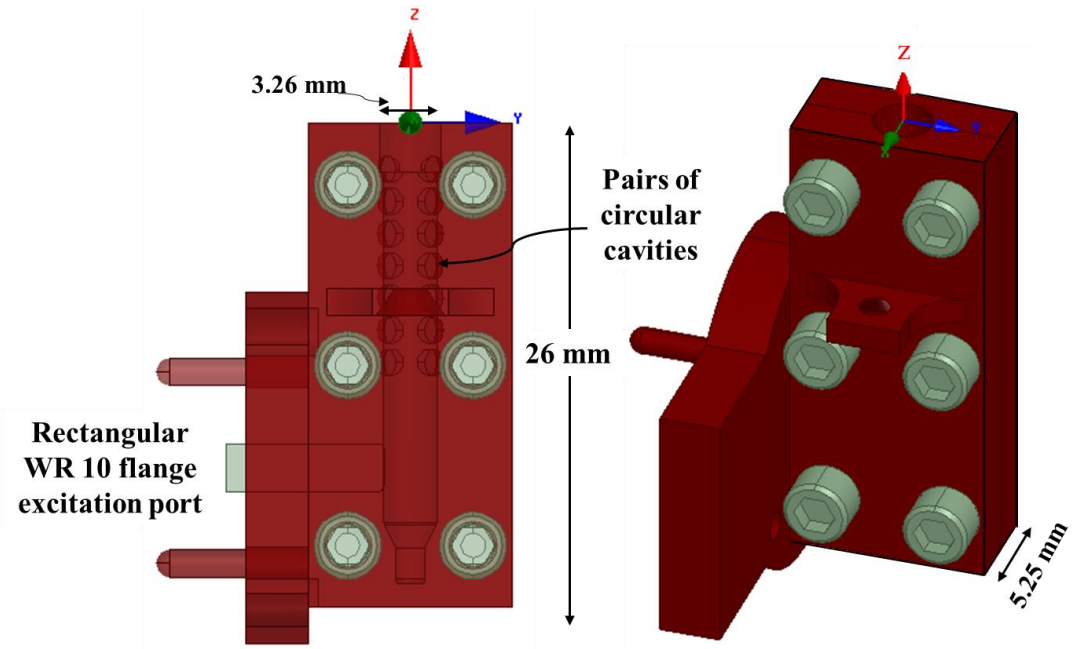

(a) (b)

Figure 3.12 Modified design #1 with extra metal thickness around the antenna walls for ease of fabrication (a) Front view and (b) Isometric view.

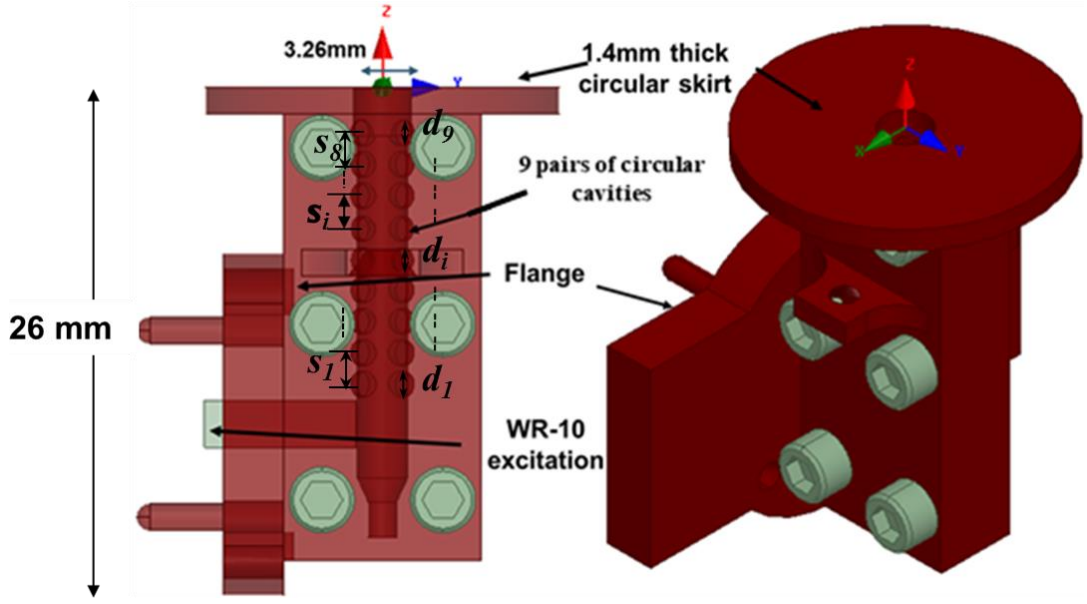

(a) (b)

Figure 3.13 Final optimized modified design with circular skirt (a) Front view, and (b) Isometric view.

matching bandwidth. The 3 dB AR beamwidth of the modified design #1 is 61°, 85°, and 82° and for the final modified design is 90°, 91°, and 108° as shown in Fig. 3.16 for three frequencies in the matching bandwidth at 79 GHz, 83 GHz, and 86 GHz, respectively. The final optimized design has a superior AR performance over a wide-angle and shows symmetric behavior in the elevation plane.

Fig. 3.17 shows the 2D normalized radiation pattern at φ = 0°, φ = 45°, and φ = 90° for the modified design #1 and final optimized design at 79 GHz, 83 GHz, and 86 GHz. The diffraction from the edges of the rectangular wall is stronger in the modified design #1. This results in higher ripples in the radiation patterns of design #1, as shown in Fig. 3.17(a, c, e). The effect of ripples

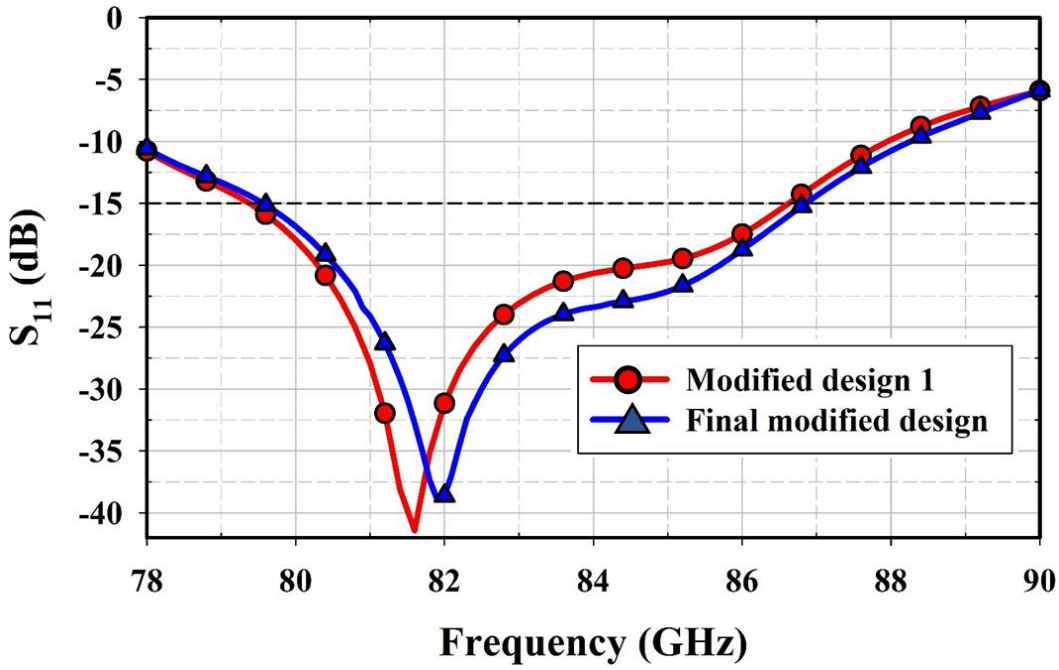

Figure 3.14 Simulated reflection coefficient of the feed horn with modified design #1 and final modified design.

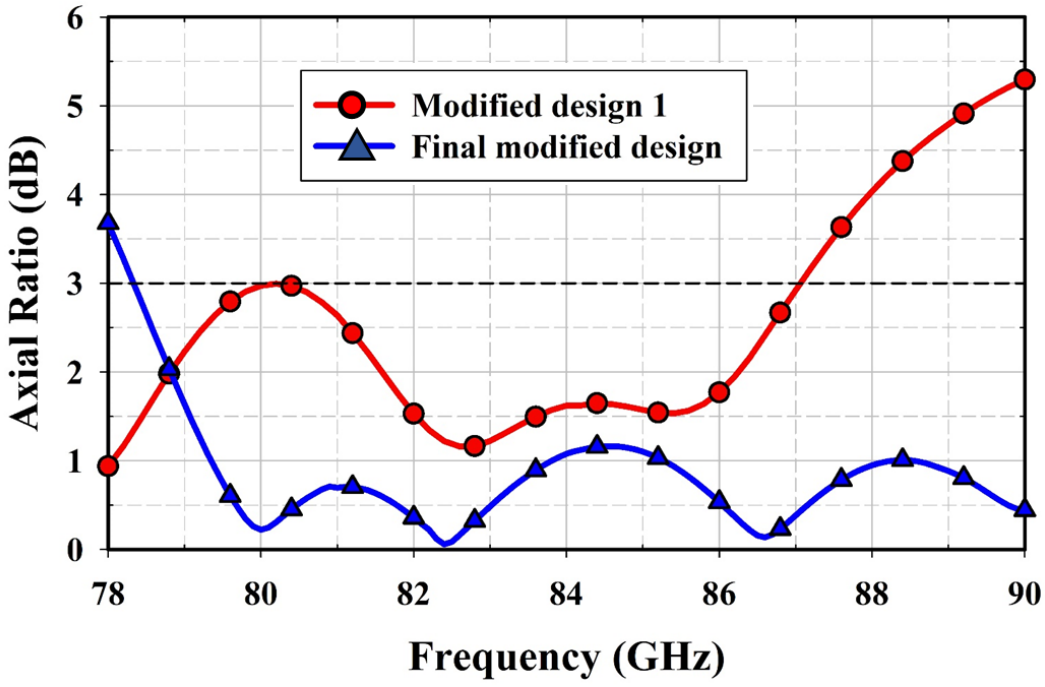

Figure 3.15 Simulated axial ratio of the feed horn with modified design #1 and final modified design as a function of frequency.

is stronger at the lower frequency at 79 GHz as opposed to the higher frequency at 86 GHz because the currents travel longer paths at lower frequency resulting in more diffraction around the edges. The presence of a circular skirt at the top of the optimized design reduces the diffraction and leads to a symmetric radiation pattern, as shown in Fig. 3.17(b, d, f). Thus, it is observed that the final optimized design provides stable and symmetric radiation patterns over the entire matching bandwidth, which satisfies the requirement of good feed source for reflector applications. The average cross-polarization isolation is more than 25 dB for the final optimized feed horn over the desired matching bandwidth.

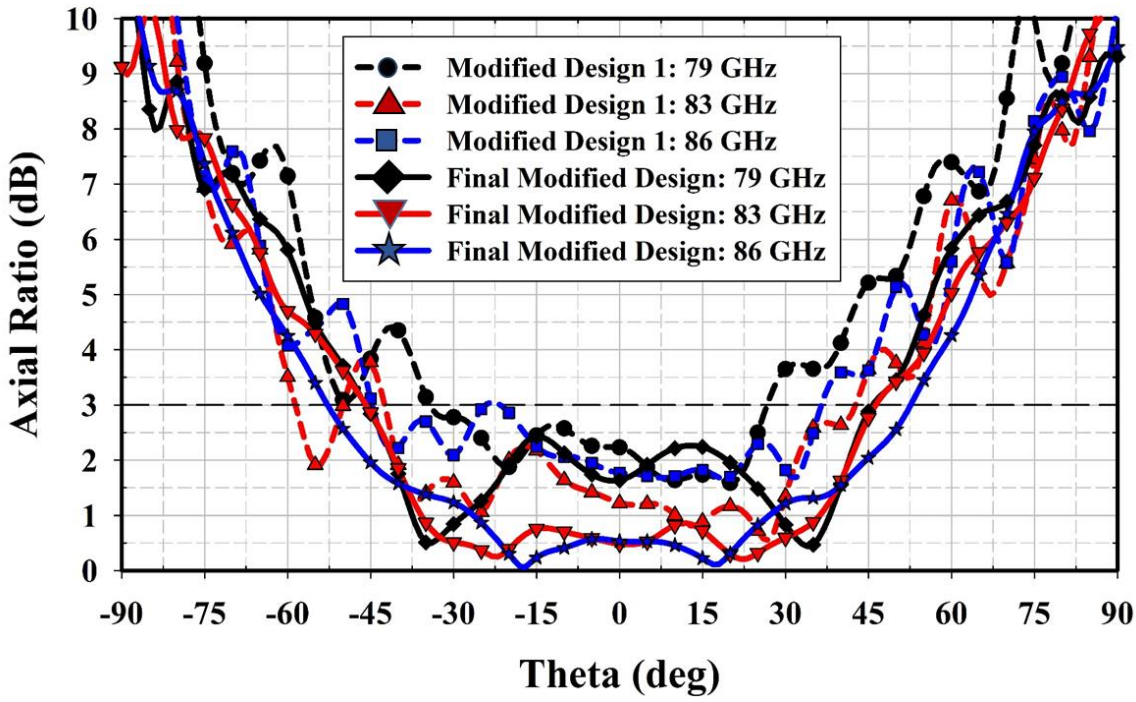

Figure 3.16 Simulated axial ratio vs. elevation angle, theta, of the feed horn with modified design #1 and final modified design at 86 GHz.

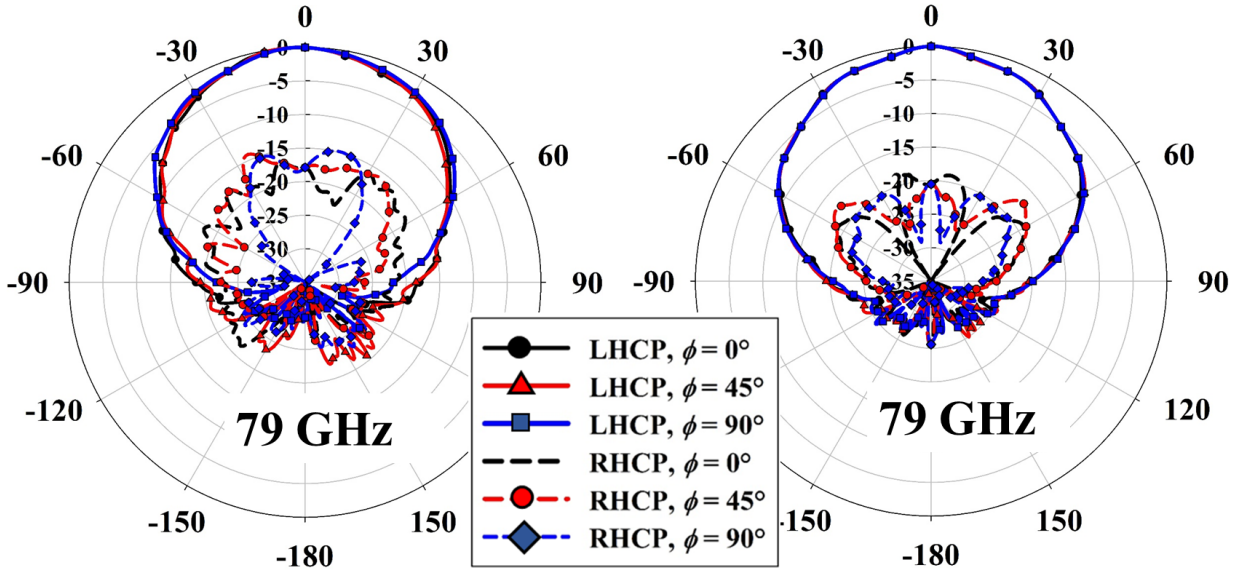

(a) (b)

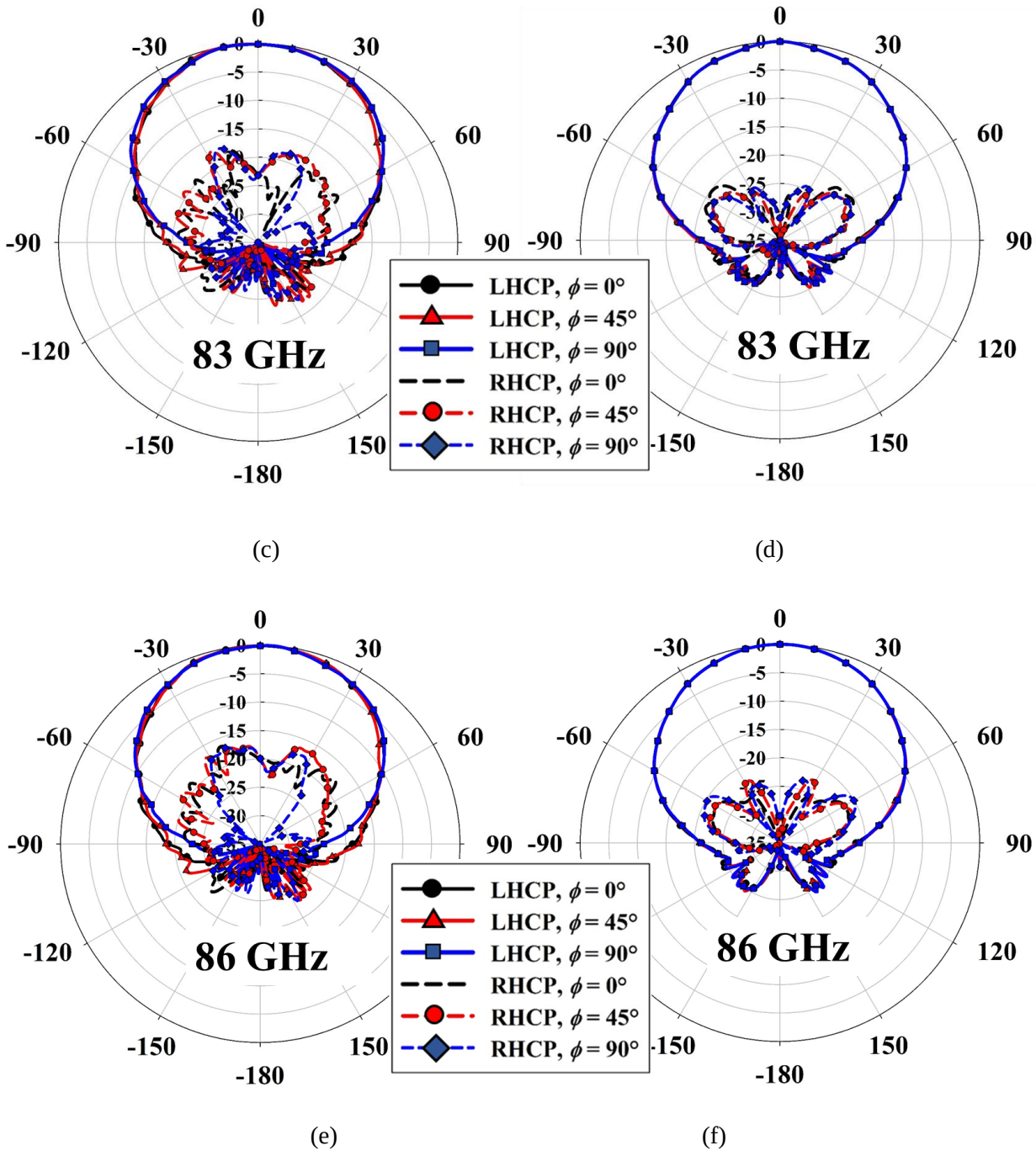

Figure 3.17 Simulated 2D normalized radiation pattern of the feed horn with modified design #1 (a, c, e) and final modified design (b, d, f).

The total simulated antenna efficiency is above 90% for both the designs from 79 GHz to 88 GHz, as shown in Fig. 3.18. The peak LHCP gain as a function of frequency is also presented

in Fig. 3.18. The average 12 dB half-edge illumination beamwidth of the final optimized design is around 65° over the matching bandwidth. The optimized feed horn antenna is used as a feed to illuminate an offset reflector with small *f/D* = 0.25.

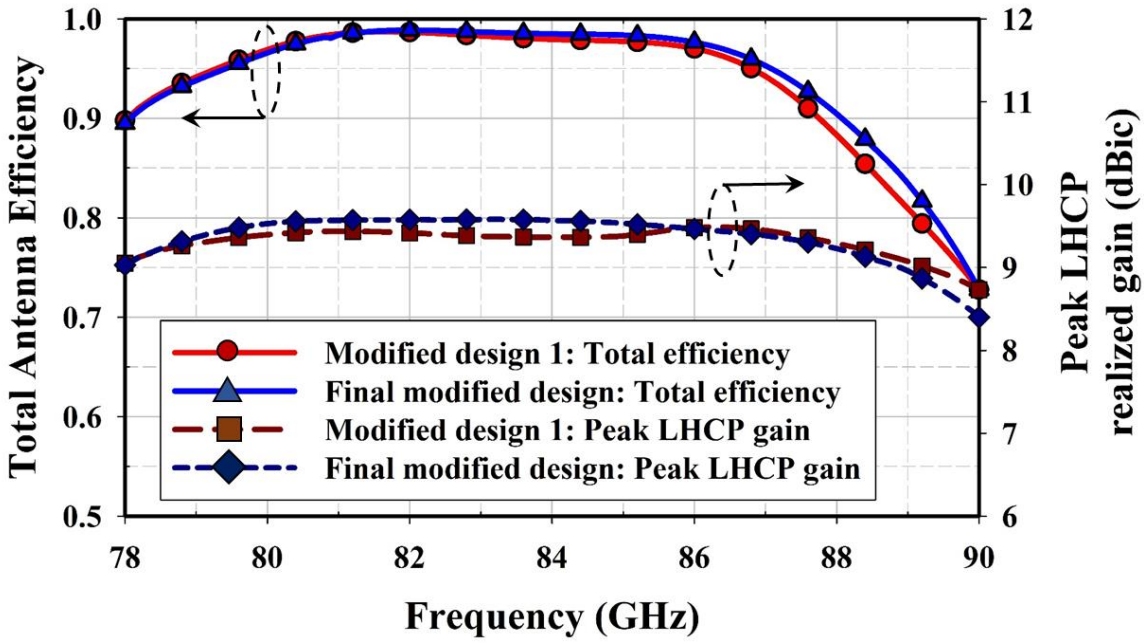

Figure 3.18 Simulated total antenna efficiency of the feed horn with modified design #1 and final modified design as a function of frequency.

3.5 Modified Feed Horn Integrated with Offset Parabolic Reflector

The proposed optimized feed horn antenna is used as a feed source to excite an offset parabolic reflector with a small *f/D* = 0.25, reflector diameter 10 cm, and no feed clearance from the focal axis. Figs. 3.19(a) and 3.19(b) show front and side view rendering of the feed reflector geometry. Extra metal thickness is added around the rim of the reflector for ease of fabrication and structural support of the strut. The feed source is directed at an angle of $\psi_f = 90°$ towards the center of the offset reflector from the focal axis. The offset reflector was analyzed using Ticra GRASP which utilizes Physical Optics (PO) currents on the reflector and Physical Theory of Diffraction

(PTD) rim currents to obtain the total induced current on the reflector. The radiation from the feed horn and the induced currents on the offset parabolic reflector are summed to get the total field.

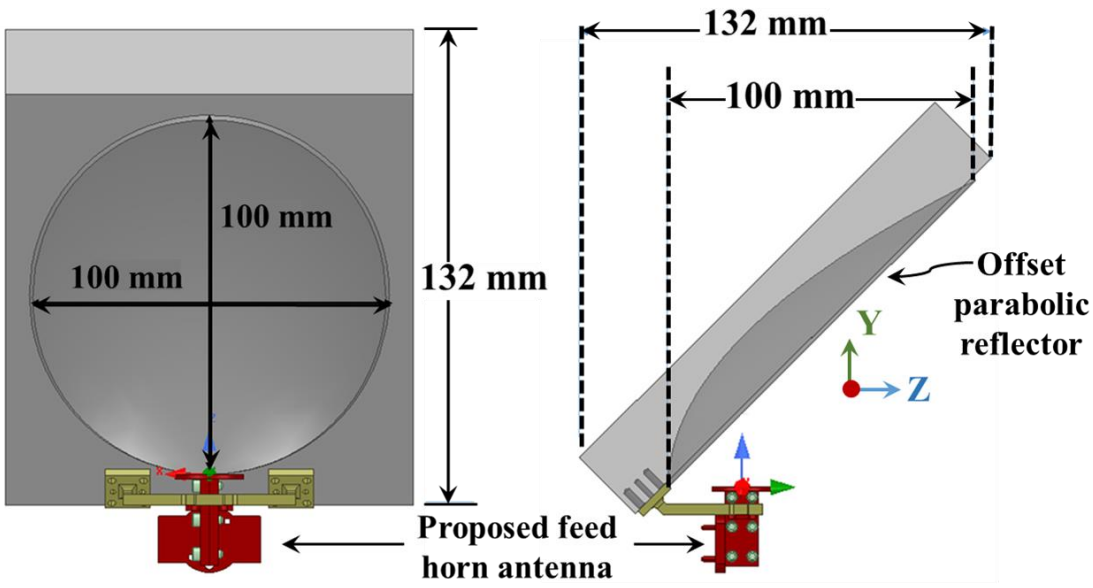

(a) (b)

Figure 3.19 Offset parabolic reflector integrated with the proposed optimized feed horn antenna (a) Front view, and (b) Side view.

3.6 Simulation and Measurement Results of the proposed antenna

The proposed feed horn and the offset parabolic reflector antenna is fabricated at the Custom Microwave Inc., facility. Figs. 3.20(a) and 3.20(b) are the photographs of the fabricated feed horn and the offset reflector integrated with the feed horn, respectively. The fabricated designs are measured at MVG spherical near-field chamber.

The impedance matching bandwidth of the feed horn is (S_{11} below -15 dB) from 79.5 GHz to 88 GHz. The simulated and measured impedance matching of the feed horn antenna is in excellent agreement, and the measured impedance matching is maintained with the feed reflector assembly as shown in Fig. 3.21. The measured AR for the feed horn antenna is below 1.2 dB over the

matching bandwidth, which is consistent with the simulation results, as shown in Fig. 3.22.

(a) (b)

Figure 3.20 Photograph of the fabricated (a) Proposed feed horn antenna, and (b) Offset parabolic reflector with feed horn assembly.

The simulated and measured polarimetric results for the AR as a function of elevation (step size $\Delta\theta$ = 1°) and azimuth ($\Delta\phi$ = 1°) angles are presented in Fig. 3.23(a-f) at 79 GHz, 83 GHz, and 86 GHz. The average simulated and measured 3 dB AR beamwidth is around 100° within the desired frequency range. The slight variation in the measured and simulated results might be due to the fabrication tolerance of the cavities in the feed horn.

The simulated and measured 2D normalized radiation patterns of the proposed feed horn antenna is presented at 79 GHz, 83 GHz, and 86 GHz in Fig. 3.24. The measured results show excellent correlation with the simulated results in terms of beamwidth and symmetrical patterns. The 3D realized gain radiation pattern is shown for the simulation (a, c, e) and measurement (b, d, f) in Fig. 3.25. It can be observed that a stable and symmetric radiation pattern is obtained over the

entire desired bandwidth. The simulated peak LHCP gain of the feed horn is 9.2 dBic, 9.5 dBic, and 9.45 dBic and the peak cross-polarization separation (separation between the peak co-polarization LHCP gain and the peak cross-polarization RHCP gain) is 20 dB, 24 dB, and 25 dB at 79 GHz, 83 GHz, and 86 GHz, respectively. The measured peak LHCP gain of the feed horn is 7.9 dBic, 8.9 dBic, and 9.1 dBic and the peak cross-polarization separation is 16 dB, 20 dB, and 19 dB at 79 GHz, 83 GHz, and 86 GHz, respectively. The discrepancy in the measured and simulated results might be due to fabrication and measurement tolerances. The measured peak LHCP gain and 12 dB half-edge illumination beamwidth of the proposed feed horn antenna as a function of frequency is presented in Fig. 3.26.

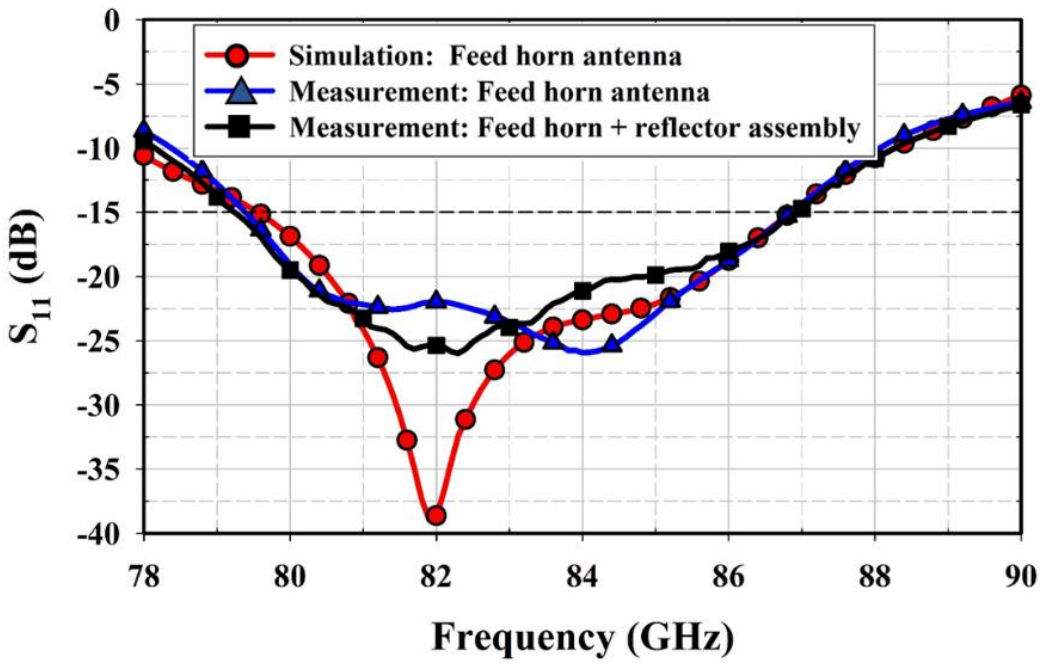

Figure 3.21 Simulated and measured S_{11} of the proposed feed horn antenna and the measured S_{11} of the integrated feed horn and reflector antenna.

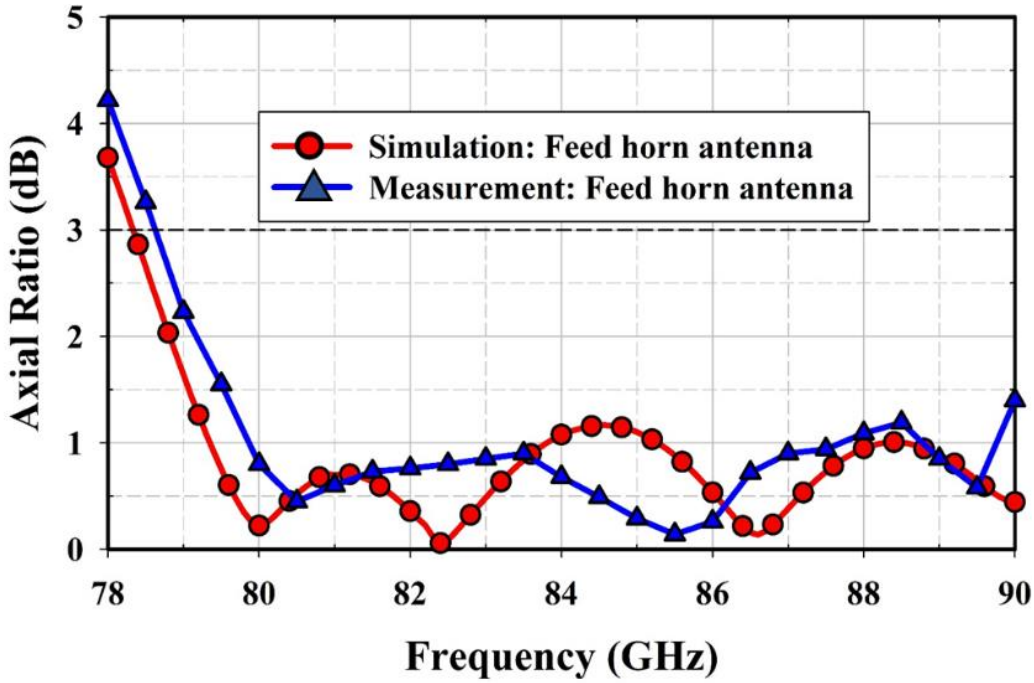

Figure 3.22 Simulated and measured axial ratio of the proposed feed horn antenna as a function of frequency.

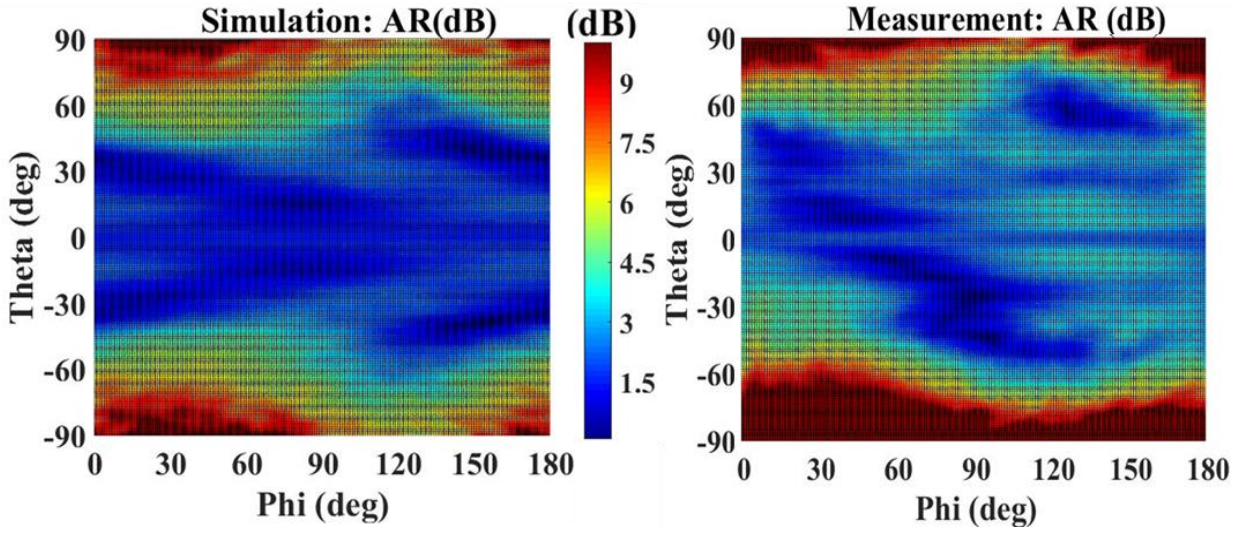

(a) (b)

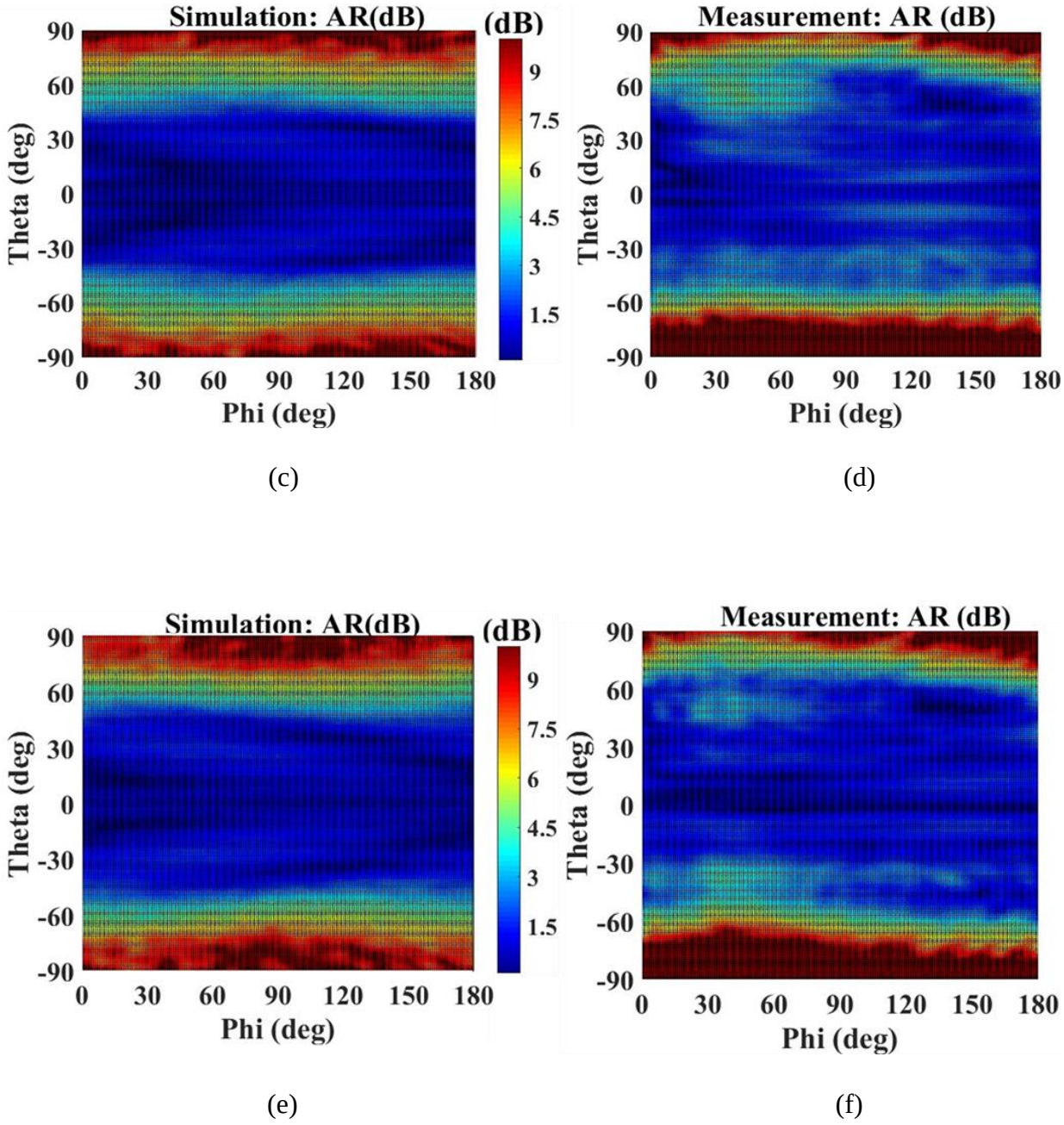

Figure 3.23 Simulated (a, c, e) and Measured (b, d, f) axial ratio vs. elevation angle, theta, of the proposed feed horn antenna at 79 GHz, 83GHz and 86 GHz.

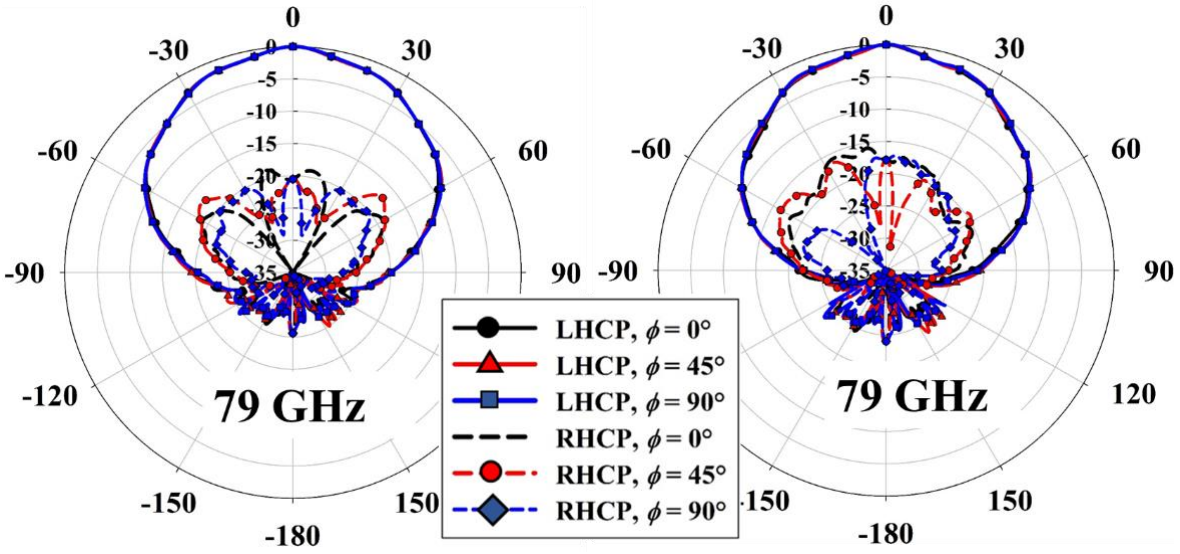
0
30
60
90
120
150
-180
-150
-120
-90
-60
-30
-5
-10
-15
-20
-25
-30
-35
79 GHz
LHCP, $\phi = 0°$
LHCP, $\phi = 45°$
LHCP, $\phi = 90°$
RHCP, $\phi = 0°$
RHCP, $\phi = 45°$
RHCP, $\phi = 90°$

(a) (b)

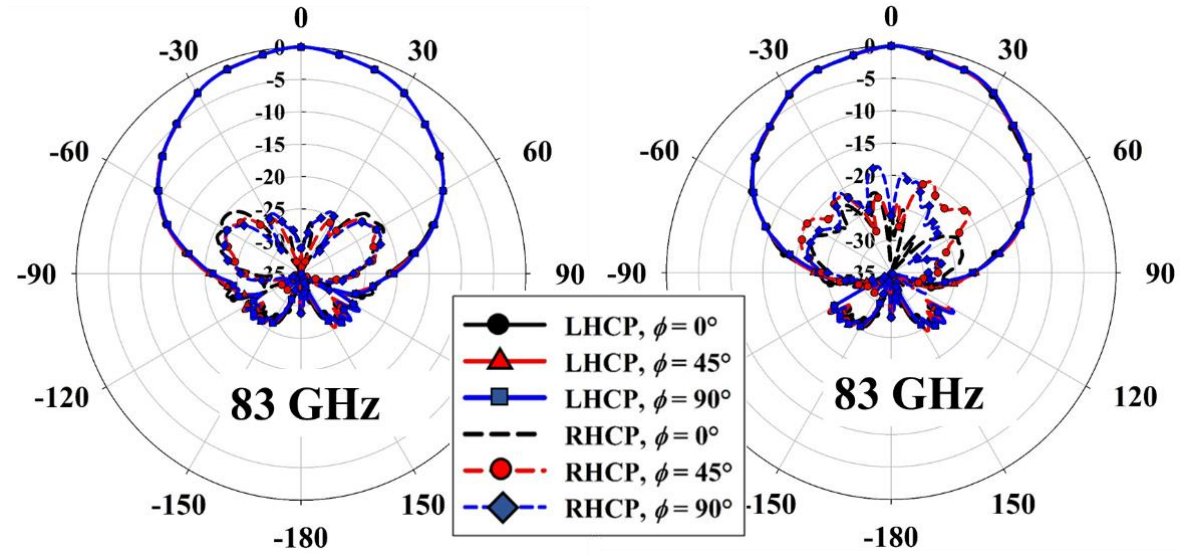
0
30
60
90
120
150
-180
-150
-120
-90
-60
-30
-5
-10
-15
-20
-25
-30
-35
83 GHz
LHCP, $\phi = 0°$
LHCP, $\phi = 45°$
LHCP, $\phi = 90°$
RHCP, $\phi = 0°$
RHCP, $\phi = 45°$
RHCP, $\phi = 90°$

(c) (d)

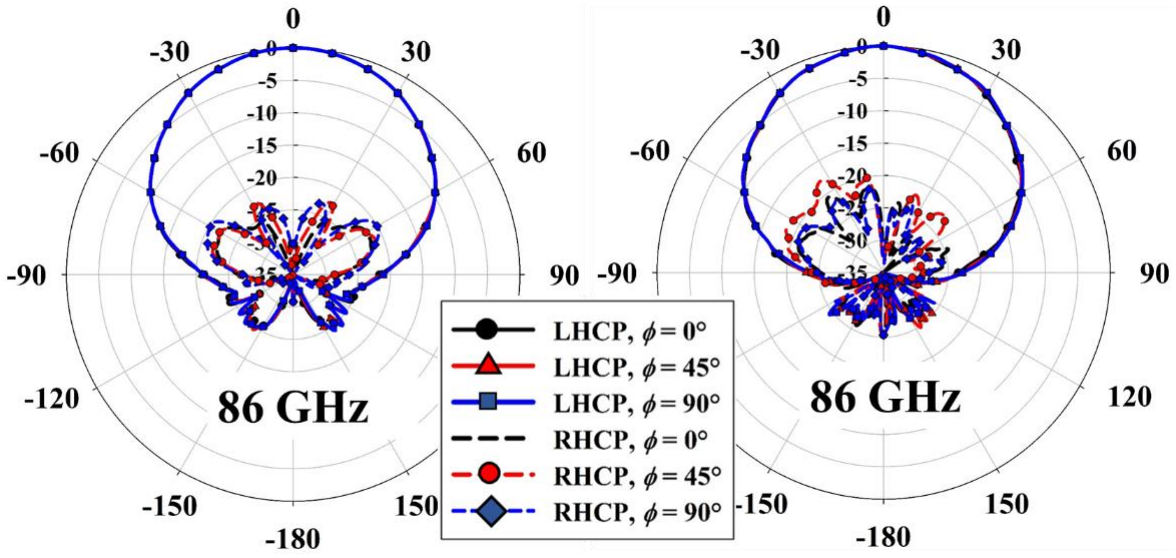

(e) (f)

Figure 3.24 Simulated (a,c,e) and Measured (b,d,f) 2D radiation pattern of the proposed feed horn antenna.

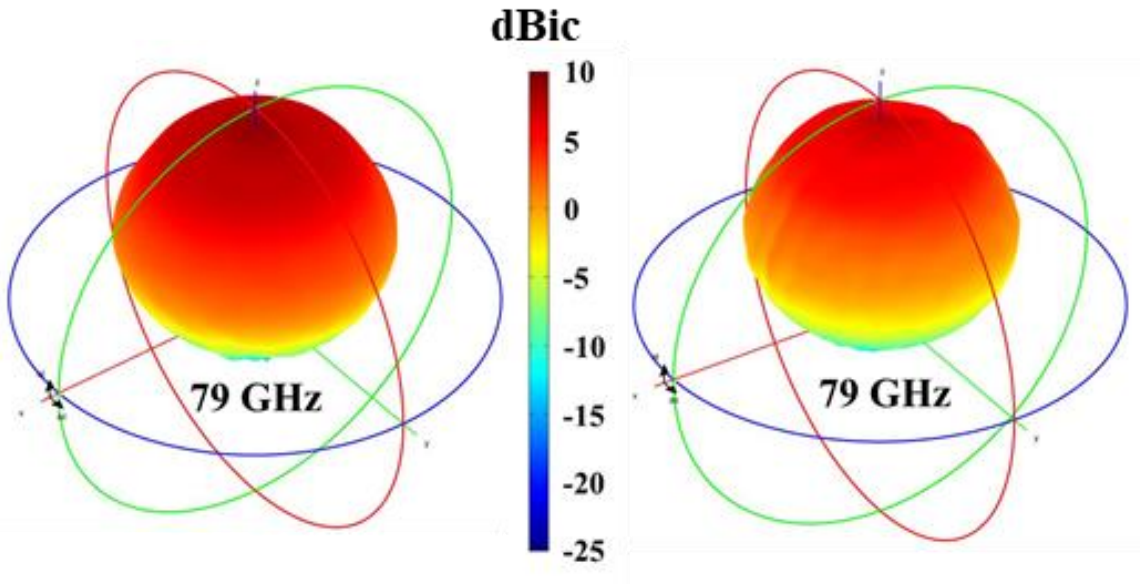

(a) (b)

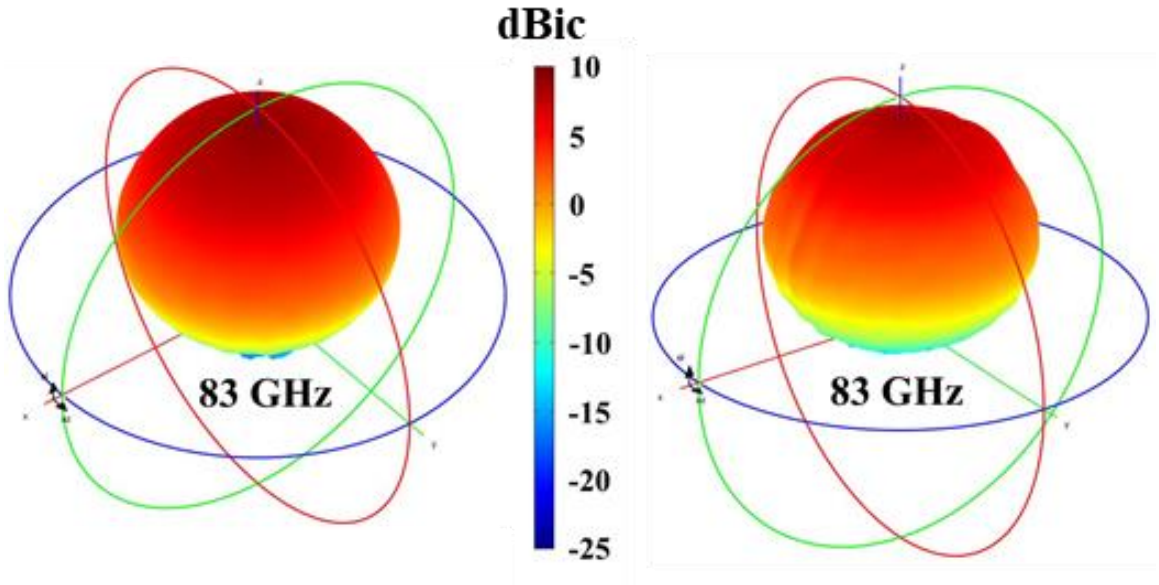

(c) (d)

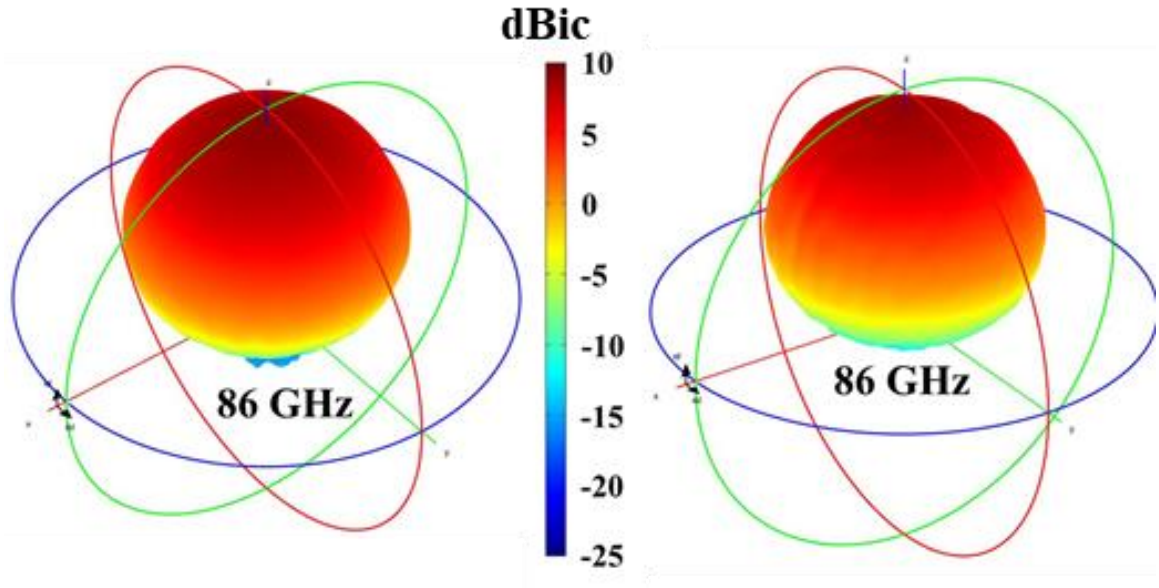

(e) (f)

Figure 3.25 Simulated (a,c,e) and Measured (b,d,f) 3D realized gain radiation pattern of the final optimized feed horn antenna.

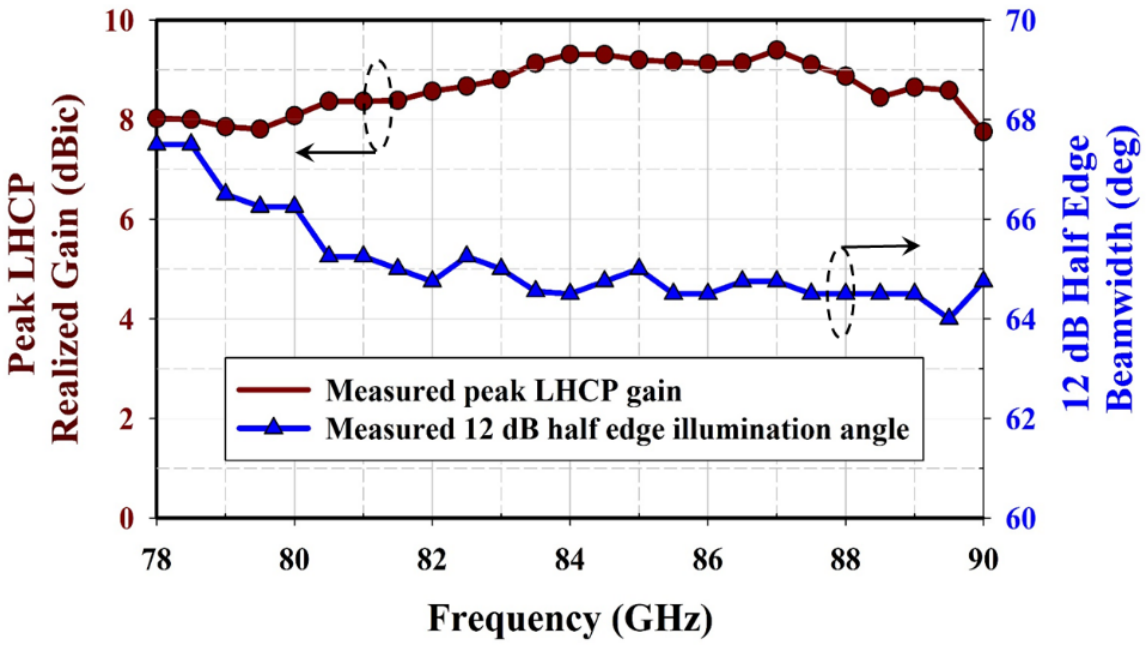

Figure 3.26 Measured peak LHCP gain and 12 dB half edge illumination beamwidth of the proposed feed horn antenna.

The proposed feed horn antenna shows the average measured 12 dB half-edge illumination of 65° over the desired matching bandwidth and meets the requirement to illuminate an offset parabolic reflector of *f/D* ratio 0.25. The feed radiation patterns are generated from HFSS simulation and incorporated as tabulated feed pattern (. cut files) into TICRA Grasp. The radiation from the feed horn and the induced currents on the offset parabolic reflector are summed to obtain the total field. Fig. 3.27(a, b, c) shows the stable surface current distribution on the reflector with edge taper of -12 dB at 79 GHz, 83 GHz, and 86 GHz, respectively. The simulated directivity pattern of the offset reflector is presented at 79 GHz, 83 GHz, and 86 GHz, in Fig. 3.28(a, b, c). The peak simulated RHCP directivity is 35.7 dBic, 36.2 dBic, and 36.6 dBic with peak cross-polarization separation of 20 dB, 28.9 dB, and 23.3 dB at 79 GHz, 83 GHz, and 86 GHz, respectively.

The spillover is calculated using Ticra GRASP, where the following equations are used to calculate the spillover loss for the reflector. When the induced PO currents are computed on a scatterer surface, the power contained in the incident field is calculated by integrating the Poynting vector $\vec{P}$ over the surface. The total power *W* on the surface is given as (3.5) [23]:

$$\begin{aligned} \vec{P} &= \frac{1}{2}\mathrm{Re}(\vec{E}\times\vec{H}^{*}) \\ W &= -\iint_{S}\vec{P}(\bar{r}^{\,'}).n(\bar{r}^{\,'})ds^{'} \end{aligned} \tag{3.5}$$

The spillover in dB is defined as (3.6) [23]:

$$spillover = 10\log_{10}\frac{4\pi}{W} \tag{3.6}$$

where the factor 4π originates from the normalization of the feed to the power 4π watt.

The simulated spillover loss of the reflector analyzed from Ticra GRASP is 0.83 dB, which is reasonable for low *f*/*D* of 0.25. The average 3 dB beamwidth is 2.5° in both φ = 0° and φ = 90° plane. The high cross-polarization level is due to the small *f*/*D* of the offset reflector. The cross-polarization separation can be improved by increasing the *f*/*D* of the reflector and with narrower half-edge illumination beamwidth feed sources. However, the current application of CubeSat limits the *f*/*D* to 0.25.

The simulated peak directivity and peak cross-polarization separation from Ticra GRASP are also compared with the Ansys HFSS-IE solver, as presented in Fig. 3.29. The HFSS-IE solver uses the method of moments (MoM) technique to solve for the sources or currents on the surfaces of conducting objects in open regions with linked sources.

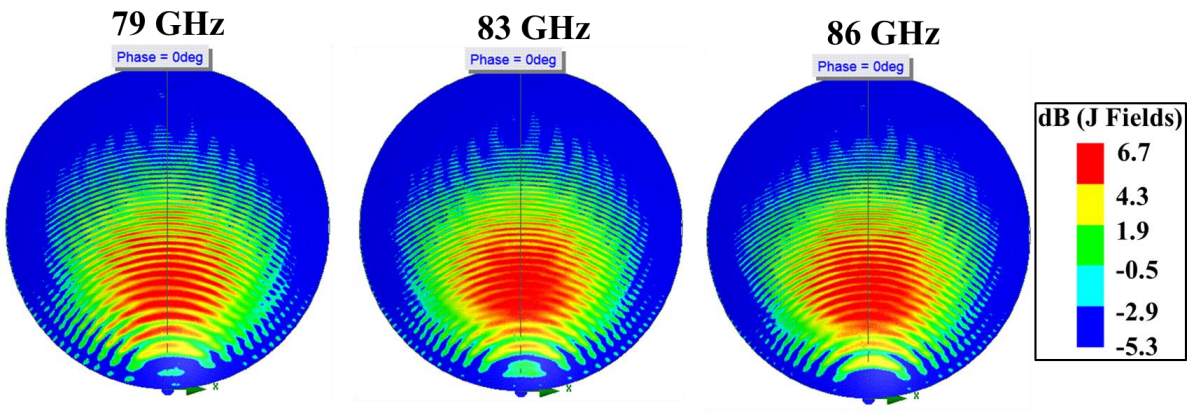

(a) (b) (c)

Figure 3.27 Current distribution on the offset parabolic reflector simulated in Ansys HFSS at (a) 79 GHz, (b) 83 GHz and (c) 86 GHz.

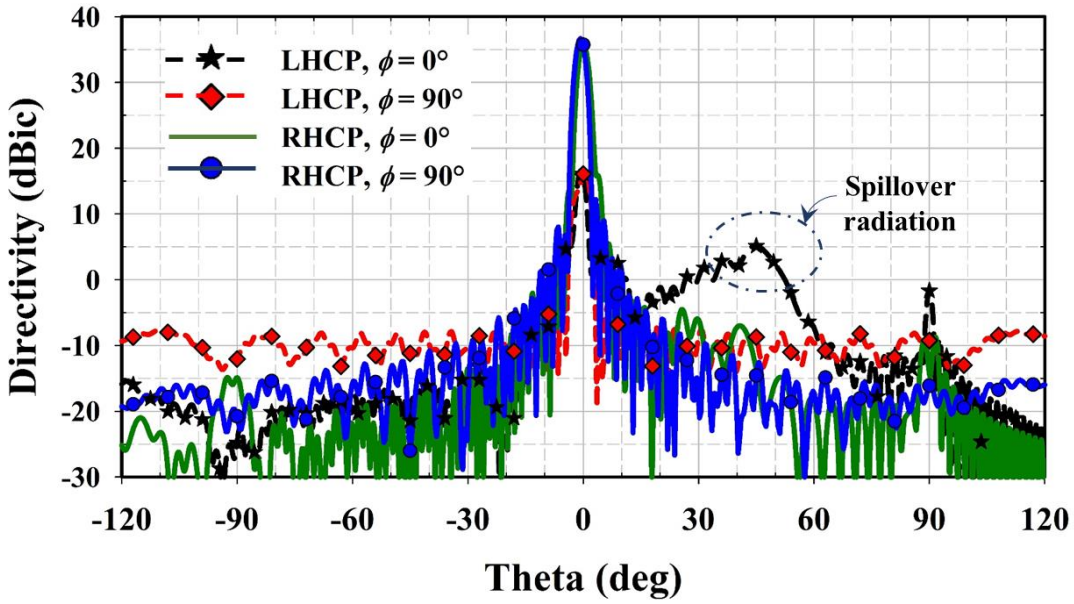

(a)

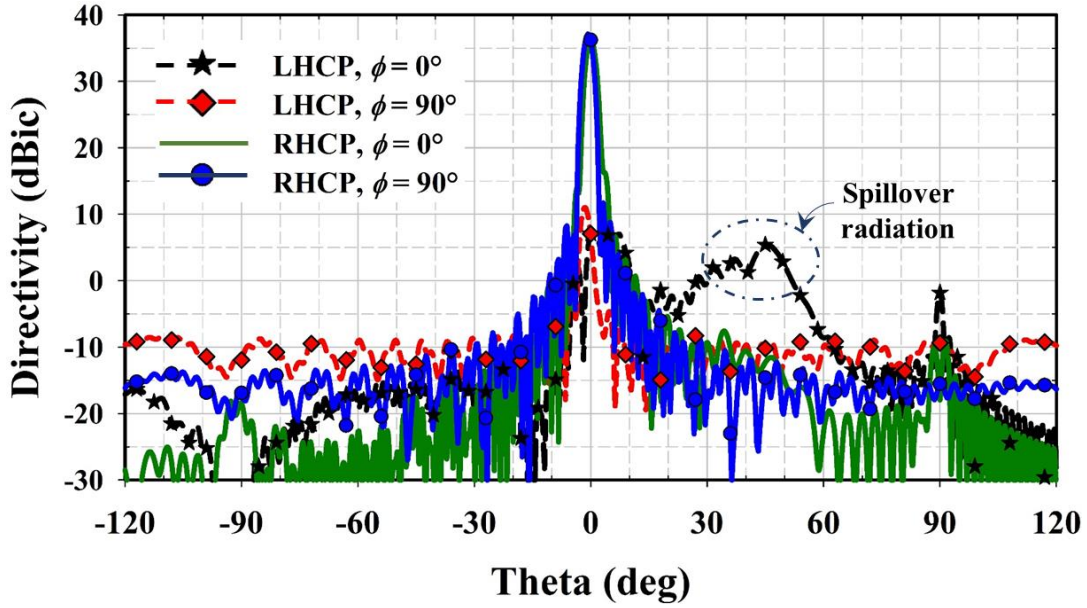

(b)

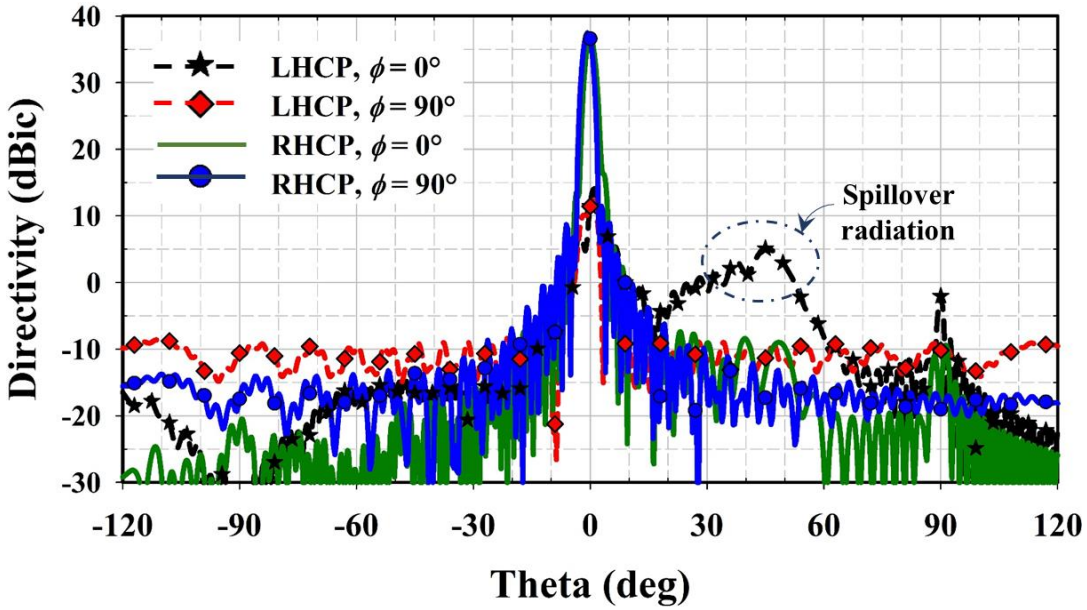

(c)

Figure 3.28 Simulated directivity pattern of the offset parabolic reflector illuminated by the proposed feed horn at (a) 79 GHz, (b) 83 GHz and (c) 86 GHz using Ticra GRASP.

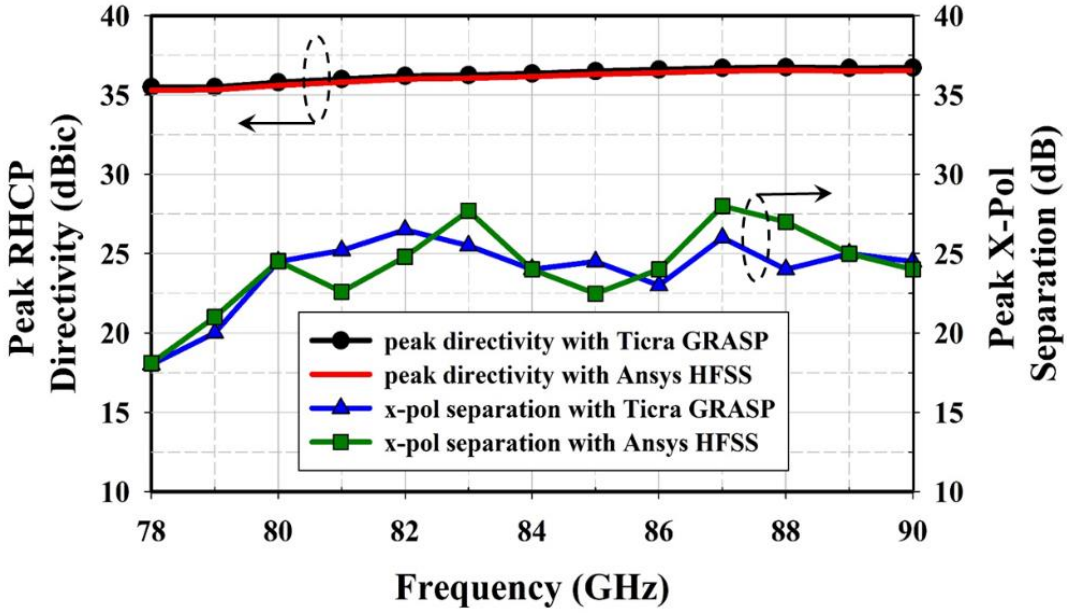

Figure 3.29 Peak simulated RHCP directivity and peak cross-polarization separation of the offset parabolic reflector illuminated by the proposed feed horn as a function of frequency using TICRA GRASP and Ansys HFSS-IE.

Fig. 3.30 illustrates the measurement setup for the integrated feed horn and offset reflector antenna at the Microwave Vision Group's MVG spherical near-field facility. Figs. 3.31(a, b, c) show the measured 2D realized gain reflector pattern at 79 GHz, 83 GHz, and 86 GHz, respectively. The small *f/D* of 0.25, along with the offset configuration of the reflector resulted in a high cross-polarization, as seen in Fig. 3.31. The measured peak RHCP gain of the proposed feed reflector antenna is 32.92 dBic, 33.77 dBic, and 34.36 dBic at 79 GHz, 83 GHz, and 86 GHz, respectively, as presented in the 3D RHCP realized gain radiation pattern Fig. 3.32.

The beam squint phenomenon is inherent to an offset parabolic reflector when illuminated by circularly polarized primary feeds [71]. The beam squint occurs in the φ = 90° plane direction that is orthogonal to the principal offset axis of the reflector. The peak of the RHCP radiation pattern occurs at a value θ_s , given by (3.7) [71]:

$$\theta_s = -\sin^{-1}\left(\frac{\lambda \sin\psi_f}{4\pi F}\right) \tag{3.7}$$

where ψ_f is the angle made by the feed at the center of the offset reflector.

At the center frequency of 83 GHz, this corresponds to the squint of -0.66° in φ = 90° plane. The measured squint angle at 83 GHz is at -0.71°, which is in a reasonable agreement to the computed value.

The average measured 3 dB beamwidth is 3° and 2.8° in φ = 0° and φ = 90° plane, respectively. Fig. 3.33 presents the peak RHCP gain and total antenna efficiency of the measured feed reflector

Figure 3.30 The measurement setup for the fabricated prototype of the feed reflector antenna at MVG spherical near-field chamber.

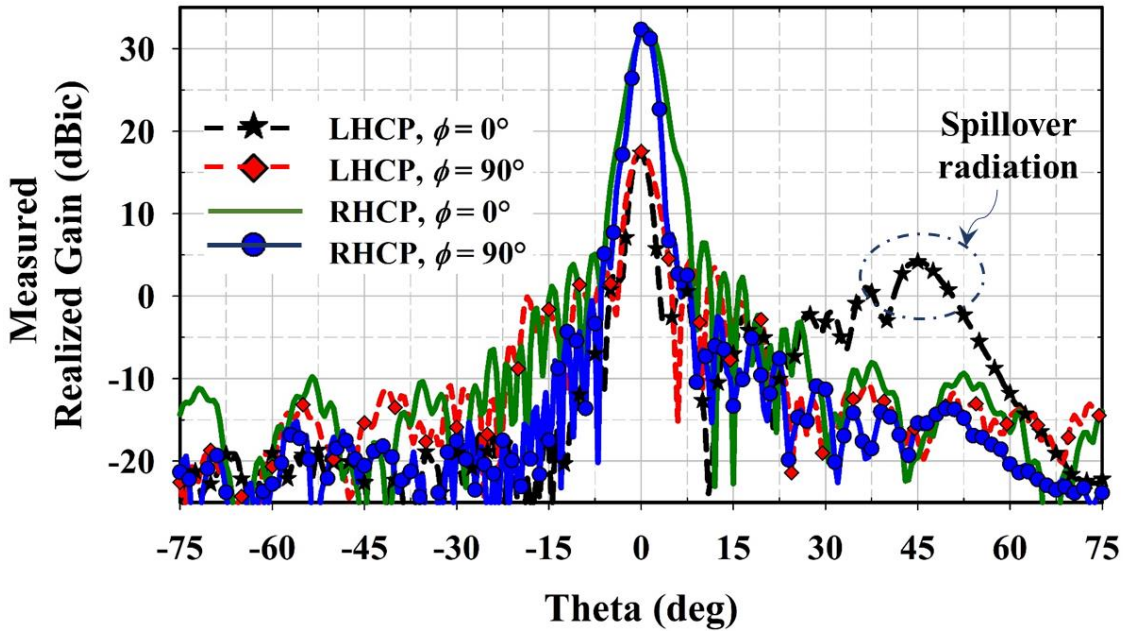
Measured
Realized Gain (dBic)
30
20
10
0
-10
-20
LHCP, $\phi = 0°$
LHCP, $\phi = 90°$
RHCP, $\phi = 0°$
RHCP, $\phi = 90°$
Spillover
radiation
-75
-60
-45
-30
-15
0
15
30
45
60
75
Theta (deg)

(a)

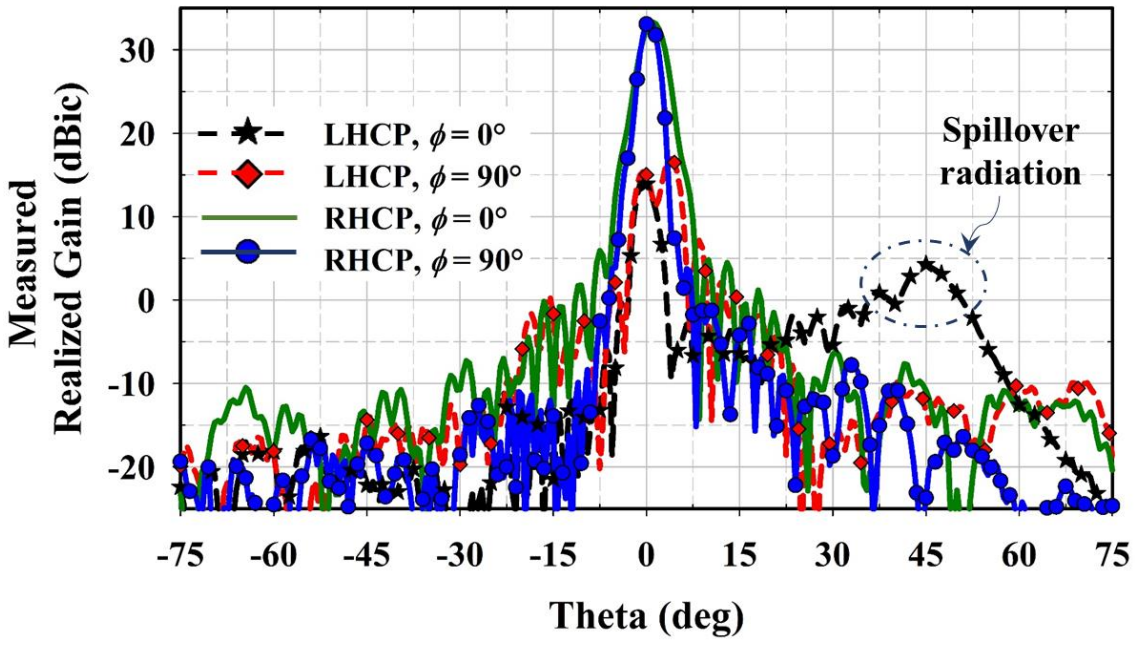
Measured
Realized Gain (dBic)
30
20
10
0
-10
-20
LHCP, $\phi = 0°$
LHCP, $\phi = 90°$
RHCP, $\phi = 0°$
RHCP, $\phi = 90°$
Spillover
radiation
-75
-60
-45
-30
-15
0
15
30
45
60
75
Theta (deg)

(b)

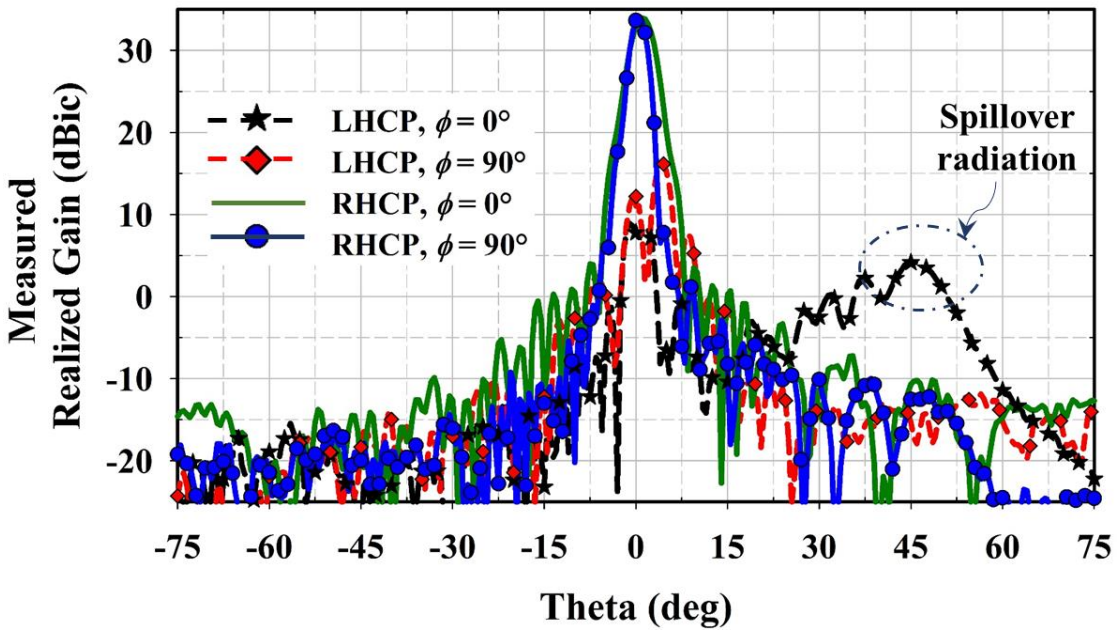

(c)

Figure 3.31 Measured realized gain pattern of the offset parabolic reflector at (a) 79 GHz, (b) 83 GHz and (c) 86 GHz.

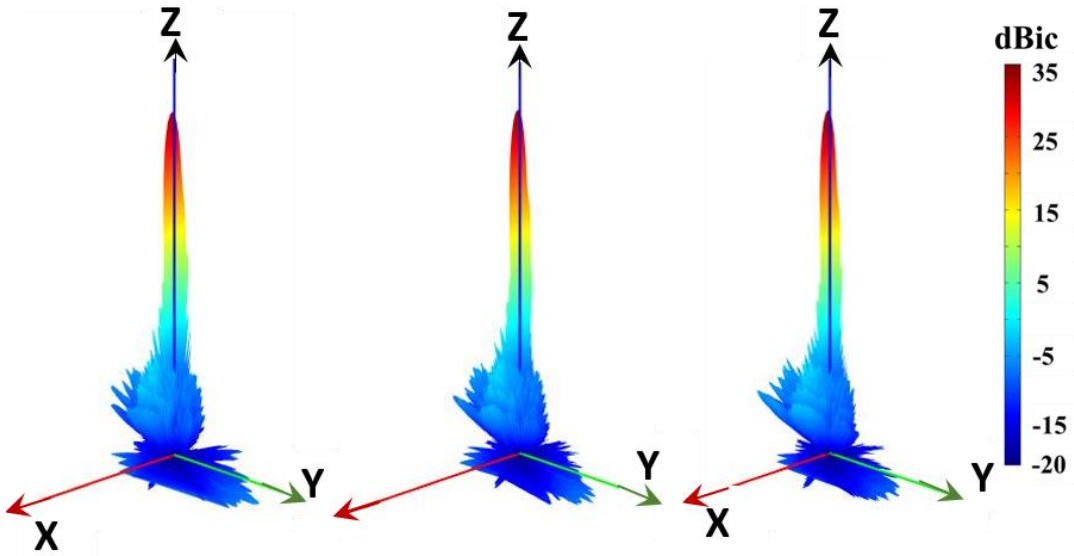

(a) (b) (c)

Figure 3.32 Measured 3D RHCP realized gain radiation pattern of the offset parabolic reflector at (a) 79 GHz, (b) 83 GHz and (c) 86 GHz.

antenna as a function of frequency. The average measured total antenna efficiency of the offset parabolic reflector is above 60% within the desired matching bandwidth from 79 GHz to 88 GHz. The total antenna efficiency includes the effect of feed horn mismatch loss, feed horn radiation efficiency, spillover, and aperture efficiency of the offset reflector.

Discussion in the research is limited to the feed horn and reflector antenna design for CubeSat application with $f/D = 0.25$. The stringent requirement on the reflector parameter led to a relatively high cross-polarization level. Applications, where space is not a constraint, a larger f/D more than 0.6 along with narrower illumination beamwidth of the feed horn, can be utilized for improved cross-polarization performance. Besides, aperture tapering and corrugations in the proposed feed aperture can be implemented to enhance the gain of the feed horn.

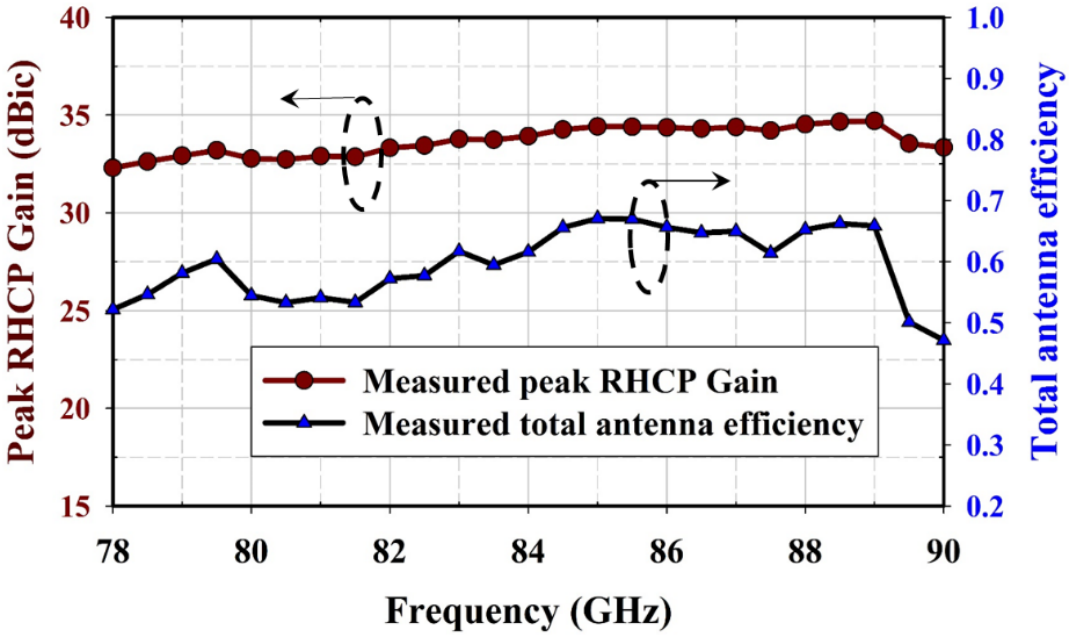

Figure 3.33 Measured peak RHCP realized gain and total antenna efficiency of the offset parabolic reflector as a function of frequency.

3.7 Effect of 6U-Cubesat Chassis

The proposed feed-reflector assembly is designed to be used in a CubeSat application at *W*-band. The impact of the CubeSat chassis on the antenna radiation performance is analyzed using the multilevel fast multipole method (MLFMM) along with the method of moments (MoM) in TICRA GRASP. The solver discretizes the geometry using higher-order quadrilateral patches and surface currents using higher-order basis functions.

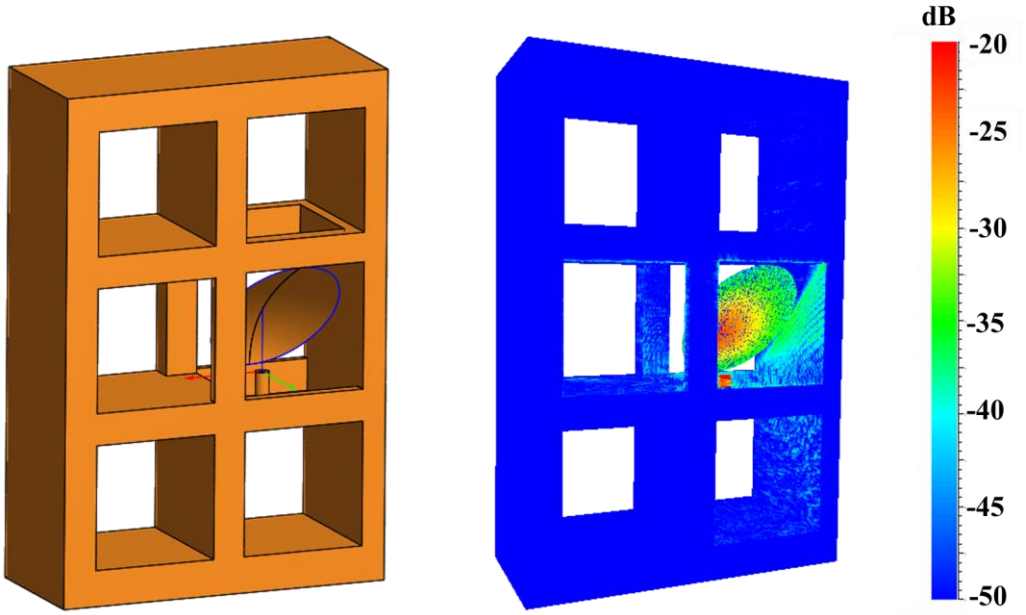

Figure 3.34 CAD rendering (left) and the simulated current distribution (right) at 86 GHz of the feed-reflector assembly inside the 6U CubeSat chassis.

The position of the feed reflector assembly inside the CubeSat chassis is chosen to study the worst-case antenna performance. The CAD rendering of the integrated feed reflector inside a 1U block of the 6U-CubeSat chassis and the simulated MoM current distribution on the entire structure at 86 GHz is presented in Fig. 3.34. The comparison of the 2D directivity pattern of the feed reflector assembly with and without the CubeSat chassis is shown in Fig. 3.35(a) and Fig. 3.35(b)

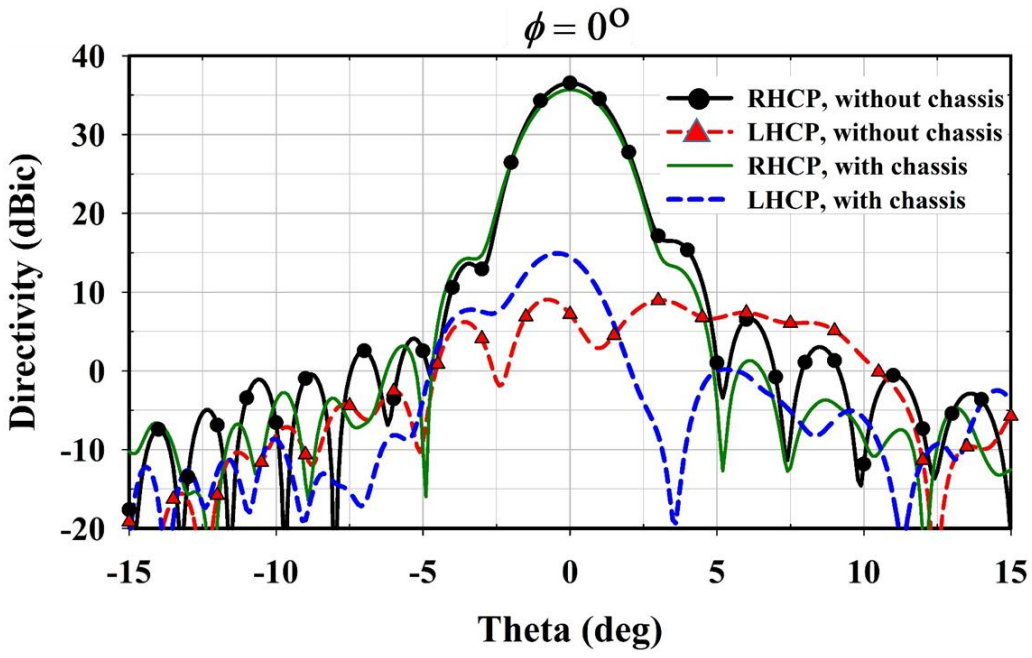

(a)

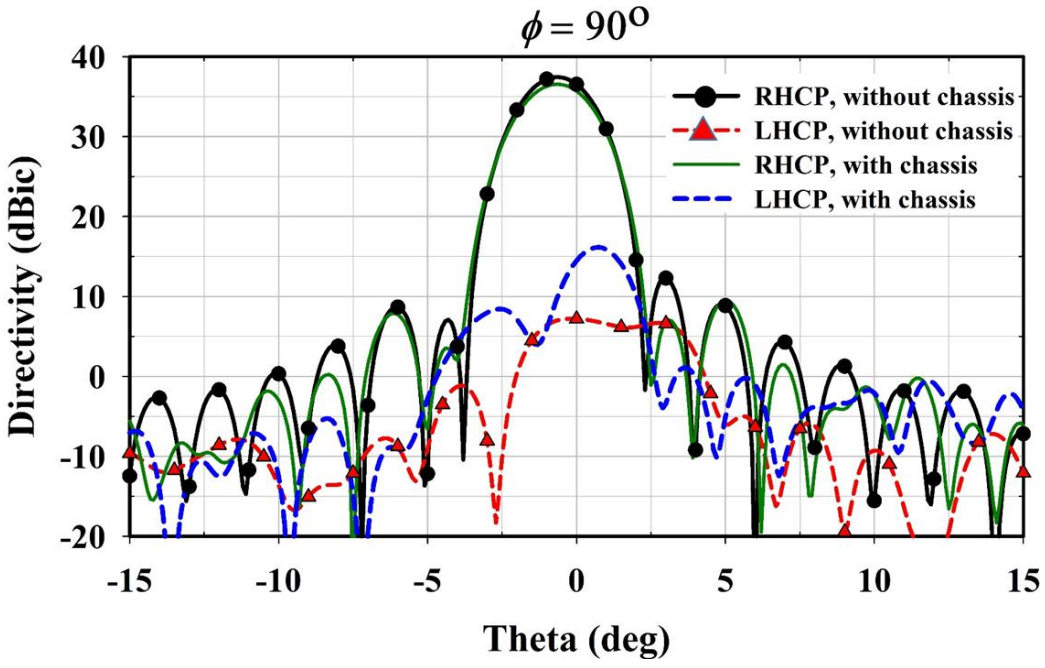

(b)

Figure 3.35 Simulated 2D directivity pattern of the feed-reflector with and without the 6U CubeSat chassis at (a) φ = 0° plane and (b) φ = 90° plane, analyzed using the MoM/MLFMM solver in TICRA GRASP.

at $\varphi = 0°$ and $\varphi = 90°$, respectively. The peak simulated RHCP directivity of the integrated feed-reflector inside the CubeSat chassis is 35.69 dBic and 36.53 dBic and the peak simulated RHCP directivity of the feed reflector antenna without the CubeSat chassis is 36.53 dBic and 37.44 dBic at $\varphi = 0°$ and $\varphi = 90°$, respectively. The LHCP cross-polarization has increased significantly by 6 dB and 8 dB at $\varphi = 0°$ and $\varphi = 90°$, respectively, in the presence of the CubeSat chassis. Thus, the CubeSat has a strong impact on the cross-polarization and reduces the peak RHCP directivity by 0.9 dB.

3.8 Conclusion

A novel circular polarized feed horn was developed at *W*-band frequency from 79 GHz to 88 GHz that eliminates the need for an external OMT or a complex septum to generate CP waves. The detailed parametric analysis was used to determine the optimum dimension of the proposed feed horn antenna. The results of the analysis and the simulation were validated in the fabrication and measurement of the proposed feed horn antenna. The proposed feed horn was shown to have an impedance matching (S_{11} below -15 dB) and AR (below 1.2 dB) from 79.5 GHz to 88 GHz. The pattern symmetry and the stable radiation performance was also verified in the radiation pattern measurement of the proposed feed horn and reflector. The effect of CubeSat chassis on the radiation performance of the proposed feed horn integrated with the offset parabolic reflector assembly was also simulated.

The next chapter discusses a new radiating element called Butterfly antenna as a phased array solution for the high gain right-hand circular polarized RHCP *W*-band CubeSat application.

Chapter 4

High Gain Series-fed Circularly Polarized Traveling-Wave Antenna at *W*-band using a New Butterfly Radiating Element

4.1 Introduction

Circular polarized antennas have gained considerable interest in the modern communication systems due to their several advantages, such as resistance to signal degradation from atmospheric conditions, insensitivity to depolarization, and higher link reliability [72]. Further, the microstrip technology makes these antennas an excellent candidate owing to their low profile and lightweight structure, ease of fabrication and integration, and low manufacturing cost [73], [74]. CP patch antennas find applications in radar, remote sensing, microwave, and millimeter-wave point-to-point communication systems [75]. A surface integrated waveguide (SIW) based structure can provide better efficiency at millimeter-wave frequencies, but it comes at the cost of increased complexity and much expensive implementation as compared to a single-layer microstrip technology.

CP waves can be generated using several techniques such as quadrature-phase excitation of two orthogonal linear polarized (LP) feeds, a single CP feed, and sequential rotation [76], [77]. Various feed networks for CP antenna arrays are presented in [78] - [82]. Various series-fed microstrip traveling-wave antenna arrays have been reported in the literature [83]. In [84], a method based on a set of canonical coefficients is used to analyze the linear series-fed array. The series-fed traveling antenna can also be analyzed using the theory of periodic leaky-wave antenna (LWA) [36], [37]. The fast-spatial harmonics produced by the periodic perturbations are

responsible for the radiation in the periodic LWA. Usually, one space harmonic (n = -1) is sufficient to represent the complex propagation constant, with β_{-1} and α [36], [37], [85], [86]. In [87] – [90], several leaky-wave antenna arrays were reported. In [91], a series-fed herringbone microstrip periodic LWA array was designed to achieve broadside radiation.

Most LWA exhibits an open-stopband (OSB) region where there is a significant gain degradation when the main beam points towards broadside. At OSB, when $\beta_{-1} \approx 0$, the summation of the internal reflections within the unit cells in the periodic LWA leads to the reduced radiation at broadside [38]. Several methods have been reported to suppress the OSB and realize a continuous beam scan [38], [39]. In [92], a composite right/left-handed (CRLH) based microstrip periodic LWA was analyzed to suppress OSB. A novel technique to suppress OSB in 1D periodic LWA was reported in [93]. Another method for suppression of the OSB was suggested for the 1D periodic combline LWA [94].

In this research, a *W*-band (86 GHz) right-hand circular polarized (RHCP) novel radiating element known as the Butterfly antenna is proposed. The Butterfly antenna element is suitable for low loss series-fed array applications requiring good quality CP at millimeter-wave frequencies. This antenna utilizes low cost printed antenna technology with sequentially-rotated antenna elements for wide axial ratio beamwidth and low cross-polarization radiation. A compact sequentially-rotated linear array structure is proposed by overlapping the last element of one unit-cell to the first element of the next cell. The compact structure exhibits a stable radiation pattern despite the overlapping elements due to the sequential-fed phase shifts.

The planar array made from these CP linear arrays makes it particularly significant for the single-plane phased array beam steering applications. A 1 × 24 linear arrays is analyzed using the periodic LWA theory, and the complex leaky wave number is computed to describe the radiation

characteristics. The linear array inherently suppresses the OSB condition and provides consistent gain through the broadside radiation. Two passive fixed-beam passive planar arrays of size 8 × 24 and 32 × 24 are fabricated using the proposed Butterfly series-fed array, and the measured results agree reasonably well with the full-wave electromagnetic (EM) analysis of the array antennas.

4.2 Unit-Cell Butterfly Antenna Geometry

The unit-cell geometry of the proposed Butterfly antenna is shown in Fig. 4.1. The antenna is designed at 86 GHz on a 5 mil (1 mil = 0.0254 mm) Rogers RO3003 substrate of $\varepsilon_r = 3$ and with rolled annealed copper-foil of 0.3 μm surface roughness. The unit cell consists of a sequentially-rotated series-fed linear array of four resonant LP microstrip patch antenna elements. The four patch elements are rotated by 45°, 135°, 225°, and 315° around its feeding point, respectively. The sequentially-rotated patch antennas are separated by d = 0.57 mm, which corresponds to the quadrature electrical distance of $\lambda_g/4$ at 86 GHz, where λ_g is the effective wavelength in the microstrip. The length of the unit cell is L_u = 2.3 mm or one λ_g at 86 GHz. The patch width is W_p = 0.32 mm, patch length is L_p = 0.95 mm and transmission line width W_t = 0.32 mm.

RHCP radiation is achieved due to the sequential-fed phase shifts when the structure is excited at the input port and match-terminated at the output port. The snapshots of the simulated instantaneous current distribution on the unit-cell at different excitation phase shifts are illustrated in Fig. 4.2. As observed, when the phase of the excitation source is step-changed per quadrature, the polarity of the total radiated field is RHCP.

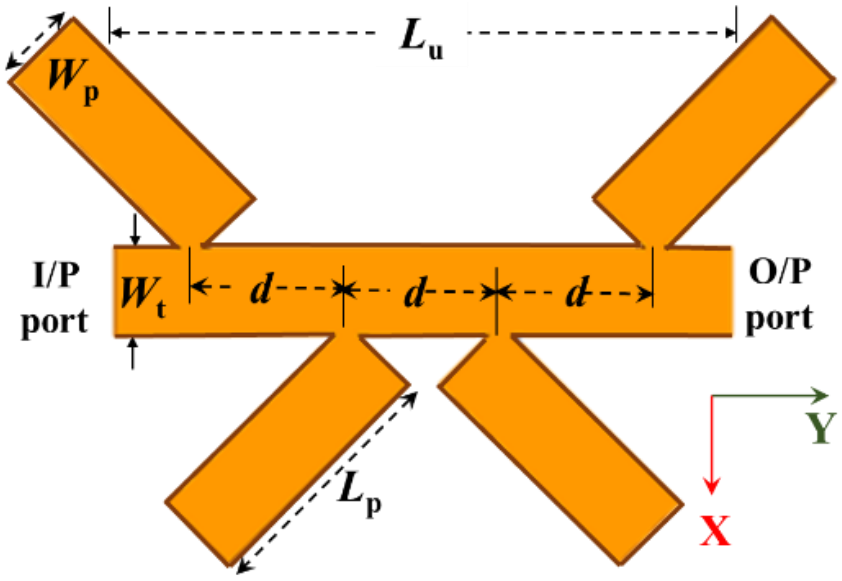

Figure 4.1 Unit-cell geometry of the proposed Butterfly antenna.

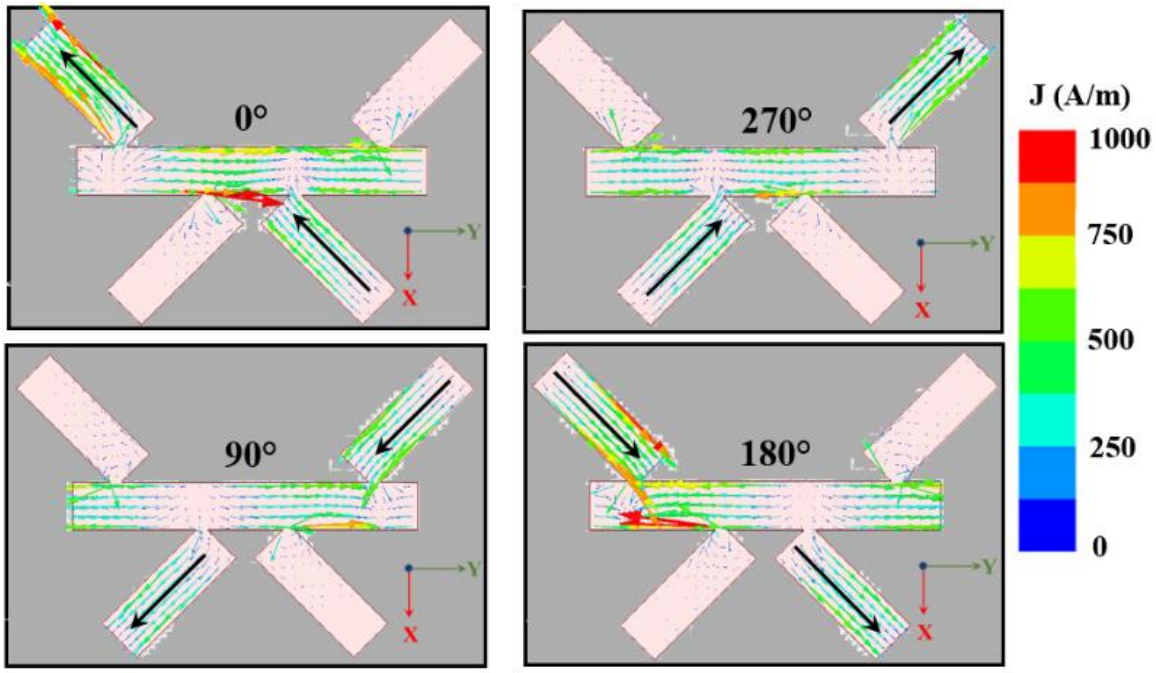

Figure 4.2 The instantaneous surface current distribution on the unit-cell Butterfly antenna at excitation source phase instances of 0°, 90°, 180°, and 270°.

4.3 Analysis, Computation and Theory of Operation

4.3.1 Analysis of Unit-Cell

The unit-cell of the Butterfly antenna consists of four sequentially rotated LP patch antenna elements. The sequential excitation phase shifts of 0°, -90°, -180° and -270° on the four rotated LP patch elements generate the desired RHCP. To analyze the total radiated field of the unit-cell, first, the far-field components are determined for the isolated LP patch antenna without rotation. The far-field components of the rectangular patch antenna can be computed using the cavity model analysis given in [32]. This method is briefly reviewed here for the patch orientation shown in Fig. 4.3(a).

In the cavity model, the patch antenna of Fig. 4.3(a) is viewed as a linear array of two identical radiating slots separated by a distance *b*. The electric vector potential F_y for one of the radiating slots, with the magnetic current source $\mathbf{M}_y$ and the dominant TM_{100} mode, can be calculated by (4.1) [32]:

$$F_y = \frac{\varepsilon}{4\pi r} e^{-jk_0 r} \int_{-a}^{0} \int_{-h}^{0} \mathbf{M}_y e^{jk_0 \sin\theta \sin\phi y'} dy' dz' \tag{4.1}$$

The corresponding normalized electric vector potential is proportional to (4.2) [32]:

$$F_y \propto \frac{\sin\left(k_0 \sin\theta \sin\phi \frac{a}{2}\right)}{\left(k_0 \sin\theta \sin\phi \frac{a}{2}\right)} = \frac{\sin\left(k_y \frac{a}{2}\right)}{\left(k_y \frac{a}{2}\right)} \tag{4.2}$$

where $k_y = k_0 \sin\theta \sin\phi$ and k_0 is the free-space wavenumber. Using the Cartesian-to-Spherical coordinate transformations, the electric vector potential can be written as (4.3) [32]:

$$\begin{aligned} F_\theta &= F_y \cos\theta \sin\phi \\ F_\phi &= F_y \cos\phi \end{aligned} \tag{4.3}$$

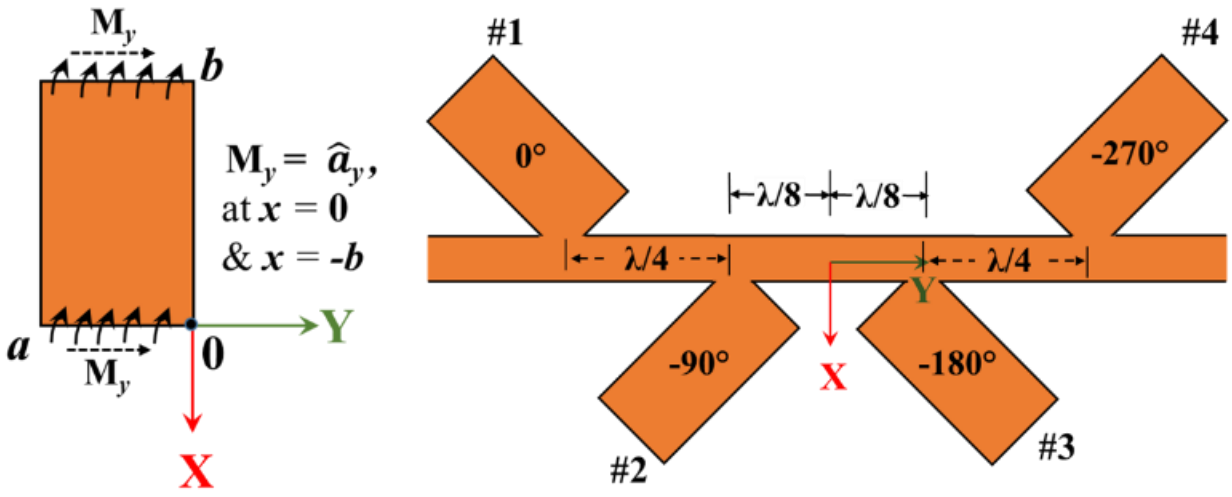

(a) (b)

Figure 4.3 (a) Magnetic current source on the isolated LP patch antenna with no rotation, and (b) Linear array of the four sequentially rotated patch antenna.

The array factor of the two slots separated by a distance *b* along the *x*-direction is (4.4) [32]:

$$\left(AF\right)_x \propto \cos\left(\frac{k_0 b}{2}\sin\theta\cos\phi\right) = \cos\left(k_x\frac{b}{2}\right) \tag{4.4}$$

$$\text{where } k_x = k_0\sin\theta\cos\phi$$

Thus, the total electric vector potential for the patch antenna of Fig. 4.3(a) is obtained by combining (4.1) – (4.4) and is given as (4.5) [32]:

$$\begin{aligned} F_\theta^t &= F_y\cos\theta\sin\phi\cos\left(k_x\frac{b}{2}\right) \\ F_\phi^t &= F_y\cos\phi\cos\left(k_x\frac{b}{2}\right) \end{aligned} \tag{4.5}$$

The radiated electric field is related to the electric vector potential by the relation (4.6) [32]:

$$E_\theta(\theta,\phi) \propto F_\phi^t \propto \frac{\sin\left(k_y\frac{a}{2}\right)}{\left(k_y\frac{a}{2}\right)}\cos\left(k_x\frac{b}{2}\right)\cos\phi$$
$$E_\phi(\theta,\phi) \propto F_\theta^t \propto \frac{\sin\left(k_y\frac{a}{2}\right)}{\left(k_y\frac{a}{2}\right)}\cos\left(k_x\frac{b}{2}\right)\cos\theta\sin\phi \quad (4.6)$$

Equation (4.6) is the total normalized far-field components of the isolated LP patch antenna with no rotation. Now, consider the linear array with patch elements rotated individually, as shown in Fig. 4.3(b), where each element is rotated around its feeding point. Accordingly, the radiation pattern is also rotated. The total radiated fields of the linear array of Fig. 4.3(b) with (N = 4) elements rotated individually can be expressed as (4.7) and (4.8):

$$E_\theta^T(\theta,\phi) = \sum_{n=1}^{N} E_{\theta n}(\theta,\phi-\alpha_n)e^{j(k_0 d_n \sin\theta\sin(\phi-\alpha_n)+\phi_n)} \quad (4.7)$$

$$E_\phi^T(\theta,\phi) = \sum_{n=1}^{N} E_{\phi n}(\theta,\phi-\alpha_n)e^{j(k_0 d_n \sin\theta\sin(\phi-\alpha_n)+\phi_n)} \quad (4.8)$$

where $\phi_n = \frac{2\pi(n-1)}{N}$ is the excitation current phase of the n^{th} element and $\alpha_n = \frac{2\pi(n-1)}{N} + \frac{\pi}{4}$ is the rotation angle of the n^{th} element. $E_{\theta n}(\theta,\phi-\alpha_n)$ and $E_{\phi n}(\theta,\phi-\alpha_n)$ are the θ- and ϕ-components of the radiated field for the rotated element n, which is transformed from the radiated field $E_\theta(\theta,\phi)$ and $E_\phi(\theta,\phi)$ of the isolated element without rotation.

The RHCP and LHCP components of the total electric field can be easily obtained from the θ- and ϕ-components of the electric field, as in (4.9) – (4.10) [23]:

$$E_{RHCP} = \left(\frac{E_\theta^T - jE_\phi^T}{\sqrt{2}}\right) \quad (4.9)$$

$$E_{LHCP} = \left(\frac{E_\theta^T + jE_\phi^T}{\sqrt{2}} \right) \tag{4.10}$$

The corresponding axial ratio (AR) of the unit-cell is given as (4.11) [23]:

$$AR_{dB} = 20\log_{10} \frac{|E_{RHCP}| + |E_{LHCP}|}{|E_{RHCP}| - |E_{LHCP}|} \tag{4.11}$$

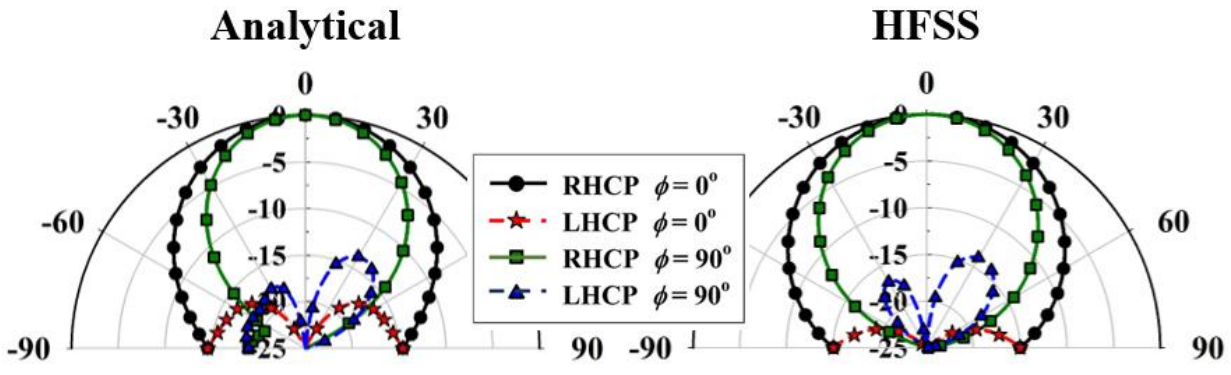

(a) (b)

Figure 4.4 Normalized CP radiation pattern of the Butterfly unit-cell using (a) Analytical equations, and (b) Full-wave EM analysis (HFSS) at 86 GHz.

The normalized CP radiation patterns using the above analytical equations and the full-wave simulation of the unit-cell are compared in Figs. 4.4(a) and 4.4(b), respectively, at 86 GHz. Since the cavity model is only valid in the upper half-space, the patterns are only shown in the corresponding angular space. The analytical results match reasonably well with the simulation results. The simulated 3 dB RHCP gain beamwidth is 70° and 53° and the cross-polarization isolation is 25 dB and 15 dB in the ϕ = 0° and ϕ = 90° plane, respectively.

The analytical AR vs. elevation angle of the Butterfly unit-cell is plotted in Fig. 4.5 at 86 GHz and compared with the full-wave EM simulation of the structure. The analytical model ignores the mutual coupling between the elements, which results in a slight variation between the

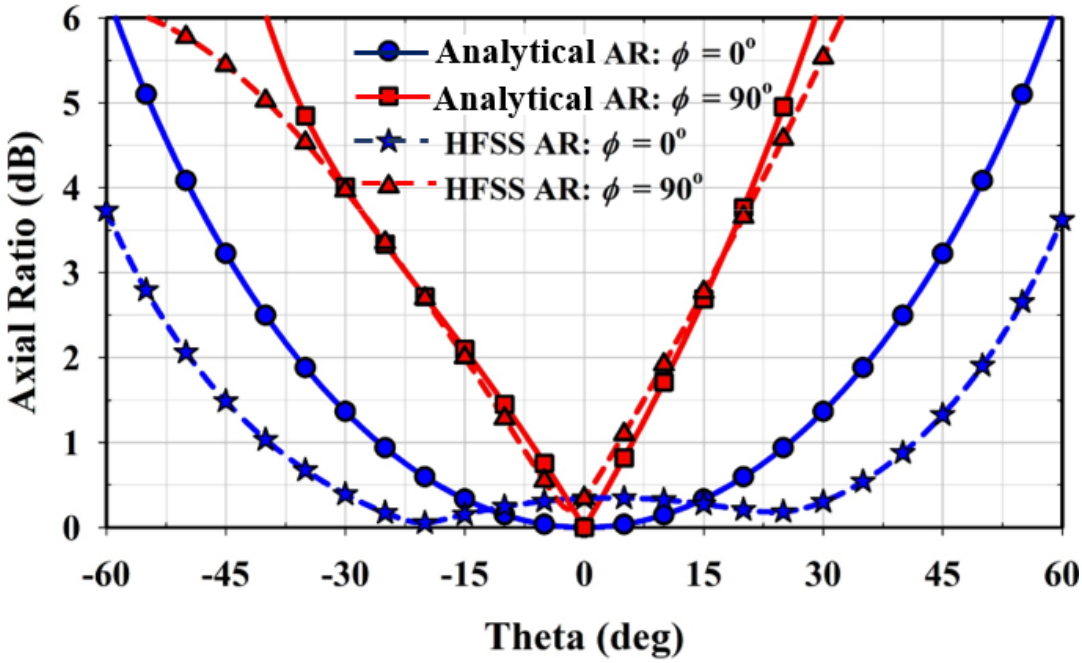

Figure 4.5 Axial ratio vs. elevation angle of the Butterfly unit-cell using analytical equations and full-wave EM analysis (HFSS) at 86 GHz.

analytical and full-wave simulation. The Butterfly unit-cell shows wide simulated 3 dB AR beamwidth of 110° in the ϕ = 0° plane and 3 dB AR beamwidth of 38° in the ϕ = 90° plane.

4.3.2 Two-Cell Butterfly Linear Array

The separation between the unit cells of the linear array is maintained to be an integer multiple of λ_g (= $n\lambda_g$). This spacing ensures that all the cells along the series-fed linear array are in-phase and thus results in the broadside radiation. Accordingly, two designs are considered, and for each design, the current distribution and the simulated normalized radiation pattern are plotted in Figs. 4.6(a) and 4.6(b), respectively. In Fig. 4.6(a), the last patch element of one cell is overlapped with the first patch element of the next cell to maintain λ_g spacing between the two unit-cells. For design in Fig. 4.6(b), the two unit-cells are separated by $2\lambda_g$ without any overlapping elements.

The overlapped elements of Fig. 4.6(a) do not cause degradation in the CP performance at the design frequency owing to two main reasons. Firstly, the patch elements in the cell get excited in phase quadrature from each other because of $\lambda_g/4$ separation between the individual elements. Secondly, the current induced in the overlapping element is along the shorter dimension of the patch, as shown in Fig. 4.6(a), which resonates at a higher frequency than the desired frequencies.

In both the designs, a stable broadside radiation pattern is obtained, as shown in Figs. 4.7(a) and 4.7(b), respectively. However, there is an onset of the grating lobe in the second case due to the larger inter-cell separation. Moreover, using the design of Fig. 4.6(a), a greater number of unit-cells can be cascaded in a smaller overall length to achieve compact linear array design and higher antenna efficiency than the other case.

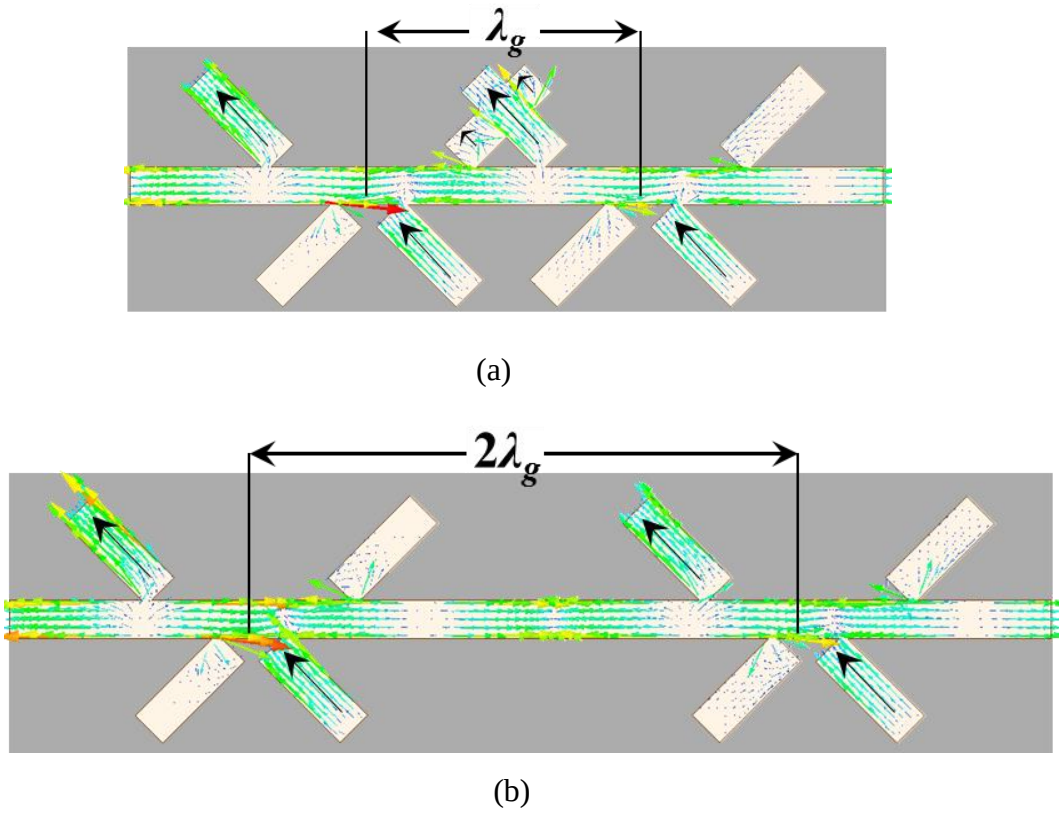

Figure 4.6 Simulated current distribution on the two-cell Butterfly linear array (a) Separated by λ_g, and (b) Separated by $2\lambda_g$.

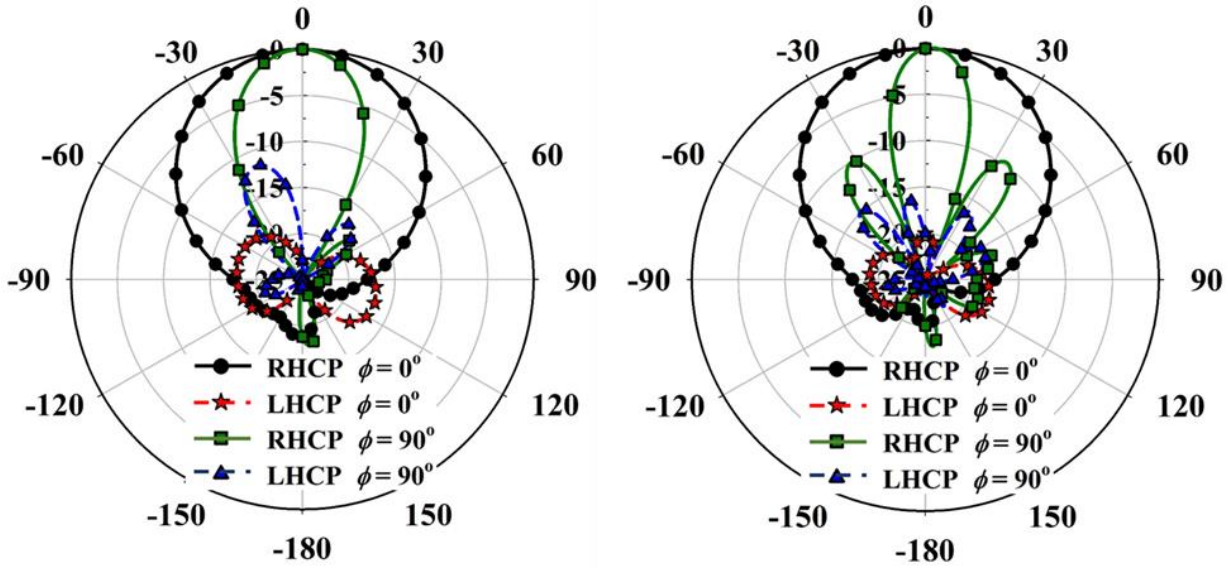

(a) (b)

Figure 4.7 Simulated normalized radiation pattern of the two-cell Butterfly linear array (a) Separated by λ_g, and (b) Separated by $2\lambda_g$.

4.3.3 Periodic LWA Analysis of Butterfly Linear Array

Series-fed Butterfly linear array antennas of size 1 × 16, 1 × 24, and 1 × 32 are designed by cascading the unit-cells, as shown in Fig. 4.8. The spacing between the cells is maintained at $1\lambda_g$ (= $0.65\lambda_0$), where λ_0 is the free space wavelength at 86 GHz. Traveling wave configuration is achieved by terminating each of the linear arrays by a resonant patch antenna that radiates any residual power reaching the load. In 1 × 32 linear array, the current significantly reduces toward the end elements due to higher feed-line loss as compared to 1 × 16 and 1 × 24 linear arrays, as depicted in Fig. 4.8. Thus, the feed-line loss in the 1 × 32 linear array overcomes the improvement in the gain and results in lower radiation efficiency (assuming matching is maintained for different cases). An optimum current distribution is achieved for the 1 × 24 linear array resulting in the maximum radiation efficiency. Accordingly, the simulated total antenna efficiency of 1 × 16, 1 × 24, and 1 × 32 linear arrays is 70%, 70.5%, and 67%, respectively, at 86 GHz. The total antenna

efficiency includes the effect of mismatch loss, conductor loss, and dielectric loss. Thus, the linear array of size 1 × 24 is selected and investigated for its radiation behavior.

Parametric study on the width of the patch W_p for impedance matching and radiation performance of the 1 × 24 linear array is also carried out. Fig. 4.9(a) shows the effect of varying W_p on the impedance matching, and it is seen that $|S_{11}| < -10$ dB is obtained for $W_p = 0.32$ mm throughout the desired bandwidth. The effect of different W_p by keeping the length constant on the axial ratio and antenna efficiency is depicted in Fig. 4.9(b). An optimum antenna efficiency and axial ratio are achieved for $W_p = 0.32$ mm.

The 1 × 24 series-fed Butterfly linear array antenna can be analyzed using the periodic LWA theory. The 1 × 24 linear array is designed by cascading 24 identical Butterfly antenna unit-cells with a periodic spacing of $1\lambda_g$. The periodic perturbations in the structure produce an infinite number of spatial harmonics that can be fast or slow. The proposed 1 × 24 periodic LWA is designed such that only one spatial harmonic ($n = -1$) is fast, i.e. $|\beta_{-1}| < k_0$. Thus, the leaky wave

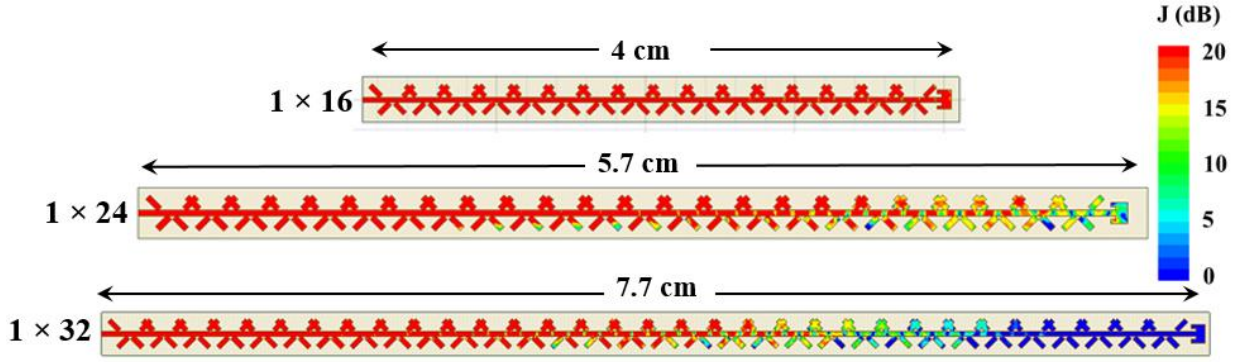

Figure 4.8 Current distribution on the linear arrays of 1 × 16, 1 × 24, and 1 × 32 series-fed Butterfly antenna.

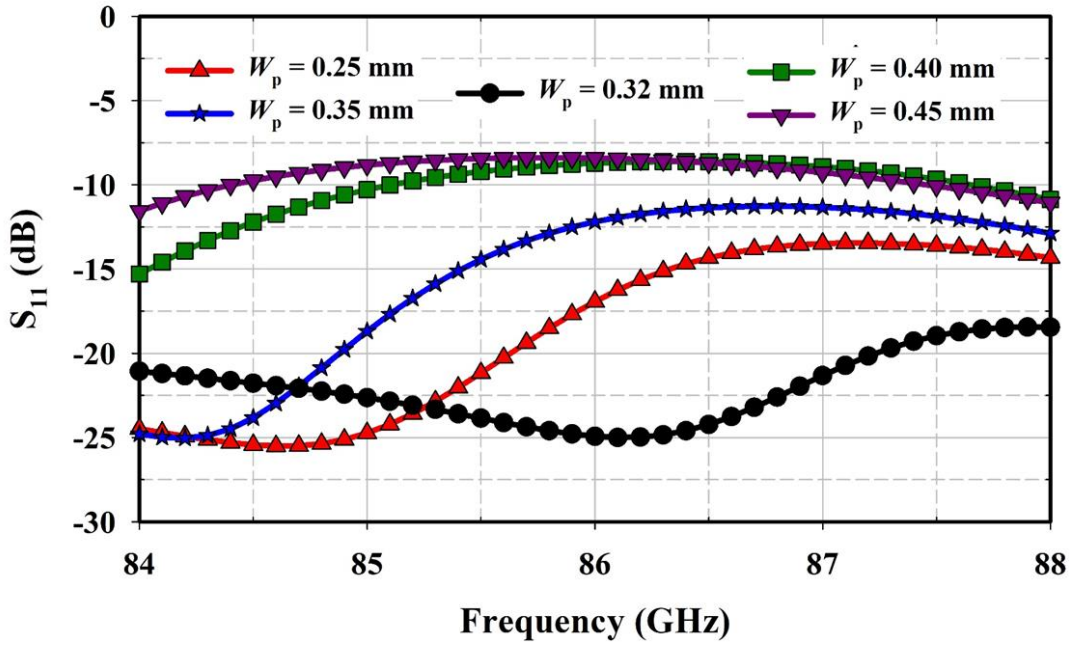

(a)

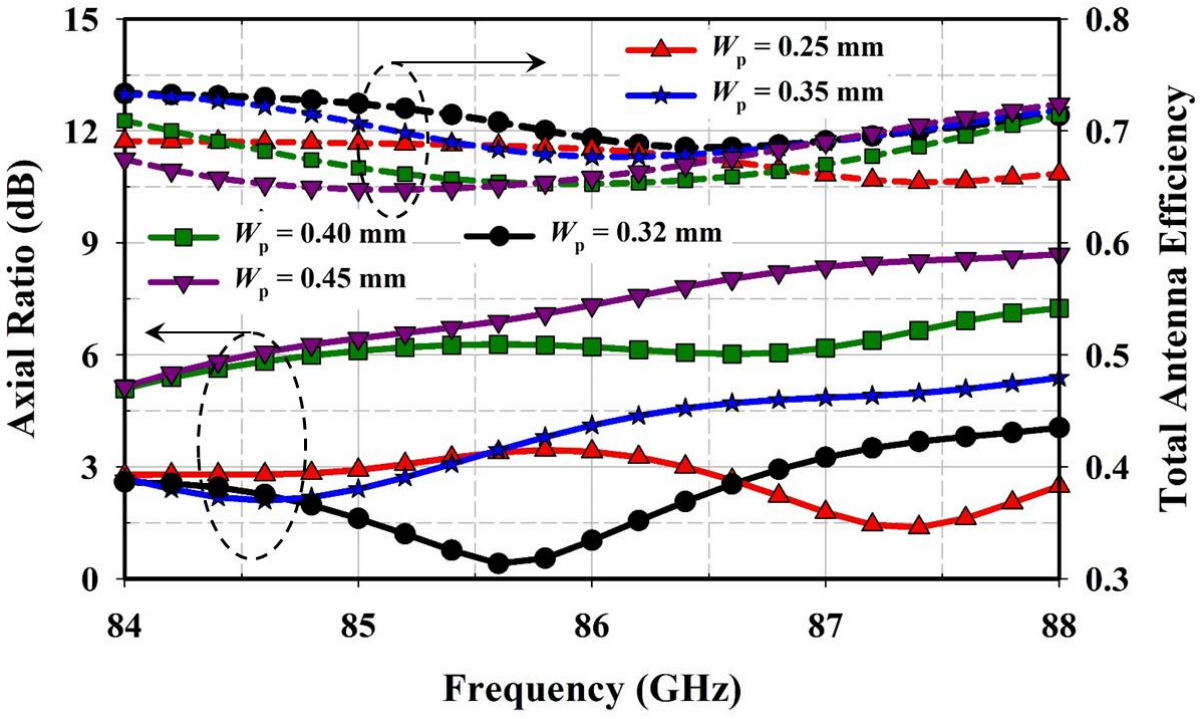

(b)

Figure 4.9 Effect on (a) Impedance matching, and (b) Axial ratio and total antenna efficiency for different width of the patch W_p of the 1 × 24 linear array antenna.

number used to compute the radiation pattern becomes $k_{LW} = \beta_{-1} - j\alpha$, as discussed in [40]. The leaky wave number k_{LW} can be computed by solving the eigenvalue of the *ABCD* matrix of the cell using a standard periodic analysis [40].

Initially, an approximate equivalent transmission line model of the Butterfly antenna unit-cell is developed to extract the complex leaky wave number, as illustrated in Fig. 4.10. The radiating edges of the patch elements are modeled by an equivalent admittance of **G** + *j***B**. The admittances are separated by a transmission line of length L_p (= λ/2 at 86 GHz) and characteristic impedance, Z_A, thereby forming the equivalent network of the patch antenna elements [32]. The approximate model neglects the effects of mutual coupling and rotation of the patch elements. The overall *ABCD* matrix of the equivalent model ($\mathbf{A}_{model}$) is found by cascading the *ABCD* matrices of the transmission line and the patch element sections.

The extraction of the complex leaky wave number from the equivalent model is not exact because of the approximations in the model. An accurate leaky wave number can be computed if the *ABCD* matrix of the cascaded 24 unit-cells of Butterfly antenna is extracted from the full-wave EM analysis since it includes the effect of mutual coupling and the finite size of the array.

Let $\mathbf{A_N} = \begin{bmatrix} A & B \\ C & D \end{bmatrix}$ be the *ABCD* matrix of the N (= 24) cascaded cells of the Butterfly series-fed linear array obtained from the full-wave EM analysis.

The eigenvalue of the matrix is computed by solving (4.12) – (4.13) [40]:

$$\det\left(\mathbf{A_N} - \lambda\mathbf{I}\right) = 0 \tag{4.12}$$

$$\left| \begin{bmatrix} A & B \\ C & D \end{bmatrix} - \begin{bmatrix} e^{\gamma Nd} & 0 \\ 0 & e^{\gamma Nd} \end{bmatrix} \right| = 0 \tag{4.13}$$

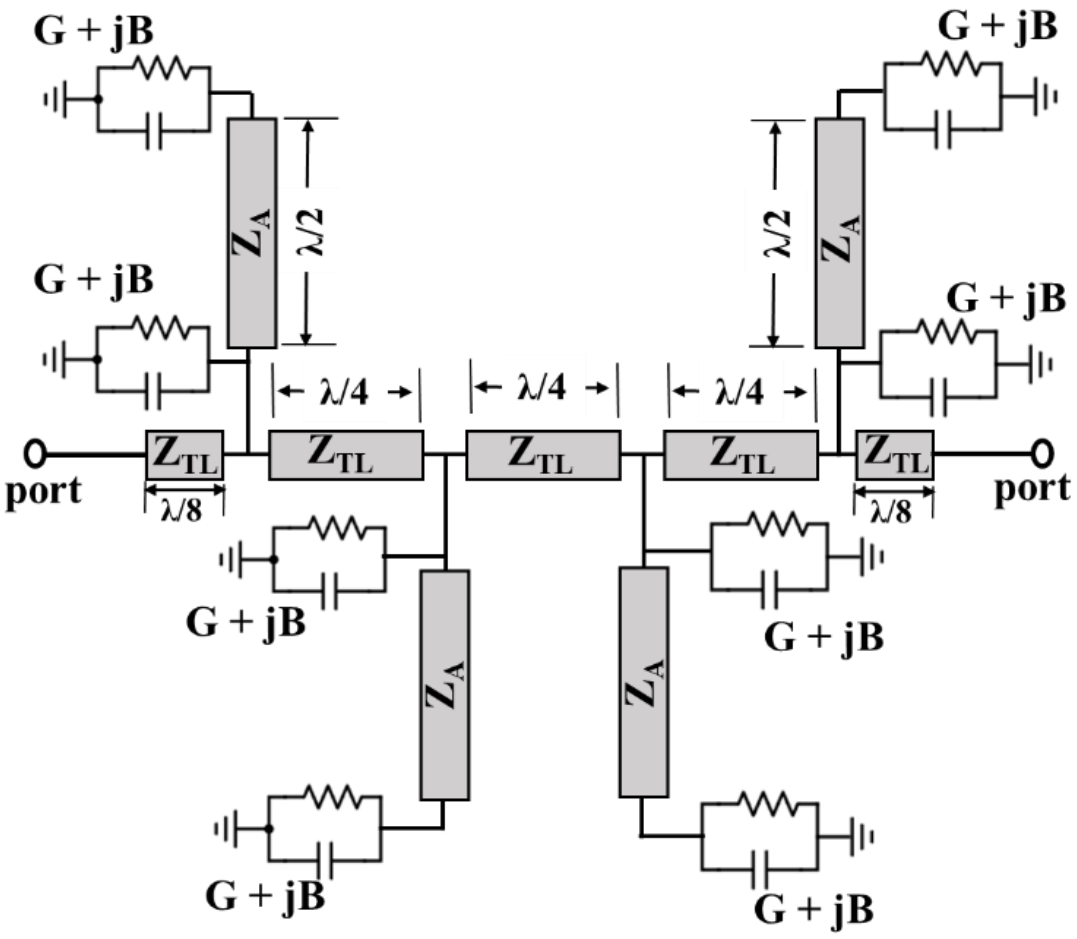

Figure 4.10 Approximate equivalent transmission line model of the unit-cell of the Butterfly antenna.

The eigenvalue of the matrix is $\lambda = e^{\gamma Nd}$, where d is the periodic spacing between the cells and $\gamma = jk_{LW} = j\beta_{-1} + \alpha$. Thus, the leakage constant α and the phase constant β_{-1} can be extracted from the computed eigenvalue of the *ABCD* matrix.

Fig. 4.11(a) shows the leakage constant, and the phase constant both normalized to the free-space wavenumber k_0 and extracted from the approximate transmission line equivalent model of the unit-cell ($\mathbf{A}_{model}$) and the full-wave EM analysis of the 1 × 24 linear array ($\mathbf{A}_{\mathbf{N}}$). The shift in the normalized leaky wave number for the two cases is due to the approximations assumed in the equivalent transmission line model of the unit-cell. To account for the mutual coupling and finite-

size effects, further leaky-wave analysis is investigated using the extracted *ABCD* matrix from the full-wave EM analysis. As can be seen from the dispersion graph, the proposed periodic LWA is a fast-wave structure since $\frac{|\beta_{-1}|}{k_0} < 1$ for the entire frequency range. The zero-crossing of the normalized phase constant dictates the center frequency of broadside radiation, which corresponds to 86.2 GHz.

The leakage constant is related to the beamwidth and the radiation efficiency of the LWA. From the dispersion graph of Fig. 4.11(a), it is observed that the leakage constant α is relatively constant across the frequency range, particularly at broadside. Most LWA exhibits the OSB region, where both $\beta_{-1} \to 0$ and $\alpha \to 0$ due to the summation of the internal reflections in the structure, which significantly reduces the broadside radiation. However, in the proposed Butterfly antenna, the OSB is suppressed, and a non-zero leakage constant is achieved even when $\beta_{-1} \approx 0$. The primary reason for OSB suppression is the nature of the sequential-phase feeding in which the elements are $\lambda_g/4$ apart. Consequently, the return phase of the reflection is 180° out of phase between the adjacent elements, and the reflection gets canceled. Thus, reflection compensation is inherent in the Butterfly antenna and leads to broadside radiation. Once β_{-1} and α are known as a function of frequency, the principal features of the leaky-wave antenna can be computed. Such features include the characteristic Bloch impedance, the variation of the scan angle with frequency, the radiation efficiency, the beamwidth, and the radiation pattern [36], [37].

The Bloch impedance Z_B is the ratio of the voltage and current waves at the input terminal of the N cascaded cells of the periodic LWA and is computed using (4.14) [40]:

$$Z_B = \frac{-B}{A - e^{\gamma N d}} \tag{4.14}$$

The knowledge of Z_B is useful for estimating the input impedance of the LWA. The input impedance of the LWA is also determined from the full-wave analysis of the linear-array and is compared with the computed Bloch impedance, as shown in Fig. 4.11(b). Both the analytical and simulation results show excellent agreement. Note that at the crossover frequency of 86.2 GHz, the Bloch impedance is $Z_B \approx 40 + j0$. The angle of the maximum of the beam or the beam squint angle (θ_m), measured from the broadside direction is given as (4.15) [36]:

$$\sin\theta_m \approx \frac{\beta_{-1}}{k_0} \tag{4.15}$$

The computed and the full-wave simulated beam squint angle of the 1 × 24 series-fed linear array is plotted in Fig. 4.12(a). The LWA analysis and the full-wave simulation show excellent correlation. The beam peak angle squints from -5° at 84 GHz to +3° at 88 GHz in the ϕ = 90° plane and the peak broadside radiation occurs at the zero-crossing frequency of 86.2 GHz.

Leakage constant α is related to the LWA gain beamwidth, and since α is consistent across the frequency band, similar behavior is expected in the gain vs. frequency of the LWA. The peak gain and the broadside gain of the full-wave EM simulated 1 × 24 Butterfly series-fed linear array antenna is depicted in Fig. 4.12(b). It is observed that the peak gain of the proposed LWA is indeed relatively constant over the frequency range, which further corroborates the LWA analysis. The peak simulated broadside RHCP gain of the 1 × 24 series-fed Butterfly linear array is 17 dBic at 86 GHz. To characterize the array radiation bandwidth near broadside, new terminology of acceptable squint-bandwidth is defined. The acceptable squint-bandwidth is defined here as the frequency range for which the broadside gain drops by 1 dB. Accordingly, it is observed from Fig. 4.12(b) that the acceptable squint-bandwidth of the 1 × 24 Butterfly linear array antenna is from 85.7 – 87.2 GHz.

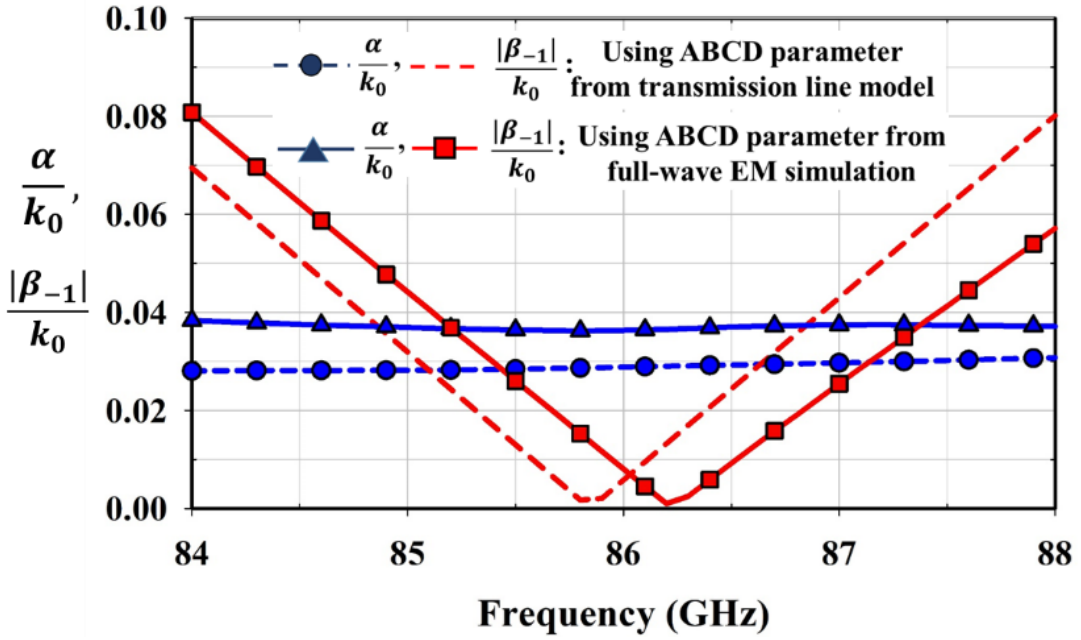

(a)

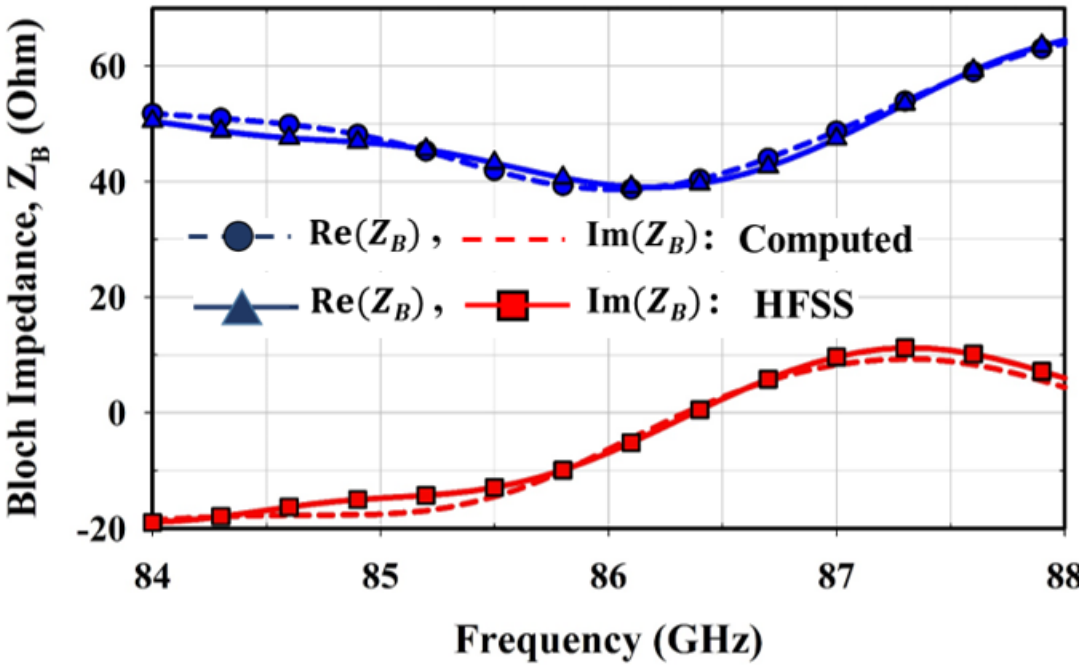

(b)

Figure 4.11 (a) Extracted normalized leakage constant and normalized phase constant for the 1 × 24 Butterfly linear array, and (b) Bloch impedance of the Butterfly linear array using periodic LWA computation and full-wave EM analysis (HFSS).

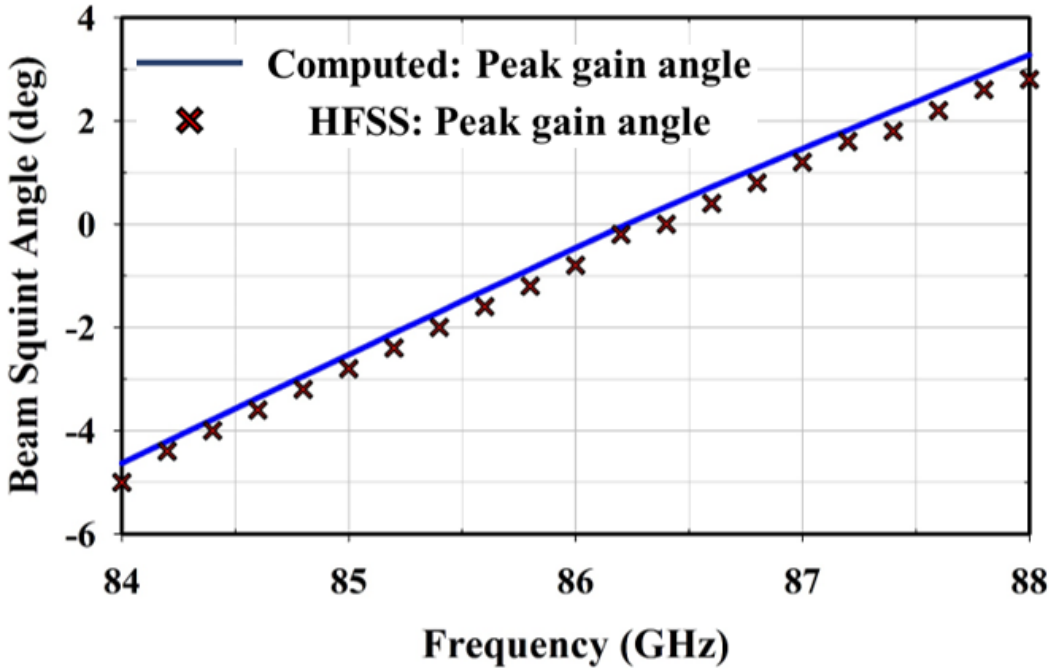

(a)

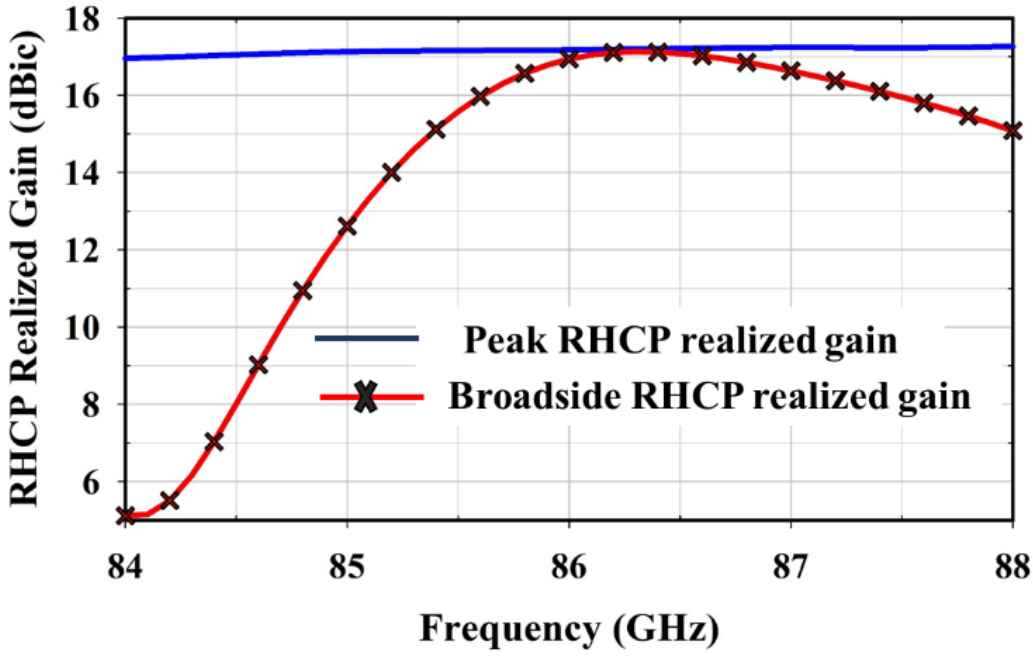

(b)

Figure 4.12 (a) LWA computed and full-wave EM simulated (HFSS) beam squint angle as a function of frequency, and (b) Full-wave EM simulated peak RHCP realized gain and broadside RHCP realized gain of the 1 × 24 Butterfly linear array.

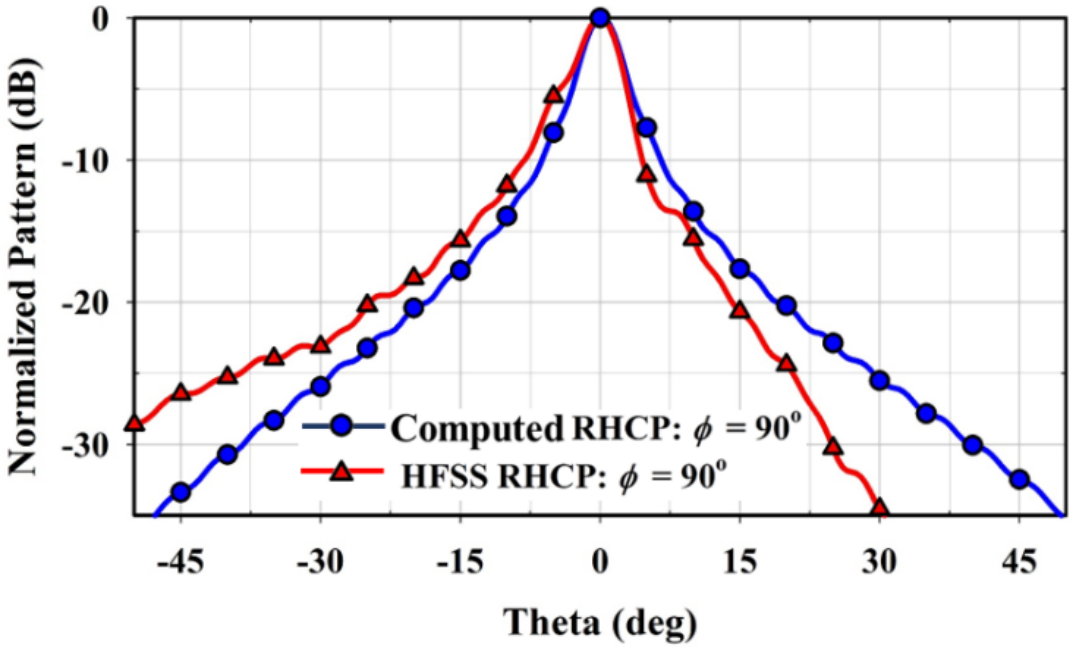

Figure 4.13 Normalized RHCP radiation pattern at 86 GHz using the periodic LWA computation and the full-wave EM simulation (HFSS) of the 1 × 24 Butterfly series-fed linear array.

The radiation efficiency of the periodic LWA can be estimated from the normalized leakage constants of the lossy and lossless LWA structures. The lossy case considers all the conductor and dielectric losses. In contrast, in the lossless case, the LWA is re-simulated with a perfect electric conductor (PEC) and zero loss tangent, i.e. $\tan\delta = 0$. Both lossy and lossless cases were computed, such that the LWA efficiency (η) can be estimated as (4.16) [37]:

$$\eta \approx \frac{\hat{\alpha}_{lossless}}{\hat{\alpha}_{lossy}} \tag{4.16}$$

where $\hat{\alpha}_{lossless} = \frac{\alpha_{lossless}}{k_0}$ and $\hat{\alpha}_{lossy} = \frac{\alpha_{lossy}}{k_0}$. For the lossless case, $\hat{\alpha}_{lossless} = 0.025$ and the lossy case, $\hat{\alpha}_{lossy} = 0.037$ at 86 GHz. The resulting LWA efficiency at 86 GHz from (4.16) is then 68%, which is very close to the full-wave EM simulated antenna efficiency of 70.5% for the 1 × 24 Butterfly

series-fed linear array antenna. Although not shown here, the antenna efficiency is relatively flat across the frequency range.

The total radiation pattern of the LWA is the product of the element pattern and the array factor, where the array factor is given by (4.17) [37]:

$$AF(\theta) = \sum_{n=1}^{N} e^{-jk_{LW} y_n} e^{jk_0 y_n \sin\theta} \tag{4.17}$$

where $y_n = (n-1)d$, for $1 \le n \le N$, and $N = 24$ is the number of radiating perturbations. The element pattern is obtained from the cavity model analysis discussed in the unit-cell analysis section. The overall normalized RHCP radiation pattern at 86 GHz using the above computation and from the full-wave EM simulation is shown in Fig. 4.13. A reasonable agreement is observed between the computed and simulated patterns, which demonstrates the merit of the leaky-wave analysis approach for the proposed design. The slight difference in the computed pattern is from the assumption that α is the same for each of the 24 cascaded cells in the LWA analysis.

4.4 Passive Butterfly Planar Array Antenna

4.4.1 Feed-Line Losses

A high gain antenna is essential to compensate for the large path-loss at millimeter-wave frequencies. The feed-line loss study is carried to determine the optimum size of the planar array, the type of copper foil laminate, and the kind of feed network that can provide the maximum array gain.

At *W*-band, the feed-network losses can increase dramatically and thereby decrease the overall gain of the antenna. Thus, it is crucial to quantify feed-network losses. A MATLAB routine

is written to compute the conductor and dielectric feed-network losses from an $N \times 24$ parallel-series fed planar antenna; however, it does include radiation losses, mutual coupling effects and mismatch loss. Additionally, the following assumptions were made: (1) the array is uniformly illuminated and uniformly spaced at $0.65\lambda_0$, and (2) the radiating elements are identical and ideal.

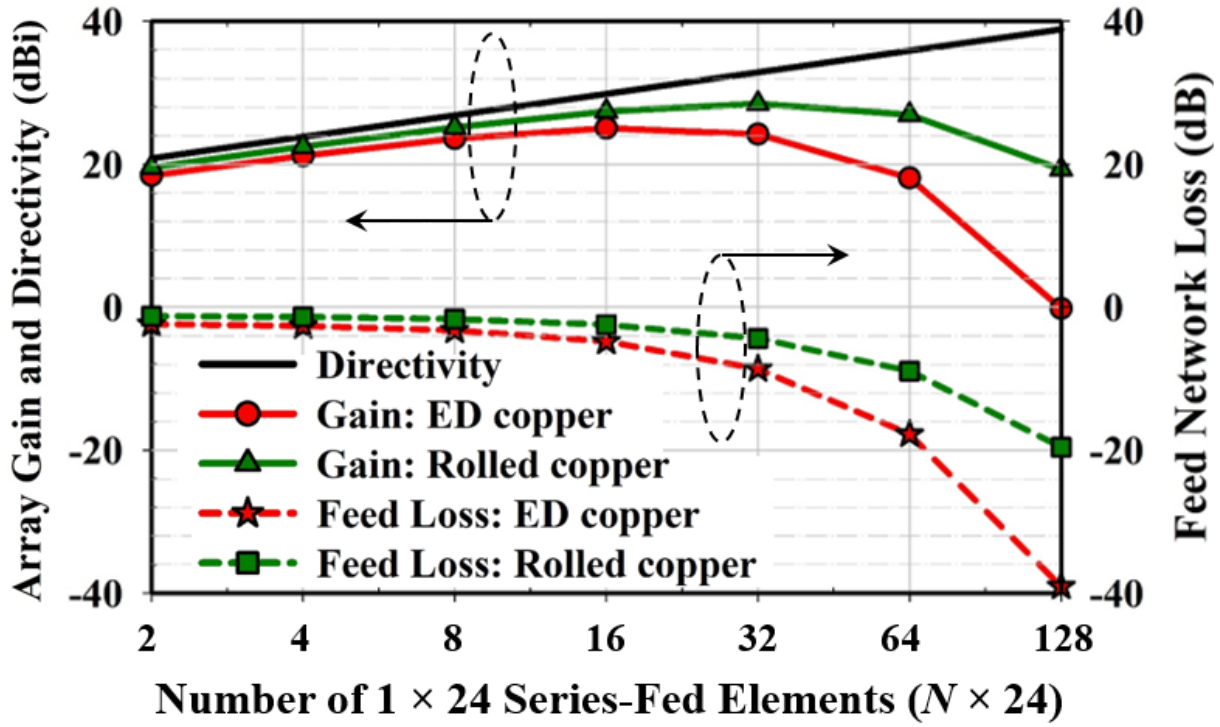

Figure 4.14 Aperture directivity, array gain, and feed-line loss for $N \times 24$ parallel-series fed planar array antenna at 86 GHz calculated using MATLAB.

Type of copper-foil used in the laminate also influences the loss, especially the copper surface roughness can significantly impact the high-frequency insertion loss. RO3003 substrate of 5 mil thickness with rolled annealed and standard electrodeposited (ED) copper-foils are considered for the feed-line loss study. The laminates with standard ED copper have a higher surface roughness (1.8 μm) as compared to the rolled annealed copper (0.3 μm). Consequently,

ED copper laminates exhibit higher microstrip transmission-line insertion loss of 2.2 dB/inch as opposed to 1 dB/inch for the rolled copper laminates at 86 GHz. Both the types of copper-foils have similar conductivity of 5.8×10^7 S/m.

The aperture directivity, array gain, and the feed-line losses for $N \times 24$ parallel-series fed planar array antenna using the rolled and ED copper-foils are plotted in Fig. 4.14 at 86 GHz. It is observed that with the rolled copper laminate, the array gain is optimum for 32 × 24 planar array size. However, increasing the dimension of the array further leads to a drop in the gain because the loss in the feed-line exceeds the added gain of the array. The maximum gain using the rolled copper laminate is 28 dBi for a 32 × 24 parallel-series fed planar array antenna, and the maximum gain using the standard ED copper laminate is 24.5 dBi for a 16 × 24 parallel-series fed planar array antenna.

The full-wave simulation of the 1 × 8 and 1 × 32 feed networks are also performed and compared with the MATLAB computed conductor + dielectric loss, as presented in Table 4.1. As can be noticed that the full-wave simulated networks include the effect of mismatch loss, quarter-wave matching transformers, port-to-port coupling loss, and radiation losses compared to only the conductor + dielectric loss in MATLAB based computation, as mentioned earlier. In view of the

Table 4.1 Full-wave simulated and MATLAB computed loss in the 1 × 8 and 1 × 32 feed network.

	MATLAB	**Full-wave Simulation**			
Feed size	**Conductor + dielectric loss (Fig. 4.14)**	**Mismatch loss**	**Conductor + dielectric loss**	**Radiation loss**	**Total loss**
1 × 8	-1.6 dB	-0.2 dB	-1.8 dB	-1.9 dB	-3.9 dB
1 × 32	-4.4 dB	-0.2 dB	-5.2 dB	-3.6 dB	-9 dB

above, it is seen that the overall full-wave simulated loss in the 1 × 8 and 1 × 32 feed network is 2.3 dB and 4.6 dB higher than the MATLAB computed conductor + dielectric losses only, respectively.

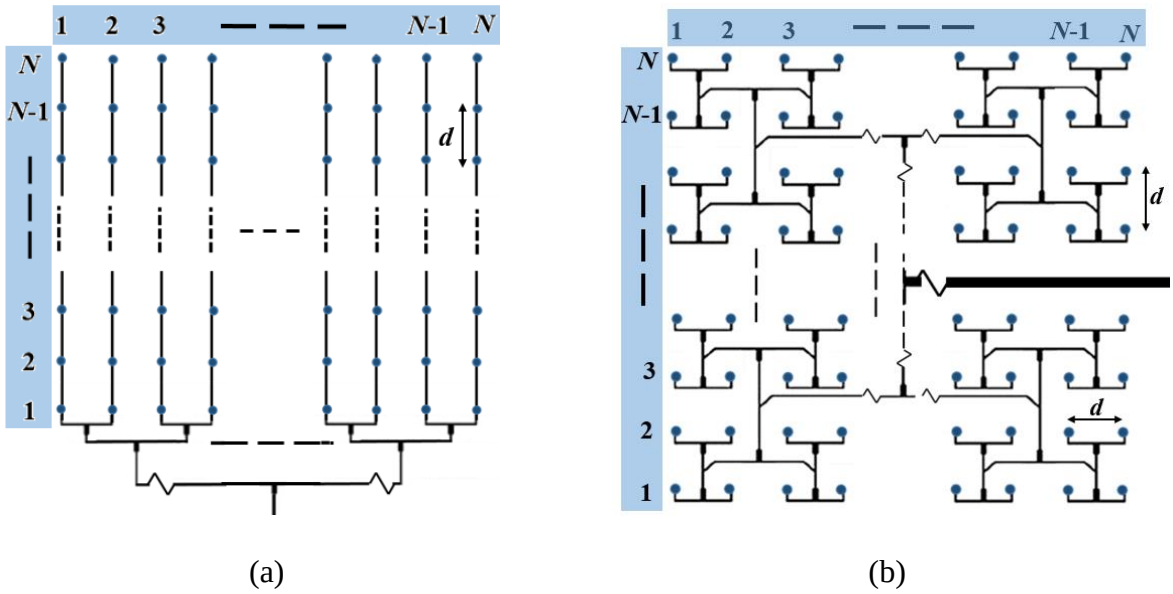

Figure 4.15 Illustration of the feed-network in (a) Parallel-series fed planar array antenna of size $N \times N$, and (b) Corporate-fed planar array antenna of size $N \times N$.

The feed-line losses are also investigated for the parallel-series fed and the corporate-fed network of $N \times N$ dimension of the planar array antenna. The general feed network for the parallel-series and the corporate-fed planar array is illustrated in Fig. 4.15. All the assumptions of the parallel-series fed network are also applied to the corporate-fed network. The aperture directivity, array gain, and the feed-line losses for $N \times N$ parallel-series fed, and $N \times N$ corporate-fed planar array antenna using the rolled copper-foil are plotted in Fig. 4.16. The array gain of the parallel-series fed network planar array is consistently higher than the gain of the corporate-fed network

planar array antenna. The optimum array dimension corresponding to the maximum array gain is 32 × 32 for both the networks, beyond which the feed-line losses exceed the added array gain.

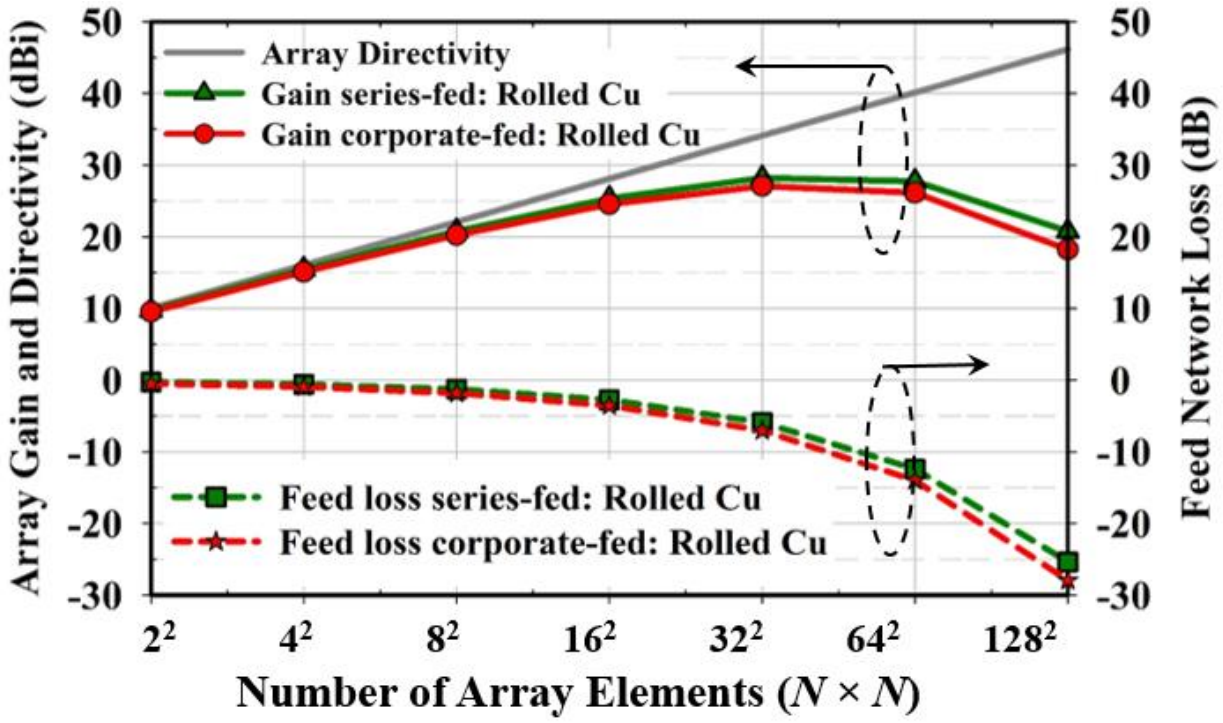

Figure 4.16 Aperture Directivity, array gain, and feed-line loss at 86 GHz for $N \times N$ parallel-series fed planar array antenna, and $N \times N$ corporate-fed planar array antenna calculated using MATLAB.

The above feed-line loss study shows that a parallel-series fed network planar array antenna when designed on a rolled annealed copper-foil laminate provides higher array gain. Thus, an 8 × 24 and a 32 × 24 planar array antennas on a 5 mil RO3003 rolled annealed copper laminate are designed, built, and tested.

4.4.2 8 × 24 Parallel-Series Fed Planar Array Antenna

The proposed Butterfly antenna is used to design a parallel-series fed passive planar array of 8 × 24 elements, as depicted in the fabricated prototype in Fig. 4.17. The inter-linear array spacing is maintained at 2.3 mm ($0.65\lambda_0$ at 86 GHz), which helps in maintaining mutual coupling around -30 dB. The total size of the planar array is 2 cm × 7 cm. A 1.0 mm end-launch connector from Southwest Microwave is used to excite the planar array. The simulated and the measured impedance matching and AR are presented in Fig. 4.18. The shaded region corresponds to the acceptable squint bandwidth of the 8 × 24 planar array antenna in which the broadside gain drops by 1 dB. The acceptable squint bandwidth of the array is from 85.2 – 86.3 GHz. Both the simulation and measurement results show good agreement within the acceptable squint bandwidth. The simulated and measured $|S_{11}|$ is less than -10 dB and the AR is below 3 dB for the acceptable squint bandwidth.

The radiation characteristics of the planar array antenna are measured in the millimeter-wave mini-compact antenna test range (M-CATR) installed by the Microwave Vision Group (MVG) at the Antenna and Microwave Laboratory (AML) at San Diego State University (SDSU), as shown in Fig. 4.19. The simulated and measured radiation pattern is stable and consistent across the entire acceptable squint bandwidth from 85.2 – 86.3 GHz. For brevity, the simulated and measured normalized CP radiation patterns are only shown at 86 GHz for the ϕ = 0° and ϕ = 90° plane in Fig. 4.20(a) and Fig. 4.20(b), respectively. The simulated peak RHCP gain of the 8 × 24 array is 19.3 dBic, 20.6 dBic, and 19.6 dBic and the peak cross-polarization isolation is 21 dB, 20 dB, and 19 dB at 85.2 GHz, 86 GHz, and 86.3 GHz, respectively. The corresponding measured peak RHCP gain of the 8 × 24 planar array is 18.2 dBic, 19.9 dBic, and 19.5 dBic and the peak cross-polarization isolation is 17 dB, 21 dB, and 18 dB at 85.2 GHz, 86 GHz, and 86.3 GHz,

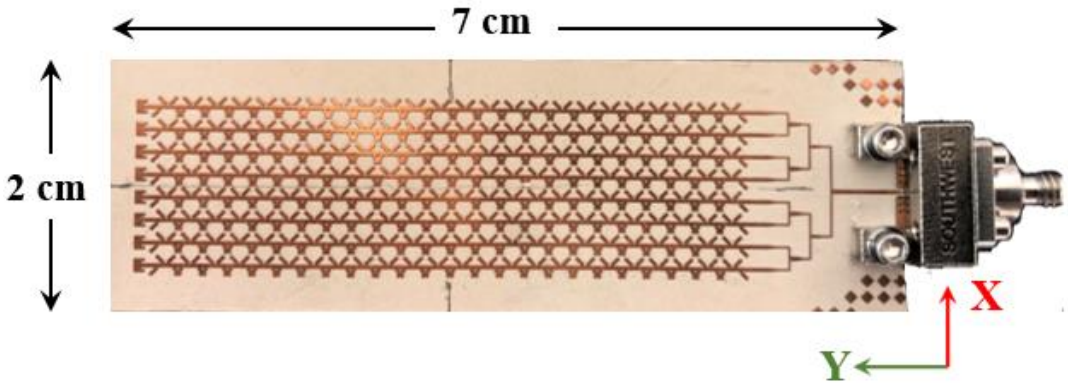

Figure 4.17 Photograph of the 8 × 24 parallel-series fed Butterfly planar array antenna prototype.

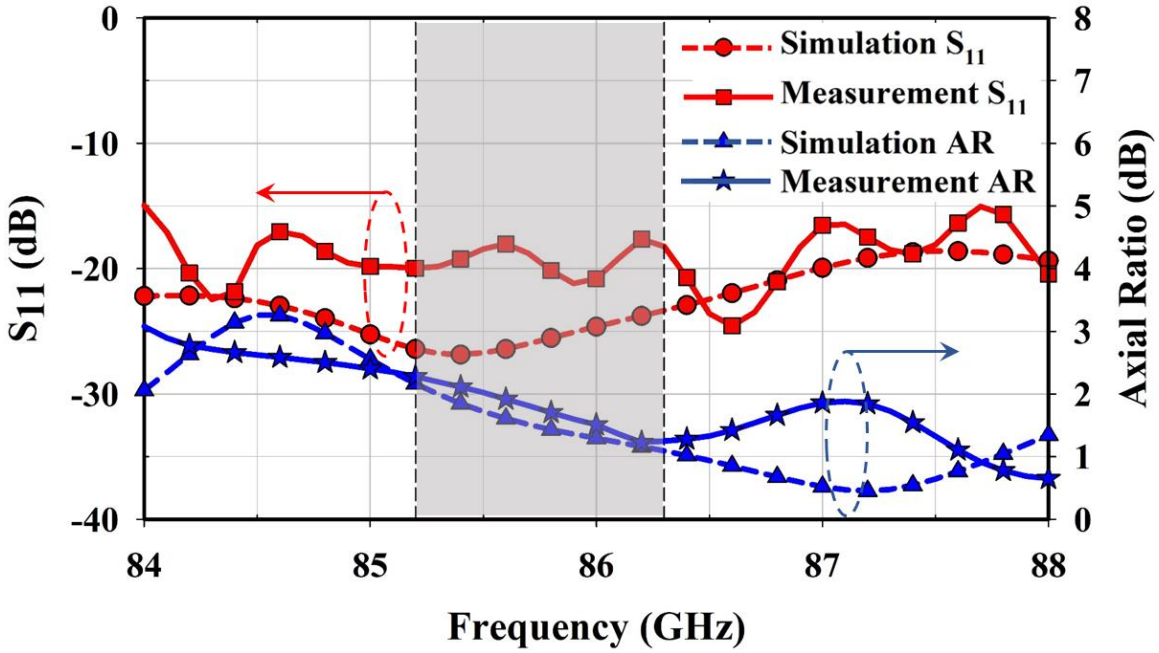

Figure 4.18 Simulated and measured reflection coefficient magnitude and AR of the 8 × 24 parallel-series fed Butterfly planar array antenna. The shaded region from 85.2 – 86.3 GHz is the acceptable squint bandwidth.

respectively. The variation in the simulated and the measured results might be due to the fabrication and the measurement tolerances. The average measured 3 dB gain beamwidth is 9.5°

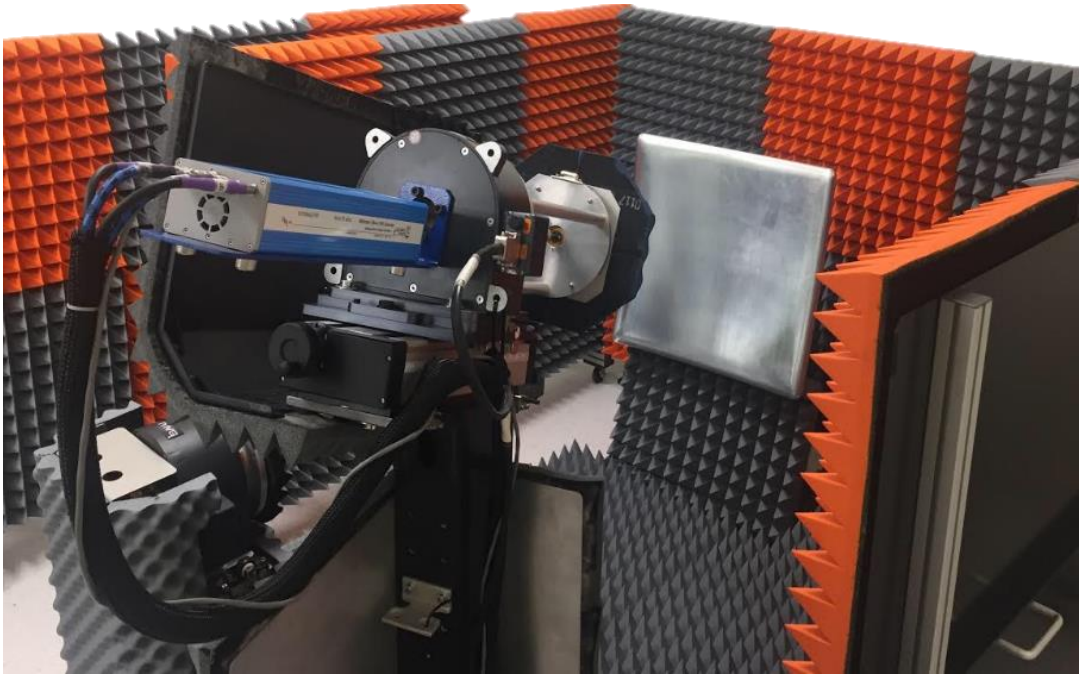

Figure 4.19 Photograph of the millimeter-wave mini-compact antenna test range (M-CATR) at AML, SDSU.

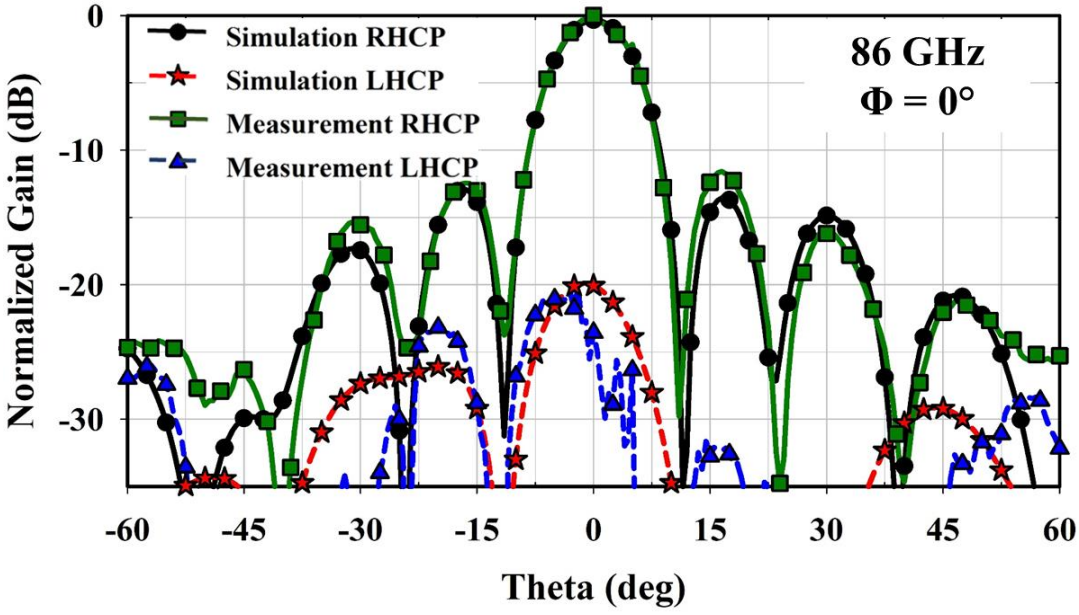

(a)

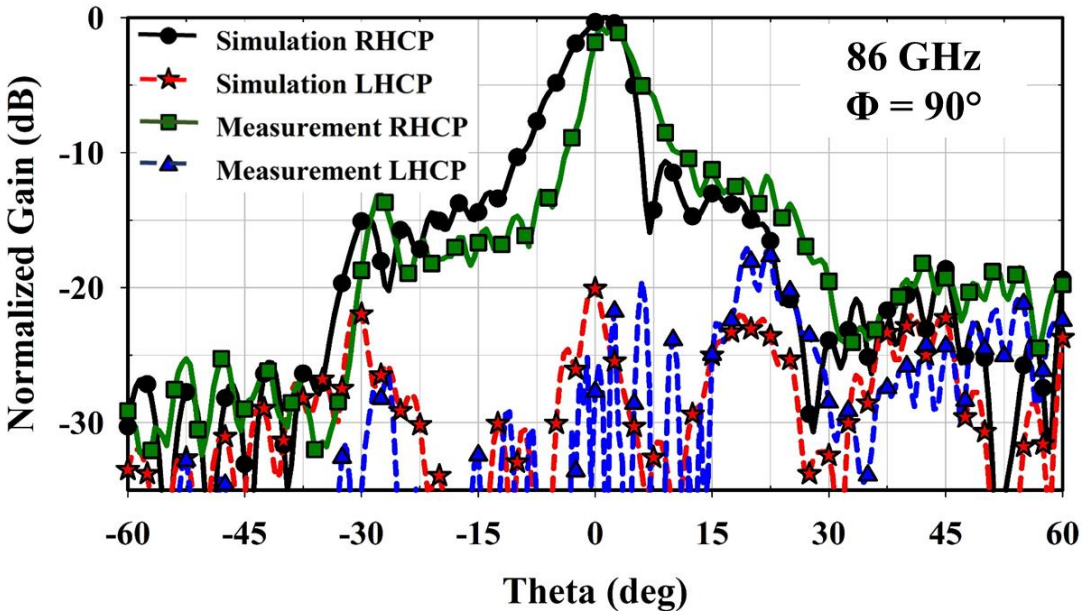

(b)

Figure 4.20 Simulated and measured normalized CP radiation pattern of the 8 × 24 parallel-series fed Butterfly planar array antenna at 86 GHz in (a) ϕ = 0° and (b) ϕ = 90° plane.

and 6° in the ϕ = 0° and ϕ = 90° plane, respectively. The average simulated total antenna efficiency of the 8 × 24 parallel-series fed Butterfly planar array is 51% within the acceptable squint bandwidth from 85.2 – 86.3 GHz. The reduced antenna efficiency is the result of the feed-network loss, as discussed in the previous section (Table 4.1).

4.4.3 32 × 24 Parallel-Series Fed Planar Array Antenna

A larger parallel-series fed planar array of size 32 × 24 is also designed, fabricated, and experimentally verified. The photograph of the 32 × 24 Butterfly parallel-series fed planar array is presented in Fig. 4.21. The total size of the planar array is 7.5 cm × 8 cm. The simulated and the measured impedance matching and AR of the 32 × 24 planar array are similar to the 8 × 24 planar array antenna in the acceptable squint bandwidth from 85.2 – 86.3 GHz.

The simulated and measured 2D normalized CP radiation pattern is plotted in Figs. 4.22(a) and 4.22(b) for the ϕ = 0° and ϕ =90° plane, respectively. The peak simulated and measured RHCP gain as a function of frequency for the 32 × 24 planar array is presented in Fig. 4.23. The measurement shows good agreement with the simulation in the acceptable bandwidth from 85.2 – 86.3 GHz. For brevity, the patterns are only shown at 86 GHz, but the results are stable across the acceptable squint bandwidth. The simulated RHCP gain of the 32 × 24 planar array is 23.7 dBic and the peak cross-polarization isolation is 16 dB at 86 GHz. The corresponding measured peak RHCP gain of the 32 × 24 planar array is 23 dBic and the peak cross-polarization isolation is 15.5 dB at 86 GHz.

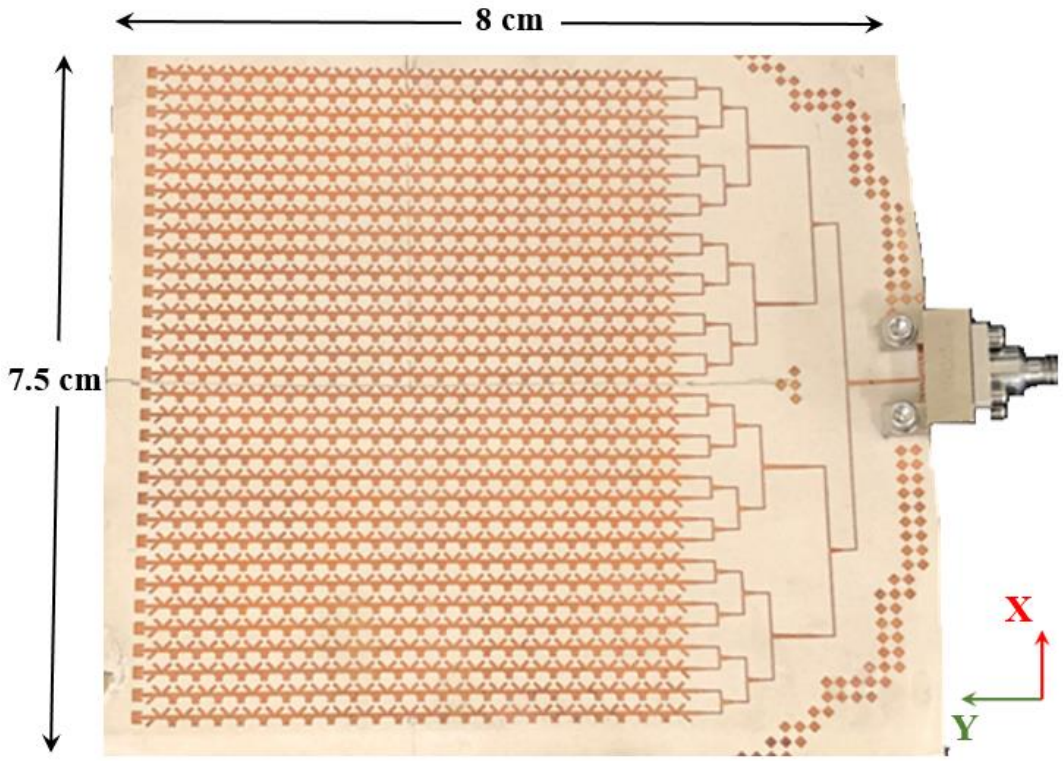

Figure 4.21 Photograph of the 32 × 24 parallel-series fed Butterfly planar array antenna prototype.

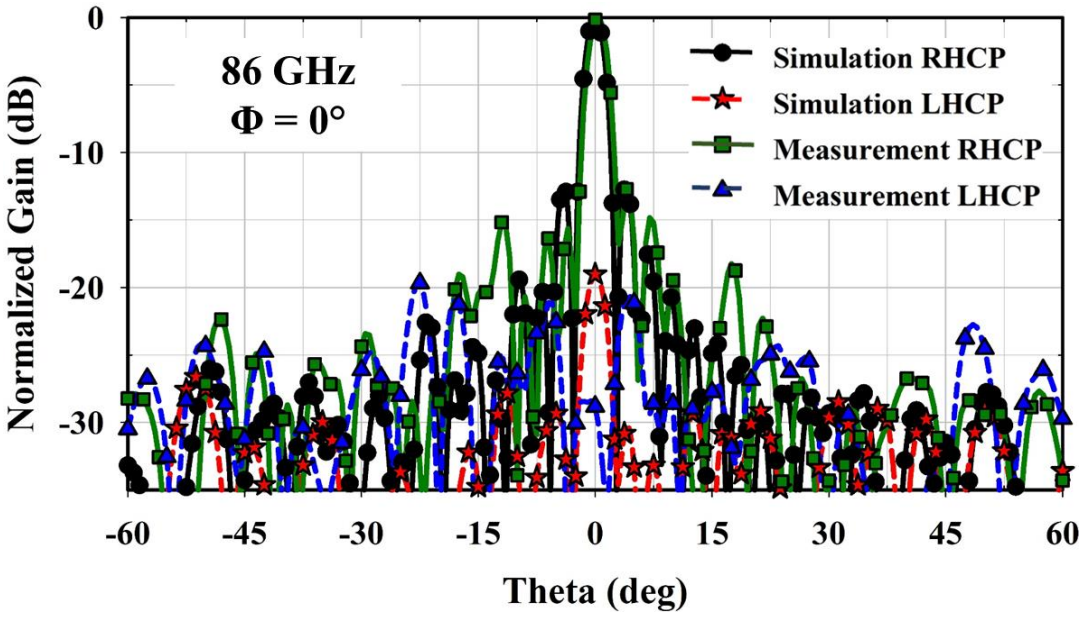

(a)

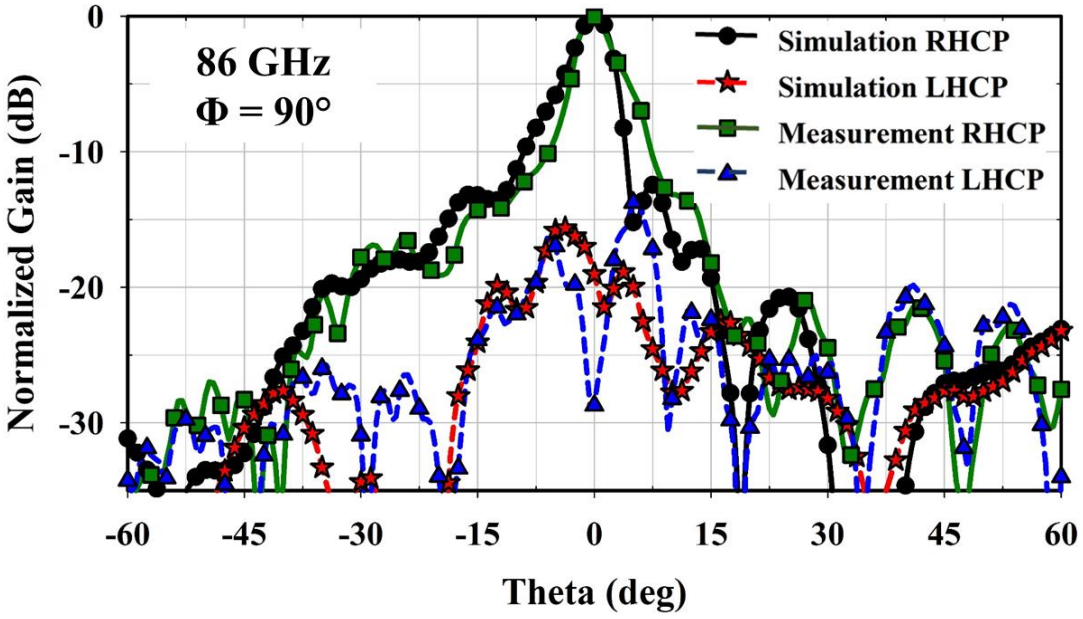

(b)

Figure 4.22 Simulated and measured 2D normalized CP radiation pattern of the 32 × 24 parallel-series fed Butterfly planar array antenna at 86 GHz in (a) ϕ = 0° and (b) ϕ = 90° plane.

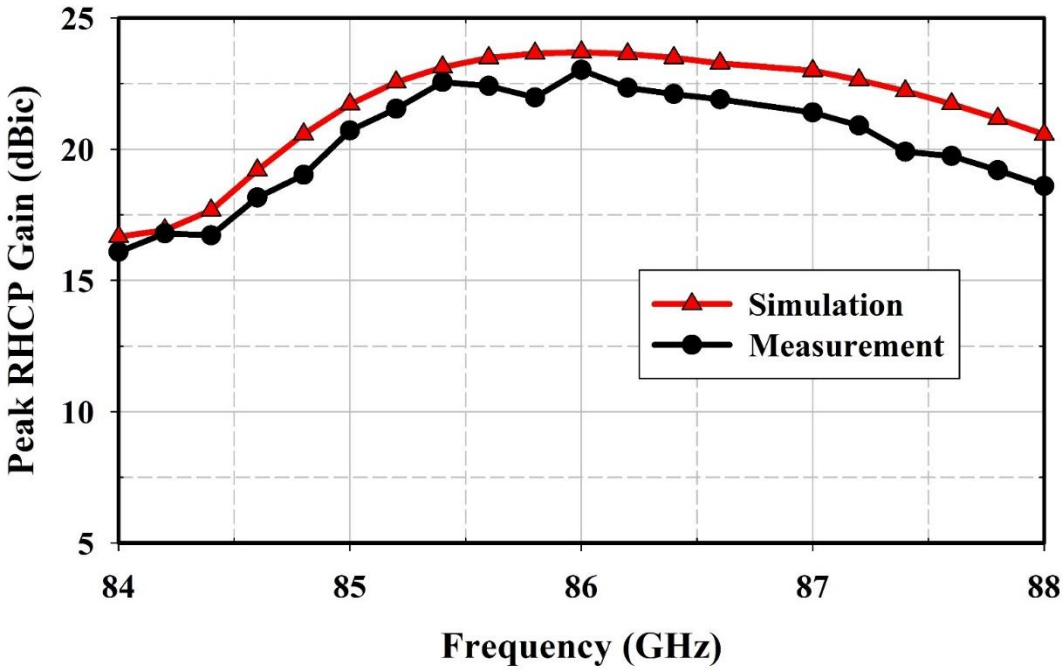

Figure 4.23 Peak simulated and measured RHCP realized gain as a function of frequency for the 32 × 24 planar array.

The average measured 3 dB gain beamwidth is 2.9° and 5.5° in the ϕ = 0° and ϕ = 90° plane, respectively. The average measured total antenna efficiency of the 32 × 24 parallel-series fed Butterfly planar array is 32% within the acceptable squint bandwidth. This significant reduction in the efficiency of the 32 × 24 planar array as compared to the 8 × 24 planar array is owing to the higher feed-network loss in the longer parallel-series network.

The comparison between the proposed 1 × 24 traveling-wave Butterfly antenna and some of the state-of-the-art traveling-wave CP antennas [95] – [101] are gathered in Table 4.2. The proposed CP traveling-wave antenna is designed using a simple single-layered microstrip technology at the millimeter-wave (86 GHz). The Butterfly linear array exhibits the lowest beam squint of only 6° around the broadside radiation in the 3 dB AR bandwidth as compared to the other reported CP traveling-wave linear arrays. The gain of the proposed linear array is higher than

most of the other work. In [99], a 2 dB higher gain is achieved due to increased antenna aperture ($8\lambda_0 \times 2.5\lambda_0$) compared to our proposed ($16.3\lambda_0 \times 0.6\lambda_0$) linear-array.

Table 4.2 Comparison of state-of-the-art traveling-wave CP antennas

Antenna	**Fabrication Method**	**Design Frequency (GHz)**	**Size without feed lines / number of unit cells**	**Squint angle variation within 3 dB AR bandwidth / Broadside Radiation**	**Maximum Gain (dBic)**
[91]	1-layer microstrip	7.82	$5.9\lambda_0 \times 1\lambda_0$ / 12 cells	35°/ Yes	12
[95]	1-layer microstrip	10	$6\lambda_0 \times 0.76\lambda_0$ / 5 cells	NR/ Yes	13
[96]	1-layer microstrip	3	$4.1\lambda_0 \times 1.1\lambda_0$ / 5 cells	NR/ Yes	NR
[97]	1-layer microstrip	24	$22\lambda_0 \times 0.6\lambda_0$ / 40 cells	10°/ Yes	18.1
[98]	1-layer SIW: complex	7.65	$5.6\lambda_0 \times 0.8\lambda_0$ / 14 cells	103°/ Yes	8.95
[99]	3-layers CPW: complex	45	$8\lambda_0 \times 2.5\lambda_0$ / 10 cells	39°/ No	19
[100]	1-layer microstrip	5	$2.4\lambda_0 \times 0.6\lambda_0$ / 2 cells	20.5°/ near broadside	7
[101]	1-layer microstrip	5.6	$4.6\lambda_0 \times 0.6\lambda_0$ / 5 cells	10.4°/ Yes	12
This work	**1-layer microstrip**	**86**	**$16.3\lambda_0 \times 0.6\lambda_0$ / 24 cells**	**6°/ Yes**	**17**

NR = not reported

4.5 Herringbone and Butterfly Series-Fed Planar Phased Array Comparison

Planar arrays consisting of eight 1 × 24 series-fed antenna are designed using the Herringbone and Butterfly unit elements, as shown in Figs. 4.24(a) and 4.24(b), respectively. The inter-element spacing between the series-fed arrays for each of the designs is maintained at $0.65\lambda_0$, where λ_0 is the free space wavelength at 86 GHz. Series-fed arrays have an inherent property of beam squint, i.e., the beam scans with frequency. We have defined an acceptable squint angle to be ± 1° from the broadside pattern. Both the Herringbone and Butterfly series-fed planar array demonstrates an acceptable beam-squint bandwidth of 1 GHz between 86 - 87 GHz in the φ = 90° plane. The broadside gain variation is around 0.5 dB across this frequency range.

The beam steering performance with 4-bit phase states at 86.5 GHz for the Herringbone and Butterfly planar array is presented in Fig. 4.25. Both the planar arrays show boresight right-hand circular polarization (RHCP) gain of around 26 dBic. The Herringbone phased array antenna demonstrates asymmetric beam scanning of -23°/+30° along the φ = 0° plane for a 3-dB reduction in the RHCP gain. More importantly, the cross-polarization component of the Herringbone array antenna, i.e., left-hand circular polarization (LHCP), increases rapidly with different scan angles, as shown in Fig. 4.25(c). The Butterfly phased array antenna shows symmetric RHCP beam

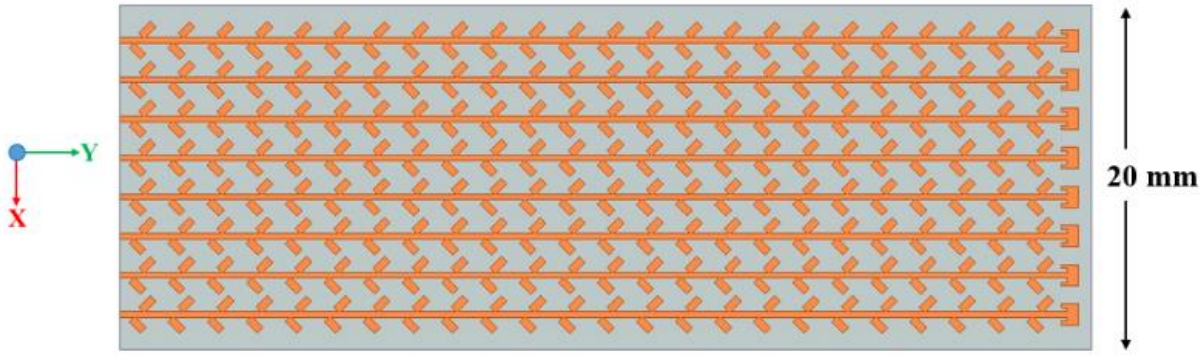

(a)

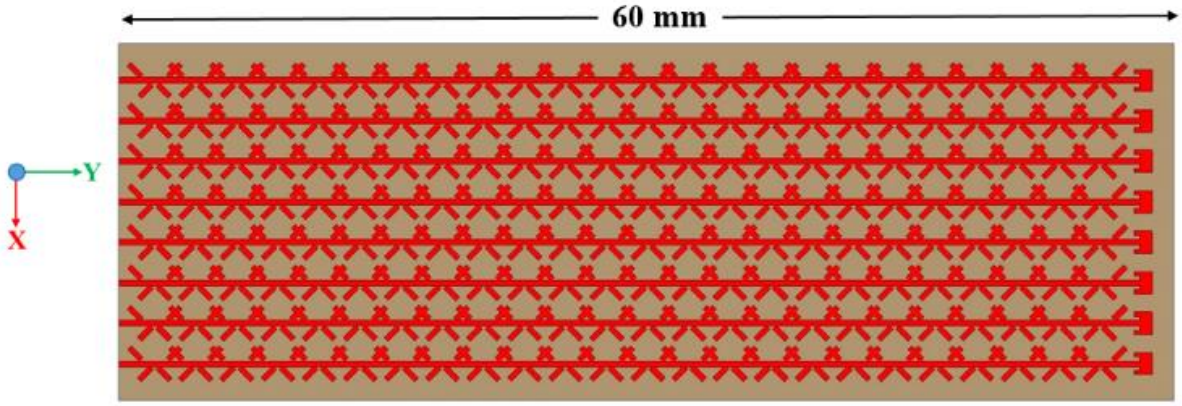

(b)

Figure 4.24 8 × 24 series-fed planar array (a) Herringbone phased array antenna, and (b) Butterfly phased array antenna.

steering of ± 34° in the φ = 0° plane for a 3-dB gain reduction, as shown in Fig. 4.25(b). Also, the cross-polarization LHCP gain of the Butterfly antenna is significantly lower than the LHCP gain of the Herringbone array antenna throughout the scanning range.

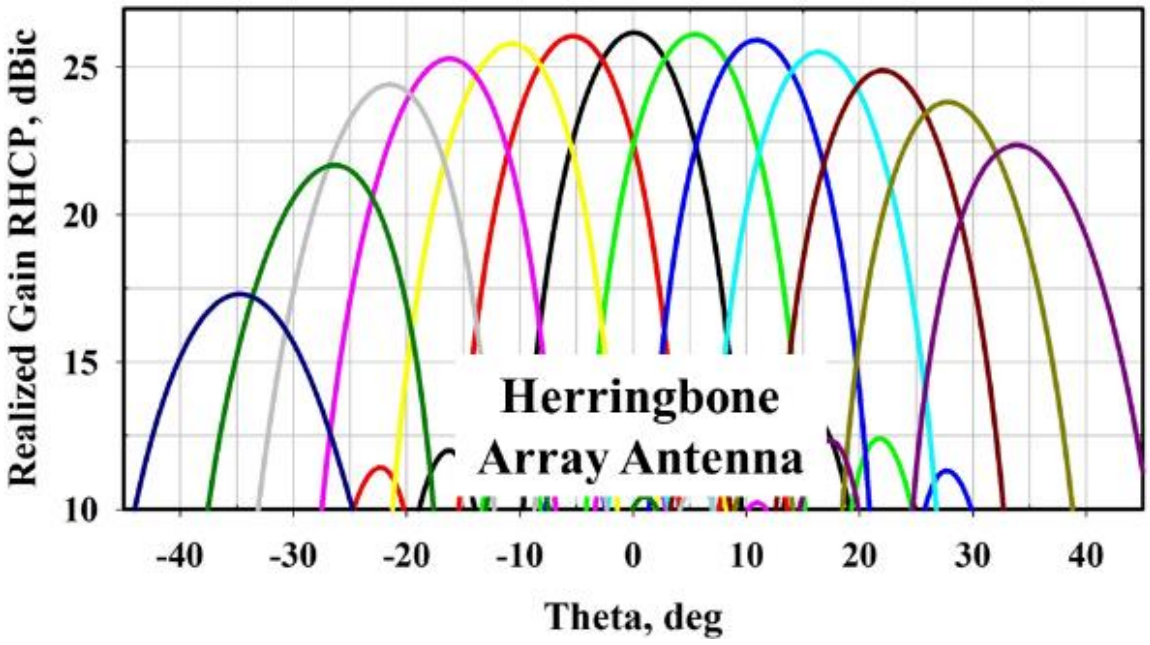

(a)

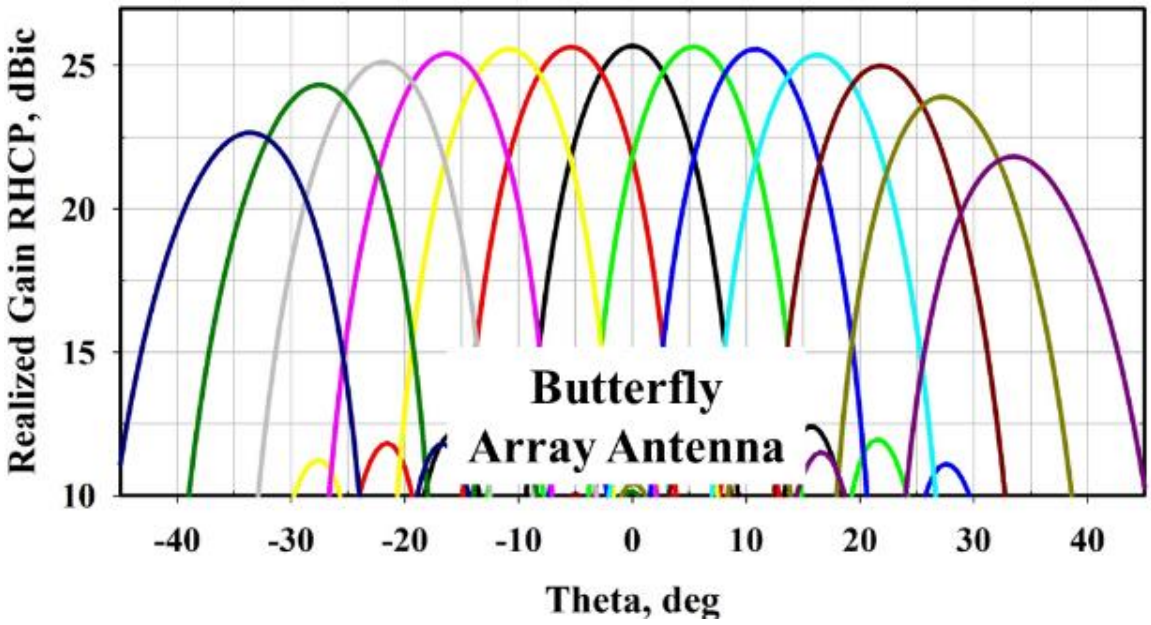
Realized Gain RHCP, dBic
25
20
15
10
Butterfly
Array Antenna
-40
-30
-20
-10
0
10
20
30
40
Theta, deg

(b)

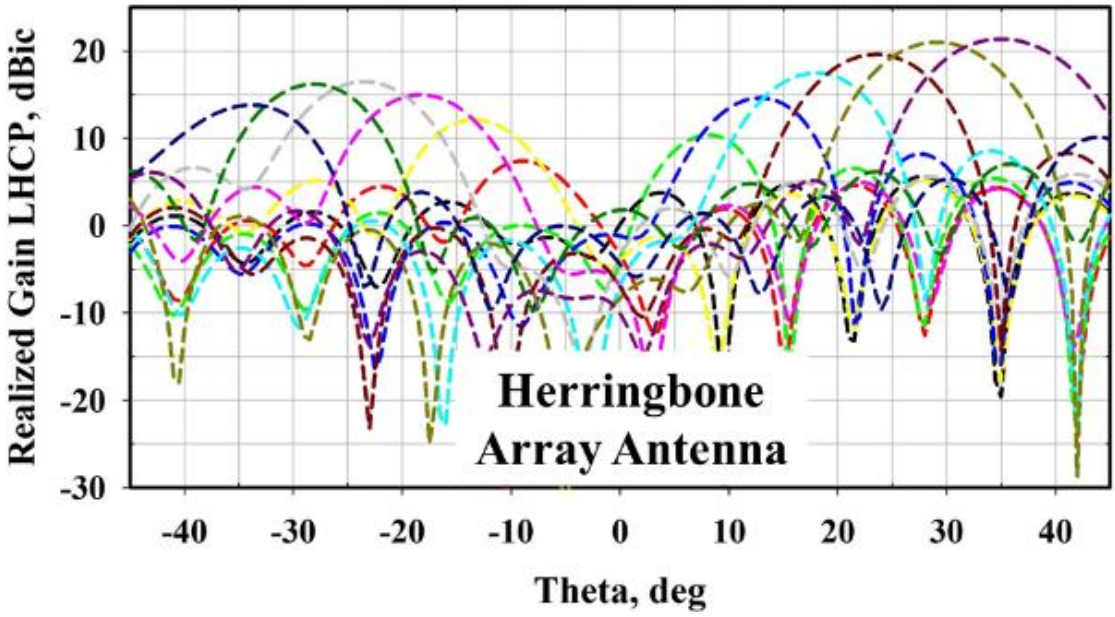
Realized Gain LHCP, dBic
20
10
0
-10
-20
-30
Herringbone
Array Antenna
-40
-30
-20
-10
0
10
20
30
40
Theta, deg

(c)

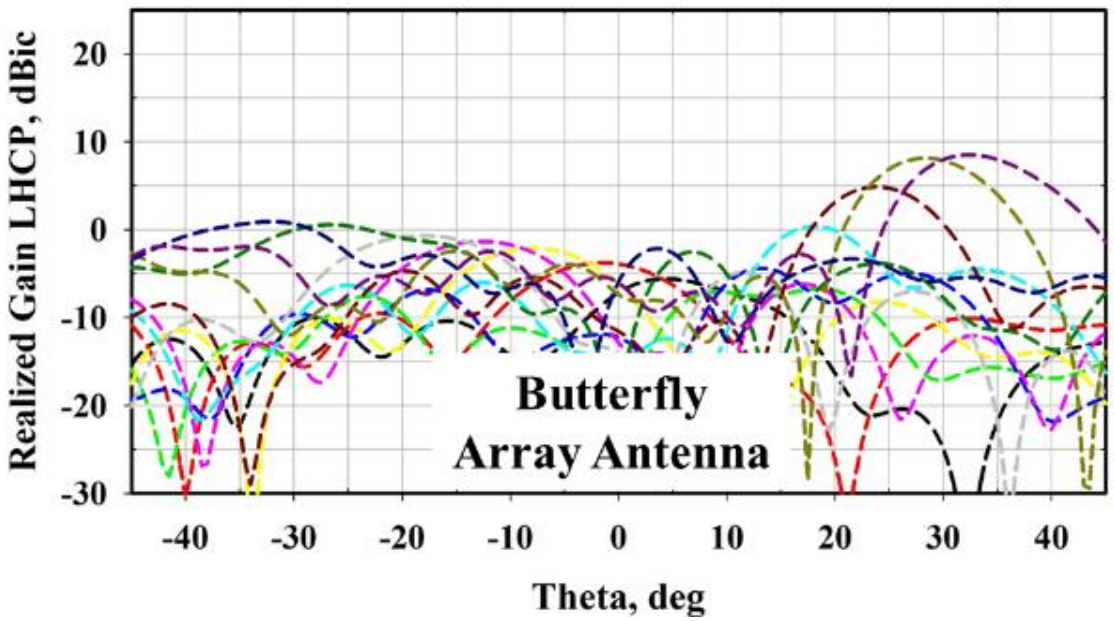

(d)

Figure 4.25 Simulated beam steering of 8 × 24 series-fed array antenna at 86.5 GHz in the φ=0° plane for (a) Herringbone co-polarization RHCP gain, (b) Butterfly co-polarization RHCP gain, (c) Herringbone cross-polarization LHCP gain, and (d) Butterfly cross-polarization LHCP gain.

4.6 Simulation Results of 8 × 24 Butterfly Phased Array Antenna

The total active reflection coefficient (TARC) accounts for scan impedance and mutual coupling from all the other antenna ports on the phased array. The TARC for the Butterfly series-fed phased array antenna is plotted in Fig. 4.26(a) for the different scan angles. It is observed that for the entire beam steering range of ± 34°, the TARC is below -10 dB between 84 – 88 GHz. The AR is below 3 dB throughout the acceptable squint bandwidth for the entire beam steering range, as shown in Fig. 4.26(b).

The peak CP realized gains and the total antenna efficiency for the Butterfly array antenna are plotted as a function of frequency and as a function of different scan angles, as presented in Figs. 4.27(a) and 4.27(b), respectively. The peak RHCP gain is above 25 dBic, and the peak LHCP

gain is more than 25 dB down the peak RHCP gain between 86 – 87 GHz. The total antenna efficiency of the Butterfly phased array is better than 65% for the desired frequency range. The RHCP gain drops by 3-dB for the beam steering angle ± 34°, and the total antenna efficiency is maintained at 65% for the different beam scan angles, as shown in Fig. 4.28(b).

The beam steering performances are studied using a 4-bit phase shifter. The simulated beam steering radiation patterns of the Butterfly phased array with conventional progressive phase shifts are demonstrated in Figs. 4.28(a) and 4.28(b), at 86 GHz, 86.5 GHz, and 87 GHz, for RHCP and LHCP gain, respectively. The beam steering angle is ± 34° for a 3-dB reduction in the RHCP gain within the desired frequency range of 86 – 87 GHz. Stable CP radiation patterns are obtained with average RHCP gain of 25.5 dBic and average cross-polarization separation (separation between the peak co-polarization RHCP gain and the peak cross-polarization LHCP gain) of 20 dB within the acceptable frequency bandwidth.

Due to finite 4-bit phase shifter states, the conventional method of progressive phase shifts provides beam scanning in coarse steps of around 5.5° with $0.65\lambda_0$ inter-element spacing. However, the phase shifts need not be uniform, and by applying the non-uniform phase shift, radiation patterns with fine beam control can be achieved. Fig. 4.29 shows that fine beam steering RHCP pattern in 0.5° scan steps can be achieved from the 4-bit phase shifter by applying non-uniform phase shifts. The RHCP gain variation is around 0.3 dB across the fine beam scan angles. Table 4.3 presents a few cases of the non-uniform phase shifts in the 8 × 24 Butterfly array antenna.

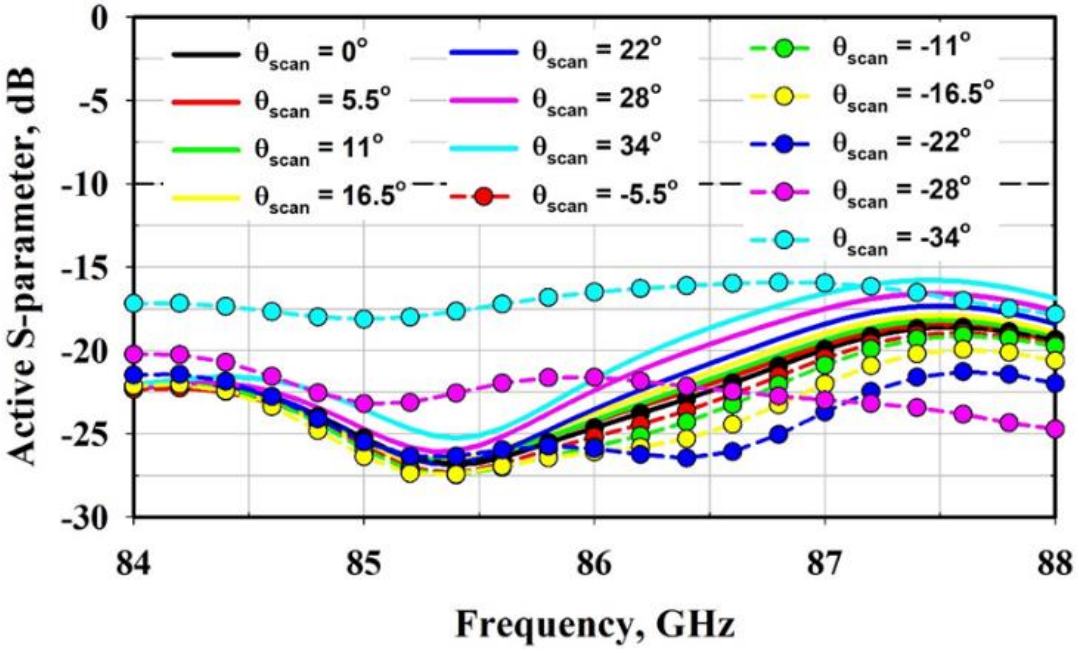

(a)

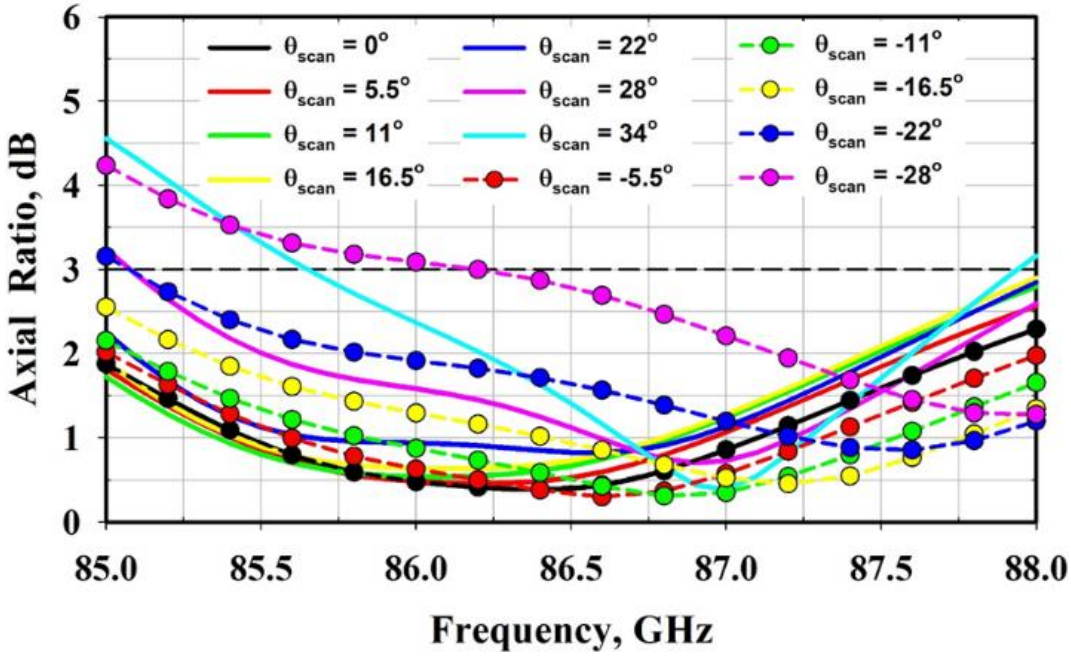

(b)

Figure 4.26 (a) Simulated active S-parameter of the 8 × 24 Butterfly phased array antenna for different scan angles, and (b) Simulated AR of the 8 × 24 Butterfly phased array antenna for different scan angles.

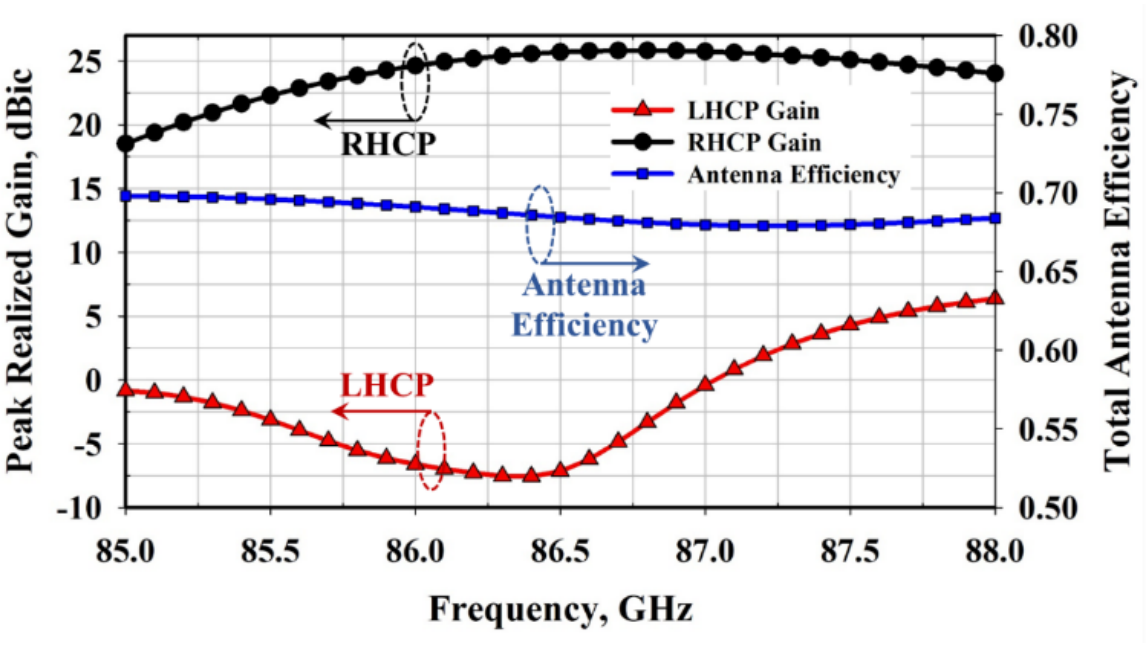

(a)

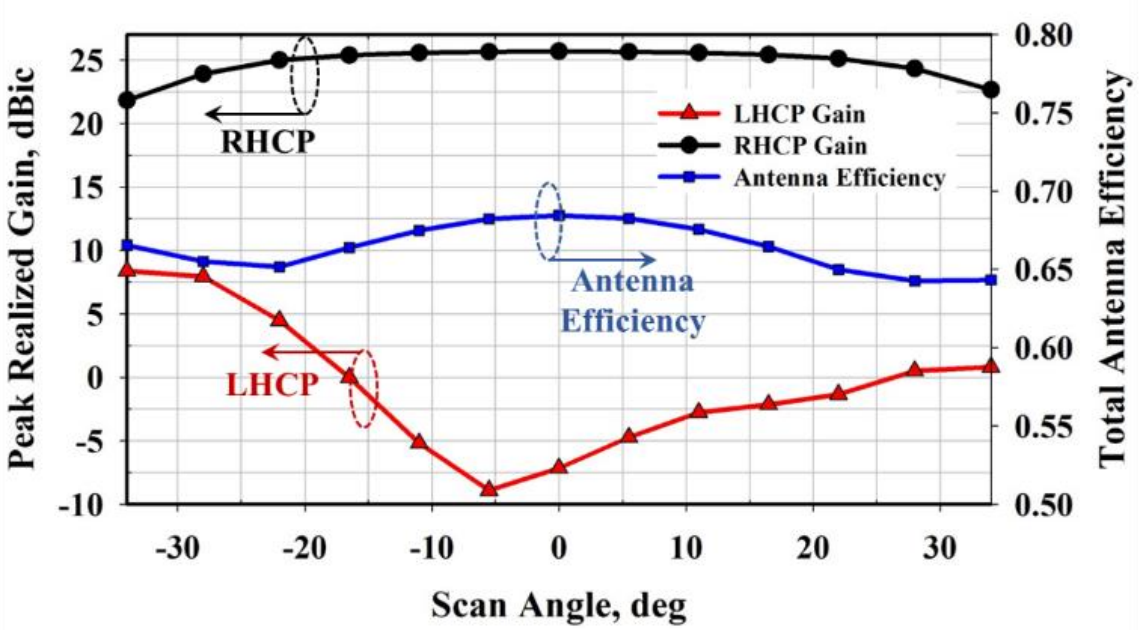

(b)

Figure 4.27 Simulated peak realized CP gains and total antenna efficiency of the 8 × 24 Butterfly phased array antenna (a) Vs. frequency and (b) Vs. different scan angles at 86.5 GHz.

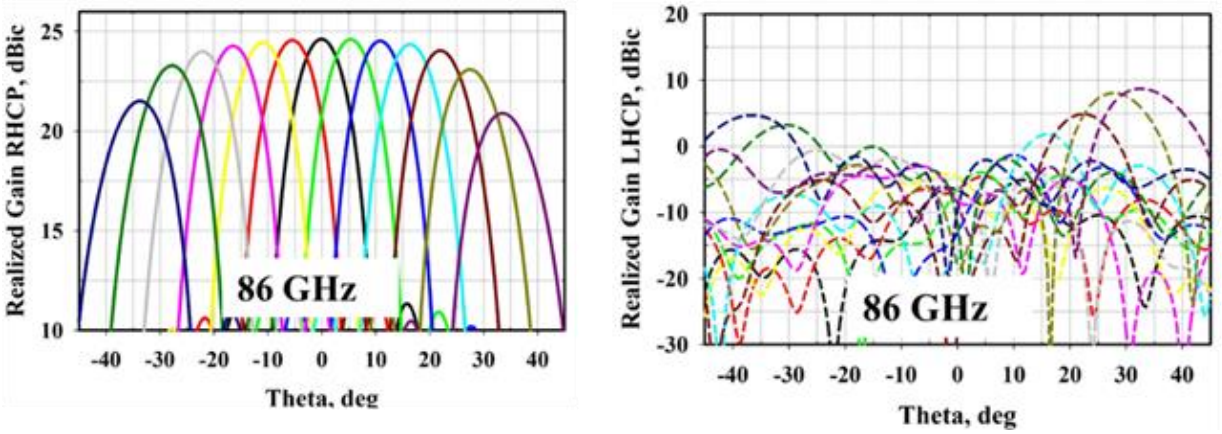

(a)

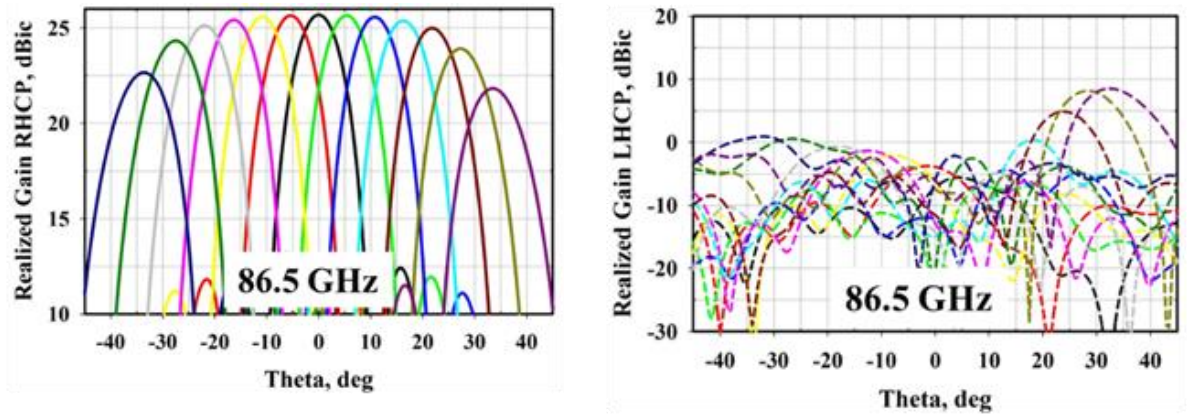

(b)

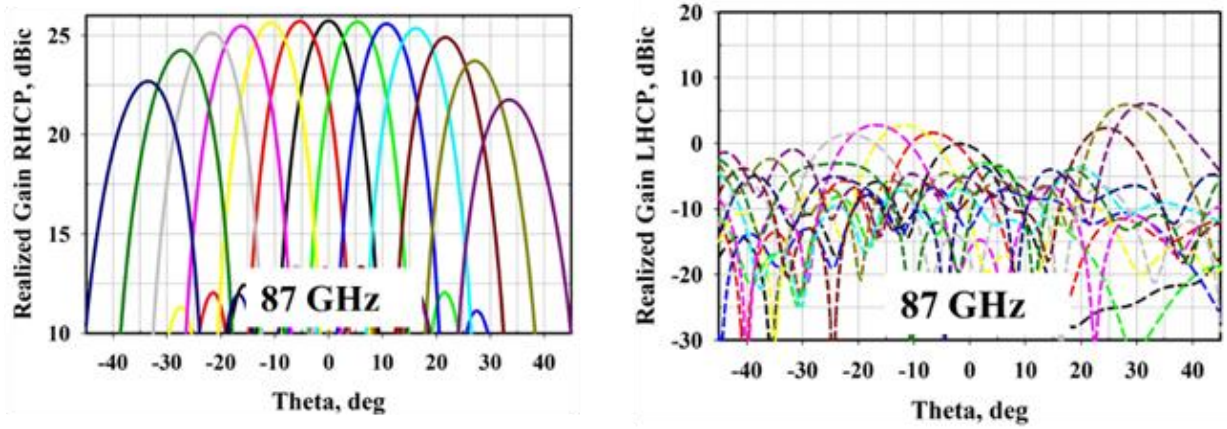

(c)

Figure 4.28 Simulated RHCP and LHCP beam steering radiation patterns of the 8 × 24 Butterfly phased array antenna at (a) 86 GHz, (b) 86.5 GHz, and (c) 87 GHz.

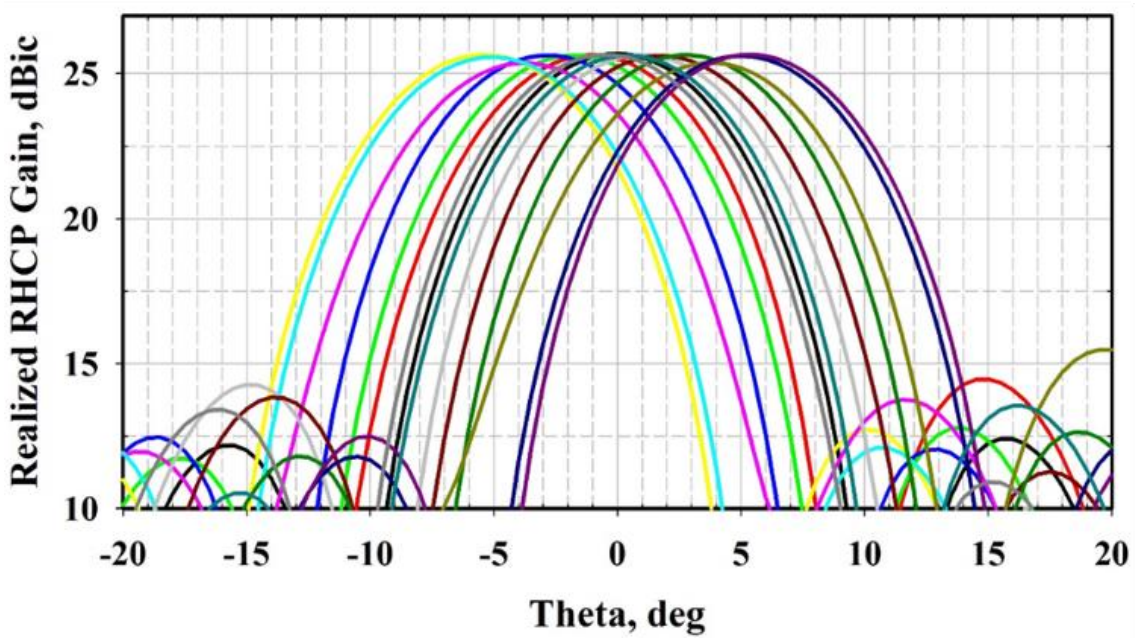

(a)

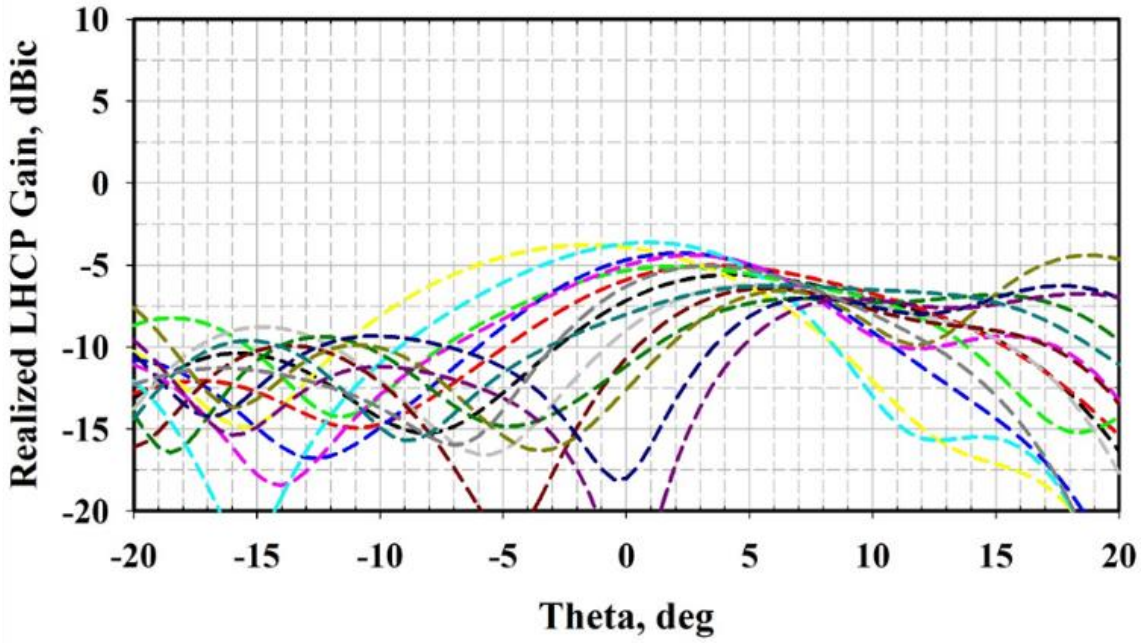

(b)

Figure 4.29 Fine beam steering in steps of 0.5° with non-uniform phase shifts of 4-bit phase shifter (a) Realized RHCP gain, and (b) Realized LHCP gains at 86.5 GHz.

Table 4.3 Non-uniform phase shifts with 4-bit phase shifter for fine beam scan control.

Beam Scan Angle	**Non-uniform Excitation Phase Shifts at the Antenna Elements with 4-bit Phase Shifter (deg)**								**Peak RHCP Gain**	**Peak LHCP Gain**
(deg)	**1**	**2**	**3**	**4**	**5**	**6**	**7**	**8**	**(dBic)**	**(dBic)**
5.5	0	-22.5	-45	-67.5	-90	-112.5	-135	-157.5	25.65	-5.28
5	0	-45	-45	-67.5	-90	-112.5	-135	-157.5	25.61	-3.31
4	0	-45	-90	-90	-90	-112.5	-112.5	-135	25.37	-4.67
3	0	-22.5	-22.5	-45	-45	-67.5	-67.5	-90	25.63	-5.29
2	0	0	-22.5	-22.5	-45	-45	-45	-45	25.61	-5.88
1	0	0	0	0	-22.5	-22.5	-22.5	-22.5	25.65	-6.22
0.5	0	0	0	0	0	0	0	-22.5	25.62	-6.25
0	0	0	0	0	0	0	0	0	25.69	-5.6

4.7 Monte-Carlo Statistical Analysis of the Proposed Butterfly Phased Array Antenna

Monte-Carlo simulations are performed using Keysight SystemVue to quantify changes in the proposed 8 × 24 phased array beam caused by variation in the array elements. Two variations in Monte-Carlo are investigated: (1) random phase shift errors; and (b) random element failures in the phased array. The key concept of the Monte-Carlo analysis is to randomize the variations across many simulation runs.

For brevity, the analysis results are only shown for the broadside beam and 30° beam scan positions. At each of the beam positions, ten rounds of Monte-Carlo runs are presented. Figs. 4.30(a) and 4.30(b) show the CP realized gain patterns with random phase shift errors at broadside and 30° beam scan positions, respectively. Random phase shift errors are assumed to have a normal distribution with a standard deviation of 10°. For example, if one phase shifter value is 45°, then the statistical parameter phase error can vary with one standard deviation from -10° to +10° on top

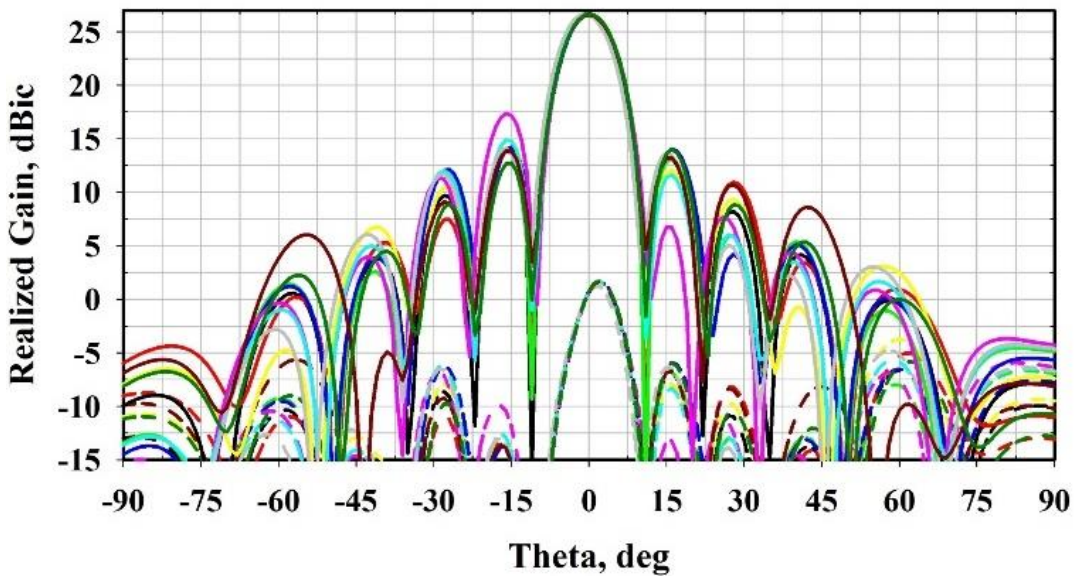

(a)

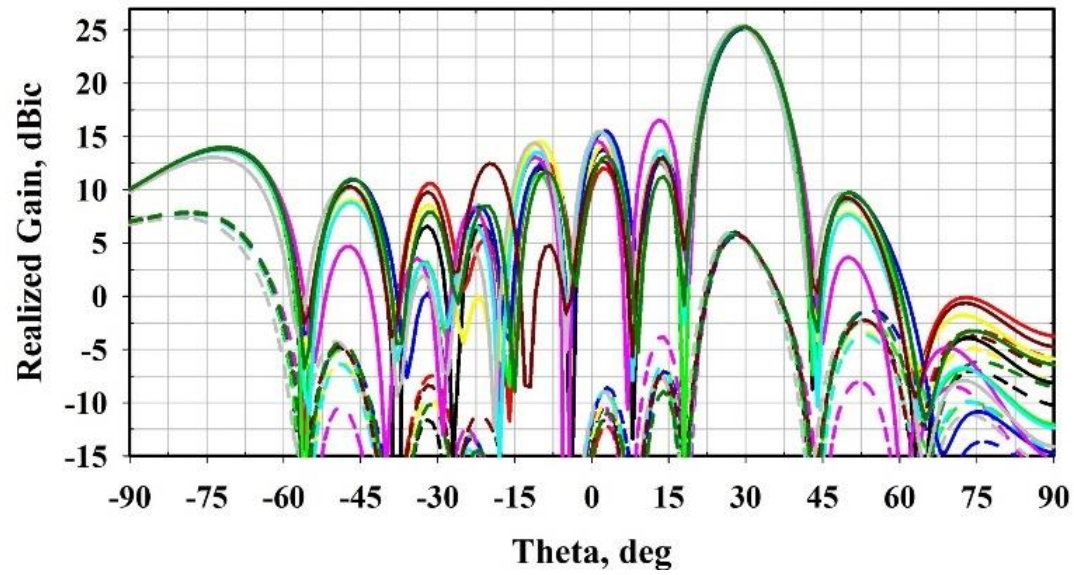

(b)

Figure 4.30 Monte-Carlo analysis on random phase shift errors in the 4-bit phase shifter for (a) Broadside beam position and (b) 30° beam scan position of the proposed 8 × 24 Butterfly phased array antenna at 86.5 GHz. (Solid lines: RHCP, Dash lines: LHCP).

of this 45° nominal, for a net variation of +35° to +55°. Table 4.4 presents the peak RHCP gain and sidelobe level for the broadside beam position for ten different Monte-Carlo runs of random

phase shift errors. It is observed that for various random phase shift errors in the 4-bit phase shifter, the main beam of the radiation pattern remains unchanged, but the sidelobe level fluctuates significantly. The maximum variation in the peak RHCP gain at broadside is only around 0.12 dB, and the change in the sidelobe level SLL is 4.8 dB.

Table 4.4 Random phase shift errors in the 4-bit phase shifter for ten different Monte-Carlo trials in the broadside beam position of the proposed 8 × 24 Butterfly phased array antenna.

Monte - Carlo Trials	**Random Error in the 4-bit Phase shift Across Antenna Array Elements (deg)**								**Peak RHCP Gain**	**Peak Sidelobe Level**
#	**1**	**2**	**3**	**4**	**5**	**6**	**7**	**8**	**(dBic)**	**(dB)**
1	0	0	0	0	0	0	0	0	**26.72**	**12.74**
2	-1.9	-8.2	-14.2	6.8	-6.2	-16	-2.1	-10.7	**26.67**	**12.53**
3	-8.1	0.5	2.5	-12.9	-1.7	-1	-7.7	-4.1	**26.68**	**12.63**
4	7.7	9.3	-11.1	7.9	-10.2	-10.5	-3.6	7.1	**26.63**	**11.63**
5	0.4	12.8	-8	-22.3	-11.3	-7.5	-5.3	-5.7	**26.61**	**14.48**
6	-17.1	6.7	16.1	9.4	-2.6	-10.9	-10.1	4.9	**26.55**	**9.07**
7	-2.8	9.1	-5.7	0.3	-0.5	-8	-6.2	7.7	**26.66**	**11.63**
8	-7	4	-8.5	-12.4	-10.2	10.1	1.7	17.1	**26.57**	**14.97**
9	15.6	-1.1	0.9	-9.6	3.7	-21.5	12.7	2.2	**26.59**	**12.57**
10	6	11.5	6.7	9.7	11.6	6.1	11.7	-9.7	**26.68**	**13.82**

Another Monte-Carlo analysis is performed on the random element failures in the Butterfly phased array antenna. Fig. 4.31(a) and 4.31(b) show the CP realized gain patterns with random element failures in the phased array for the broadside and 30° beam scan positions, respectively. Random element failures are assumed to have a 10% discrete probability of failure, i.e., each element along the phased array has a 10% chance of failure. A value of 0 for the element failure statistical parameter indicates that the element has failed, whereas a value of 1 indicates that the element is fully functional. Table 4.5 presents the peak RHCP gain and sidelobe level for the broadside beam position for ten different Monte-Carlo runs of random element failures. It is

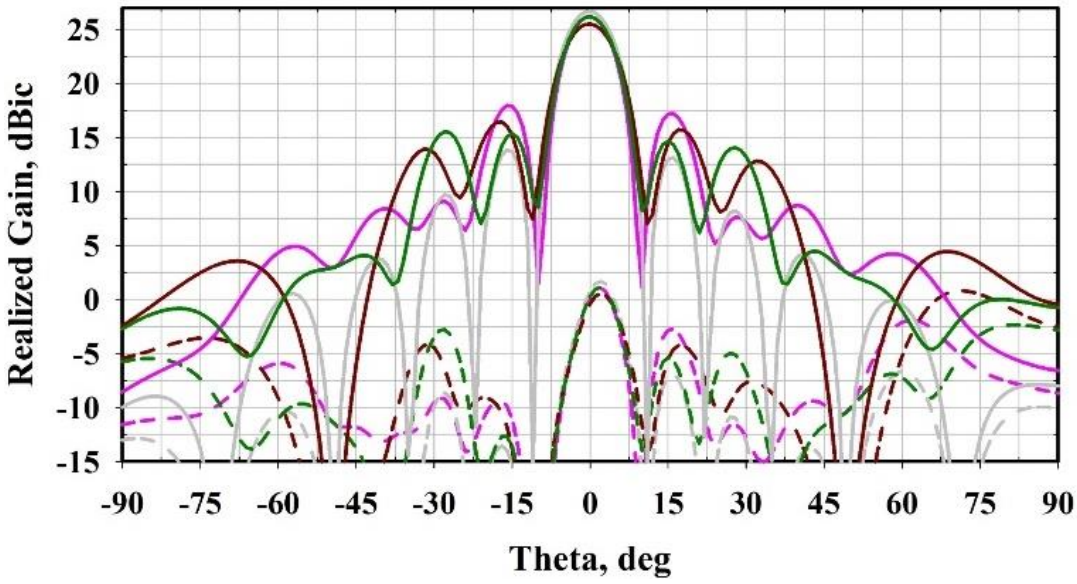

(a)

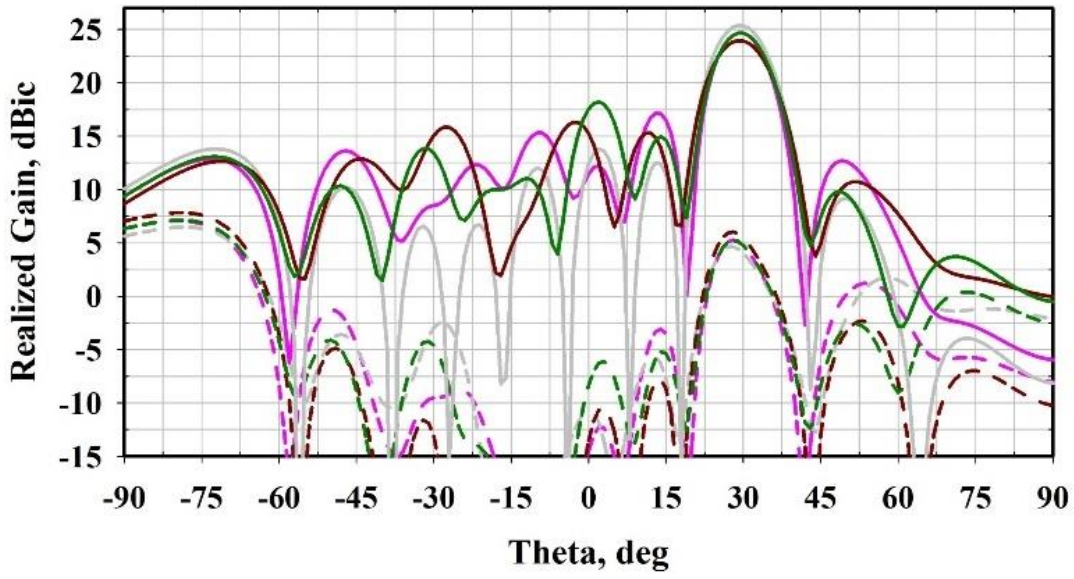

(b)

Figure 4.31 Monte-Carlo analysis on random element failure for (a) Broadside beam position and (b) 30° beam scan position of the proposed 8 × 24 Butterfly phased array antenna at 86.5 GHz. (Solid lines: RHCP gain, Dash lines: LHCP gain).

observed that for different random element failures, both the peak RHCP gain and sidelobe level show large fluctuations.

From Table 4.5, the maximum pattern deterioration happens when two of the series-fed linear arrays in the 8 × 24 phased arrays fail, as seen in the Monte-Carlo run # 9. The maximum variation in the peak RHCP gain at broadside is 1.2 dB, and the change in the SLL is 4.52 dB.

Table 4.5 Random element failures for ten different Monte-Carlo trials in the broadside beam position of the proposed 8 × 24 Butterfly phased array antenna.

Monte - Carlo Trials	**10 % Probability of Element Failure**								**Peak RHCP Gain**	**Peak Sidelobe Level**
#	**1**	**2**	**3**	**4**	**5**	**6**	**7**	**8**	**(dBic)**	**(dB)**
1	1	1	1	1	1	1	1	1	**26.72**	**12.74**
2	1	1	1	1	1	1	1	1	**26.72**	**12.74**
3	1	1	1	1	1	1	1	1	**26.72**	**12.74**
4	1	1	1	1	1	1	1	1	**26.72**	**12.74**
5	1	1	0	1	1	1	1	1	**26.21**	**9.6**
6	1	1	1	0	1	1	1	1	**26.2**	**8.12**
7	1	1	1	1	1	1	1	1	**26.72**	**12.74**
8	1	1	1	1	1	1	1	1	**26.72**	**12.74**
9	1	1	1	1	0	1	1	0	**25.53**	**8.2**
10	1	1	1	1	1	0	1	1	**26.21**	**9.6**

4.8 Integrated Phased Array and Beamforming Board

4.8.1 Development of 4-bit phase shifter

A 4-bit millimeter-wave switched delay line phase shifter is also designed in Cadence Virtuoso and simulated in Keysight Momentum [102]. Figs. 4.32(a) and 4.32(b) show the simulated layout of the 4-bit phase shifter and the fabricated phase shifter chip designed on the Global Foundries 9HP SiGe process, respectively. The 4-bit phase shifter uses SP4T switches with

PIN diodes and has high P_{sat} due to the PIN diodes. The control bias voltage ranges from -4 to +1 V, and the overall size of the phase shifter chip is 2.3 mm × 1.3 mm. The detailed simulation and measurement results of the 4-bit phase shifter is presented in [102]. The simulation phase-shift states and insertion loss of the 4-bit phase shifter are presented in Fig. 4.33. The 4-bit phase shifter shows an average RMS phase error of 10° and an average insertion loss of 9 dB at 86 GHz.

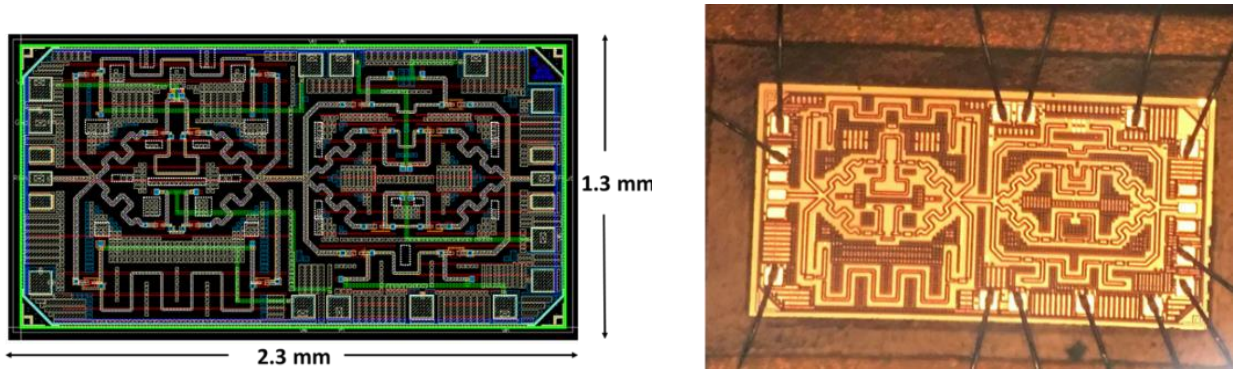

(a) (b)

Figure 4.32 4-bit phase shifter (a) Simulation layout and (b) Fabricated chip photograph.

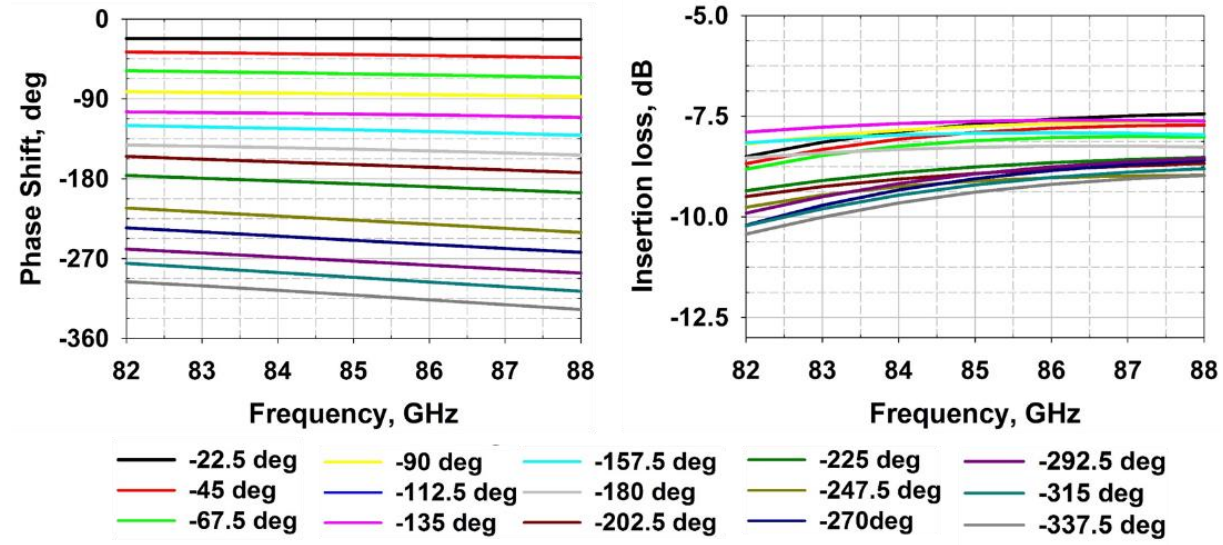

Figure 4.33 Simulated phase shift states and insertion loss of 4-bit phase shifter.

4.8.2 Fabricated Butterfly phased array antenna integrated with Beamforming board

The integrated 8 × 24 series-fed Butterfly array antenna aperture with the analog beamforming network was fabricated, as shown in Fig. 4.34. The integrated board includes the proposed Butterfly 8 × 24 series-fed CP array antenna aperture, designed 4-bit phase shifters, COTS GaAs HEMT MMIC LNAs, SPI controller, and voltage regulators. However, due to the mirroring of the phase shifter during the fabrication process, the experimental verification of the beam steering could not be carried out at this stage.

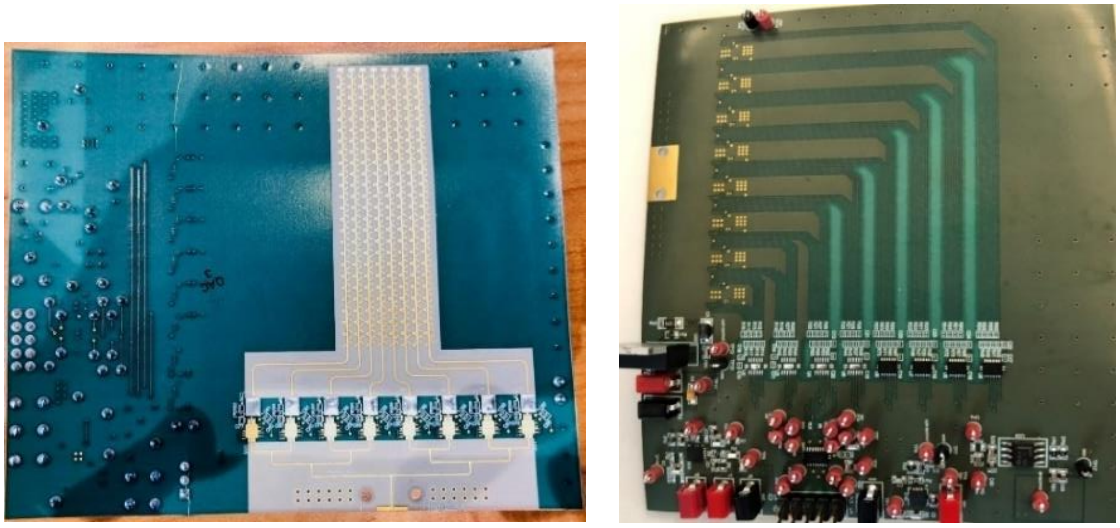

(a) (b)

Figure 4.34 Fabricated photograph of the integrated Butterfly phased array aperture and the beamforming board (a) Top view and (b) Bottom view.

4.9 Conclusion

A novel Butterfly traveling wave antenna for circularly polarized millimeter-wave (*W*-band) high gain application was designed, analyzed, and experimentally verified. The analysis of the Butterfly unit-cell was in excellent agreement with the full-wave EM simulation. We also

introduced an overlapped unit-cells based approach to achieve a compact sequentially-rotated series-fed linear array antenna without degradation in the radiation performance. Furthermore, periodic LWA analysis was shown to provide insights into the radiation characteristics of the proposed linear array. The inherent open-stopband (OSB) suppression was obtained from the Butterfly structure to ensure consistent gain near broadside. The passive fixed-beam prototypes of 8 × 24 and 32 × 24 parallel-series fed planar array were fabricated, and reasonable agreements were found between simulated and measured results.

The next chapter discusses a hybrid reflector-phased array solution for high gain 1D-Beam steering antenna application at *Ku*-band (12 – 14 GHz). The reflector is parabolic-cylindrical (cylindrically shaped with a parabolic cross-section) fed with an 8 × 4 phased array antenna placed along the focal line.

Chapter 5

Ku-Band Dual Linear-Polarized 1D Beam Steering Antenna using Parabolic-Cylindrical Reflector Fed by a Phased Array Antenna

5.1 Introduction

An ever-increasing demand for the high data rate wireless communication has augmented the interest in the design of energy-efficient and cost-effective antenna systems. The antennas enabling high data rate wireless networks require wide impedance bandwidth, stable radiation pattern, high gain, and beam steering characteristics. Parabolic reflector antenna and phased array antenna are the most common solutions in achieving the required objectives. Both standard technologies provide high gain and stable radiation patterns. Parabolic reflectors can usually offer higher efficiencies compared to the phased arrays with full amplitude and phase controls. However, the parabolic reflector antenna is inconvenient for scanning applications. Some scanning can be achieved by translating the feed; however, as the feed is moved off-boresight, phase aberrations between the wavefront arriving from different portions of the reflector degrade the antenna's ability to focus the desired wavefront coherently [3], [4], [103]. Various limited beam scanning reflectors, including single-surface parabolic reflectors and spherical reflectors, have been reported in the literature [104] - [106].

On the other hand, the phased array antenna offers a wider beam steering range. Further, the microstrip technology makes these antennas an excellent candidate owing to their low profile and lightweight structure, ease of fabrication and integration, and low manufacturing cost [73], [74]. However, the cost of the phased array antenna scales with the number of elements in the

array. As the number of radiator elements increases, the number of active RF components also scales, thereby increasing the power requirement of the system. Over the years, numerous phased array antenna with integrated beamforming networks have been investigated [107], [108].

Parabolic-cylindrical reflector-based beam steering antenna is, in fact, particularly interesting because this combines the advantages of the two standard antenna techniques, the reflector technique, and the phased array technique. This may well represent a cost-effective

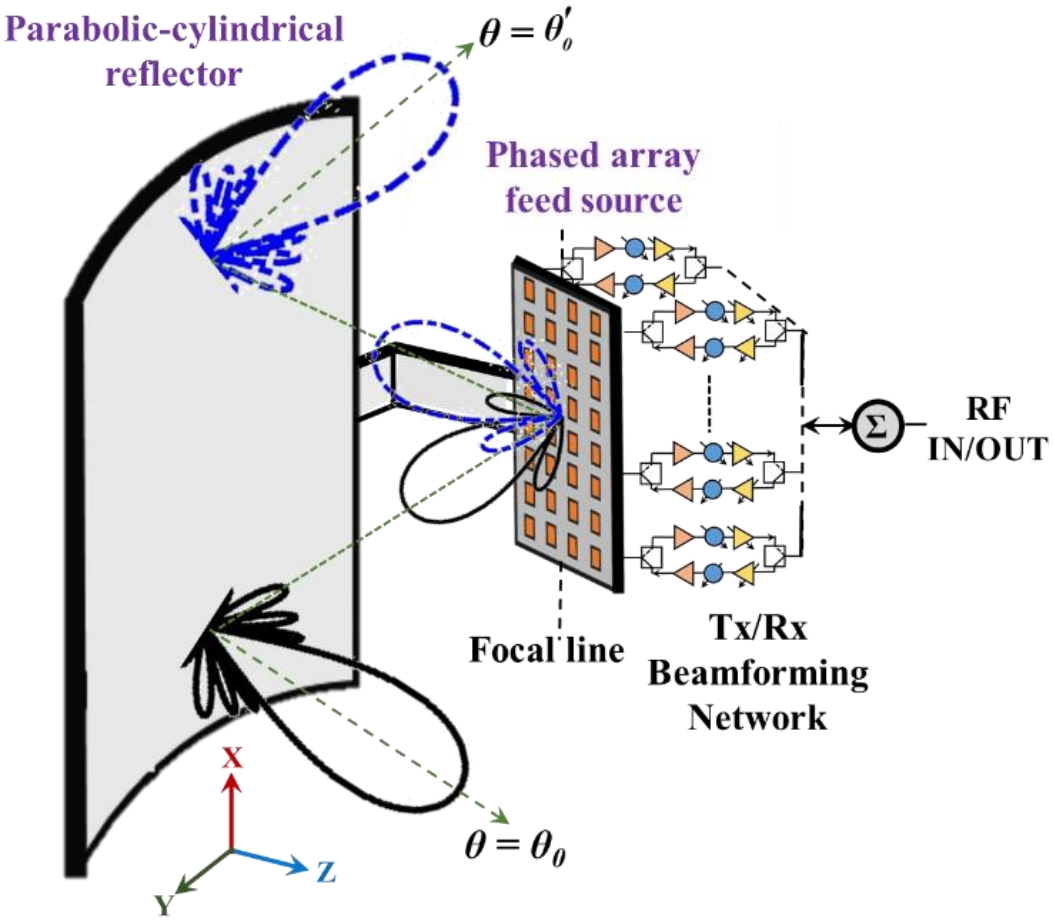

Figure 5.1 Illustration of the parabolic-cylindrical reflector fed by a phased array antenna for single beam high gain 1D beam steering along the cylindrical axis. (Figure shows two independent beam scan positions θ_0 and θ_0' based on the beam steering from the phased array antenna).

approach, especially when the requirements for steerability are different in two orthogonal planes or when the radiation pattern does not require rotational symmetry. Several comprehensive analyses for the parabolic-cylindrical reflector antenna are discussed in [109] - [113].

In this research, a hybrid reflector-phased array antenna system for a high data rate directional wireless communication network is proposed at *Ku*-band (12 – 14 GHz). The reflector is a parabolic-cylindrical reflector (cylindrically shaped with a parabolic cross-section) fed with a phased array antenna placed along the focal line, as illustrated in Fig. 5.1. The parabolic-cylindrical reflector provides a wide-angle beam steering along the cylindrical axis (1D-beam steering) compared to a conventional parabolic reflector [8], [9], [114]. The feed source is an 8 × 4 dual linear-polarized stacked patch phased array antenna integrated with the Anokiwave AWMF-0117 silicon core chips. The phased array, when used as a feed source for the reflector, requires significantly fewer antenna elements and active RF components as compared to a stand-alone phased array antenna. For instance, a 6 dB improvement in the directivity means four times the size of the stand-alone phased array antenna and four times the RF components and its associated losses. However, with the hybrid reflector-phased array approach, similar directivity improvement can be achieved without increasing the size, loss, and power requirement of the phased array antenna. Thus, the power requirement and cost of the proposed hybrid antenna system is significantly reduced compared to a conventional stand-alone phased array providing similar antenna gain.

A novel practical implementation of the parabolic-cylindrical reflector illuminated with an active phased array feed source is demonstrated for the 1D-beam steering performance. The reflector's feed source is an all flat-panel RFIC phased array antenna, which includes the complete serial peripheral interface (SPI) controlled beamforming network. A comprehensive graphical user

interface (GUI) is developed to vary the amplitude and phase shifts of each element of the array using the beam synthesis algorithm for different beam scan positions and sidelobe levels. This feed-reflector antenna system investigation is supported by the theory, analysis, full-wave simulation, fabrication, and experimental verification.

The proposed antenna attains four primary objectives: (1) wideband dual-polarized antenna for transmit and receive communications; (2) stable radiation pattern with low cross-polarization; (3) high antenna gain of at least 25 dBi; and (4) beam steering of at least ±30°. Besides, dynamic beam shaping can also be achieved with adaptive control of the beamforming amplitude and phase weights. As a result, the proposed hybrid antenna is a cost-effective and energy-efficient alternative to standard antenna technologies for high gain and 1D beam steering applications.

5.2 Antenna Geometry, Theory, and Analysis

The hybrid reflector-phased array antenna consists of a parabolic-cylindrical reflector and an 8 × 4 planar microstrip patch array. The planar microstrip patch array is used as the feed of the parabolic-cylindrical reflector antenna and is located along the focal line of the reflector. The geometry and the coordinate system of the parabolic-cylindrical reflector fed by the phased array antenna are shown in Fig. 5.2.

The reflector geometry is defined using (5.1) and (5.2) as [24]:

$$z(y) = \frac{y^2}{4F_c} - F_c \tag{5.1}$$

$$\hat{n} = \hat{y}\cos\phi_n + \hat{z}\sin\phi_n \text{ and } \phi_n = \tan^{-1}\left(-\frac{2F_c}{y}\right) \tag{5.2}$$

where $\hat{n}$ is the unit normal vector of the reflector surface and F_c is the focal length of the parabolic cross-section of the reflector.

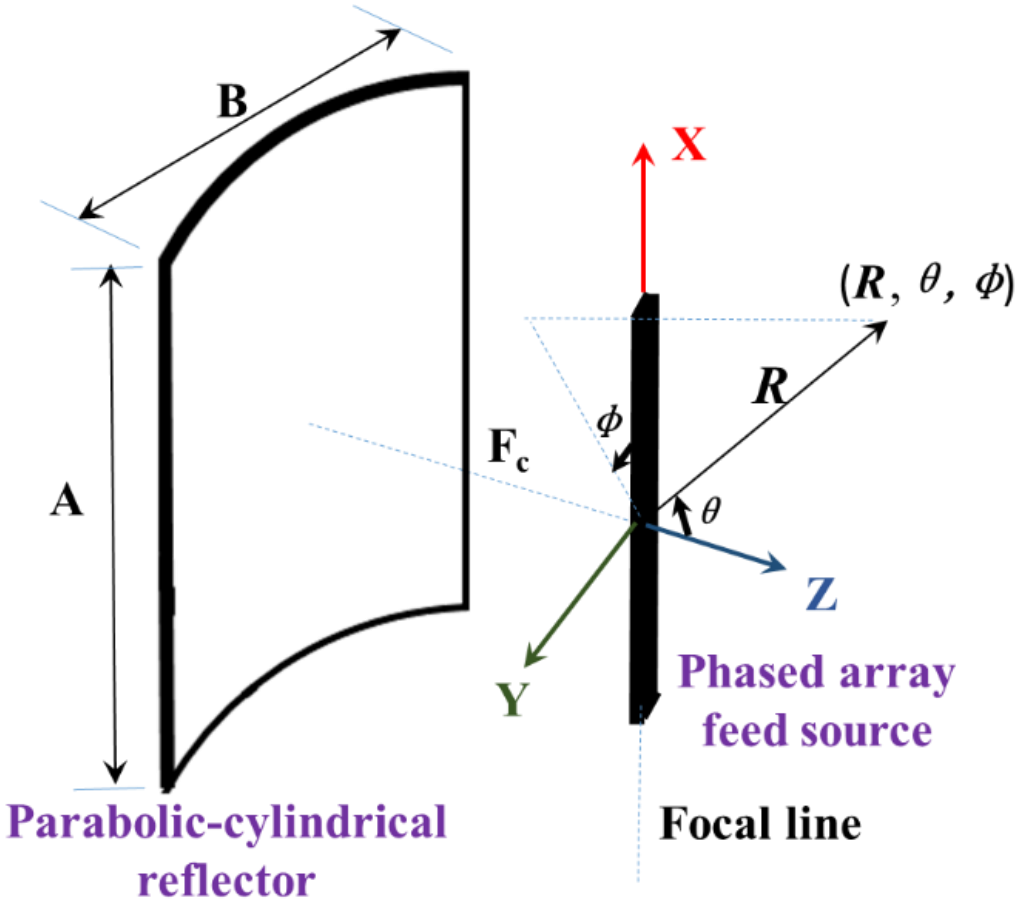

Figure 5.2 Geometry and coordinate system of the parabolic-cylindrical reflector fed by the phased array antenna.

Cavity model and physical optics approximations are used to analyze the patch array and the induced currents on the reflector surface, respectively. The far-field patterns of the parabolic-cylindrical antenna are then calculated by integrating the contribution of the induced currents over the reflector surface.

5.2.1 Microstrip Patch Planar Array Antenna

The number of array elements is chosen as 8 × 4 with the inter-element spacing of 12 mm ($0.52\lambda_0$ at f_0 = 13 GHz). The inter-element spacing is chosen to achieve a wide-angle beam steering range for the phased array of ±45° without any grating lobes. If 4 × 4 element phased array is used as a feed source for this reflector, the spill-over loss of reflector will increase along the cylindrical axis resulting in lower gain as compared to a reflector fed with 8 × 4 phased array source. On the other hand, if 8 × 8 number of elements are used in the phased array, the reflector will be partially illuminated along the parabolic axis as compared to 8 × 4 array, and thereby, will result in lower aperture efficiency. Also, the number of RF components in the phased array will double in the 8 × 8 array resulting in the increased cost and power consumption of the system. For instance, with 8 × 8 array 64 RFIC chips will be required and the power consumption of the system in receive (Rx) mode will be around 12.6 W, whereas the proposed 8 × 4 array will require only 32 RFIC chips with the power consumption of 6.3 W.

The far-field components of the rectangular patch antenna are computed using the cavity model analysis [32]. In the cavity model, the patch antenna of Fig. 5.3(a) is viewed as a linear array of two identical radiating slots separated by a distance b. The electric vector potential F_x for one of the radiating slot, with the magnetic current source $\mathbf{M}_x$ and the dominant TM_{010} mode can be calculated by (5.3) [32]:

$$F_x = \frac{\varepsilon}{4\pi r} e^{-jk_0 r} \int_0^a \int_{-h}^0 \mathbf{M}_x e^{jk_0 \sin\theta\cos\phi x'} dx' dz' \tag{5.3}$$

The corresponding normalized electric vector potential is proportional to (5.4) [32]:

$$F_x \propto \frac{\sin\left(k_0 \sin\theta\cos\phi \frac{a}{2}\right)}{\left(k_0 \sin\theta\cos\phi \frac{a}{2}\right)} \frac{e^{-jk_0 r}}{r} = \frac{\sin\left(k_x \frac{a}{2}\right)}{\left(k_x \frac{a}{2}\right)} \frac{e^{-jk_0 r}}{r} \tag{5.4}$$

where $k_x = k_0 \sin\theta\cos\phi$ and k_0 is the free-space wavenumber.

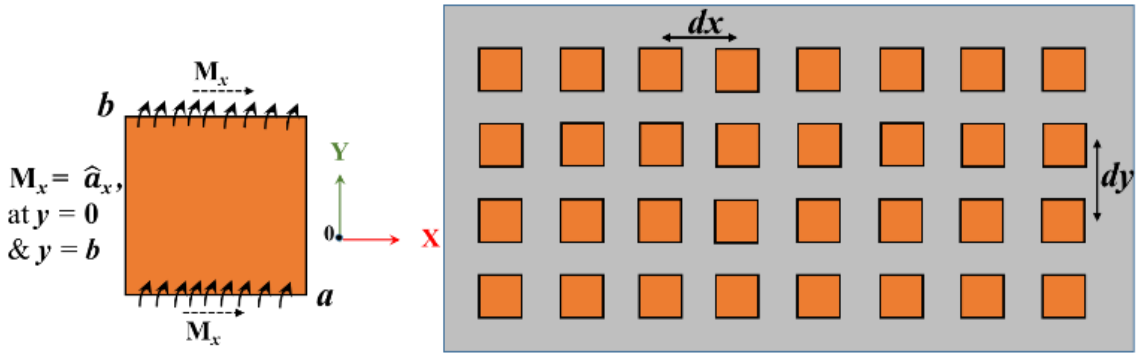

(a) (b)

Figure 5.3 (a) Magnetic current source on the linear polarized microstrip patch antenna, and (b) Microstrip patch planar array of size 8 × 4.

Using the Cartesian-to-Spherical coordinate transformations, the electric vector potential can be written as (5.5) [32]:

$$\begin{aligned} F_\theta &= F_x \cos\theta\cos\phi \\ F_\phi &= -F_x \sin\phi \end{aligned} \tag{5.5}$$

The array factor of the two radiating slots separated by a distance b along the y-direction is given by (5.6) [32]:

$$\left(AF\right)_y \propto \cos\left(\frac{k_0 b}{2}\sin\theta\sin\phi\right) = \cos\left(k_y \frac{b}{2}\right) \tag{5.6}$$

where $k_y = k_0 \sin\theta\sin\phi$

Thus, the total electric vector potential for the microstrip patch antenna is obtained by combining (5.4) – (5.6) and is given in (5.7) [32]:

$$F_\theta^t = F_x \cos\theta \cos\phi \cos\left(k_y \frac{b}{2}\right)$$
$$F_\phi^t = -F_x \sin\phi \cos\left(k_y \frac{b}{2}\right) \tag{5.7}$$

The radiated magnetic field is related to the electric vector potential by the relation (5.8) [32]:

$$H_\phi \propto E_\theta \propto F_\phi^t \propto \frac{\sin\left(k_x \frac{a}{2}\right)}{\left(k_x \frac{a}{2}\right)} \cos\left(k_y \frac{b}{2}\right) \sin\phi \frac{e^{-jk_0 r}}{r}$$
$$H_\theta \propto E_\phi \propto F_\theta^t \propto \frac{\sin\left(k_x \frac{a}{2}\right)}{\left(k_x \frac{a}{2}\right)} \cos\left(k_y \frac{b}{2}\right) \cos\theta \cos\phi \frac{e^{-jk_0 r}}{r} \tag{5.8}$$

Equation (5.8) is the total normalized far-field component of the single microstrip patch antenna. The total radiated magnetic fields of the planar array of Fig. 5.3(b) with (M = 8 and N = 4) elements can be expressed by (5.9) and (5.10) as [32]:

$$H_\theta^T = H_\theta \sum_{m=1}^{M} \sum_{n=1}^{N} A_{mn} e^{j(m-1)\psi_x} e^{j(n-1)\psi_y} \tag{5.9}$$

$$H_\phi^T = H_\phi \sum_{m=1}^{M} \sum_{n=1}^{N} A_{mn} e^{j(m-1)\psi_x} e^{j(n-1)\psi_y} \tag{5.10}$$

where $\psi_x = k_0 dx \sin\theta \cos\phi + \beta_x$ and $\psi_y = k_0 dy \sin\theta \sin\phi + \beta_y$, β_x and β_y are the progressive phase shifts along the x-direction and y-direction, respectively. Here, H_θ^T and H_ϕ^T are the total radiated magnetic fields of the 8 × 4 planar array antenna, and A_{mn} is the amplitude excitation of the elements in the planar array. To simplify the analysis, the finite ground plane effect and the mutual coupling of the patch elements are neglected.

The normalized radiation patterns of the single microstrip patch and the 8 × 4 planar array antenna using the above analytical equations are presented in Fig. 5.4. A non-uniform amplitude excitation using the Taylor window with sidelobe level -30 dB is used to reduce the sidelobe level.

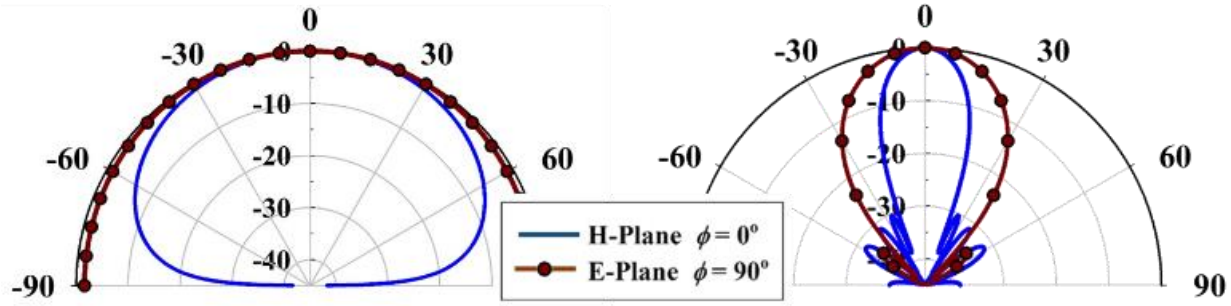

(a) (b)

Figure 5.4 *E*-plane and *H*-plane normalized radiation patterns at 13 GHz for (a) Single rectangular patch antenna, and (b) Planar patch array antenna of size 8 × 4 using the analytical equations.

5.2.2 Analysis of Far-Field Radiation of the Parabolic-Cylindrical Reflector

The planar phased array antenna is used as the feed source for the parabolic-cylindrical reflector. The physical optics (PO) approximate method is used to find the induced current on the reflector surface [24]. The PO analysis assumes that the incident field from the feed is known and that it excites surface currents ($\mathbf{J_s}$) on the reflector's surface given by (5.11) [24]:

$$\mathbf{J_s} = 2\hat{\mathbf{n}} \times \mathbf{H}^i \tag{5.11}$$

where, $\mathbf{H}^i = H_\theta^T \hat{\theta} + H_\phi^T \hat{\phi}$ is the incident magnetic field on the reflector surface.

Once the induced surface currents $\mathbf{J_s}$ are found on the reflector's surface, the magnetic vector potential **A** and the far-zone field can be calculated by (5.12) [24]:

$$\mathbf{E}^{far} = -j\omega\mu \frac{e^{-jk_0 R}}{4\pi R} \iint_{S_r} \left[\mathbf{J_s} - \left(\mathbf{J_s} \cdot \hat{a}_R \right) \hat{a}_R \right] e^{jk_0 \vec{r} \cdot \hat{a}_R} ds \tag{5.12}$$

Thus, for the parabolic-cylindrical reflector antenna, the electric field can be expressed as (5.13) [24]:

$$\mathbf{E}^{far} = \frac{j}{2} \frac{\eta_0}{\lambda} \frac{e^{-jk_0 R}}{R} \int_{-A/2}^{A/2} \int_{-B/2}^{B/2} \left[\mathbf{J_s} - \left(\mathbf{J_s} \cdot \hat{a}_R \right) \hat{a}_R \right] \sqrt{1 + \frac{y^2}{4F_c^2}} e^{jk_0 \vec{r} \cdot \hat{a}_R} dx dy \tag{5.13}$$

Based on the above analytical equations, a MATLAB routine is written to evaluate the far-field components of the parabolic-cylindrical reflector fed by the phased array antenna. Two cases are investigated: (1) symmetric parabolic-cylindrical reflector and (2) offset parabolic-cylindrical reflector of size $A \times B$ = 50 cm × 50 cm and f/D = 0.4. The results for the current distribution, broadside radiation pattern and the beam steering patterns of the symmetric parabolic-cylindrical reflector are shown in Fig. 5.5, Fig. 5.6 and Fig. 5.7, respectively. A stable and symmetric radiation pattern is obtained across the frequency range. For brevity, the computed results are only shown at 13 GHz. The analytically computed 3 dB beamwidth of the symmetric parabolic-cylindrical reflector is 12° and 4.2° along the ϕ = 0° and ϕ = 90° plane, respectively. The cross-polarization isolation is 40 dB at 13 GHz. The co-polarization and cross-polarization beam steering patterns of the reflector corresponding to the different scan angles from the phased array feed source is shown in Figs. 5.7(a) and 5.7(b). The beam steering of about ±35° is achieved for a 3 dB gain reduction.

The computed results for the current distribution, broadside radiation pattern and the beam steering patterns of the offset parabolic-cylindrical reflector fed by the 8 × 4 phased array antenna is shown in Fig. 5.8, Fig. 5.9 and Fig. 5.10, respectively. The analytically computed 3 dB beamwidth of the offset parabolic-cylindrical reflector is 12° and 4° along the ϕ = 0° and ϕ = 90° plane, respectively. The offset arrangement leads to an increase in the cross-polarization level compared to the symmetric reflector. The cross-polarization isolation decreases to 20 dB for the beam scan angle of ±35°. The beam steering range for both the symmetric and offset reflector is limited by its dimension, *A*, along the cylindrical axis.

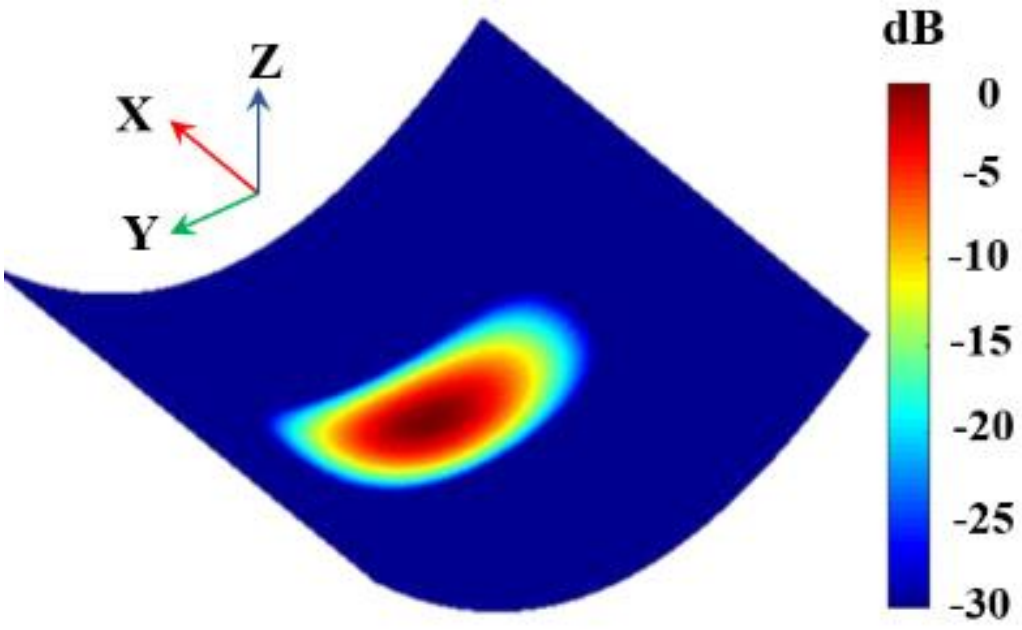

(a)

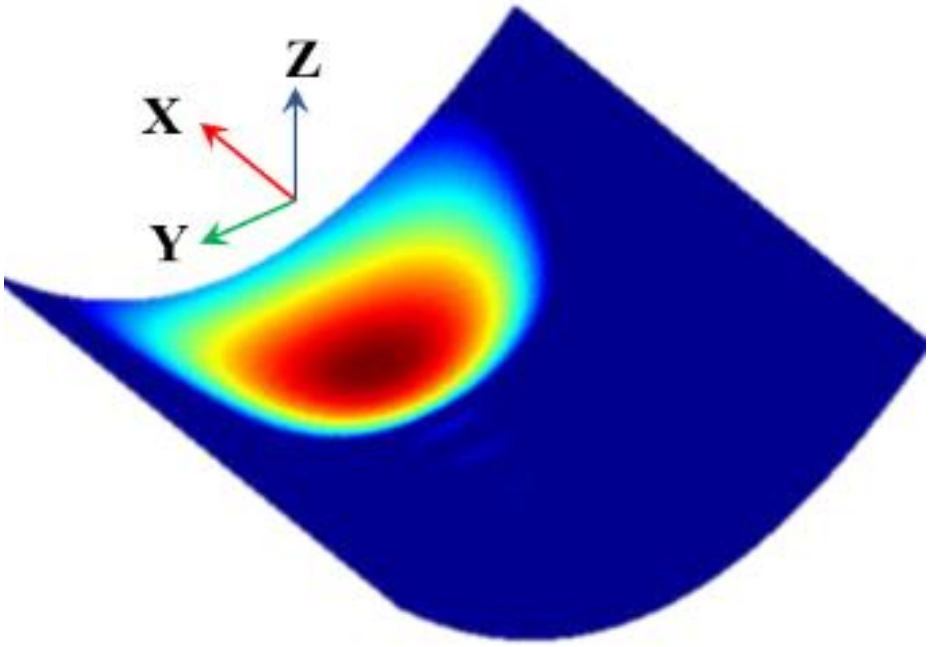

(b)

Figure 5.5 PO computed current density using MATLAB for the symmetric parabolic-cylindrical reflector fed by 8 × 4 phased array antenna at 13 GHz (a) Broadside angle, and (b) 30° beam scan angle.

There is a steep increase in the spillover loss after the ±35° beam scan angle due to the limited size of the reflector (A = 50 cm). As a result, the gain drops, and the radiation pattern degrades for large steering angles. The beam steering range can be further increased by increasing the dimension of the reflector without increasing the spillover loss. For instance, with A = 75 cm reflector, the beam steering can be achieved till ± 40° for a 3 dB reduction in the gain. For the sake of brevity, the result for A = 75 cm is not discussed in further detail. The computed 3 dB beamwidth and cross-polarization isolation of the reflector as a function of frequency is depicted in Fig. 5.11.

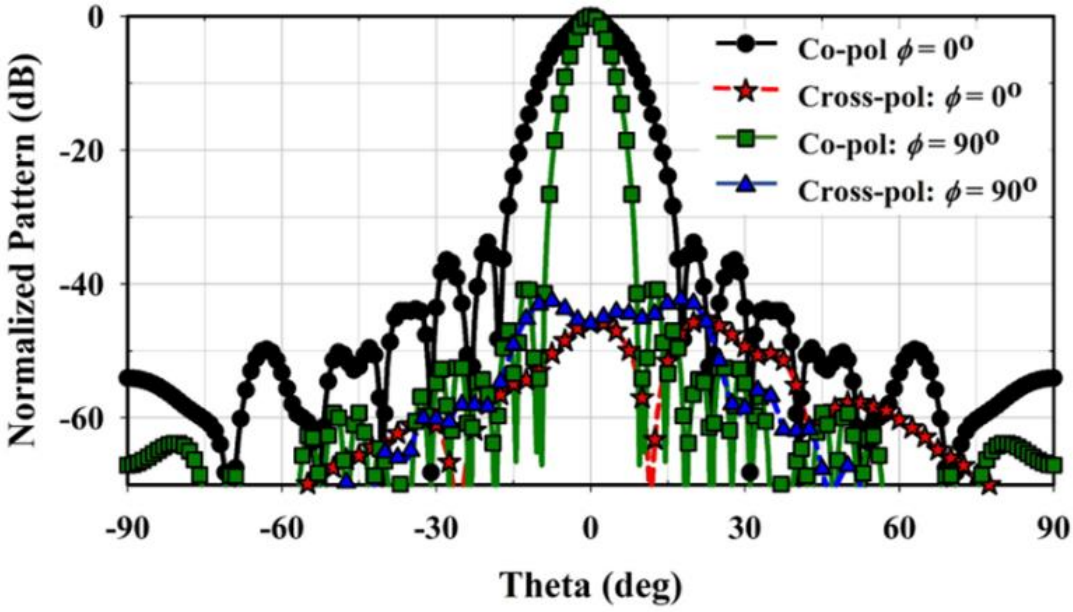

Figure 5.6 PO computed broadside 2D normalized radiation pattern of the symmetric parabolic-cylindrical reflector fed by an 8 × 4 phased array antenna at 13 GHz.

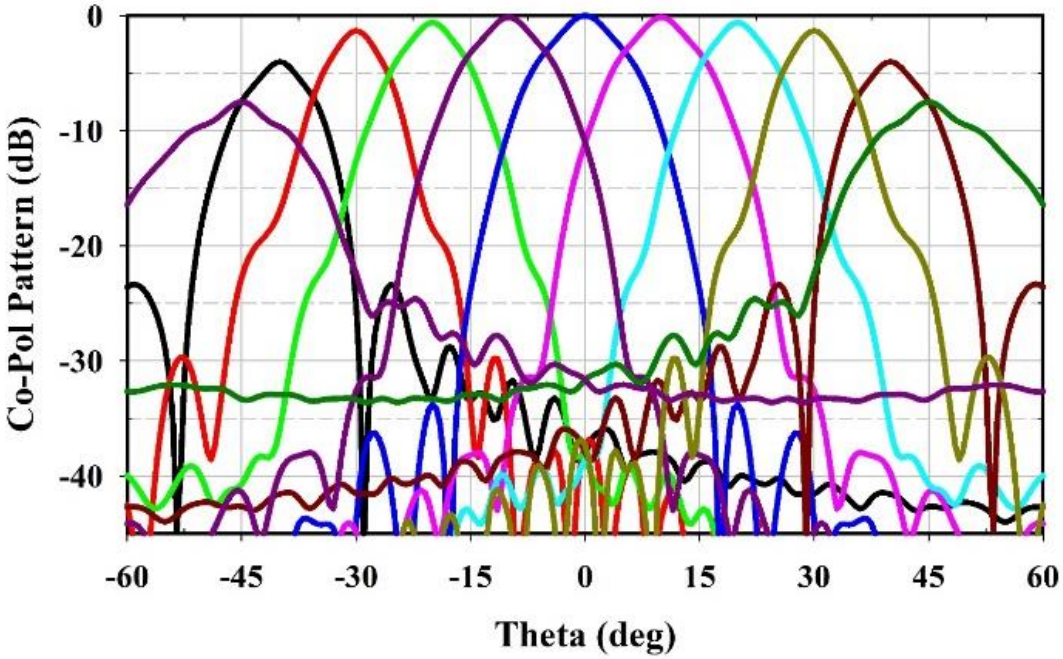

(a)

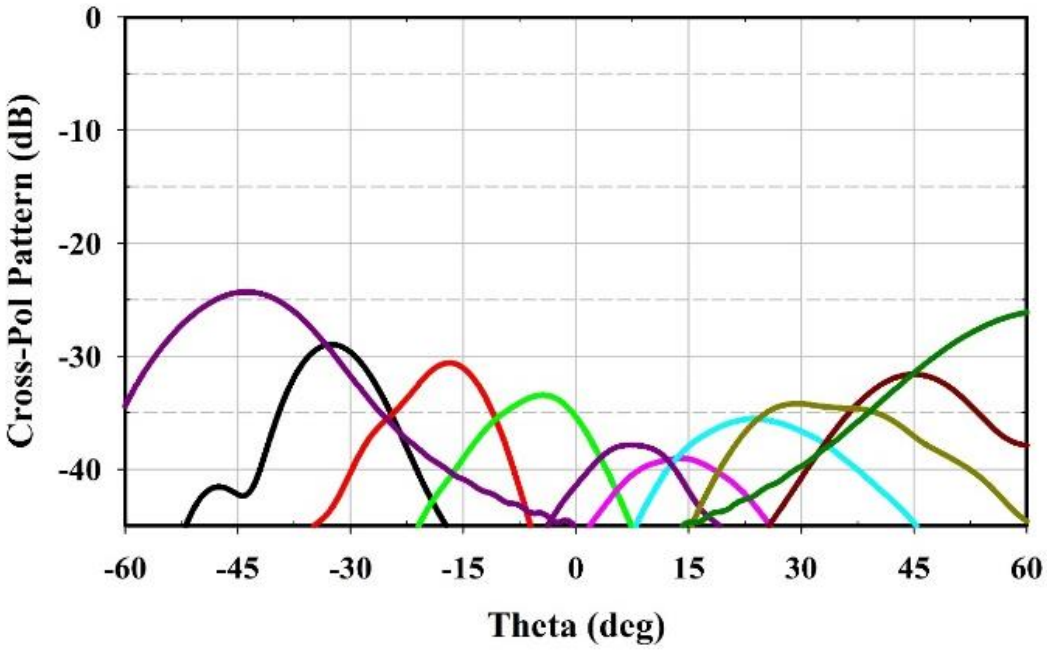

(b)

Figure 5.7 PO computed symmetric parabolic-cylindrical reflector (A = 50 cm) beam steering at 13 GHz (a) Co-polarization beam steering, and (b) Cross-polarization beam steering normalized with respect to the broadside gain.

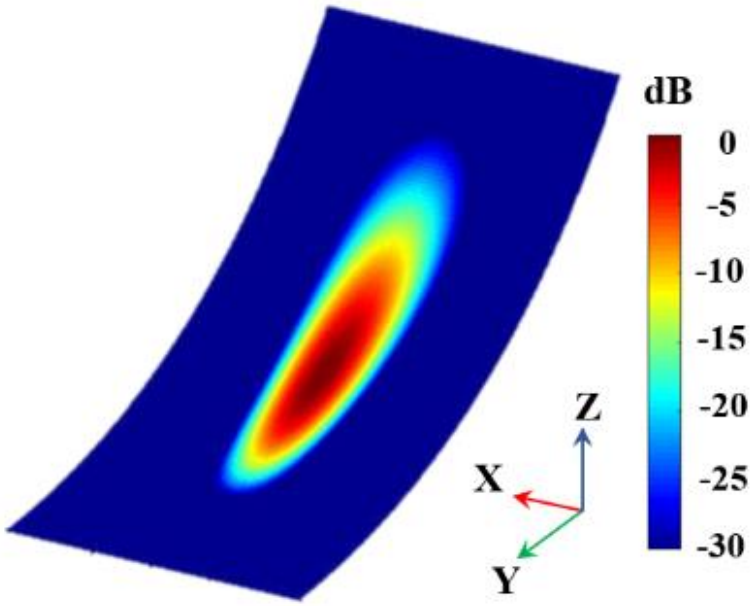

(a)

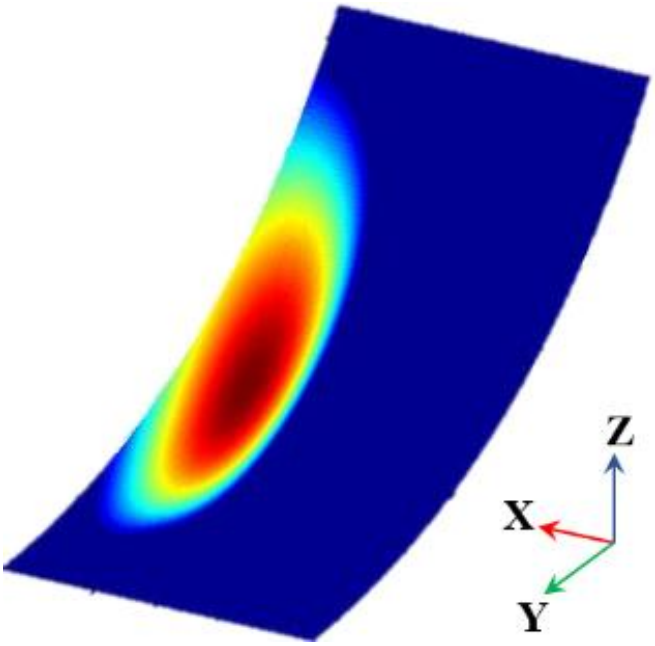

(b)

Figure 5.8 PO computed current density using MATLAB for the offset parabolic-cylindrical reflector fed by 8 × 4 phased array antenna at 13 GHz (a) Broadside angle, and (b) 30° beam scan angle.

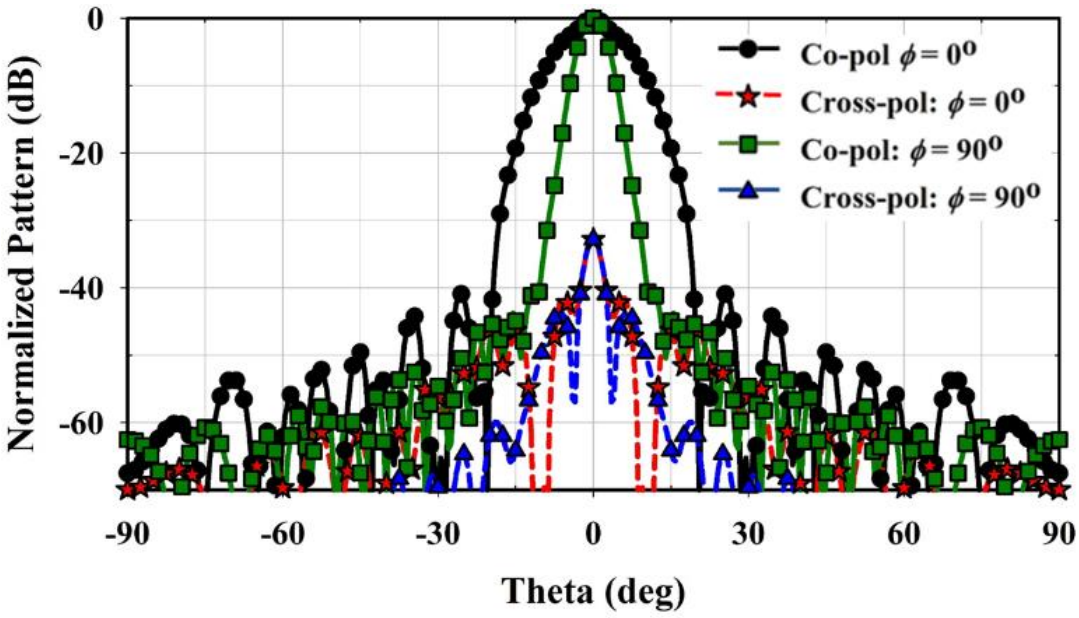

Figure 5.9 PO computed broadside 2D normalized radiation pattern of the offset parabolic-cylindrical reflector fed by an 8 × 4 phased array antenna at 13 GHz.

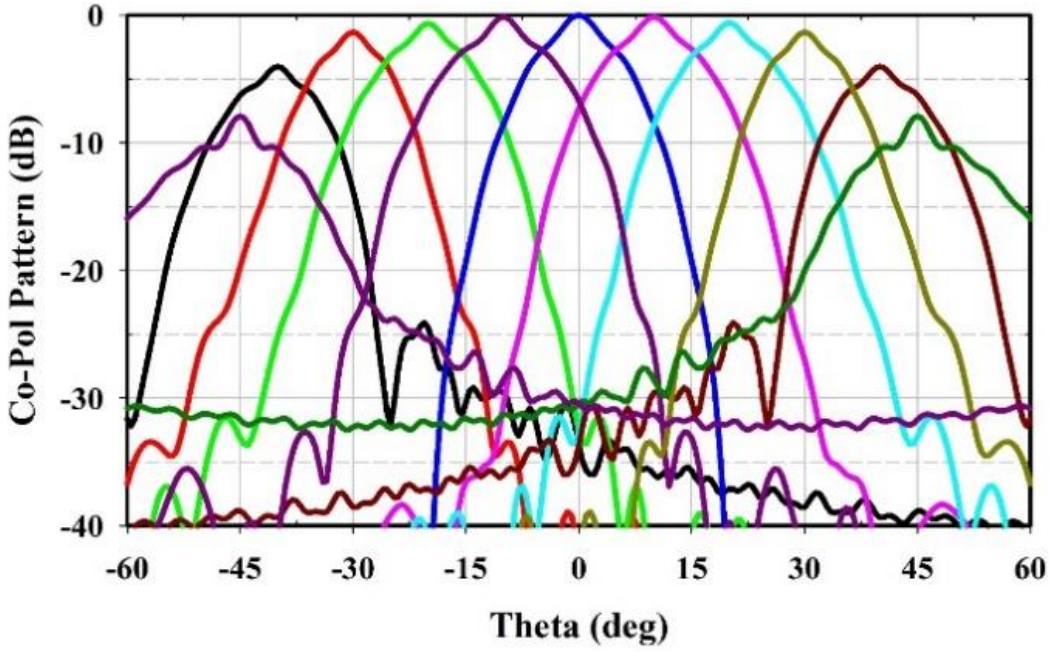

(a)

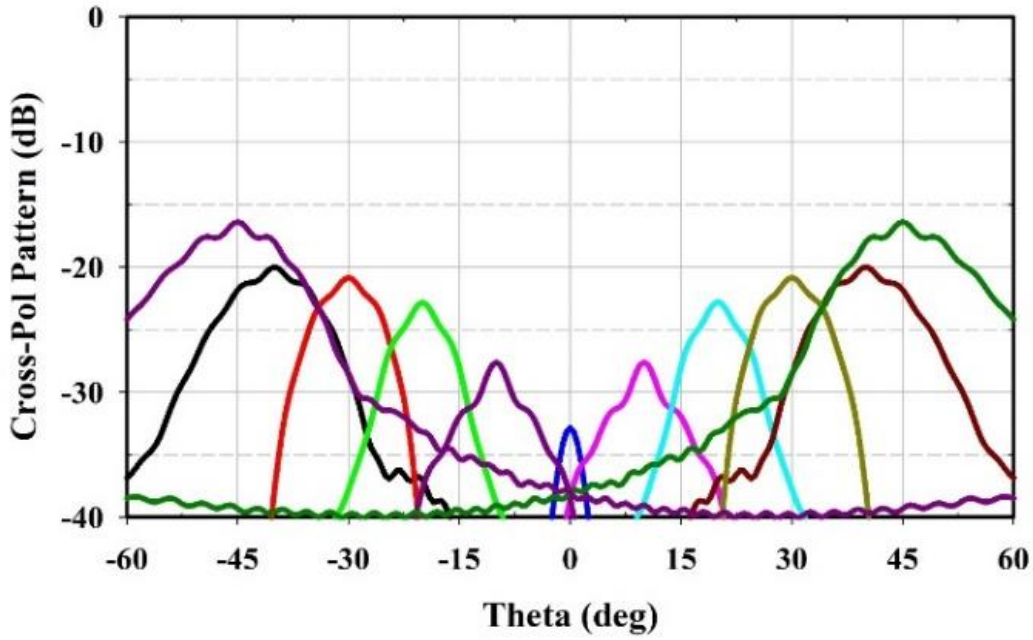

(b)

Figure 5.10 PO computed offset parabolic-cylindrical reflector (A = 50 cm) beam steering at 13 GHz (a) Co-polarization beam steering, and (b) Cross-polarization beam steering normalized with respect to the broadside gain.

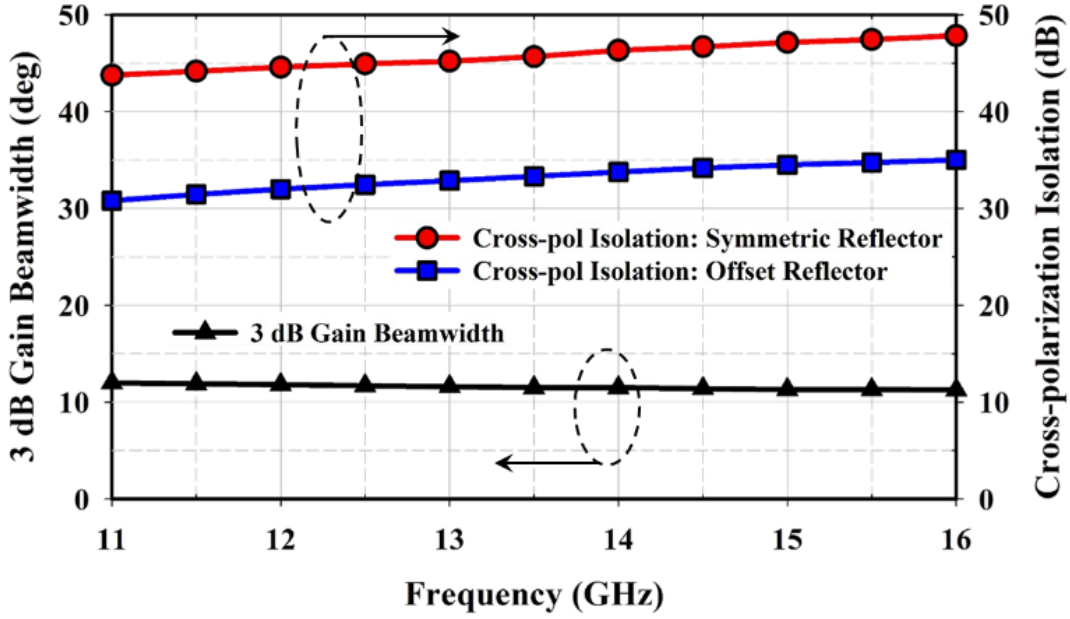

Figure 5.11 PO computed 3 dB gain beamwidth and cross-polarization isolation vs. frequency at the broadside angle for the symmetric and offset parabolic-cylindrical reflector using MATLAB.

The PO computed cross-polarization isolation for the offset parabolic-cylindrical reflector is shown in Table 5.1. It is observed that the cross-polarization isolation decreases with increasing the beam scan angle and increases with increasing the frequency. The computational aspect of the PO analysis is shown in Table 5.2. For mesh size less than $0.2\lambda \times 0.2\lambda$, the convergence error is less than 1.5%. By decreasing the mesh size further leads to a small improvement in the convergence accuracy but at the cost of increased execution time. As a result, for an acceptable convergence error of less than 1.5%, the mesh size of the order of $0.2\ \lambda \times 0.2\lambda$ should be sufficient. The cross-polarization isolation varies by 0.4 dB for different mesh sizes of the reflector.

Table 5.1 PO computed cross-polarization isolation at different beam scan positions as a function of frequency for offset parabolic-cylindrical reflector

Frequency (GHz)	**Cross-polarization Isolation (dB)**		
	Broadside	**15° scan**	**30° scan**
11	30.79	23.21	19.58
13	32.88	24.82	20.85
16	35	26.38	22.35

Table 5.2 Execution time and convergence error for the PO analysis of the offset parabolic-cylindrical reflector for different mesh sizes.

Reflector size = 21.67λ at 13 GHz			
Maximum mesh size	**Convergence error magnitude**	**Execution time (min.)**	**Cross-pol isolation (dB)**
0.75λ × 0.75λ	131.05	0.33	32.52
0.5λ × 0.5λ	3.51	0.45	32.88
0.25λ × 0.25λ	0.15	1.05	32.86
0.2λ × 0.2λ	0.012	1.32	32.88
0.1λ × 0.1λ	0.018	4.88	32.90
0.05λ × 0.05λ	0.0098	36.77	32.92

5.3 RFIC Beamforming Chipset Based Flat Panel Phased Array Antenna

5.3.1 Proposed Dual Linear-Polarized Stacked Patch Unit Element

The unit-element geometry, feeding mechanism, and side-view of the dual linearly-polarized stacked patch antenna are shown in Figs. 5.12(a), 5.12(b), and 5.12(c), respectively. The S-parameters of the proposed dual linear-polarized stacked patch antenna is shown in Fig. 5.12(d). A stacked patch antenna configuration is analyzed and optimized to increase the impedance matching bandwidth and to achieve dual linear-polarization. The antenna is designed on Rogers RO4350 substrate with $\varepsilon_r = 3.66$ and is analyzed using Ansys HFSS. The dimension of the driven patch is L_p = 173.6 mil, and the size of the parasitic patch is U_p = 152.2 mil. In the feeding mechanism (Fig. 5.12(b)) for the dual linearly-polarized stacked patch antenna, the coplanar

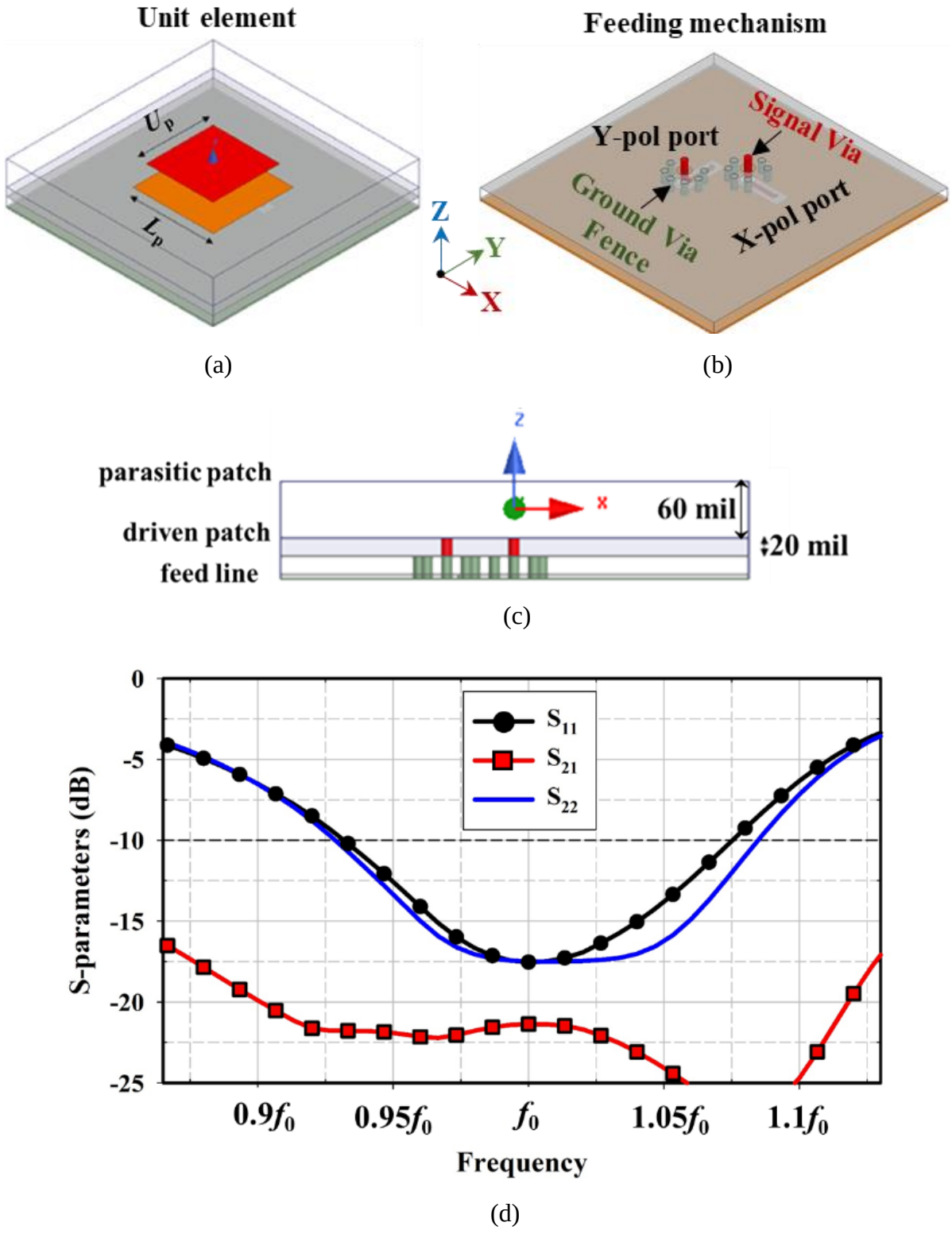

Figure 5.12 (a) Unit element geometry, (b) Feeding mechanism, (c) Side-view, and (d) Simulated S-parameters of the proposed dual linear-polarized stacked patch antenna at *Ku*-band.

waveguide (CPW) transmission lines excite the driven patch element through the signal via. Ground via fencing is implemented around the signal via to ensure proper characteristics impedance of the transmission line and port-to-port isolation. The effects of the stack-up layers and via fencing are considered in the full-wave analysis of the unit element. The impedance matching bandwidth ($|S_{11}| < -10$ dB) is around 2 GHz in the *Ku*-band (fractional bandwidth ≈ 15%), and the mutual coupling between the ports is less than 22 dB.

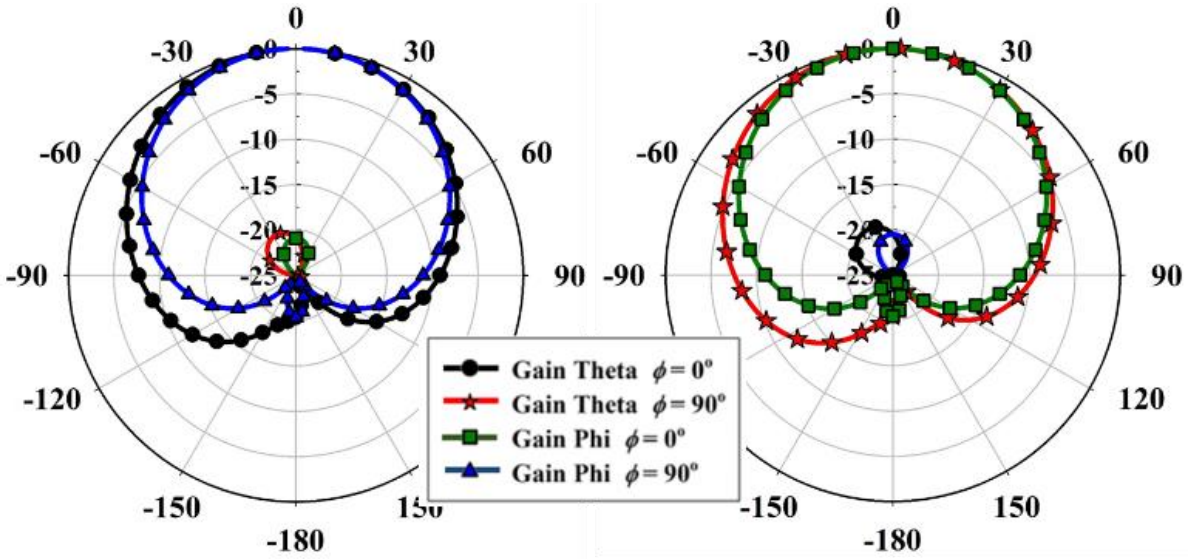

(a) (b)

Figure 5.13 The simulated normalized gain pattern of the stacked patch unit element for (a) X-polarization, and (b) Y-polarization at f_0 = 13 GHz.

Fig. 5.13 shows the normalized gain radiation pattern for the X-polarization and Y-polarization, respectively, at 13 GHz. The average peak realized gain is 5 dBi, and the cross-polarization isolation is 20 dB. An infinite array analysis is also carried on the proposed dual-polarized stacked patch unit cell. The corresponding active S-parameter of the proposed dual linear-polarized stacked patch antenna for different scan angles is presented in Fig. 5.14. It is

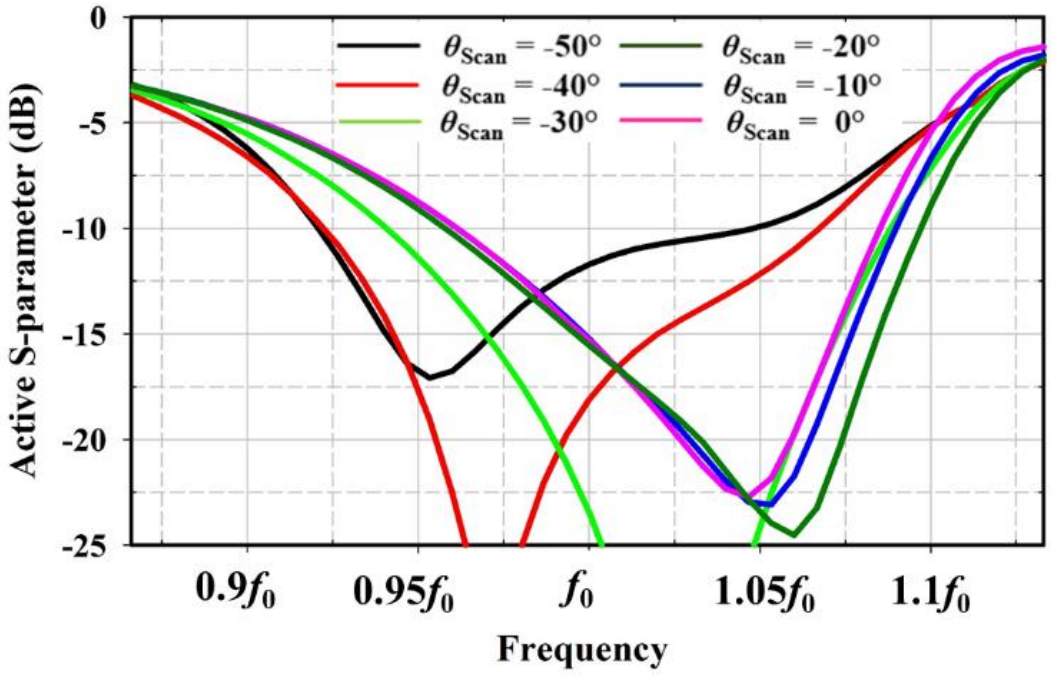

Figure 5.14 Simulated active S-parameters of the proposed dual linear-polarized stacked patch antenna for different scan angles.

observed that the fractional bandwidth is maintained at around 15% up to scan angle of -40° and reduces to about 12% for scan angle of -50°.

5.3.2 8 × 4 Array Aperture and Integrated Beamforming Network

The dual linear-polarized stacked patch antenna is used as an element of the 8 × 4 phased array antenna with the inter-element spacing of $dx = dy = 12$ mm, as presented in Fig. 5.15. The proposed dual-linear polarized stacked patch antenna with the beamforming network is prototyped at *Ku*-band to provide the beam steering range of ±45° for a 3 dB reduction in the gain. Anokiwave AWMF-0117 integrated silicon core chips are used in the beamforming network for achieving the beam steering. This chipset is a single-element transmit/receive (T/R) chip that can support dual-polarization and operates between 10.5 – 16 GHz. The chip size is 2.5 mm × 2.5 mm with a flip-

chip package and features half-duplex operations with +20 dB transmit channel gain, +28 dB receive channel gain, 3 dB noise figure, 6-bit amplitude, and 6-bit phase controls. The power consumption is 200 mW on receive and 250 mW on the transmit mode per chip. In this research, the radiation performance measurements are only performed in the Rx mode as antennas are reciprocal. The Tx effective isotropic radiated power (EIRP) measurement was not an emphasis on this work.

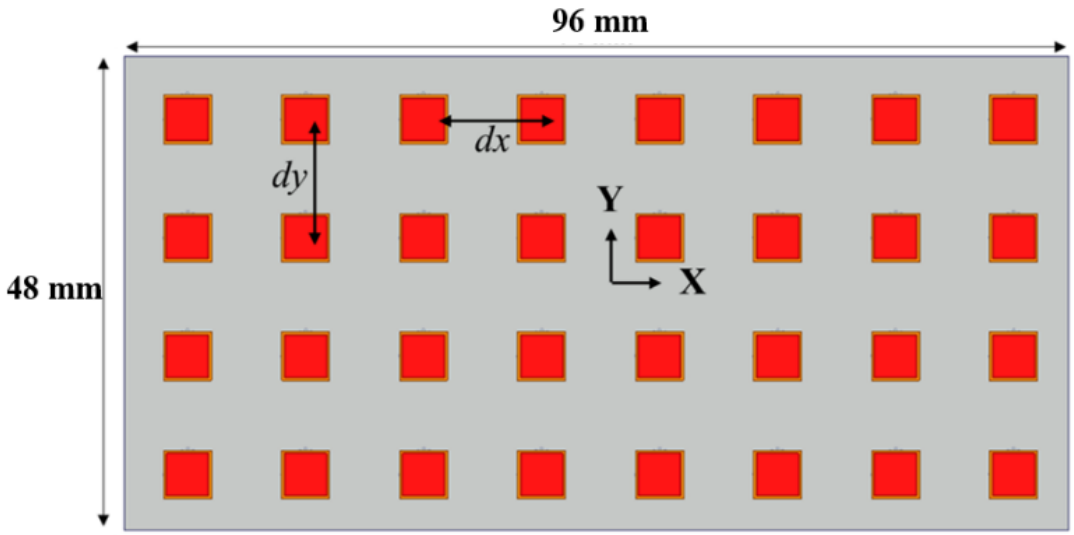

Figure 5.15 Proposed 8 × 4 dual linear-polarized stacked patch phased array antenna.

Fig. 5.16(a) shows the multilayer stack-up of the dual linear-polarized stacked patch antenna designed in Altium and Fig. 5.16(b) shows the photograph of the fabricated phased array with the beamforming network. The effect of the multilayer stack-up is considered in the full-wave analysis of the phased array. The 8 × 4 array utilizes a stripline corporate feed network using Wilkinson combiners. Embedded *NiCr* thin-film resistors are used as the feed network resides in between the dielectric layers. Via fencing is implemented on the stripline layer to ensure proper characteristic impedance of the transmission lines. The functional block diagram of the proposed phased array antenna and the test setup used to characterize the array is shown in Fig. 5.17. The

beamforming network on the board includes a serial peripheral interface (SPI) programmable integrated phase and amplitude shifting components on the silicon-core Anokiwave chips that are

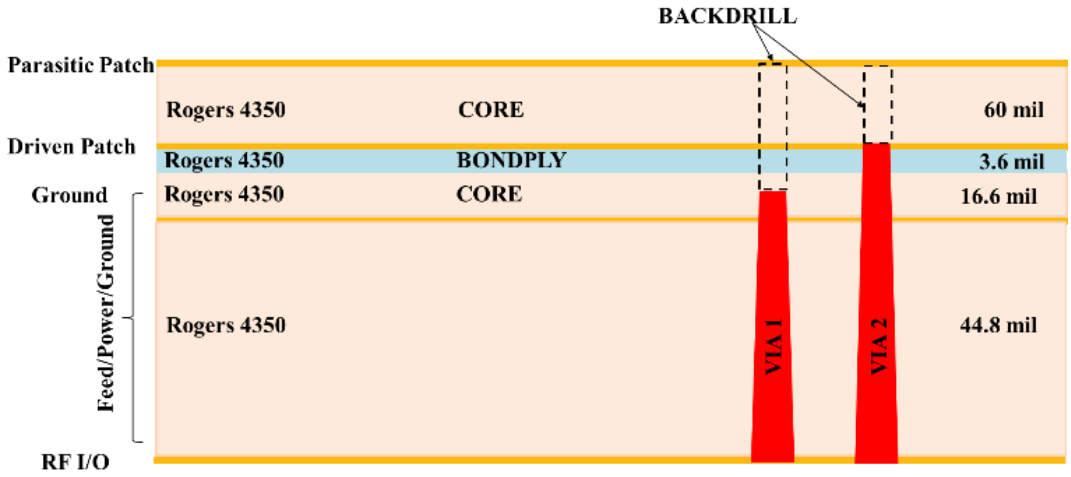

(a)

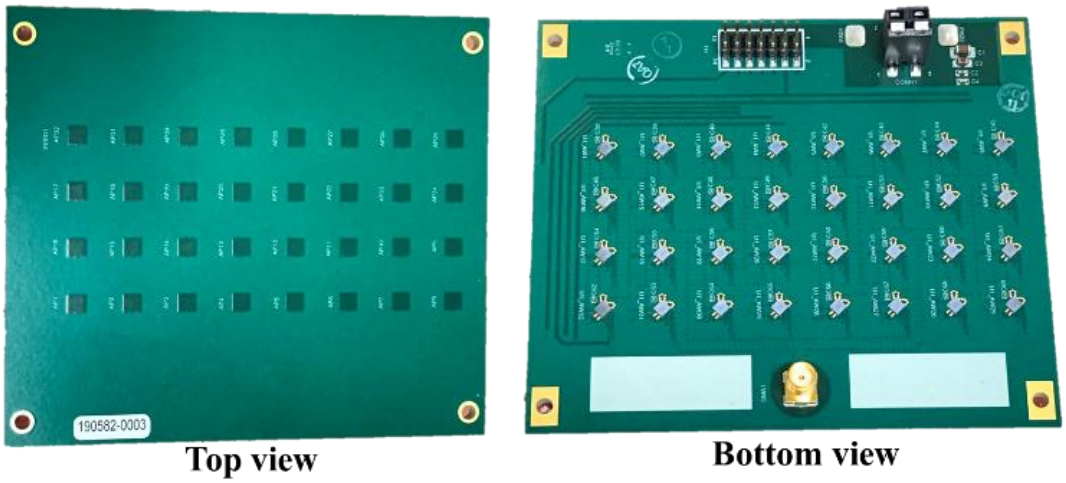

(b)

Figure 5.16 (a) Multilayer stack-up of the phased array board (b) Photograph of fabricated dual linear-polarized phased array antenna integrated with the Anokiwave AWMF-0117 silicon RFIC chips based beamforming network.

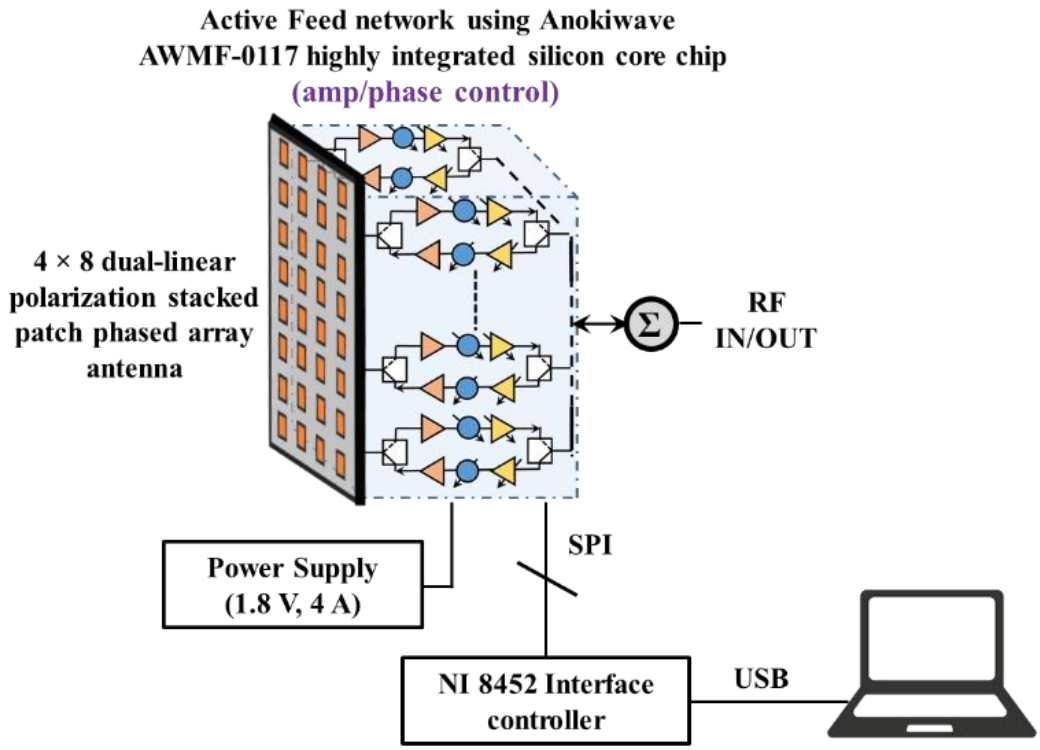

Figure 5.17 Functional block diagram for the measurement of the phased array antenna.

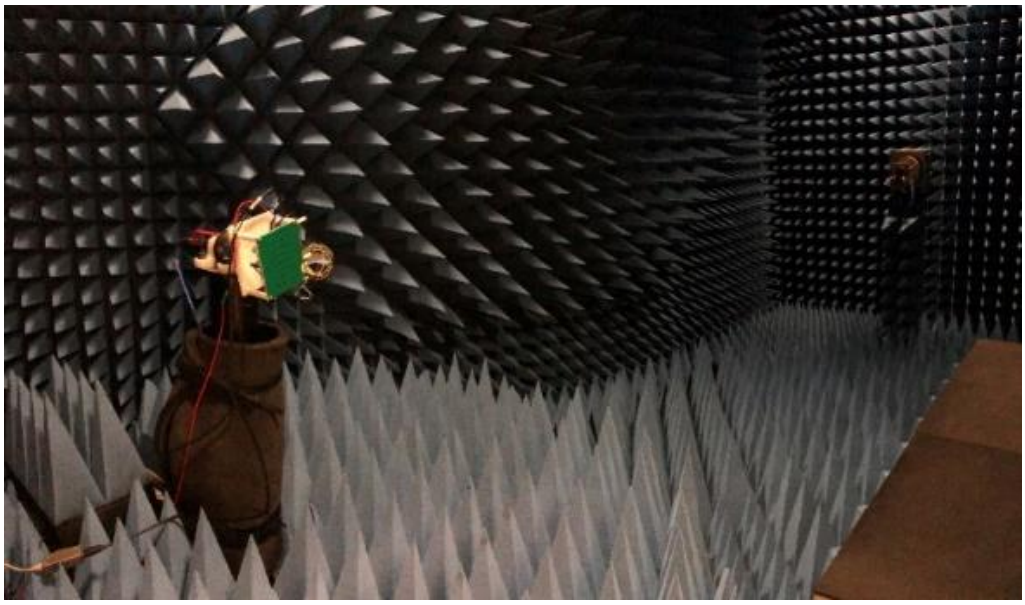

Figure 5.18 Far-field anechoic measurement chamber (800 MHz – 40 GHz) facility at the AML laboratory at SDSU.

controlled from a remote computer. A National Instrument NI 8452 interface controller is used to translate messages from the laptop's universal serial bus (USB) interface to the SPI interface. The radiation pattern of the phased array is measured in the far-field anechoic chamber at the Antenna and Microwave Laboratory (AML) at San Diego State University (SDSU), as depicted in Fig. 5.18.

The simulated and measured broadside normalized radiation pattern of the phased array antenna at 13 GHz is shown in Fig. 5.19(a) and Fig. 5.19(b) for the X-polarization and Y-polarization, respectively. A Taylor distribution with a sidelobe level of -30 dB is used to generate the appropriate amplitude excitation weights. The simulated broadside 3 dB beamwidth at 13 GHz for the phased array antenna in the ϕ = 0° plane is 14° for both the X-polarization and Y-polarization and the simulated 3 dB beamwidth in the ϕ = 90° plane is 26° for both X-polarization and Y-polarization. The corresponding measured 3 dB beamwidth in the ϕ = 0° plane is 15° for both the X-polarization and Y-polarization, and the measured 3 dB beamwidth in the ϕ = 90° plane is 26° and 28° for X-polarization and Y-polarization, respectively.

A stable, consistent radiation pattern is observed across the bandwidth from 12 – 14 GHz. However, the results are only shown at 13 GHz for brevity. The simulated and measured co-polarization and cross-polarization beam steering response of the phased array for the X-polarization is presented in Figs. 5.20(a) and 5.20(b), respectively. The simulated and measured beam steering response of the phased array for the Y-polarization is presented in Figs. 5.21(a) and 5.21(b), respectively. Both the polarizations show simulated and measured scan range of ±45° for 3 dB reduction in the gain. The discrepancy in the simulated and measured scan loss at large scan angles can be attributed to possible higher active reflection coefficients in the fabricated prototype and measurement uncertainties.

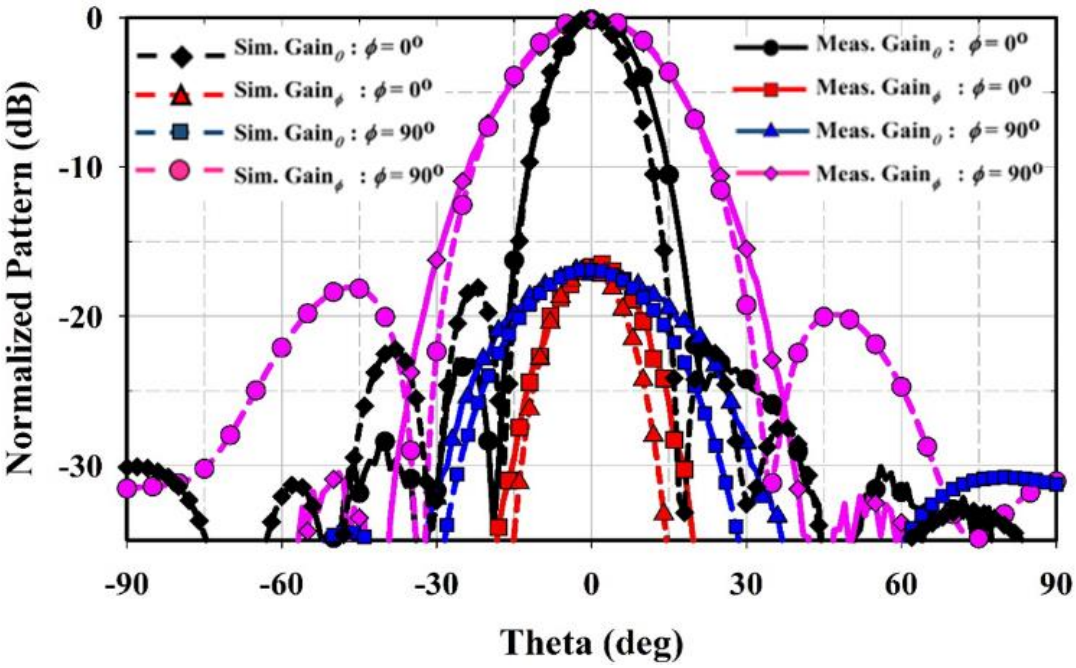

(a)

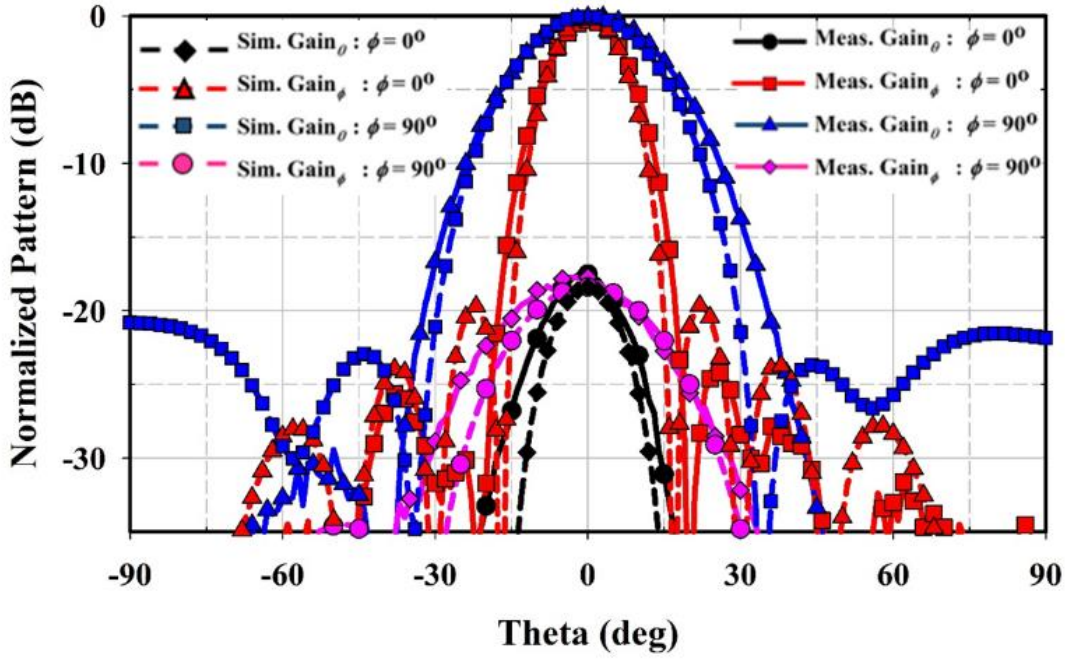

(b)

Figure 5.19 Simulated and measured broadside normalized radiation pattern of the 8 × 4 dual-polarized stacked patch phased array antenna at 13 GHz for (a) X-polarization, and (b) Y-polarization.

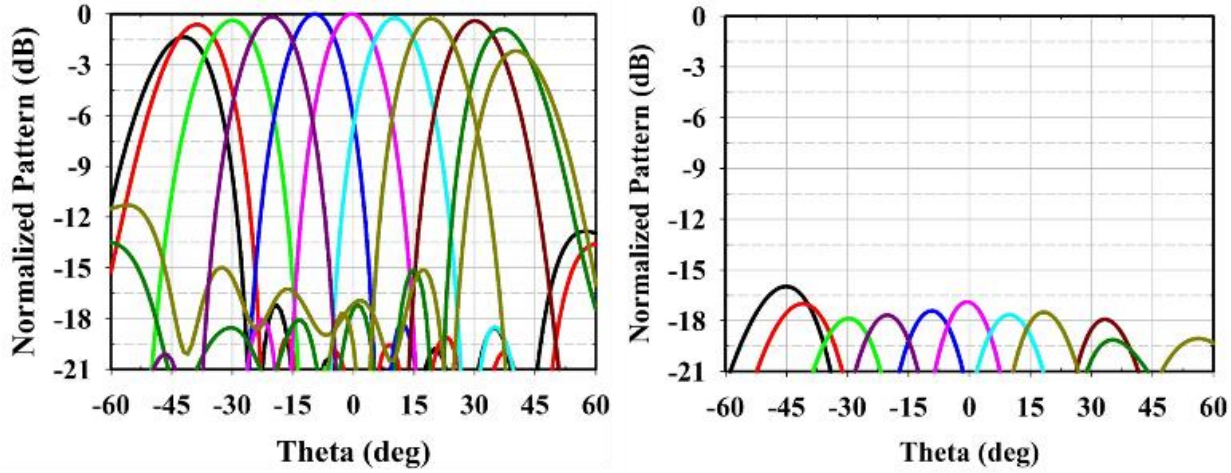

(a)

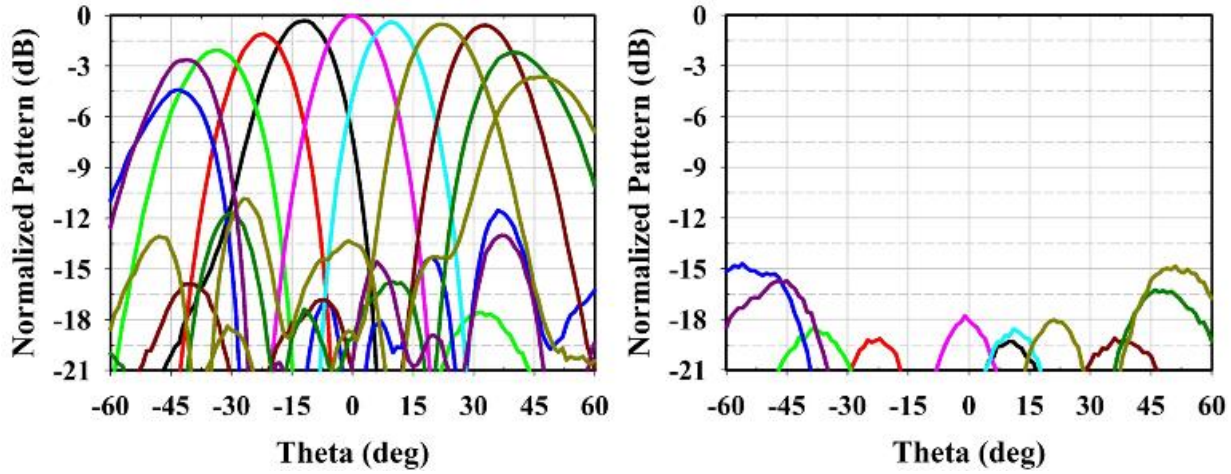

(b)

Figure 5.20 Co-polarization and cross-polarization normalized beam steering radiation pattern of the 8 × 4 dual-polarized stacked patch phased array antenna at 13 GHz for X-polarization (a) Simulation, and (b) Measurement.

The peak simulated realized gain of the phased array antenna is 19 dBi and 19.5 dBi for the X-polarization and Y-polarization, respectively. The measurement of the realized gain requires the separate characterization of the beamforming network. Since the beamforming board was integrated with the phased array aperture, the beamforming board could not be calibrated separately and thus the measured results of the phased array only show the uncalibrated normalized

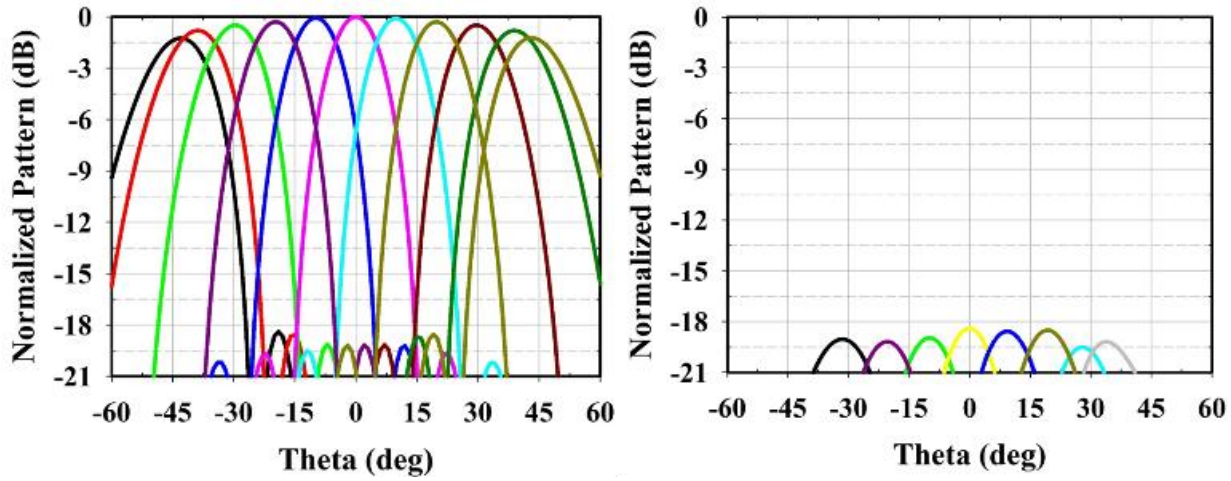

(a)

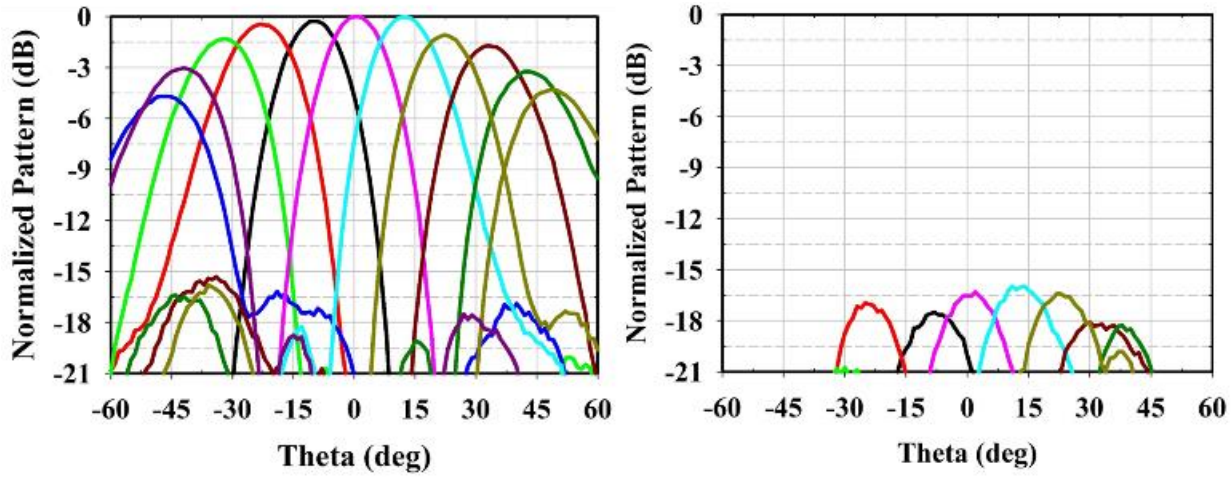

(b)

Figure 5.21 Co-polarization and cross-polarization normalized beam steering radiation pattern of the 8 × 4 dual-polarized stacked patch phased array antenna at 13 GHz for Y-polarization (a) Simulation, and (b) Measurement.

gain. The simulated realized gain for the phased array antenna and the simulated and measured 3 dB beamwidth for different scan angles for the X-polarization and Y-polarization are shown in Fig. 5.22. The simulated antenna efficiency of the proposed phased array antenna is more than 85% for both the X-polarization and Y-polarization at 13 GHz.

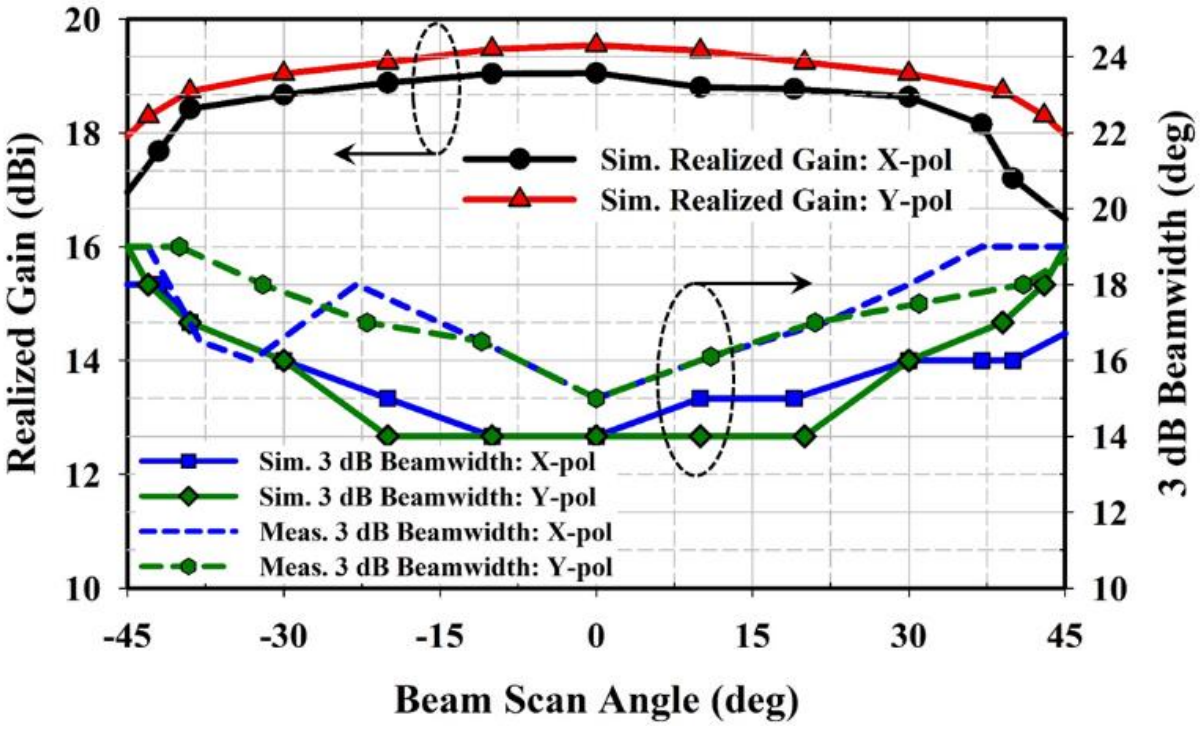

Figure 5.22 The simulated realized gain for the phased array antenna and the simulated and measured 3 dB beamwidth for different scan angles for X-polarization and Y-polarization along $\phi = 0°$ plane.

The measured peak power consumption on the Rx mode of the phased array antenna is 6.3W (3.5A at 1.8V). The temperature measured using the infrared (IR) camera for the phased array system is 58.4°C, as shown in Fig. 5.23. The visible-light image of the phased array is shown in Fig. 5.16(b). It is observed that there are no thermal issues, and the peak power consumption is within the rated power consumption of the chips (0.2W per chip).

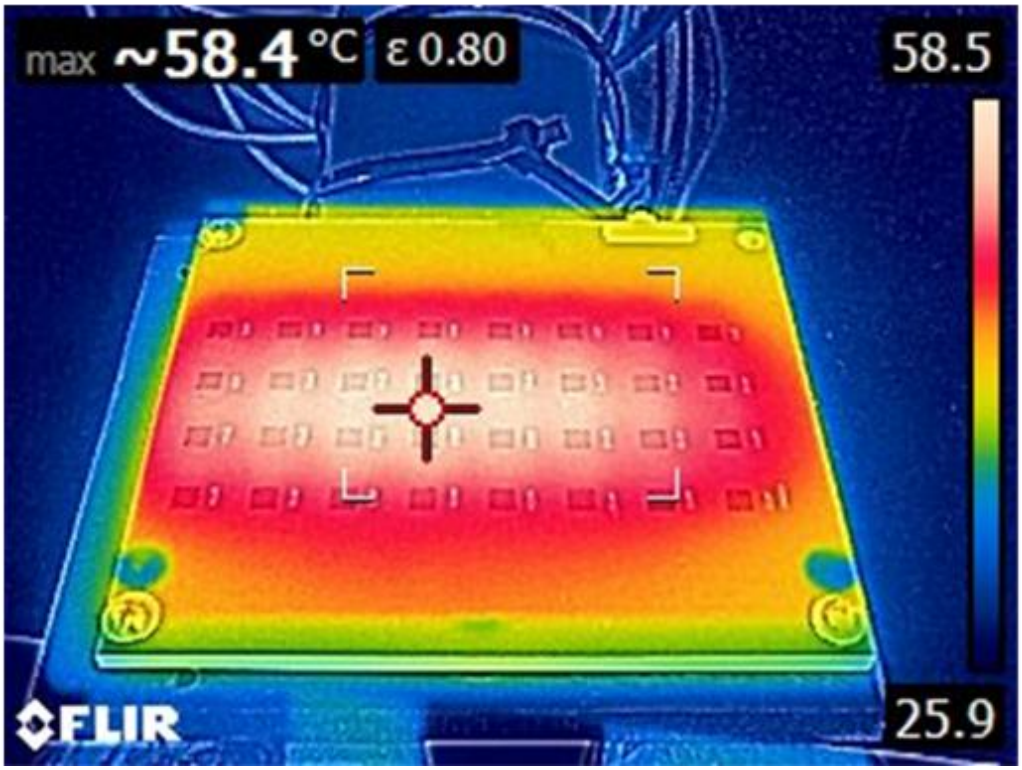

Figure 5.23 Thermal IR imaging of the phased array system.

5.4 Parabolic-cylindrical Reflector integrated with phased array

The proposed phased array antenna is used as a feed source to illuminate the offset parabolic-cylindrical reflector of f/D = 0.4 and a maximum dimension of 50 cm, as illustrated in Fig. 5.24(a). The multilevel fast multipole method (MLFMM) is used along with the method of moments (MoM) in TICRA GRASP to analyze the reflector. Fig. 24(b) shows the simulated current density for the broadside beam analyzed in TICRA GRASP. The parabolic-cylindrical reflector is partially illuminated along the cylindrical axis to accommodate the beams for different beam scan angles. The simulated broadside normalized radiation pattern of the parabolic-cylindrical reflector at 13 GHz is shown in Fig. 5.25(a) and Fig. 5.25(b) for the X-polarization and Y-polarization, respectively.

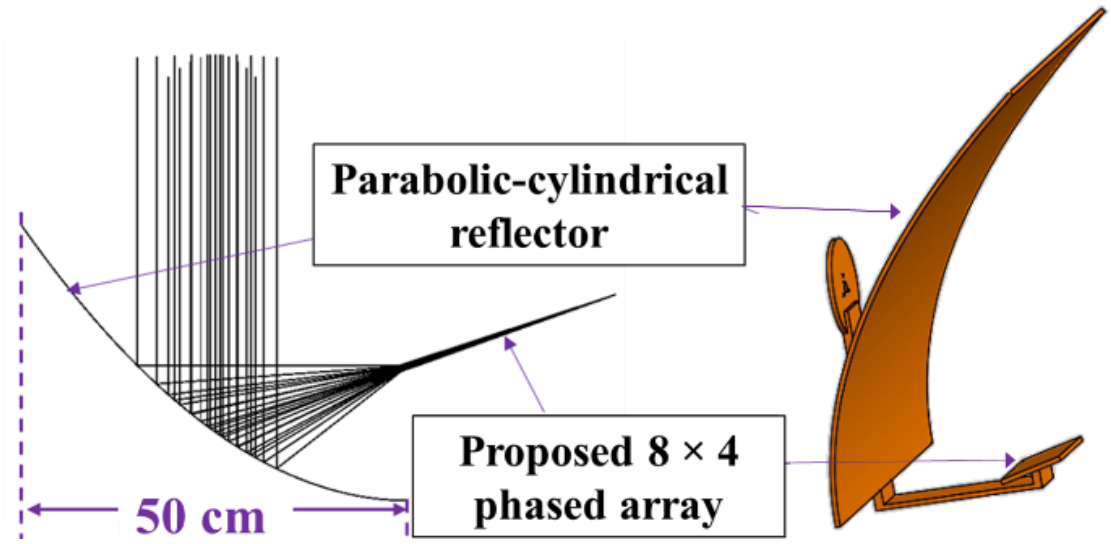

(a)

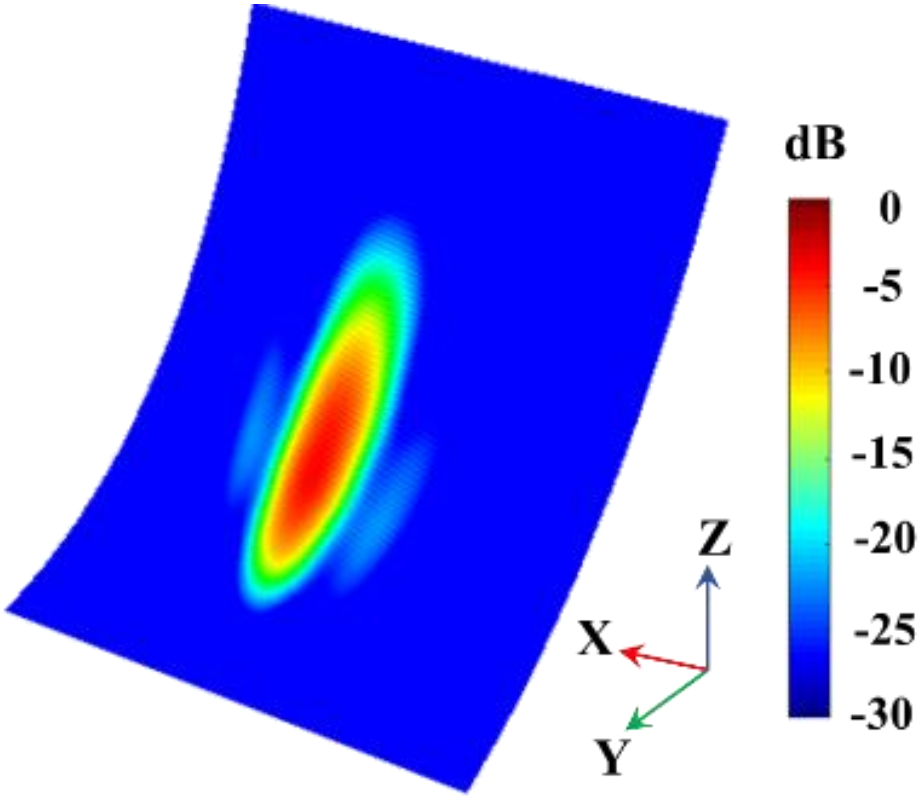

(b)

Figure 5.24 (a) Illustration of the offset parabolic-cylindrical reflector with 8 × 4 phased array as a feed source, and (b) simulated current density on the reflector for broadside beam analyzed using MoM solver in TICRA GRASP.

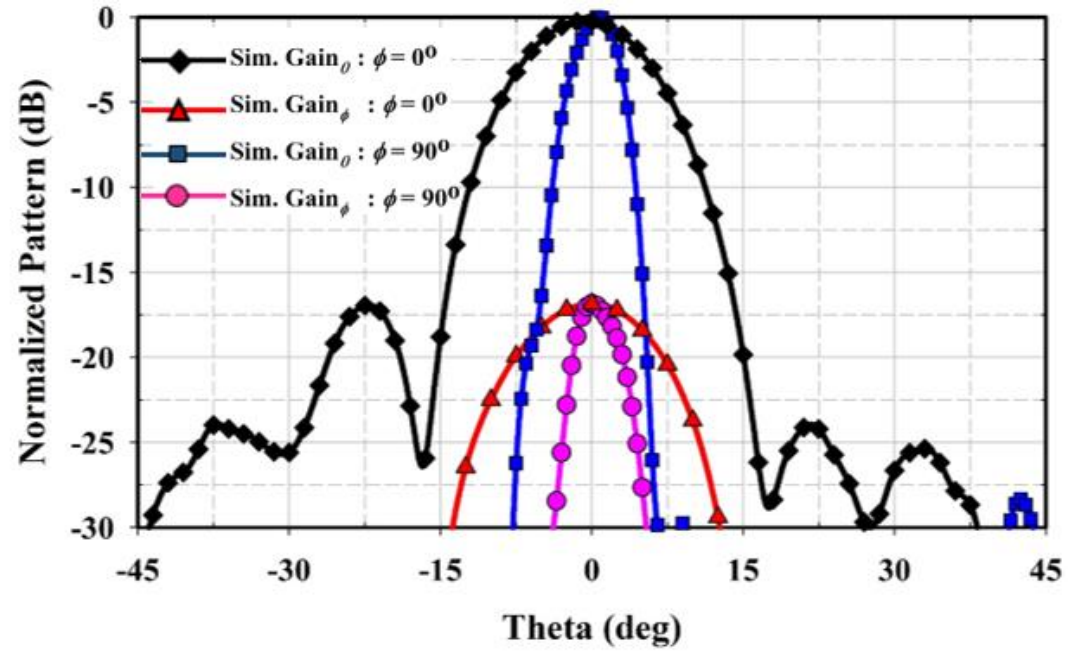

(a)

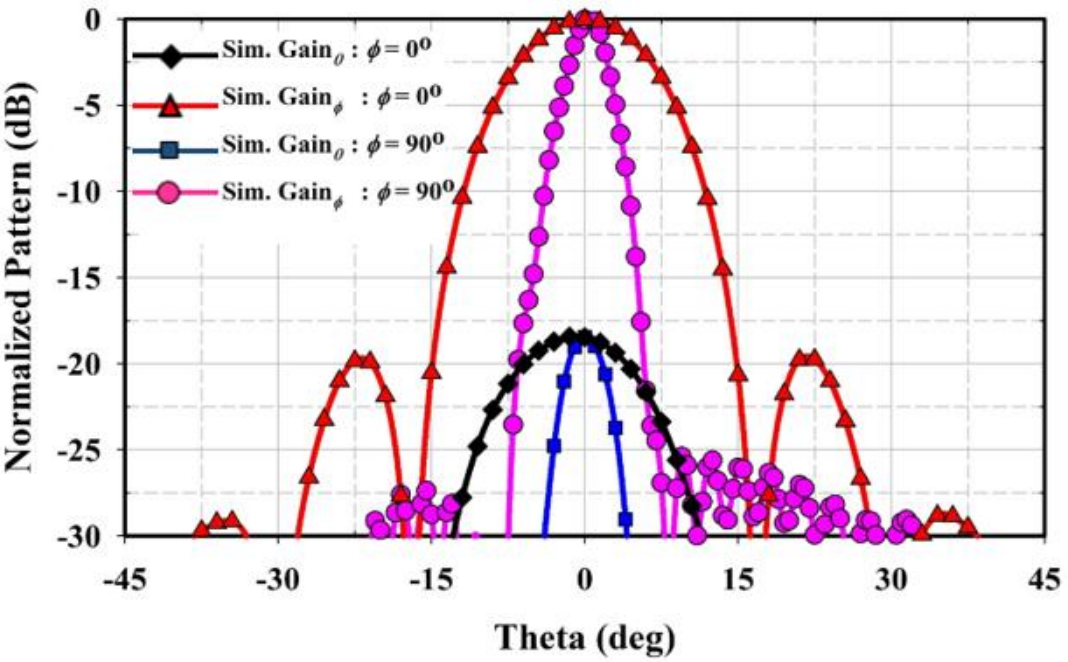

(b)

Figure 5.25 Simulated broadside normalized radiation pattern of the proposed parabolic-cylindrical reflector antenna at 13 GHz for (a) X-polarization, and (b) Y-polarization.

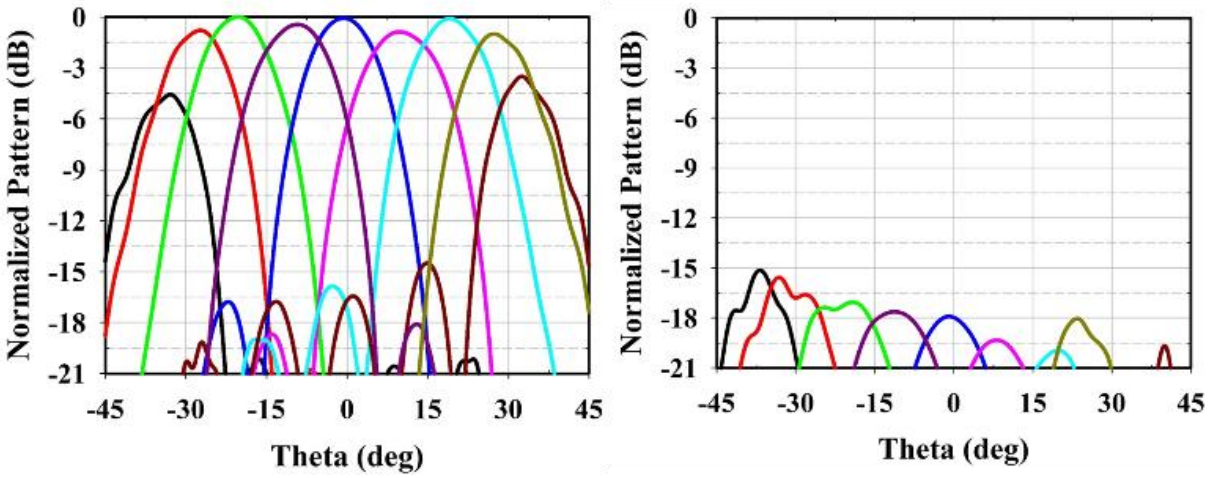

(a)

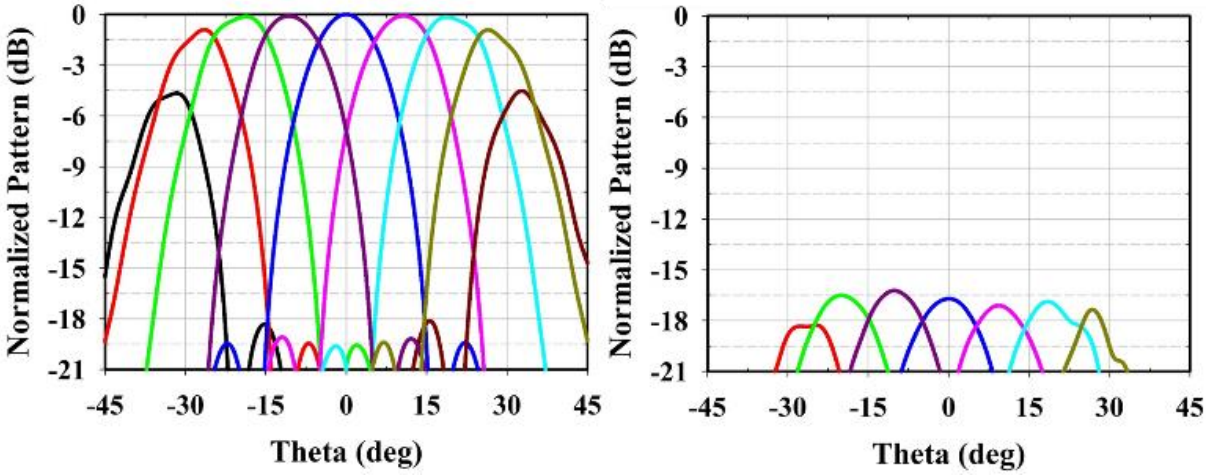

(b)

Figure 5.26 Simulated normalized co-polarization and cross-polarization beam steering radiation pattern of the parabolic-cylindrical reflector along the cylindrical axis for (a) X-polarization, and (b) Y-polarization at 13 GHz.

The simulated broadside 3 dB beamwidth at 13 GHz for the parabolic-cylindrical reflector antenna in the ϕ = 0° plane is 13.5°, and 14.1° for the X-polarization and Y-polarization, respectively and the simulated 3 dB beamwidth in the ϕ = 90° plane is 4.1° and 4° for the X-polarization and Y-polarization, respectively.

The simulated co-polarization and cross-polarization beam steering response of the proposed parabolic-cylindrical reflector of size 50 cm for the X-polarization and Y-polarization are presented in Figs. 5.26(a) and 5.26(b), respectively. Both the polarization show a simulated scan range of about ±30° for a 3 dB reduction in the gain. The simulated spillover losses for the proposed 50 cm offset parabolic-cylindrical reflector fed by the 8 × 4 dual linear-polarized phased array for different scan angles are presented in Table 5.3. As observed from the table, there is a steep increase in the spillover loss after the ±30° beam scan angle due to the limited size of the reflector (A = 50 cm). Thus, the beam steering range can be further increased by increasing the dimension of the reflector without increasing the spillover loss.

Table 5.3 Simulated spillover loss for the proposed 50 cm offset parabolic-cylindrical reflector fed by the phased array antenna for different scan angles analyzed in TICRA GRASP.

Spillover Loss		
Beam scan angle (deg)	**X-polarization (dB)**	**Y-polarization (dB)**
-40	4.14	3.8
-30	0.97	0.96
-20	0.25	0.23
-10	0.12	0.18
0	0.13	0.18
10	0.22	0.18
20	0.25	0.23
30	1.02	0.97
40	3.56	3.81

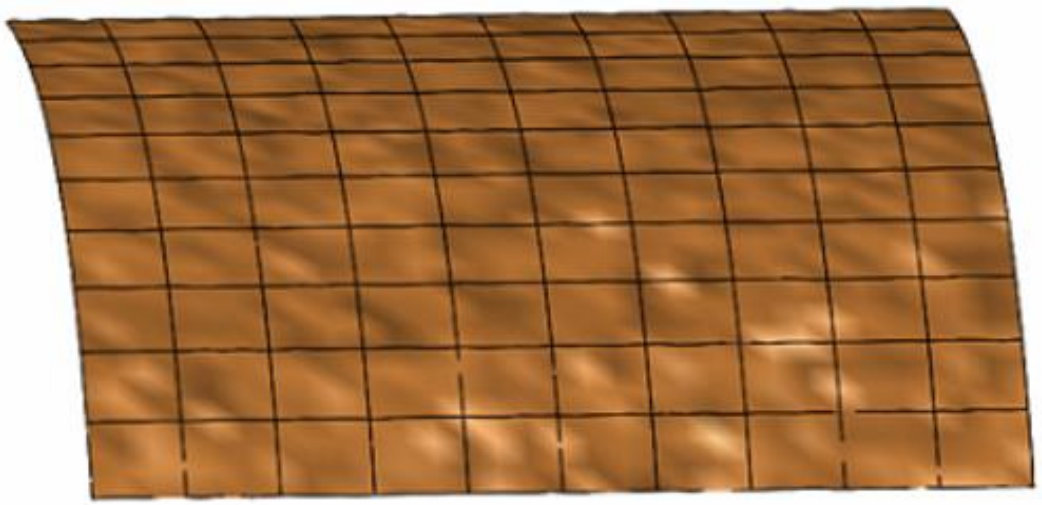

Figure 5.27 Parabolic-cylindrical reflector with random surface RMS of λ/23 (= 1mm) at 13 GHz analyzed in TICRA GRASP.

Random surface errors, which are primarily caused by structural inaccuracies, introduce pattern degradation in the reflector antenna's performance. A standard parameter typically used to characterize the random error is the surface root mean square (RMS) normalized to the wavelength [115]. The geometry of the offset parabolic-cylindrical reflector with surface RMS of λ/23 (= 1mm) at 13 GHz is depicted in Fig. 5.27. It is noted that once the surface RMS error is less than λ/20, not much difference is obtained for the gain loss values of the reflector pattern. The boresight gain loss is only about 0.12 dB for the assumed surface RMS error of 1 mm at 13 GHz.

The parabolic-cylindrical reflector is manufactured using the aluminum sheet metal technique, and Fig. 5.28 shows the photograph of the integrated reflector-phased array prototype. A 3D printed strut support is used to integrate the phased array with the reflector. The strut is fastened to the reflector using flathead surface flushed bolts, as shown in Fig. 5.28. The effects of the strut and the bolts have been analyzed in the modeling of the reflector. The hybrid reflector-phased array beam steering radiation pattern is characterized in the compact antenna test range

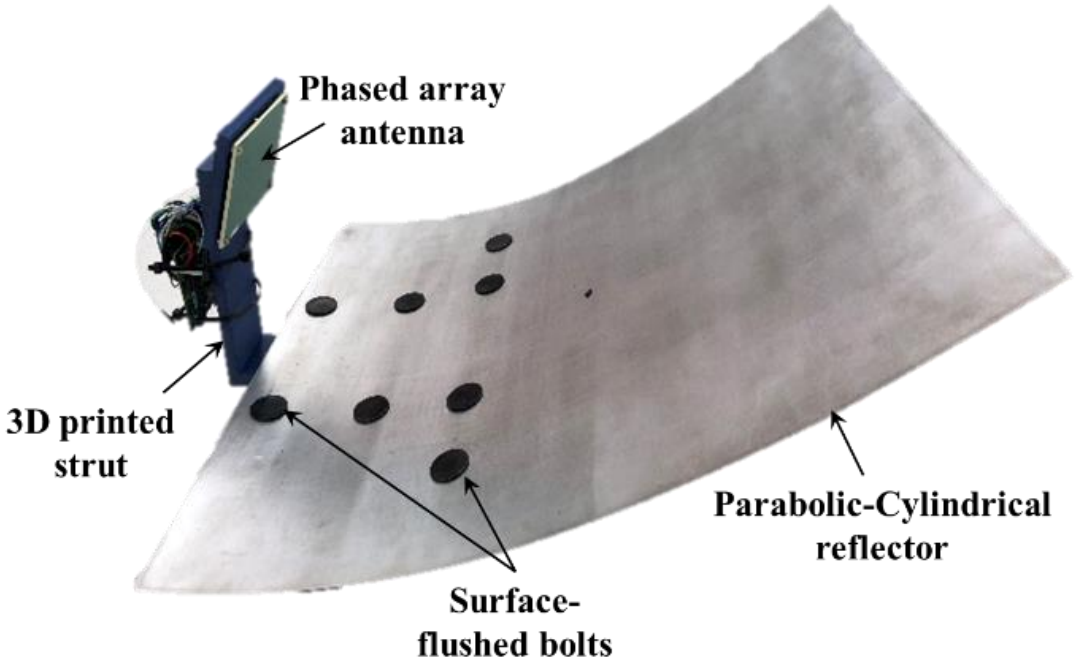

Figure 5.28 Photograph of the fabricated parabolic-cylindrical reflector using sheet metal technique and integrated with the phased array antenna.

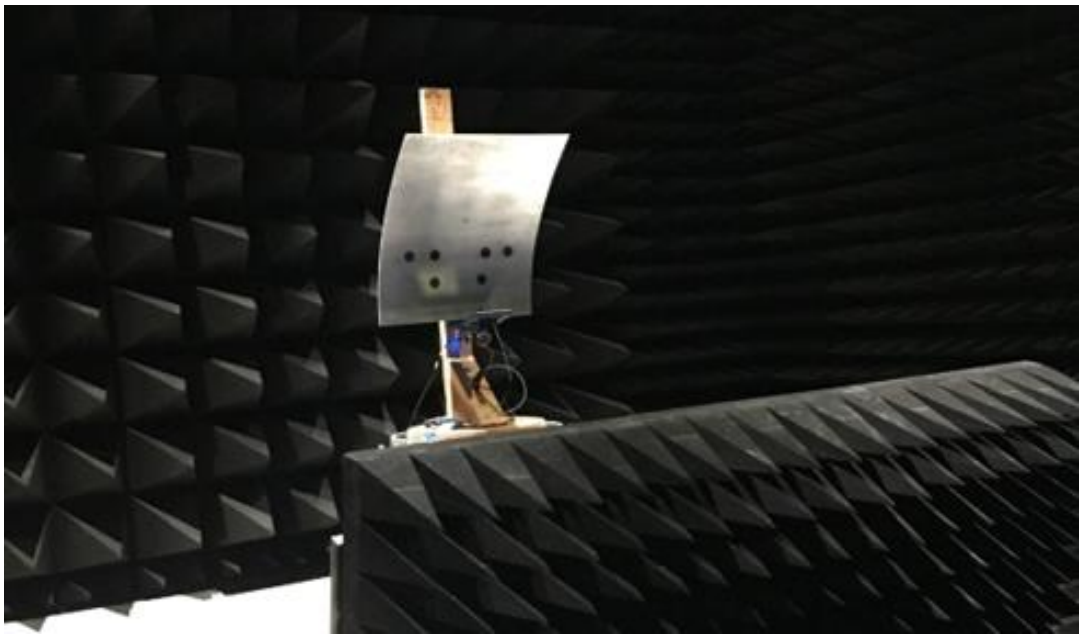

Figure 5.29 Parabolic-cylindrical reflector measurement setup in the CATR facility at the Naval Information Warfare Center Pacific, San Diego.

(CATR) facility at the Naval Information Warfare Center Pacific, as depicted in Fig. 5.29. The measurement of the parabolic-cylindrical reflector also exhibited the beam steering range of ±30° for a 3 dB reduction in the gain for both the X-polarization and Y-polarization, as presented in Fig. 5.30. The measured broadside 3 dB beamwidth at 13 GHz for the parabolic-cylindrical reflector antenna in the ϕ = 0° plane is 14°, and 14.5° for the X-polarization and Y-polarization, respectively and the measured 3 dB beamwidth in the ϕ = 90° plane is 4.2° for both the X-polarization and Y-polarization. The peak simulated directivity of the proposed parabolic-cylindrical reflector fed by the phased array is 26.85 dBi and 27.2 dBi for the X-polarization and Y-polarization, respectively. The simulated directivity for the reflector antenna and the simulated and measured 3 dB beamwidth for different scan angles for the X- and Y-polarization are shown in Fig. 5.31.

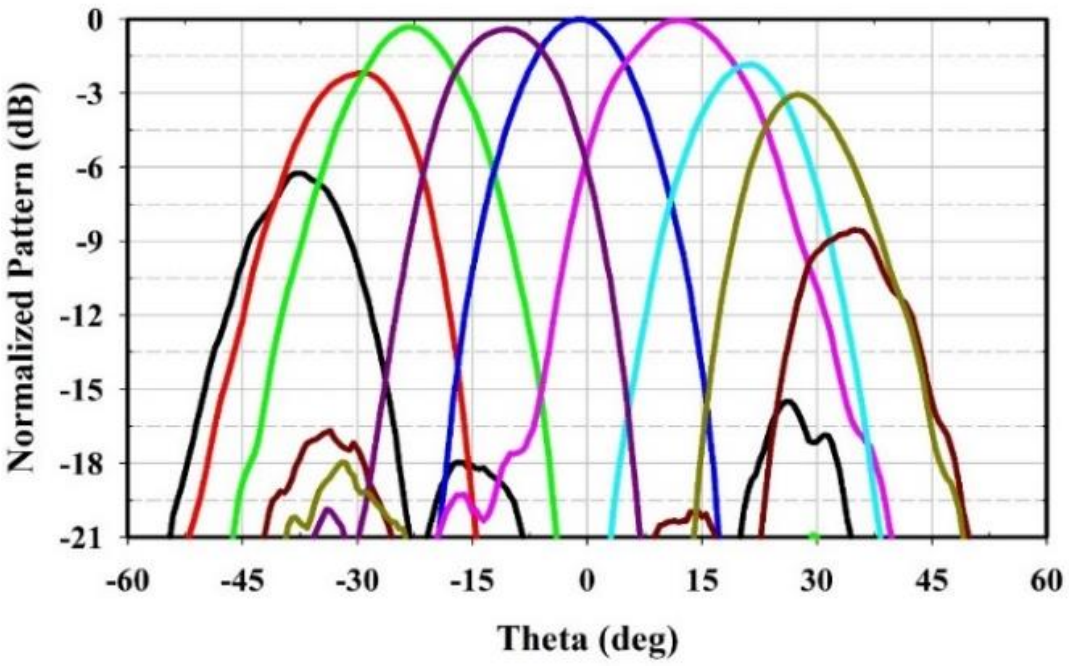

(a)

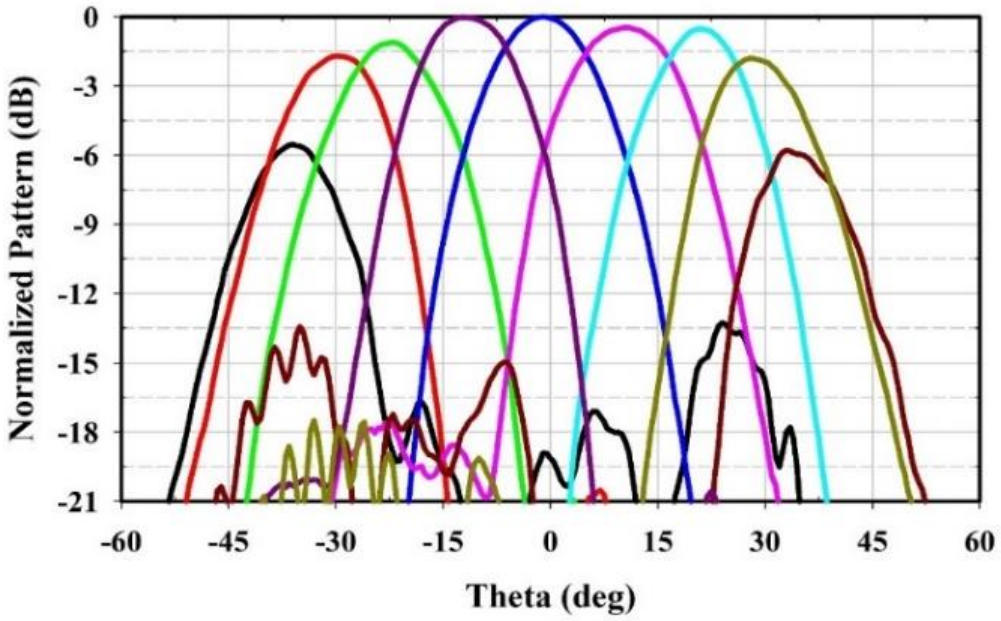

(b)

Figure 5.30 Measured normalized co-polarization beam steering radiation pattern of the parabolic-cylindrical reflector along the cylindrical axis (a) X-polarization, and (b) Y-polarization at 13 GHz.

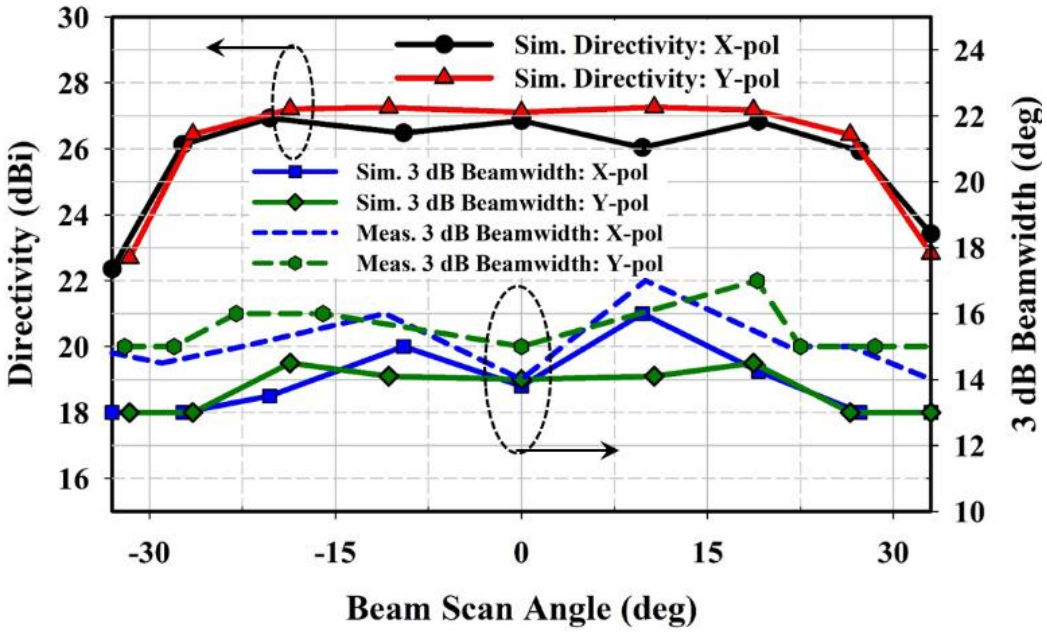

Figure 5.31 The simulated peak directivity of the proposed parabolic-cylindrical reflector antenna and the simulated and measured 3 dB beamwidth for different scan angles for X-polarization and Y-polarization along $\phi = 0°$ plane.

Discussions in this research are limited to the uncalibrated normalized measured gain as the beamforming board was not calibrated separately. However, the measured radiation 3 dB beamwidth agrees reasonably well with the simulation 3 dB beamwidth for both the X-polarization and Y-polarization, which implies similar directivities for the simulated and measured cases. There will not be a significant difference in the cross-polarization performance of a center-fed and offset-fed reflectors because it is limited by the cross-polarization of the feed source. Additionally, the offset-fed reflector assembly can achieve higher gain as the feed array blockage can be significantly lowered than the center-fed reflector antenna. The primary objectives of wideband dual linear-polarization, high gain, stable radiation pattern, and beam steering range of around ±30° are achieved using the proposed hybrid reflector-phased array antenna.

5.5 Conclusion

A cost-effective and energy-efficient high gain beam steering solution for the enhanced data rate wireless communication application using a hybrid reflector-phased array system was presented at *Ku*-band. The radiation characteristics of the parabolic-cylindrical reflector were analyzed using the physical optics approximation, and the analytically computed results of the reflector were compared with the MoM solver based TICRA GRASP simulations. A multilayered stack-up of the proposed dual-linear polarized 8 × 4 phased array antenna with the beamforming network was designed and fabricated. The Anokiwave AWMF-0117 integrated silicon core chips were used in the beamforming network for achieving the desired beam steering. An aluminum parabolic-cylindrical reflector was also built and integrated with the phased array antenna to provide the measured beam scanning up to ± 30° for 3 dB reduction in the gain for both the X-polarization and Y-polarization.

The next chapter discusses a multi-functional modified Butterfly planar array antenna in a staggered configuration at *Ka*-band (28 GHz). This antenna array is capable of full-polarization reconfiguration (RHCP, LHCP, Linear-X, and Linear-Y), wide-angle 1D-beam steering, and flexible radiation patterns.

Chapter 6

A Multi-Functional Full-Polarization Reconfigurable 28 GHz Staggered Butterfly 1D-Beam Steering Antenna

6.1 Introduction

The fifth-generation (5G) wireless communication has increased the demand for efficient antennas to improve the system capacity and cellular coverage with lower power requirements and installation costs [116]. Multi-functional antennas can facilitate these goals by combining features of polarization reconfiguration, wide-angle beam steering, and flexible radiation patterns in a single antenna aperture. The full-polarization reconfigurable antenna can switch between right-hand circular polarization (RHCP), left-hand circular polarization (LHCP), Linear-X, and Linear-Y polarization, depending on the system requirements. The polarization-reconfigurable antenna offers advantages of reduction in the installation space, eliminating multipath fading, and increasing the channel capacity [117] – [122]. In addition to polarization reconfiguration, a wide-angle beam steering array antenna can further enhance multi-functionality by providing connectivity with the mobile communication device [123]. Another feature of a multi-functional antenna is flexible radiation patterns to provide varying 3 dB gain-beamwidth for dynamic control of the transmit power, thereby optimizing the system efficiency and cost [124] – [125]. Microstrip technology can be utilized to fabricate these antennas as it has advantages of being low profile, low fabrication cost, and light-weight design [73], [74].

A modified version of the Butterfly series-fed antenna reported in [126] can be utilized to achieve the multi-functional capabilities. The series-fed traveling wave antenna is analyzed using

the periodic leaky-wave antenna (LWA) theory. The fast-spatial harmonics produced by the periodic perturbations are responsible for the radiation in the periodic LWA.

In this research, a multi-functional modified Butterfly planar array antenna in a staggered configuration is proposed at *Ka*-band (28 GHz). The staggered configuration allows a compact spacing between the Butterfly linear arrays, resulting in wide-angle 1D-beam steering without any grating lobes. The proposed multi-functional antenna is an 8 × 12 staggered Butterfly array antenna capable of full-polarization reconfiguration, wide-angle 1D-beam steering, and flexible radiation pattern. A *Ka*-band silicon-germanium (SiGe) Analog Devices ADMV4821 16-channel analog beamformer is integrated with the proposed staggered Butterfly array antenna to provide experimental verification of the desired reconfiguration and flexible patterns. The conventional Butterfly antenna reported in [126] – [128] is a single polarization RHCP without staggered arrangement and has a limited beam steering range of ±34° due to larger inter-linear array spacing.

6.2 Unit-Cell Butterfly Antenna Geometry

The unit-cell of the proposed design is a modification of the Butterfly unit-cell [126]. In [126], there was an onset of grating lobe for similar Butterfly unit-cell due to the larger inter-cell separation in terms of free-space wavelength. The proposed unit-cell shown in Fig. 6.1 is a two-port structure consisting of two Butterfly radiating elements separated by $2\lambda_g$, where λ_g = 5 mm is the effective wavelength at 28 GHz. Due to $2\lambda_g$ spacing, both the Butterfly radiating elements are in-phase and thus results in broadside radiation. The spacing of 2λg also ensures a staggered arrangement when implemented in a planar array. The antenna is designed on a 15-mil thick TMM6 substrate with ε_r = 6 and tanδ = 0.0023. Each Butterfly radiating element consists of four sequentially-rotated series-fed resonant microstrip patch antennas. The patch width is W_p = 0.8

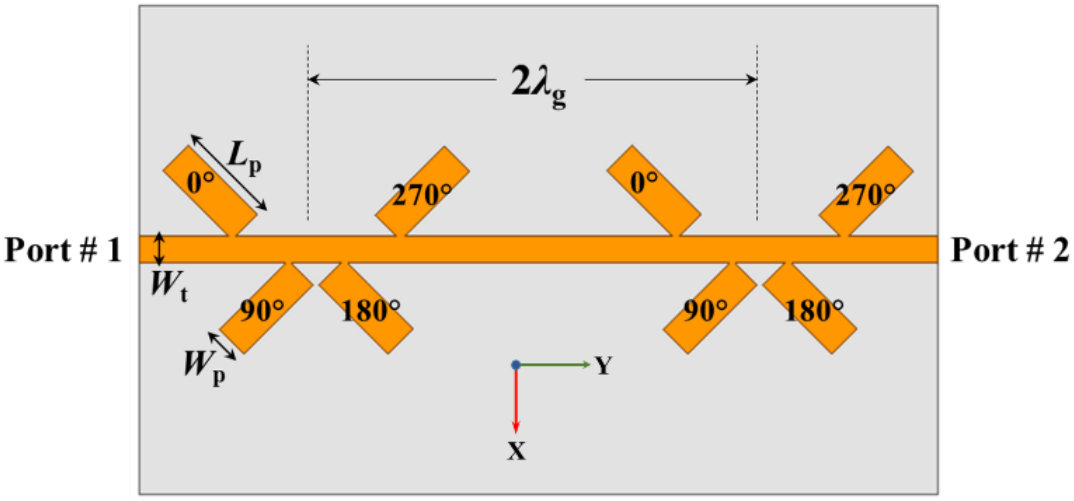

Figure 6.1 Unit-cell geometry consisting of two Butterfly radiating antennas separated by $2\lambda_g$.

Table 6.1 Excitation weights for full polarization reconfiguration.

Port 1 Excitation (Mag.∠Phase)	**Port 2 Excitation (Mag.∠Phase)**	**Polarization**
1∠0°	0∠0°	RHCP
0∠0°	1∠0°	LHCP
1∠0°	1∠0°	Linear-X
1∠0°	1∠180°	Linear-Y

mm, patch length is L_p = 2.2 mm and feed line width W_t = 0.6 mm. The proposed structure can achieve full-polarization reconfiguration (RHCP, LHCP, Linear-X, and Linear-Y polarization) with proper port excitations. The excitation weights for generating these polarizations are shown in Table 6.1.

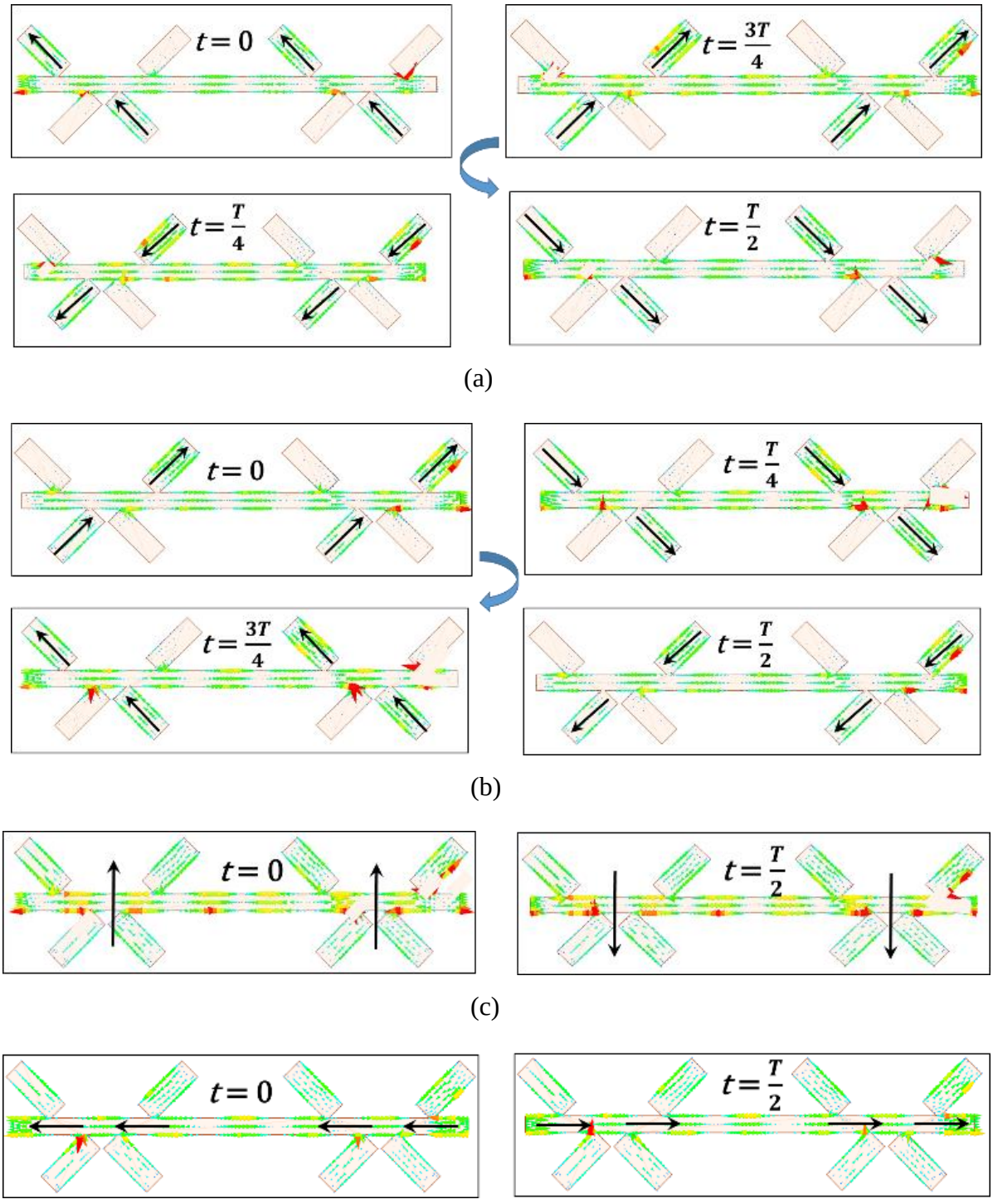

Figure 6.2 The instantaneous current distribution on the unit-cell Butterfly antenna for different port excitations (a) Port 1 excited (b) Port 2 excited (c) Both port 1 and port 2 excited in phase, and (d) Port 1 and port 2 excited out of phase. (black arrows denote the resultant current direction)

The instantaneous current distributions of the four polarizations are presented in Figs. 6.2(a) – 6.2(d). When port 1 is excited and port 2 is matched terminated, then the fields rotate counter-clockwise to generate RHCP, as shown in Fig. 6.2(a). Similarly, when port 2 is excited and port 1 is matched terminated, then the fields rotate clockwise to generate LHCP, as shown in Fig. 6.2(b). When both port 1 and port 2 are excited in-phase, then Linear-X polarization is generated, as shown in Fig. 6.2(c) and when port 1 and port 2 are excited out-of-phase, then Linear-Y polarization is achieved, as shown in Fig. 6.2(d).

6.3 Analysis and Theory of Operation

6.3.1 Cavity Model Analysis of Unit-Cell

The radiation pattern of the full-polarization reconfiguration unit-cell antenna of Fig. 6.1 can be analyzed using the cavity model [32]. The following design equations are valid for the RHCP polarization when port 1 is excited with port 2 matched terminated.

The radiated electric field of the patch antenna without any rotation is proportional to (6.1) [126]:

$$E_\theta(\theta,\phi) \propto \frac{\sin\left(k_y \frac{a}{2}\right)}{\left(k_y \frac{a}{2}\right)} \cos\left(k_x \frac{b}{2}\right) \cos\phi$$
$$E_\phi(\theta,\phi) \propto \frac{\sin\left(k_y \frac{a}{2}\right)}{\left(k_y \frac{a}{2}\right)} \cos\left(k_x \frac{b}{2}\right) \cos\theta \sin\phi \quad (6.1)$$

The total radiated fields of the linear array of Fig. 6.1 with (M = 8) patch elements rotated individually can be expressed by (6.2) and (6.3) [126]:

$$E_\theta^T(\theta,\phi) = \sum_{n=1}^{M} E_{\theta n}(\theta,\phi-\alpha_n) e^{j(k_0 d_n \sin\theta \sin(\phi-\alpha_n)+\phi_n)} \quad (6.2)$$

$$E_{\phi}^{T}(\theta,\phi)=\sum_{n=1}^{M}E_{\phi n}(\theta,\phi-\alpha_n)e^{j(k_0 d_n \sin\theta\sin(\phi-\alpha_n)+\phi_n)} \tag{6.3}$$

where, $\phi_n=\frac{4\pi(n-1)}{M}$ is the excitation current phase of the n^{th} element and $\alpha_n=\frac{4\pi\left(n-1\right)}{M}+\frac{\pi}{4}$ is the rotation angle of the n^{th} element. $E_{\theta n}(\theta,\phi-\alpha_n)$ and $E_{\phi n}(\theta,\phi-\alpha_n)$ are the θ- and ϕ-components of the radiated field for the rotated element *n*, which is transformed from the radiated field $E_{\theta}(\theta,\phi)$ and $E_{\phi}(\theta,\phi)$ of the isolated element without rotation.

The RHCP and LHCP components of the total electric field can be obtained from the θ- and ϕ-components of the electric field, as in (6.4) – (6.5) [23]:

$$E_{RHCP}=\left(\frac{E_{\theta}^{T}-jE_{\phi}^{T}}{\sqrt{2}}\right) \tag{6.4}$$

$$E_{LHCP}=\left(\frac{E_{\theta}^{T}+jE_{\phi}^{T}}{\sqrt{2}}\right) \tag{6.5}$$

Owing to the symmetry of the structure, similar equations would follow for LHCP polarization when port 2 is excited, and port 1 is matched terminated. The in-phase and out-of-phase superposition of the fields from the two cases will generate the Linear-X and Linear-Y fields, respectively.

A MATLAB analysis for the four polarization reconfigurable states based on the above equations is executed and compared with the full-wave Ansys HFSS simulation. Figs. 6.3(a) – 6.3(d) show the analytical and simulated normalized patterns at 28 GHz for the different polarization reconfigurable states of the proposed Butterfly unit-cell. The analytical and full-wave simulation results agree well with an average simulated 3 dB gain-beamwidth of 90° and 26° along the ϕ = 0° and ϕ = 90° plane, respectively.

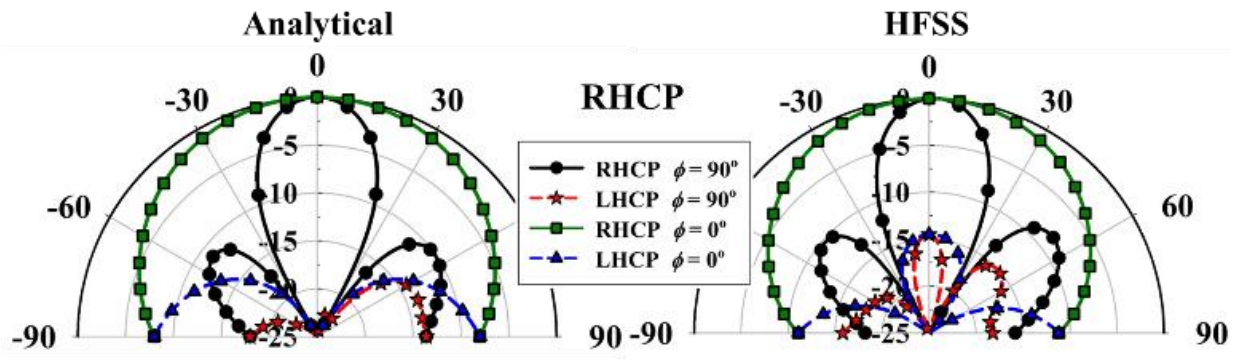
Analytical
HFSS
RHCP
RHCP $\phi = 90°$
LHCP $\phi = 90°$
RHCP $\phi = 0°$
LHCP $\phi = 0°$
0
30
60
90
-30
-60
-90
-5
-10
-15
-20
-25

(a)

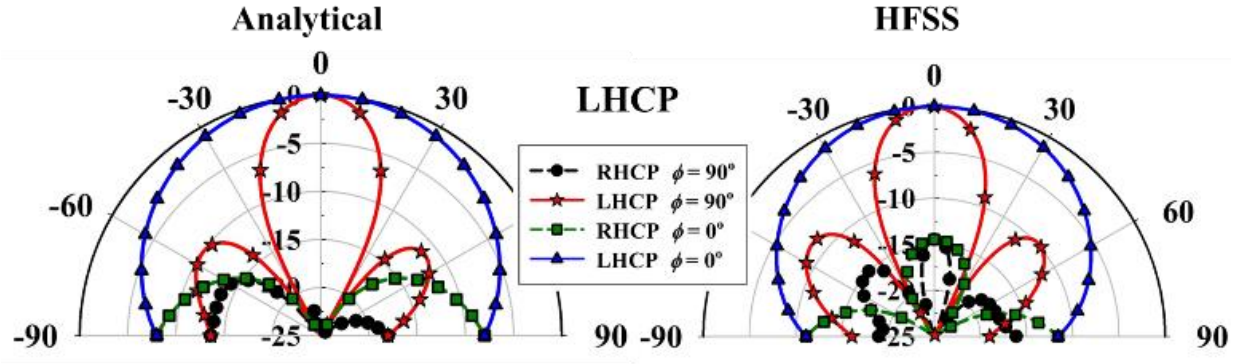
Analytical
HFSS
LHCP
RHCP $\phi = 90°$
LHCP $\phi = 90°$
RHCP $\phi = 0°$
LHCP $\phi = 0°$
0
30
60
90
-30
-60
-90
-5
-10
-15
-20
-25

(b)

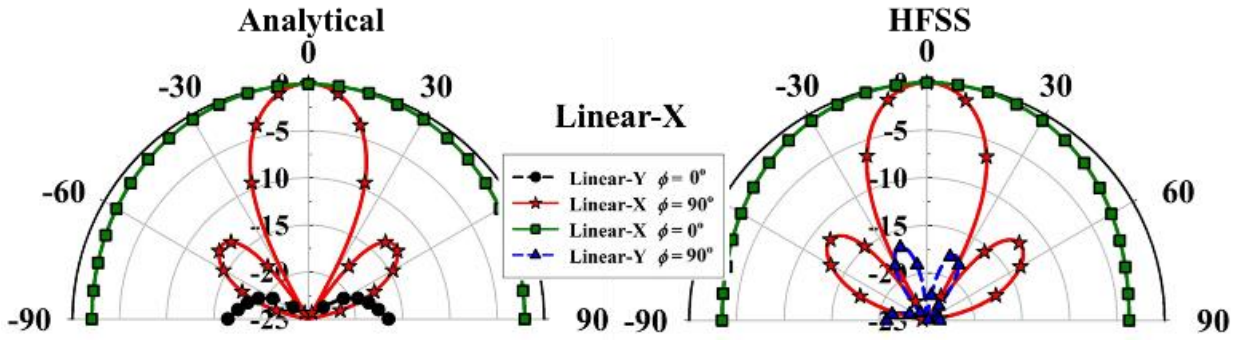
Analytical
HFSS
Linear-X
Linear-Y $\phi = 0°$
Linear-X $\phi = 90°$
Linear-X $\phi = 0°$
Linear-Y $\phi = 90°$
0
30
60
90
-30
-60
-90
-5
-10
-15
-20
-25

(c)

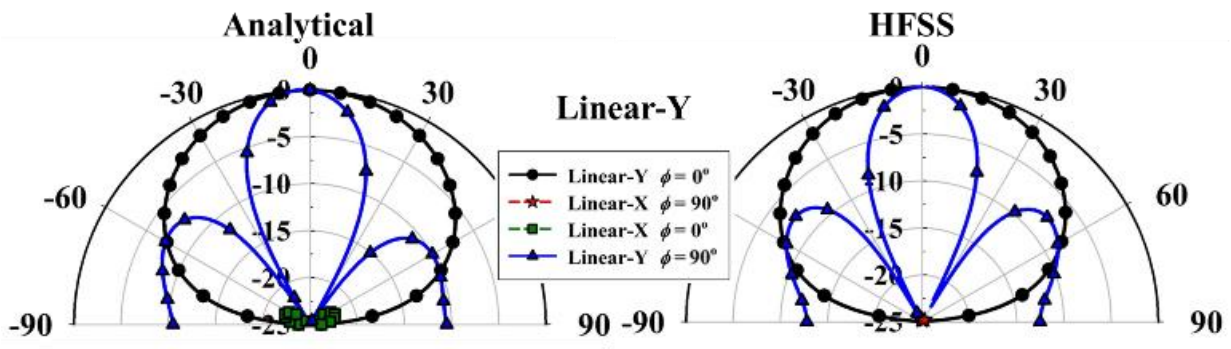

(d)

Figure 6.3 Normalized polarization reconfigurable radiation pattern of the unit-cell using analytical equations and full-wave EM analysis (HFSS) at 28 GHz for (a) RHCP (b) LHCP (c) Linear-X, and (d) Linear-Y polarization.

6.3.2 Periodic LWA Analysis of 1 × 12 Butterfly Linear Array

The periodic leaky-wave antenna theory (LWA) [36], [37] is used to provide insights into the radiation characteristics of the proposed Butterfly linear array antenna. Fig. 6.4 shows the proposed series-fed linear array of N = 6 (12 Butterfly radiators) cascaded unit-cells. The size of the linear-array with N = 6 unit-cells is chosen as it provided the optimum antenna efficiency. The periodic LWA analysis is shown for RHCP when port 1 is excited, and port 2 is matched terminated. A similar analysis is carried in [126], but with the overlapped Butterfly radiators separated by λ_g.

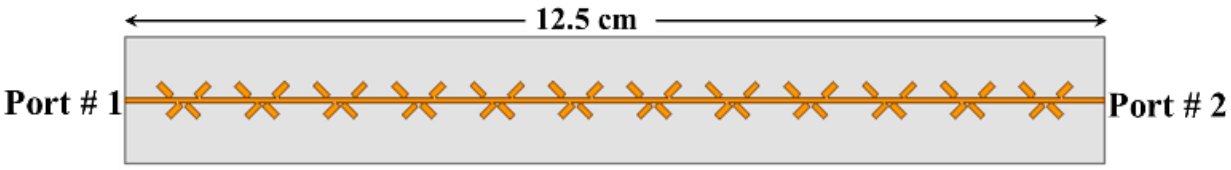

Figure 6.4 Linear Array of N = 6 (12 Butterfly radiators) cascaded series-fed unit cells.

In this periodic LWA analysis, to understand the radiation behavior, the leaky wave number k_{LW} is calculated from the eigenvalue of the *ABCD* matrix of the linear-array. Let $\mathbf{A_N} = \begin{bmatrix} A & B \\ C & D \end{bmatrix}$ be the *ABCD* matrix of the N (= 6) cascaded unit-cells of the Butterfly series-fed linear array obtained from the full-wave EM analysis.

The eigenvalue of the matrix is computed by solving (6.6) and (6.7) [40]:

$$\det\left(\mathbf{A_N} - \lambda \mathbf{I}\right) = 0 \tag{6.6}$$

$$\left| \begin{bmatrix} A & B \\ C & D \end{bmatrix} - \begin{bmatrix} e^{\gamma N d} & 0 \\ 0 & e^{\gamma N d} \end{bmatrix} \right| = 0 \tag{6.7}$$

The eigenvalue of the matrix is $\lambda = e^{\gamma N d}$, where $d = 2\lambda_g$ is the periodic spacing between the cells and $\gamma = jk_{LW} = j\beta_{-1} + \alpha$. Thus, the leakage constant α and the phase constant β_{-1} can be extracted from the computed eigenvalue of the *ABCD* matrix. The normalized leakage constant and the normalized phase constant of the proposed linear-array is presented in Fig. 6.5. The zero-crossing of the phase constant determines the frequency of the broadside radiation of the LWA. The leakage constant, which determines the beamwidth of the LWA, is relatively flat across the frequency range, which means the peak gain must be relatively flat across the frequency.

The Bloch impedance (input impedance) of the LWA is calculated using (6.8) [40]. The computed Bloch impedance is compared with the full-wave simulated design, as shown in Fig. 6.6. Both the computed and full-wave simulation show excellent correlation.

$$Z_B = \frac{-B}{A - e^{\gamma N d}} \tag{6.8}$$

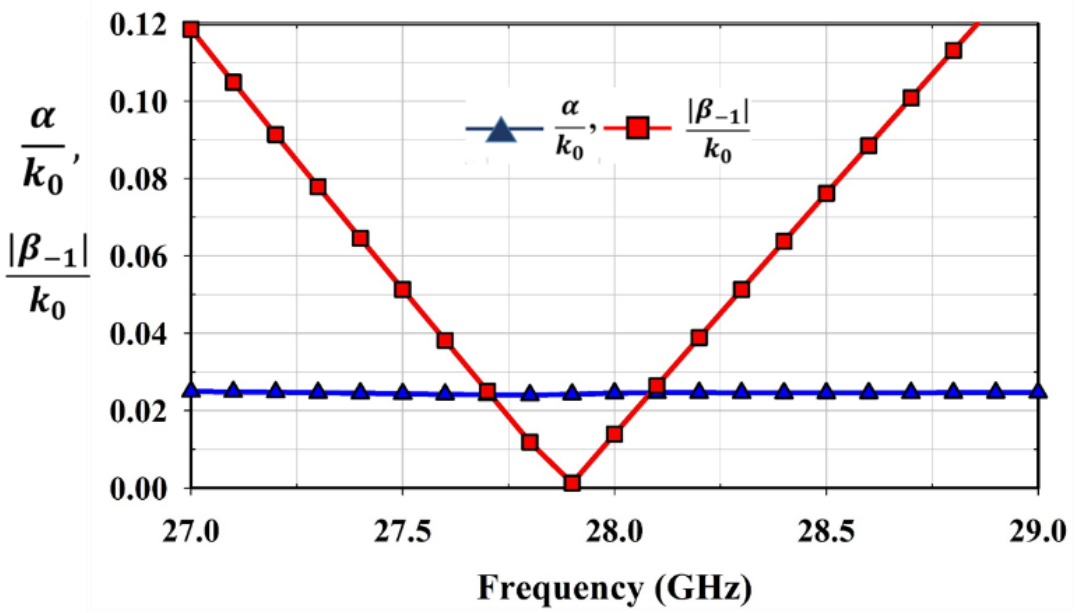

Figure 6.5 Extracted normalized leakage constant and normalized phase constant for the 1 × 12 Butterfly linear array.

An inherent property of the series-fed traveling wave antenna is the scanning of the beam with frequency, and the leaky wave phase constant β_{-1} can be used to determine the beam squint angle. The beam squint angle (θ_m) of the peak gain, measured from the broadside direction is computed by (6.9) [36] and compared with the full-wave simulation, as shown in Fig. 6.7.

$$\sin\theta_m \approx \frac{\beta_{-1}}{k_0} \tag{6.9}$$

It is observed from Fig. 6.7 that for the 27. 5 – 28.35 GHz of the 5G communication band, the beam squints between ±3° and the broadside radiation occurs near 28 GHz.

The radiation efficiency of the periodic LWA can be estimated by (6.10) [37]:

$$\eta \approx \frac{\hat{\alpha}_{lossless}}{\hat{\alpha}_{lossy}} \tag{6.10}$$

where $\hat{\alpha}_{lossless} = \frac{\alpha_{lossless}}{k_0}$ and $\hat{\alpha}_{lossy} = \frac{\alpha_{lossy}}{k_0}$. For the lossless case, $\hat{\alpha}_{lossless} = 0.016$ and for the lossy case, $\hat{\alpha}_{lossy} = 0.025$ at 28 GHz. The resulting estimated LWA radiation efficiency is then 62% at 28 GHz.

The total radiation pattern of the LWA can also be obtained from the leaky wave number and is given by the product of the element pattern and the array factor, where the array factor is (6.11) [37]:

$$AF(\theta) = \sum_{n=1}^{N} e^{-jk_{LW}y_n} e^{jk_0 y_n \sin\theta} \tag{6.11}$$

where $y_n = (n-1)d$, for $1 \le n \le N$, and $N = 6$ is the number of cascaded unit-cells. The element pattern is computed from the cavity model analysis.

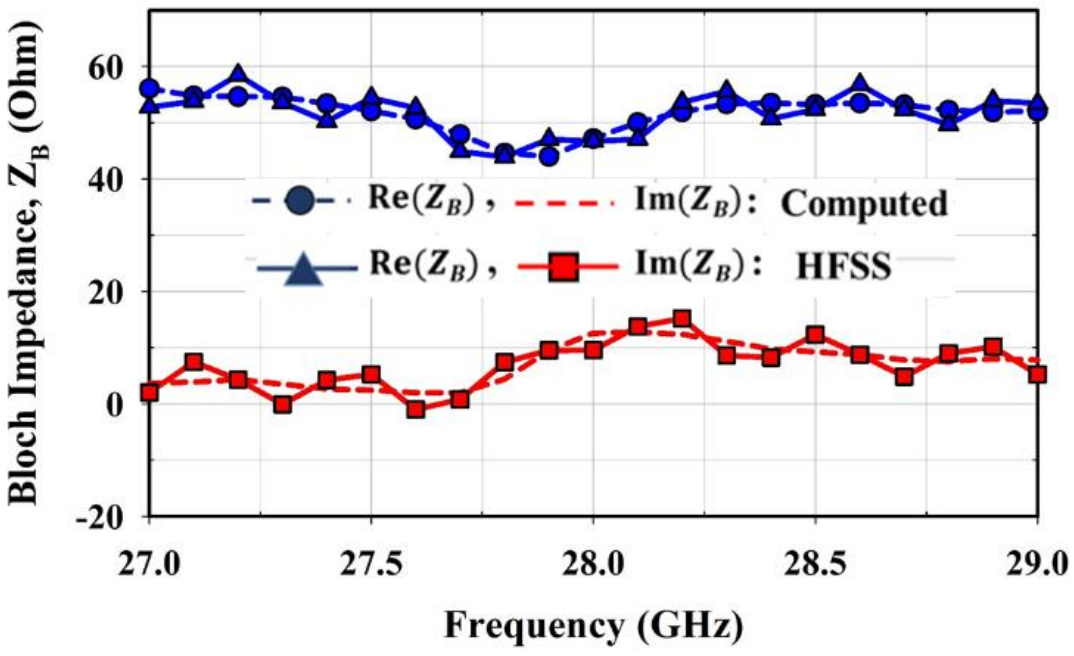

Figure 6.6 The Bloch impedance of the 1 × 12 Butterfly linear array using periodic LWA computation and full-wave EM analysis (HFSS).

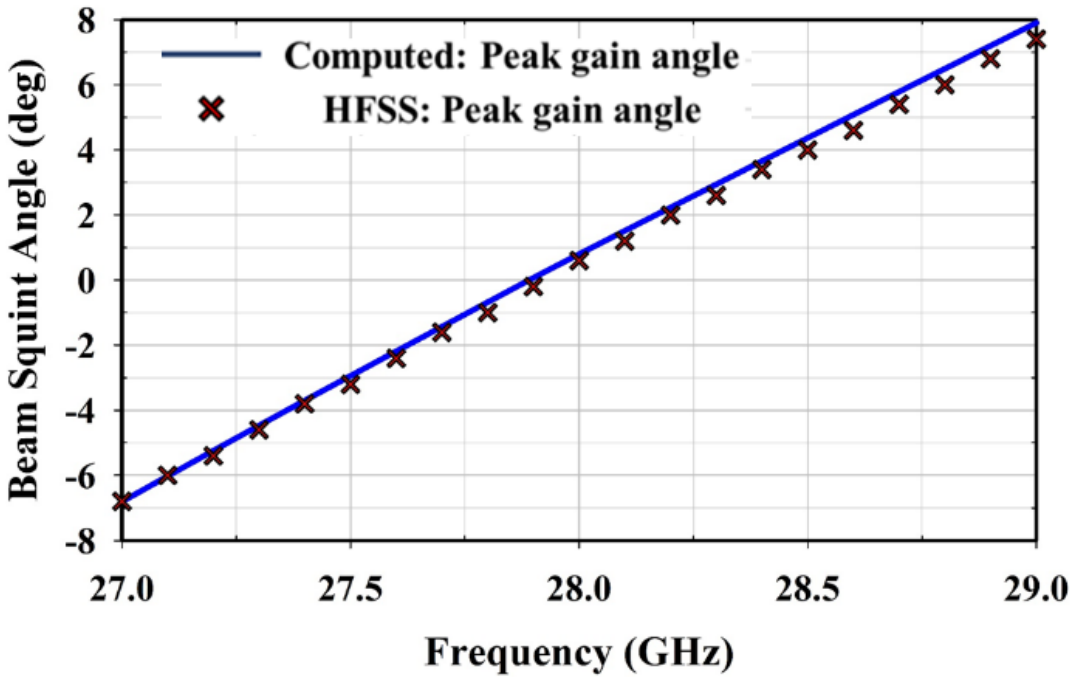

Figure 6.7 LWA computed and full-wave EM simulated (HFSS) beam squint angle as a function of frequency.

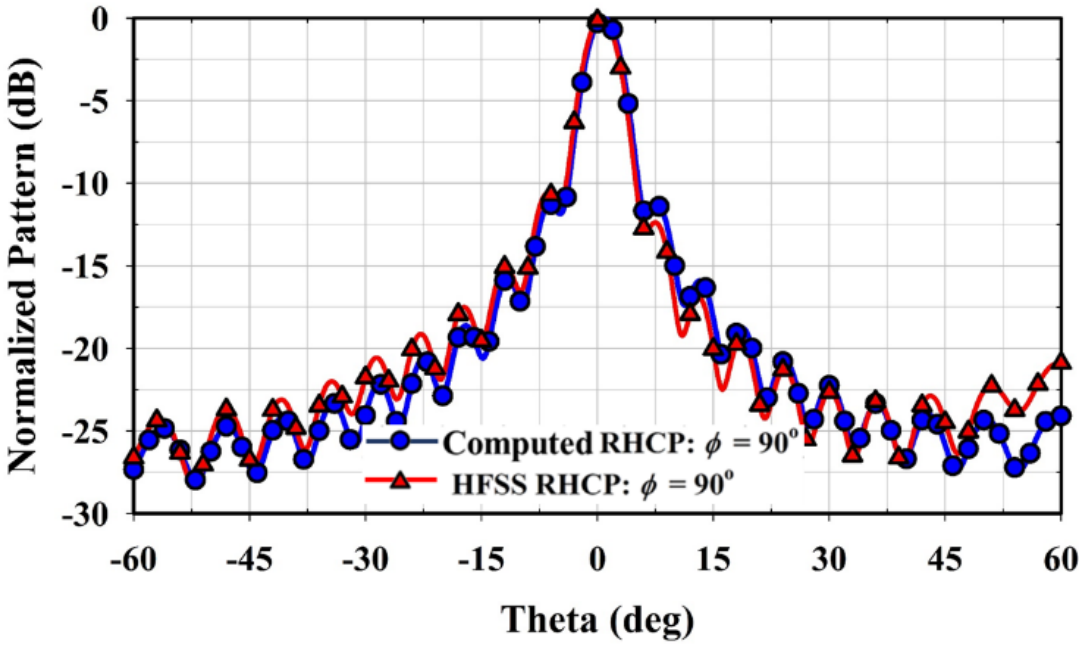

(a)

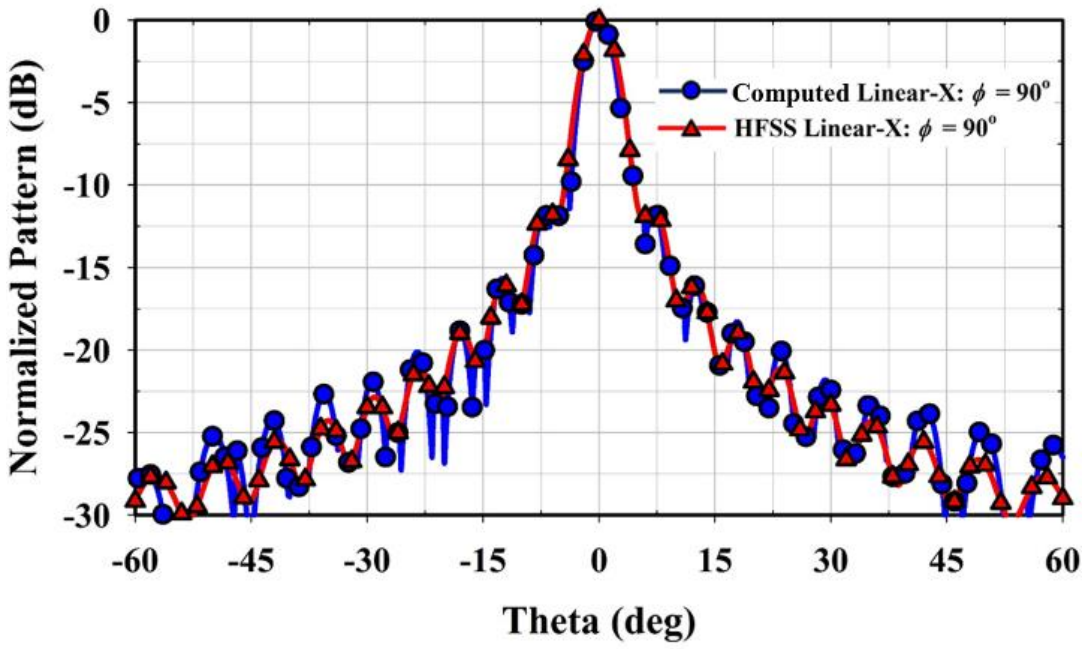

(b)

Figure 6.8 Normalized polarization reconfigurable radiation pattern at 28 GHz using the periodic LWA analysis and the full-wave EM simulation of the 1 × 12 Butterfly linear array (a) RHCP (b) Linear-X polarization.

Fig. 6.8(a) compares the computed and the full-wave simulated normalized radiation pattern of the LWA for the RHCP polarization, which are in excellent agreement. Similar periodic LWA analysis can be carried for the LHCP polarization when port 2 is excited, and port 1 is matched terminated. Fig. 6.8(b) presents the computed Linear-X polarization pattern, which is obtained by the in-phase superposition of the RHCP and LHCP LWA fields and is compared with the full-wave simulation.

6.3.3 Staggered Arrangement of 2 × 12 Butterfly Array

One of the novel features of the proposed antenna is the ability to form a staggered planar array geometry, as shown in Fig. 6.9. In this arrangement, the adjacent linear arrays are offset from each other, which ensures that the inter-linear array spacing d is less than $0.5\lambda_0$, where λ_0 is the free-space wavelength at 28 GHz. The compact structure of the staggered arrangement provides a wider 1D-beam steering range along the $\phi = 0°$ plane, without any grating lobes. The inter-linear array separation of the proposed design is d = 4.75 mm ($0.45\lambda_0$).

A parametric study on the inter-linear array separation d for the impedance matching and inter-port isolation is carried out for the 2 × 12 Butterfly staggered array. Fig. 6.10 shows the effect of varying d on the S-parameters. The impedance matching $|S_{11}| < -10$ dB and inter-port isolation better than 23 dB is obtained with d = 4.75 mm throughout the desired bandwidth.

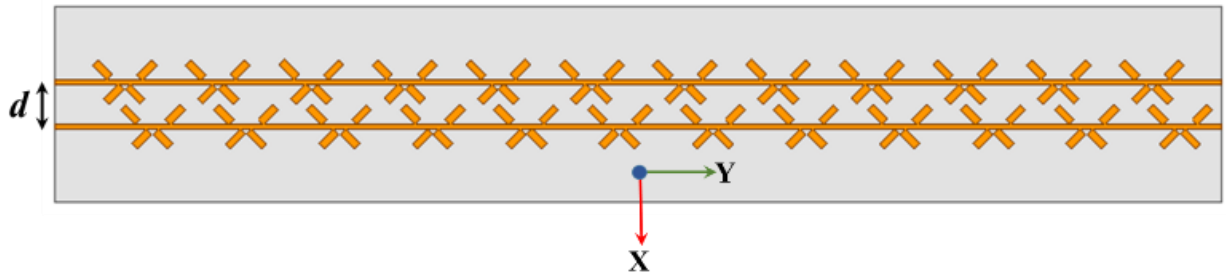

Figure 6.9 The staggered arrangement of two 1 × 12 Butterfly linear arrays separated by d = 4.75 mm.

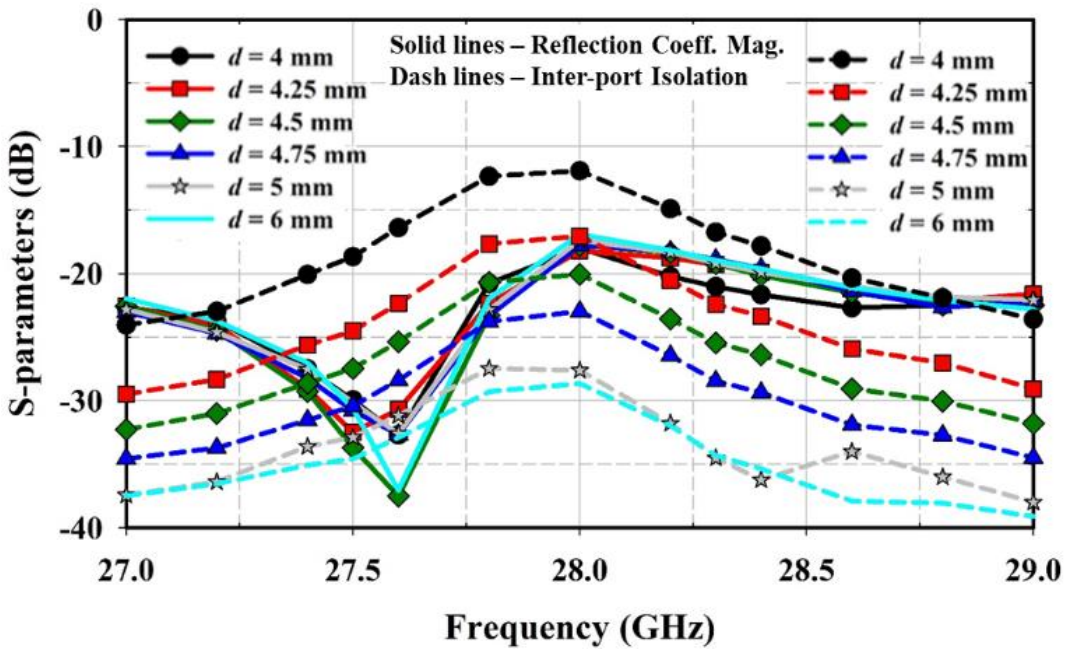

Figure 6.10 Effect of different separation on the reflection coefficient and inter-port isolation of the 2 × 12 staggered array.

6.4 Simulation of Multi-Functional 8 × 12 Staggered Butterfly Planar Array Antenna

Based on the staggered array configuration, a novel 8 × 12 staggered planar array configuration is proposed, as shown in Fig. 6.11. The dummy elements are placed on either side of the planar array to provide uniform mutual coupling behavior and consistent radiation patterns for the linear arrays along the edges. With the correct excitation of the ports, full-polarization reconfiguration can be achieved. The simulated AR of the planar array for the RHCP and LHCP cases, along with the peak gain and broadside CP realized gains, are presented in Fig. 6.12. The AR is well below 3 dB for the entire desired frequency range of 27.5 – 28.35 GHz. The peak gain is relatively flat across the entire frequency bandwidth, which is consistent with the periodic LWA analysis presented in previous section. Due to the beam squint along the series-fed direction with frequency, the broadside gain of the planar array drops, as shown in Fig. 6.12. It is observed that

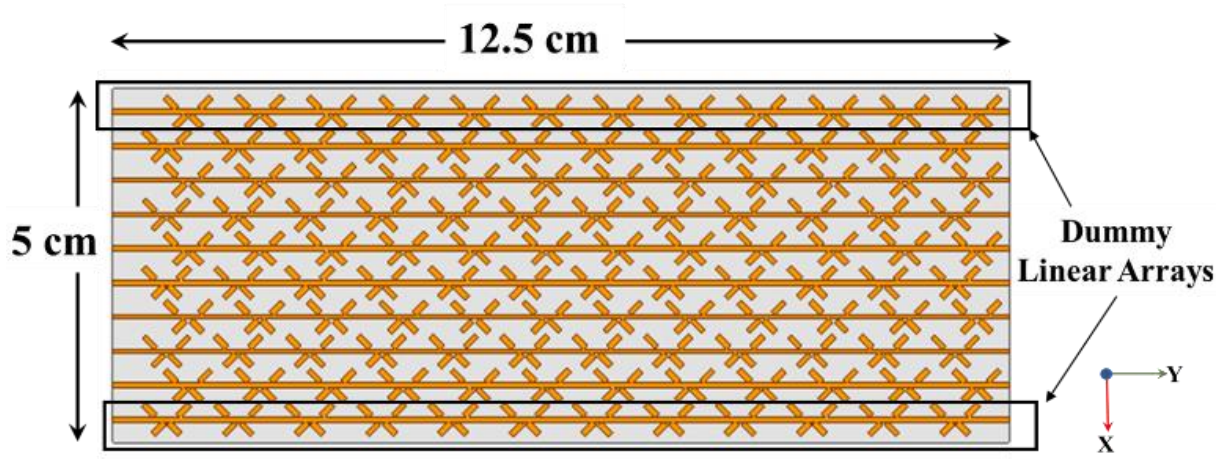

Figure 6.11 8 × 12 Staggered Butterfly planar array antenna with match-terminated dummy linear arrays on either side.

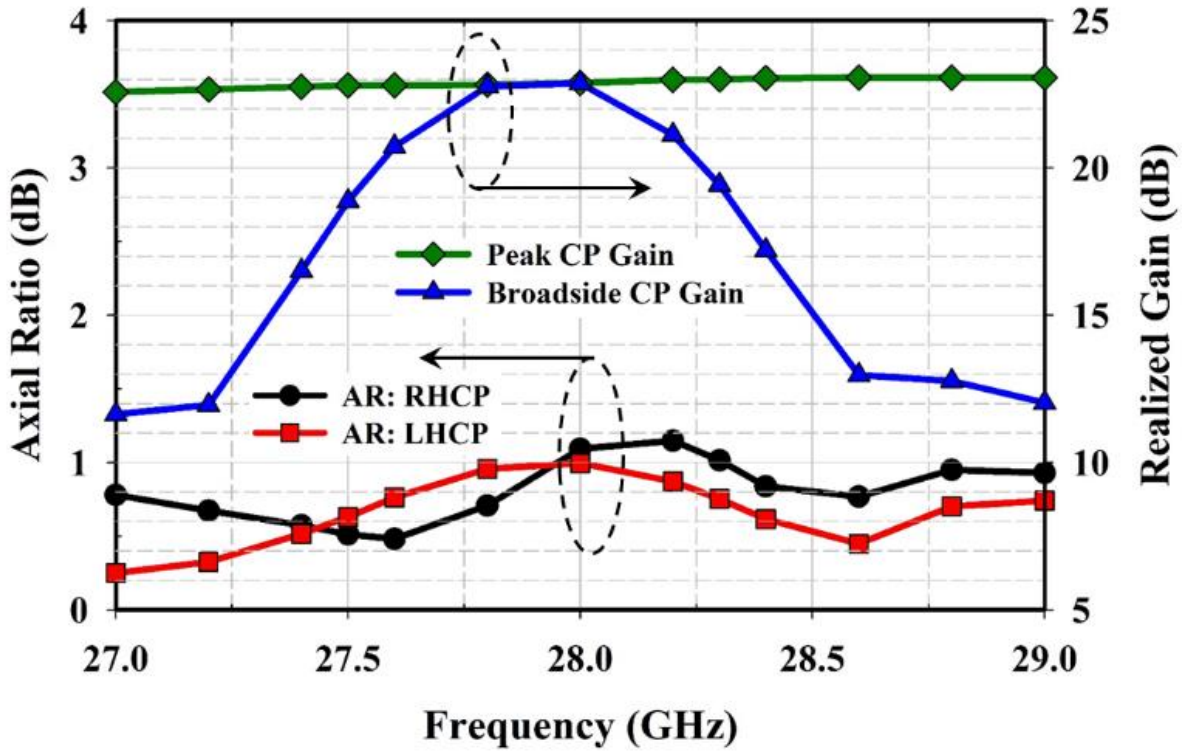

Figure 6.12 Simulated AR and realized gain vs. frequency of the 8 × 12 staggered Butterfly planar array antenna.

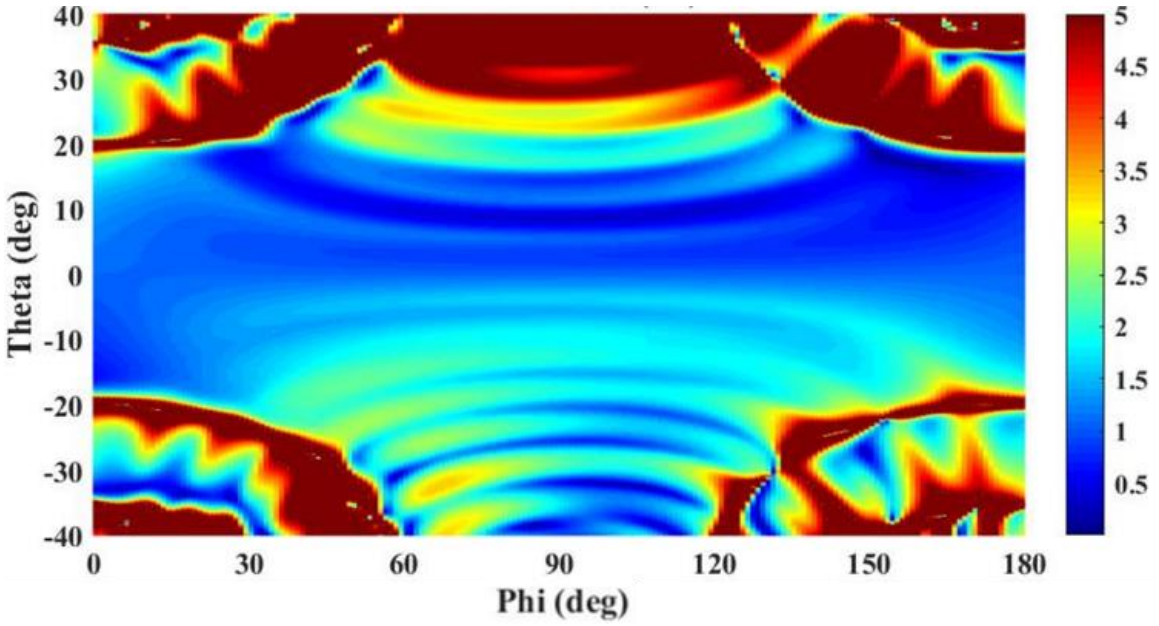

(a)

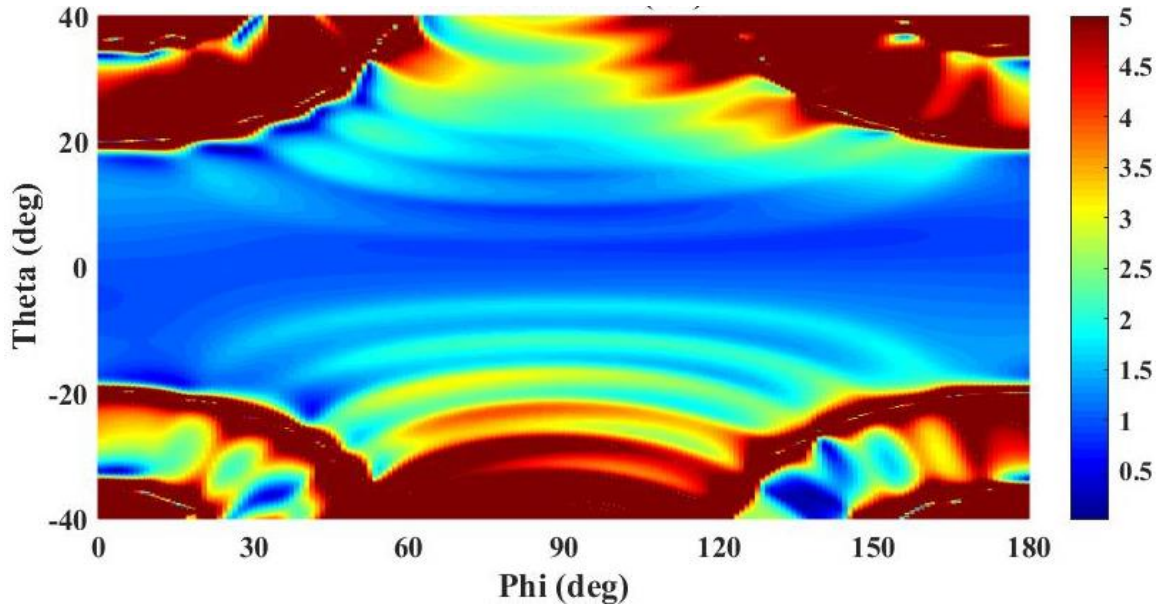

(b)

Figure 6.13 Simulated AR intensity plot for the 8 × 12 Staggered Butterfly planar array antenna at 28 GHz (a) RHCP (b) LHCP polarization.

there is around 3.5 dB variation in the broadside gain relative to the peak gain within the desired 5G band. The simulated AR beamwidth intensity plot at 28 GHz for the RHCP and LHCP polarization is depicted in Fig. 6.13(a) and Fig. 6.13(b), respectively. For both the CP cases, the AR is below 3 dB within the main lobe beam of the planar array for all the phi cut-planes. The average 3 dB AR beamwidth is around 45° across the desired frequency bandwidth.

The full-polarization reconfiguration simulated realized gain radiation patterns of the 8 × 12 planar staggered Butterfly array antenna are presented in Figs. 6.14(a) – 6.14(d). For brevity, the results are only shown at 28 GHz. Sidelobe level (SLL) reduction of 25 dB is achieved with the amplitude tapering using Chebyshev polynomial. The peak simulated broadside co-polarization realized gain is 22.9 dBic, 23 dBic, 23 dBi, and 22.6 dBi and the cross-polarization isolation is 23.1 dB, 23.2 dB, 24 dB, and 21.2 dB for the RHCP, LHCP, Linear-X, and Linear-Y polarization, respectively. The corresponding 3 dB gain-beamwidth in the ϕ = 0° plane is 16°, 16°, 16°, and 16.2° and the 3 dB gain-beamwidth in the ϕ = 90° plane is 5.1°, 5.1°, 4.5°, and 4.5° for the RHCP, LHCP, Linear-X, and Linear-Y polarization, respectively.

The simulated 1D-beam steering characteristics along ϕ = 0° plane of the 8 × 12 staggered array for two of the polarization reconfigurable states, namely, RHCP and Linear-X is presented in Fig. 6.15(a) and Fig. 6.15(b), respectively, at 28 GHz. Both the RHCP and Linear-X polarizations exhibit a symmetric stable beam steering range of ±63° without any grating lobes. The RHCP gain drops by 5 dB for the beam steering angle ± 60° and the Linear-X gain drops by 3 dB for the beam steering angle of ±63°. The gain roll-off for the RHCP is steeper than the Linear-X due to the narrower RHCP element pattern beamwidth along the ϕ = 0° plane (Fig. 6.3(a)) as compared to the Linear-X element pattern (Fig. 6.3(c)). In both the polarization cases, the SLL is well below 15 dB, even for the farthest beam steered angles.

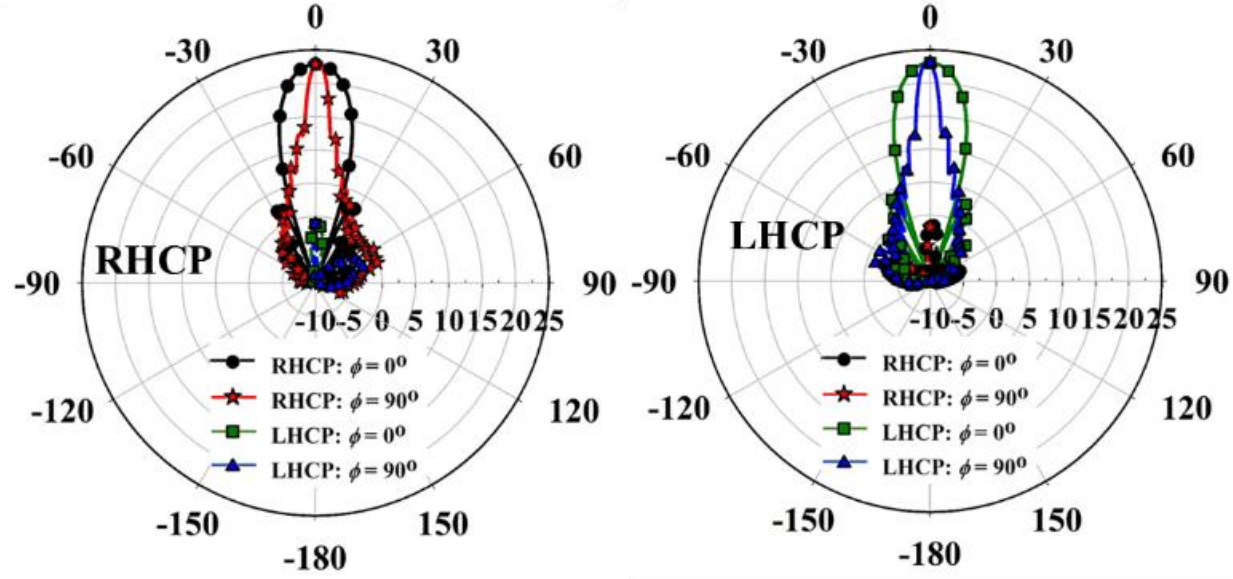

(a) (b)

(c) (d)

Figure 6.14 Simulated polarization reconfigurable realized gain pattern for the 8 × 12 Staggered Butterfly planar array antenna at 28 GHz for (a) RHCP (b) LHCP (c) Linear-X, and (d) Linear-Y polarization.

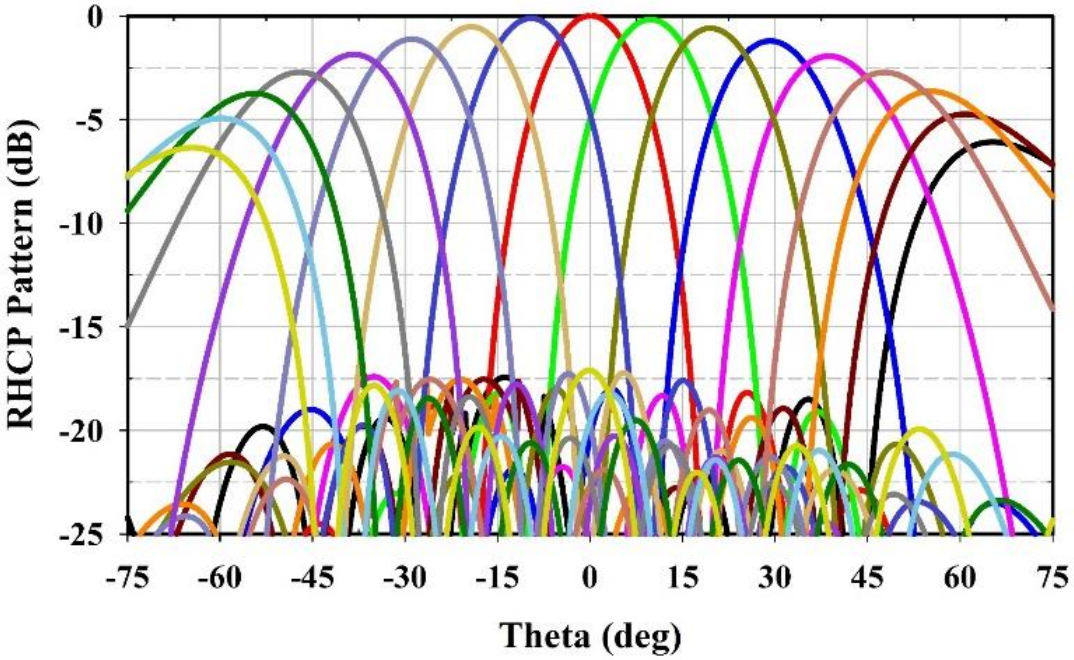

(a)

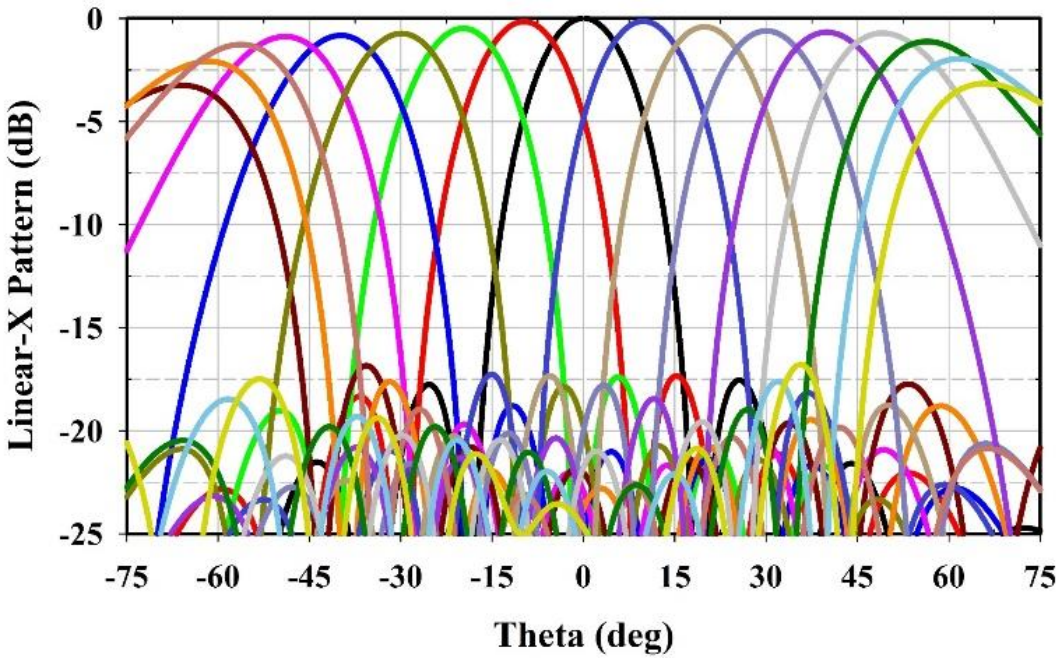

(b)

Figure 6.15 Simulated polarization reconfigurable 1D-beam steering pattern along ϕ = 0° plane of the 8 × 12 Staggered Butterfly planar array antenna at 28 GHz for (a) RHCP and (b) Linear-X polarization.

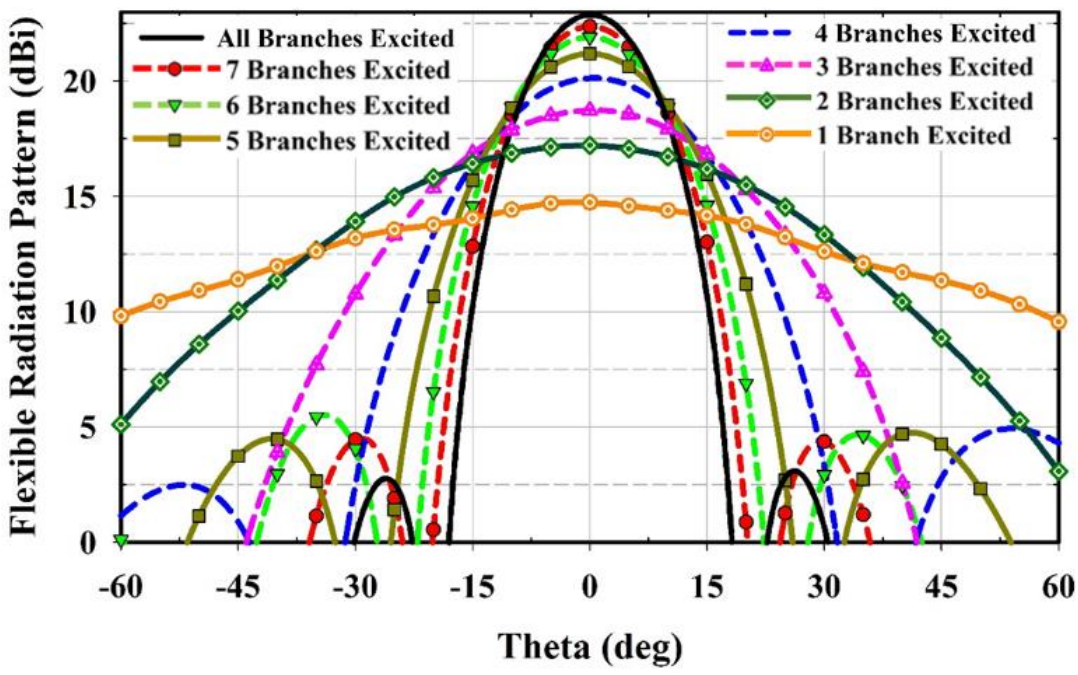

Figure 6.16 Simulated flexible realized gain radiation pattern along ϕ = 0° plane for the 8 × 12 Staggered Butterfly planar array antenna at 28 GHz.

Besides full-polarization reconfiguration and 1D-beam steering, the proposed array can be used to achieve flexible radiation patterns with different beamwidths, as shown in Fig. 6.16. Flexible patterns can be used to optimize the transmit power of the 5G base station in the dynamic environment for a user with varying cell range, angle, and gain requirements. By selective excitation of the linear arrays of the staggered Butterfly antenna, beams with different 3 dB gain-beamwidth can be formed. As observed, the 3 dB gain-beamwidth can vary from 16° when all the 8 linear-array branches are excited to 90° when only one linear-array branch is excited.

The maximum beam steering range of the 8 × 12 staggered phased array is limited to ±63° due to its broader array factor. However, the beam steering range can be further increased with a larger size array. The element pattern of the Butterfly linear-array is combined with the array factor of different sizes in MATLAB. Fig. 6.17 shows the maximum scan range possible for different

sizes of the staggered Butterfly array antenna. Table 6.2 summarizes the maximum scan angle of the array and its corresponding realized gain at that steered angle. As observed, using a larger staggered Butterfly planar array of size 128 × 12, a wide-angle 1D-beam steering range of ±84° can be achieved without any grating lobes.

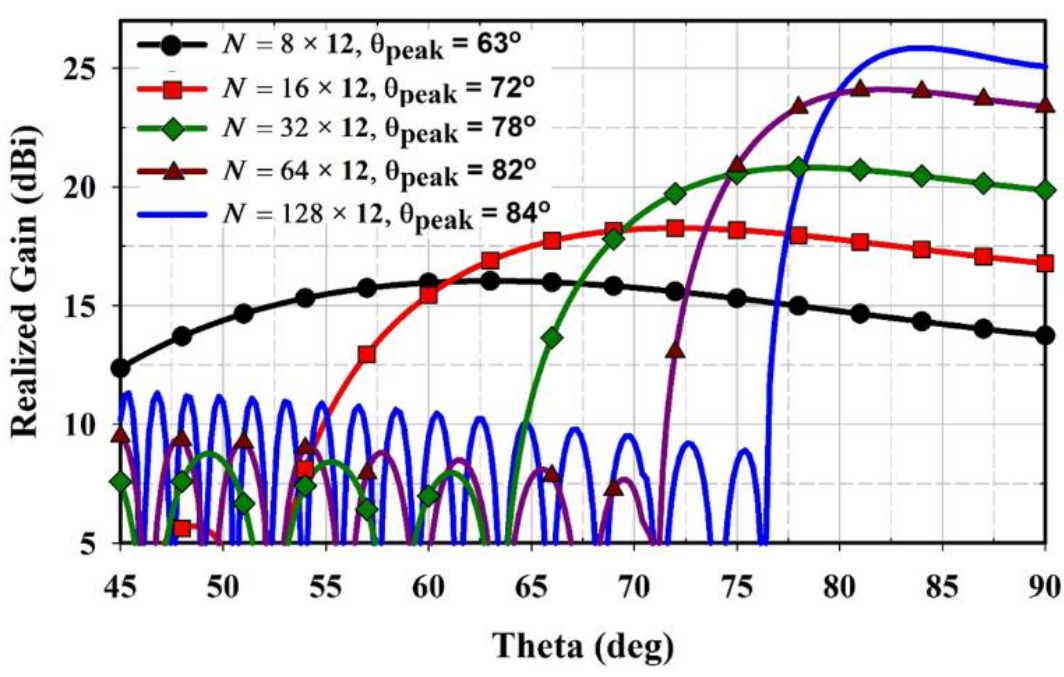

Figure 6.17 Simulated maximum scan angle ranges possible for different sizes of the staggered Butterfly planar array antenna at 28 GHz.

Table 6.2 Maximum Beam Steering angle for varying Butterfly array sizes.

Maximum Beam Steering angle for Different Number of Phased Array Elements					
Number of Elements	**8 × 12**	**16 × 12**	**32 × 12**	**64 × 12**	**128 × 12**
Realized Gain (dBi)	15.8	18.4	21	23.7	25.85
Max. Beam Steered Peak Angle (deg)	63°	72°	78°	82°	84°

6.5 Experimental Verification of 8 × 12 Staggered Butterfly Planar Array Antenna

6.5.1 Passive 8 × 12 Staggered Butterfly Planar Array Antenna

The top and bottom-side view of the 8 × 12 staggered Butterfly planar array antenna prototype is depicted in Fig. 6.18(a) and Fig. 6.18(b), respectively. This array antenna with all the feed lines and connectors are also modeled and simulated. The simulated and measured S-parameters of different branches of the array are presented in Figs. 6.19(a) and 6.19(b), respectively. The S-parameters include the impedance matching and inter-port isolation between the adjacent array elements. The impedance matching $|S_{ii}| < -10$ dB and inter-port isolation is better than 20 dB for both the simulation and measurement in the entire desired frequency bandwidth from 27.5 – 28.3 GHz.

The embedded element patterns of different branches of the array are measured with suitable excitation of the ports for the different polarization reconfigurable states. The embedded element patterns are obtained by exciting one branch at a time and match terminating other branches. For brevity, the embedded patterns are only shown for RHCP and Linear-X polarization at 28 GHz. The simulated and measured embedded RHCP element patterns of the 8 branches of the staggered Butterfly array along $\phi = 0°$ plane and $\phi = 90°$ plane are shown in Fig. 6.20(a) and Fig. 6.20(b), respectively. The slight variation in the results is due to the fabrication and measurement tolerance of the array. The simulated and measured Linear-X embedded element pattern at 28 GHz for the different branches are presented in Fig. 6.21(a) and Fig. 6.21(b), respectively.

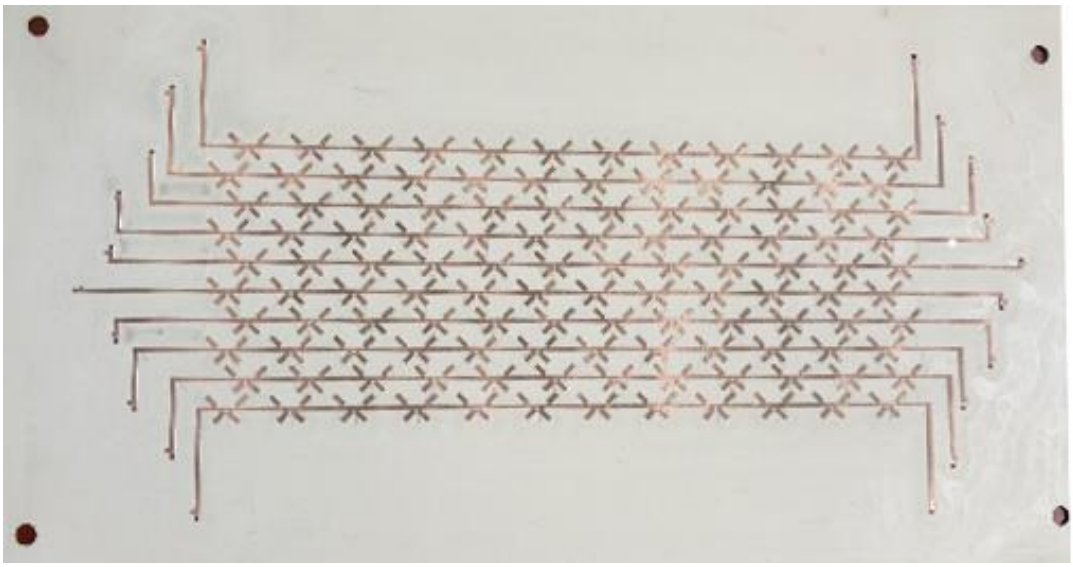

(a)

(b)

Figure 6.18 Photograph of the 8 × 12 series-fed Butterfly planar array antenna prototype (a) Top-side and (b) Bottom-side.

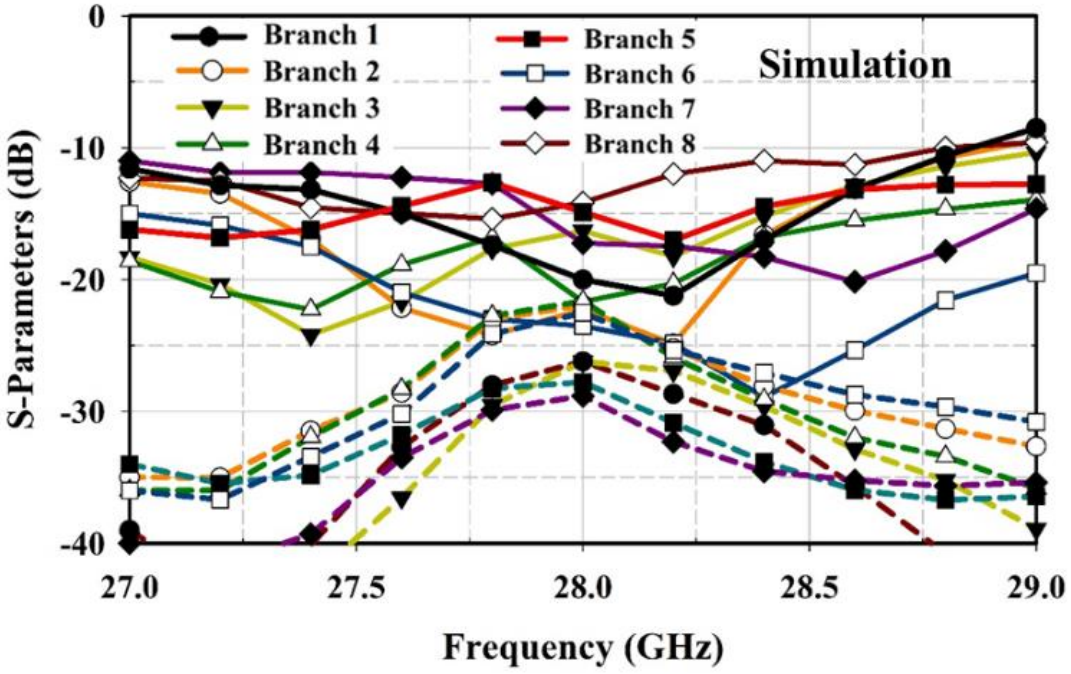

(a)

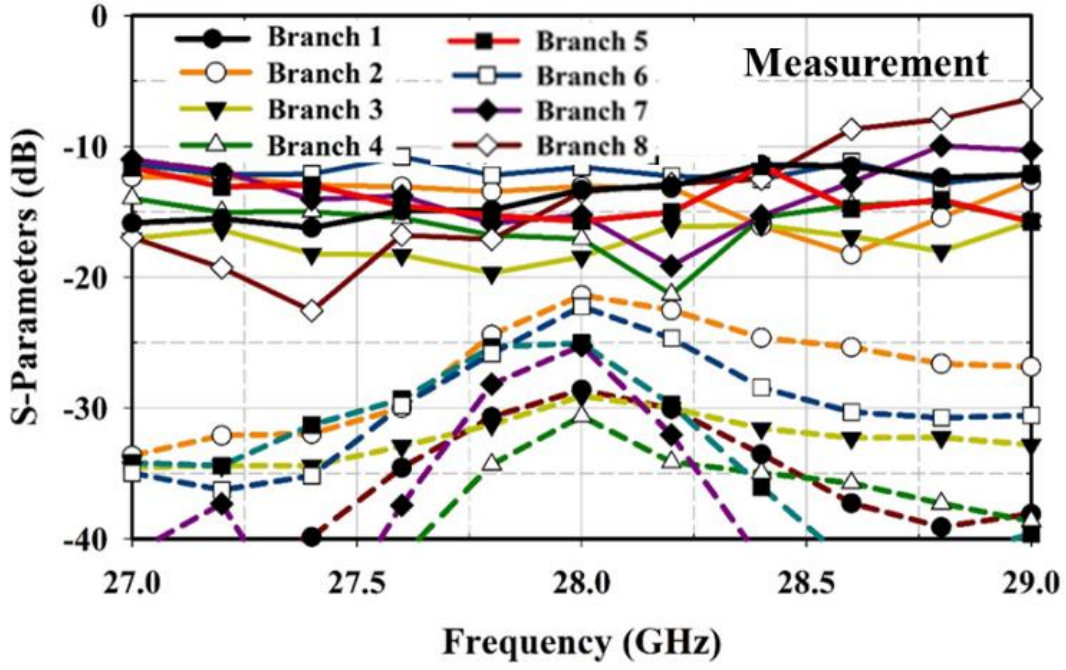

(b)

Figure 6.19 (a) Simulated and (b) Measured S-parameters for different branches of the 8 × 12 Staggered Butterfly planar array antenna. (Solid lines are impedance matching and dash lines are inter-port isolation).

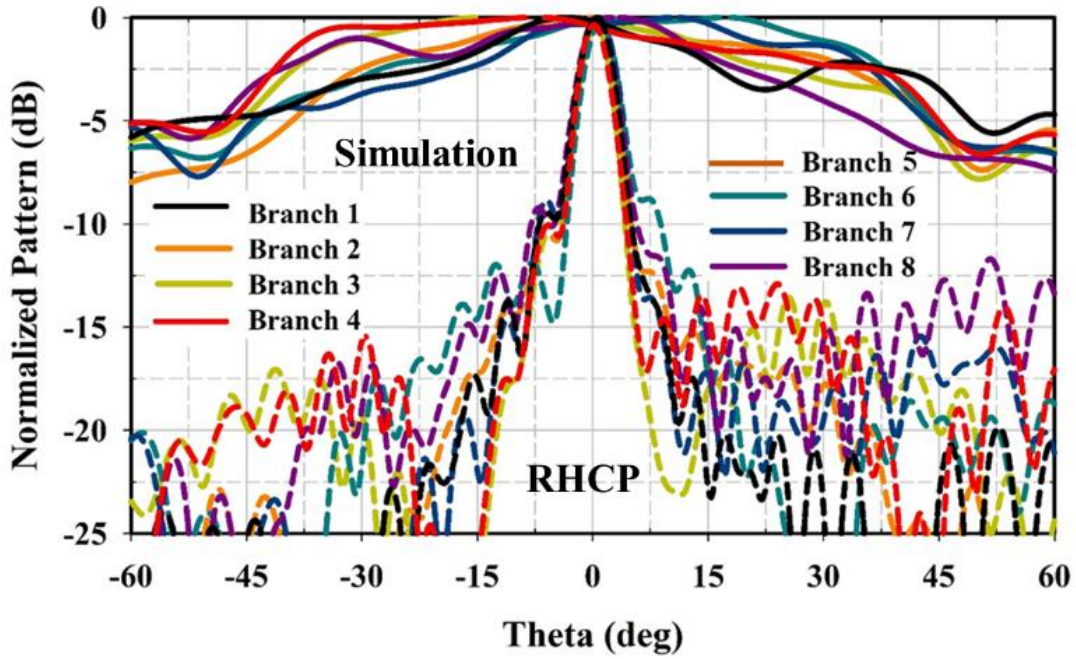

(a)

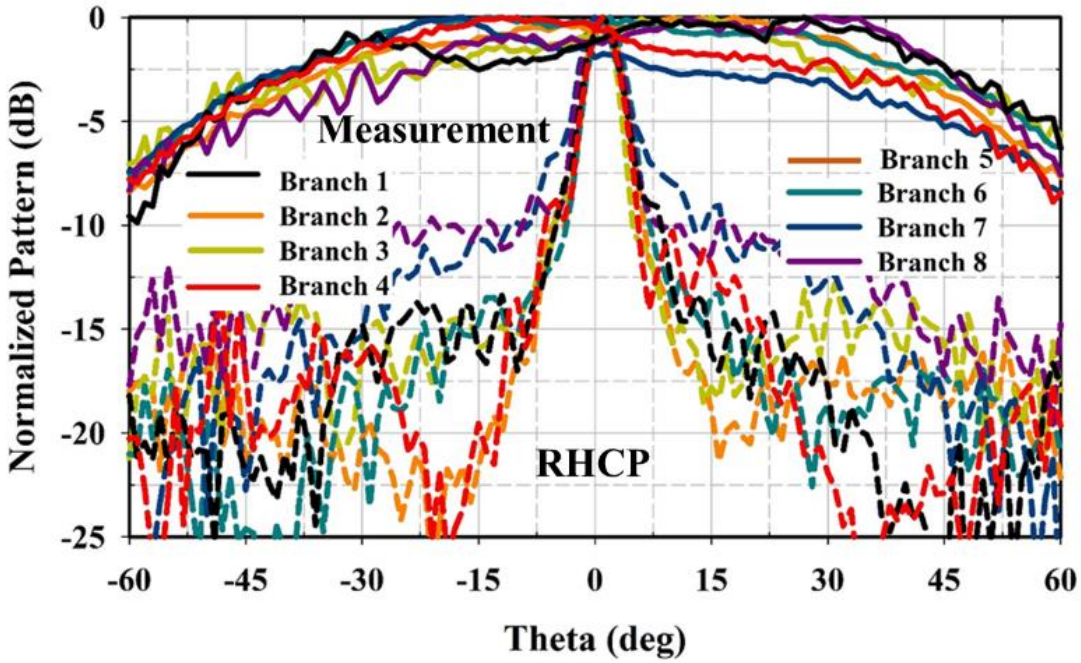

(b)

Figure 6.20 (a) Simulated and (b) Measured embedded RHCP element patterns of different branches of the 8 × 12 Butterfly planar array antenna at 28 GHz. Solid lines are along ϕ = 0° plane and dash lines are along ϕ = 90° plane.

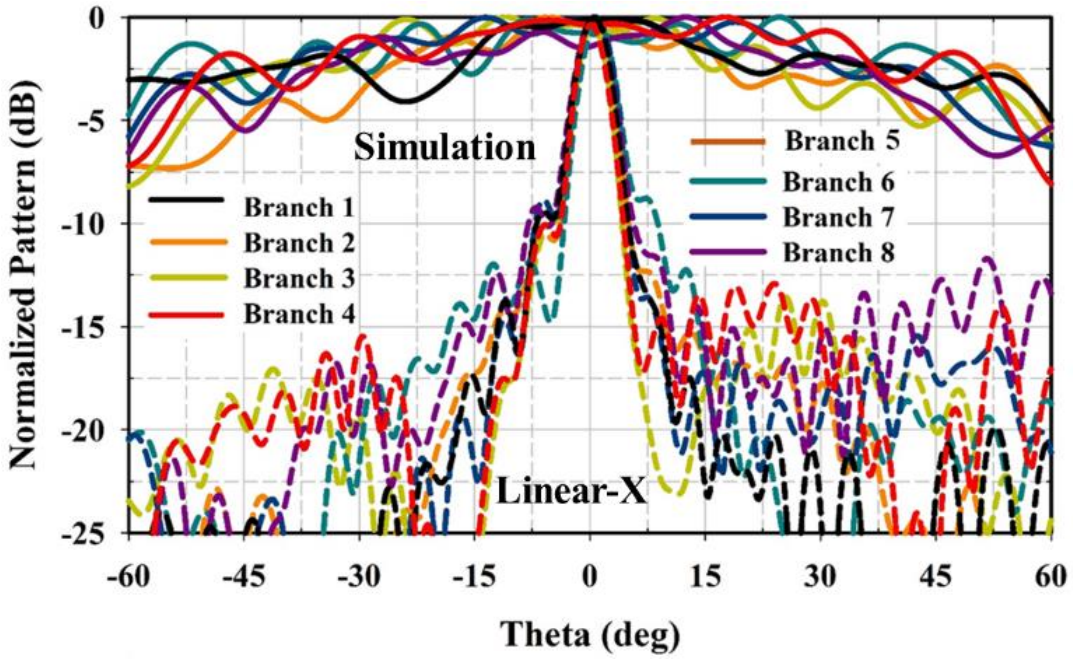

(a)

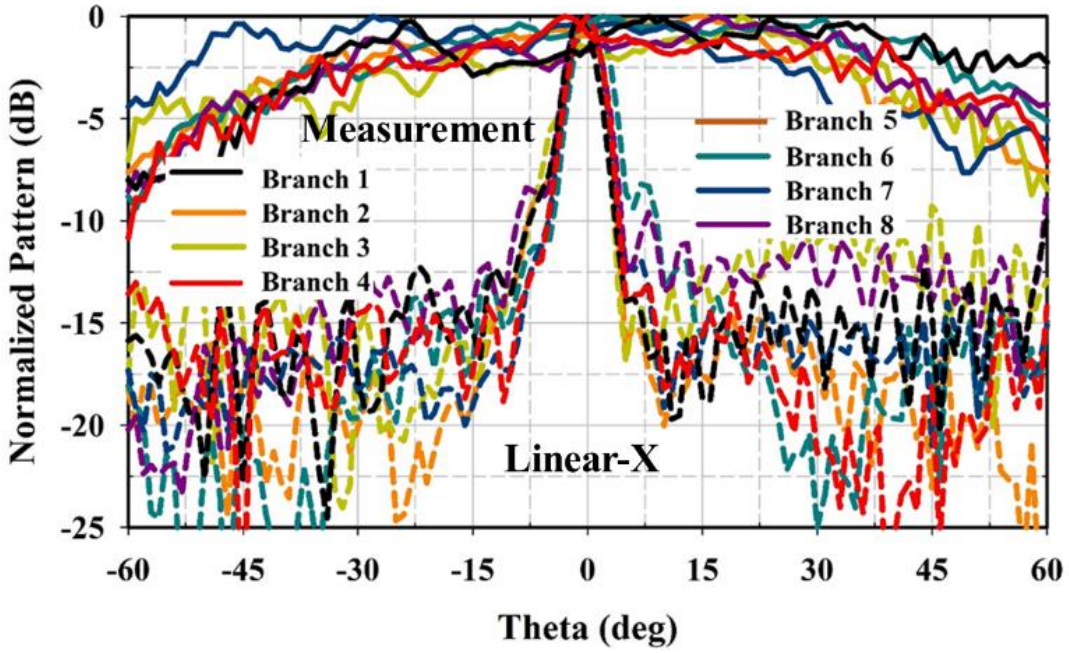

(b)

Figure 6.21 (a) Simulated and (b) Measured embedded Linear-X element patterns of different branches of the 8 × 12 Butterfly planar array antenna at 28 GHz. Solid lines are along ϕ = 0° plane and dash lines are along ϕ = 90° plane.

6.5.2 Computed Beam Steering of 8 × 12 Staggered Butterfly Planar Array Antenna Using Measured Embedded Patterns

The beam steering capability of the 8 × 12 staggered Butterfly array is computed by combining the measured embedded element patterns with the array factor using (6.12) [32]:

$$E^T\left(\theta,\phi\right)=\sum_{n=1}^{N}A_nE_n(\theta,\phi)e^{j(k_0x_n\sin\theta\cos\phi+\beta_n)} \tag{6.12}$$

where $\beta_n=-k_0x_n\sin\theta_{peak}$, x_n = (n-1)d, d is the inter-array spacing, N = 8 is the total number of linear arrays, $E_n(\theta, \phi)$ is the individual measured embedded element patterns, A_n is the amplitude excitation taper of each element corresponding to Chebyshev polynomial for SLL of 25 dB, and β_n is the progressive phase shift to steer the beam peak at θ_{peak} along ϕ = 0° plane.

The normalized computed 1D-beam steering of the 8 × 12 staggered Butterfly array antenna using the measured embedded element patterns are shown for RHCP and Linear-X polarization in Fig. 6.22(a) and Fig. 6.22(b), respectively. In both the polarization, the array is capable of steering to at least ±45° for 3 dB reduction in gain and without any grating lobes. The worst-case SLL is below 15 dB for the farthest beam steered angle. These computed beam steering patterns include the measured mismatch effects and mutual coupling between the different branches of the staggered array.

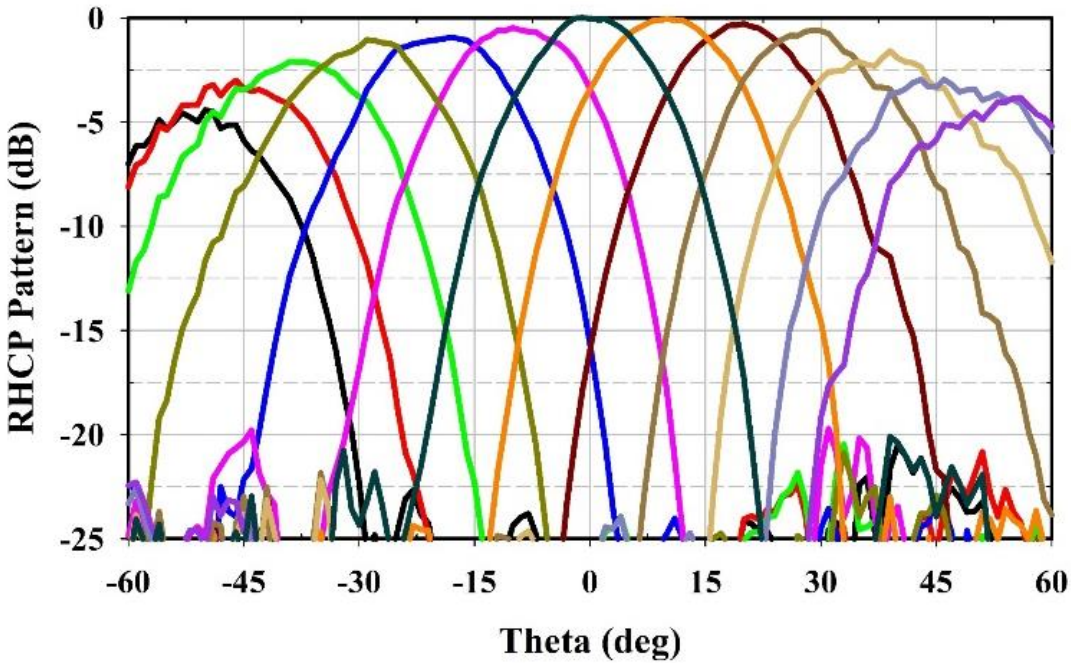

(a)

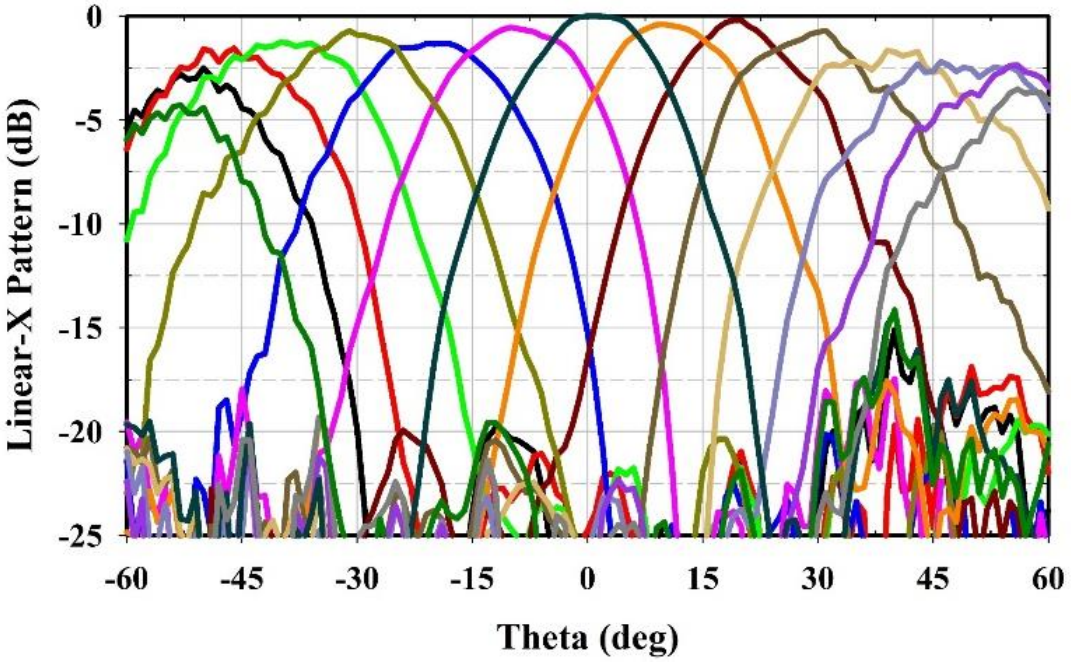

(b)

Figure 6.22 Computed 1D-beam steering radiation performance of the 8 × 12 Butterfly planar array antenna at 28 GHz along ϕ = 0° plane using measured embedded element patterns for (a) RHCP and (b) Linear-X polarization.

6.5.3 8 × 12 Staggered Butterfly Array Antenna Integrated with the ADMV4821 5G Beamformer Board

The radiation characteristics of the Butterfly staggered array antenna integrated with the Analog Devices ADMV4821 beamformer board is measured in the far-field anechoic chamber facility at the Antenna and Microwave Laboratory (AML) at San Diego State University (SDSU), as shown in Fig. 6.23. The beam synthesis algorithm is developed to provide the excitation weights for achieving the beamforming of full-polarization reconfiguration, and flexible radiation patterns.

The functional block diagram test set-up for the Analog Devices ADMV4821 beamformer board is shown in Fig. 6.24. The controller provides the serial peripheral interface (SPI) between the computer and the beamforming board to deliver the necessary beamforming excitation weights.

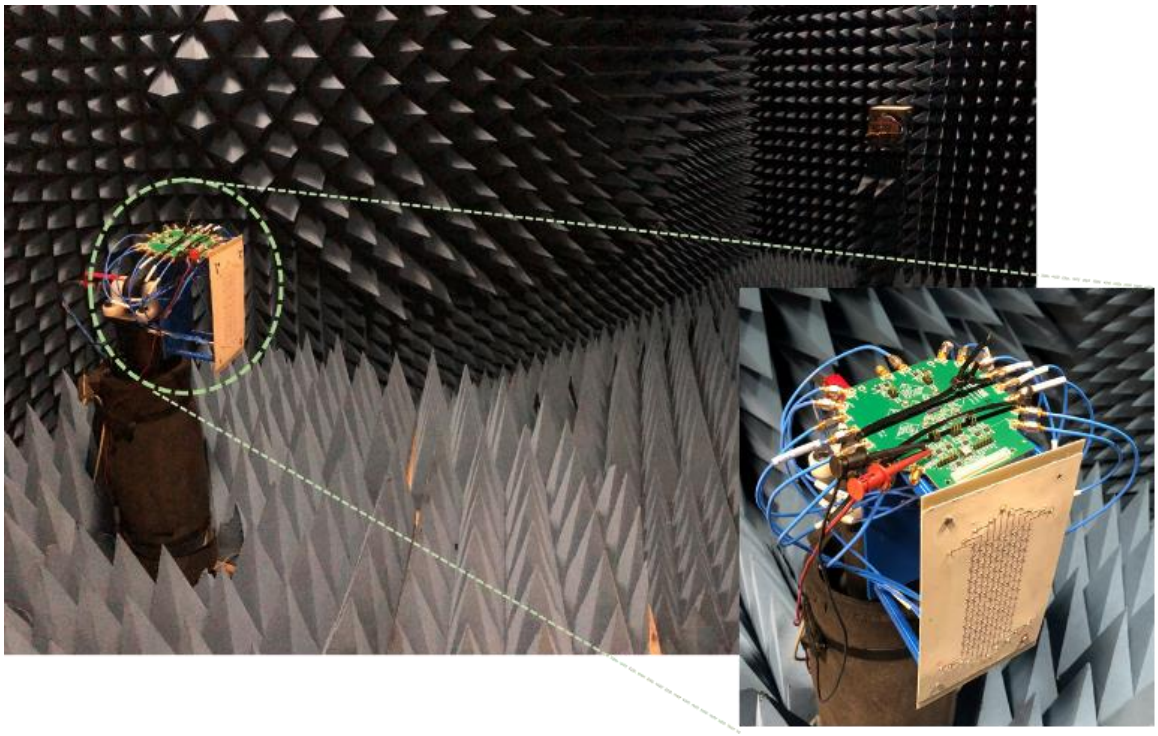

Figure 6.23 Photograph of the antenna integrated with the beamforming board inside the anechoic chamber at AML, SDSU.

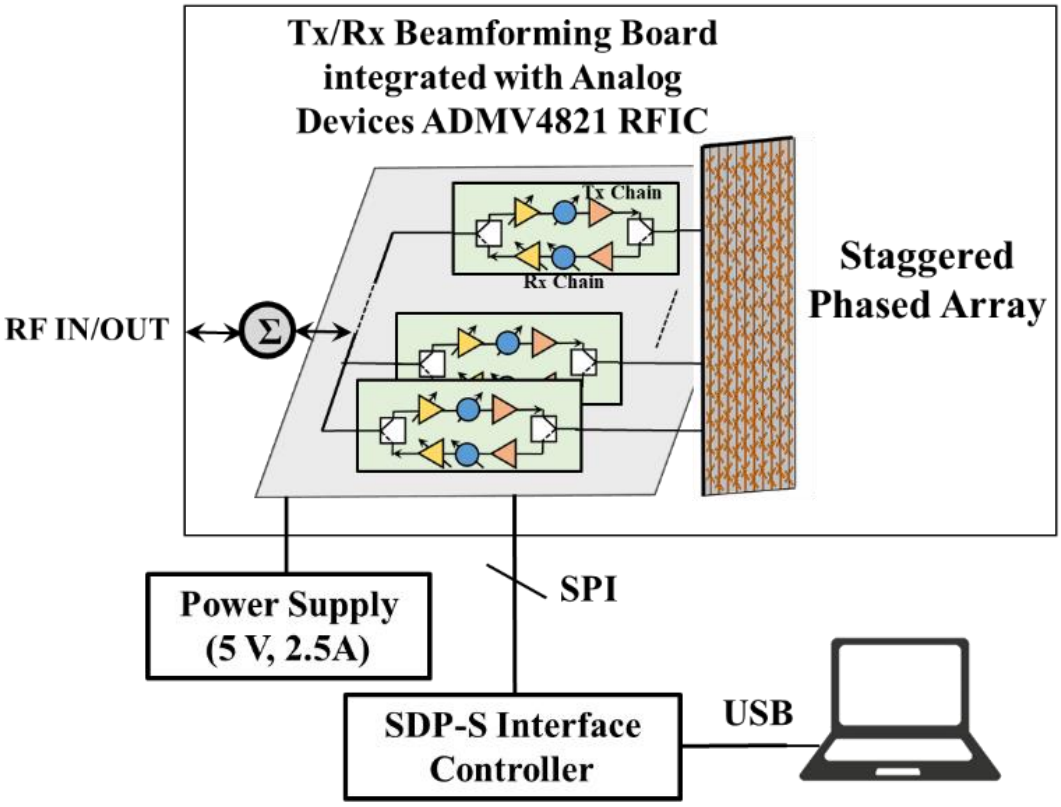

Figure 6.24 Functional block diagram set-up for the beamforming measurement of the integrated staggered Butterfly array antenna and beamforming board.

The ADMV4821 is a SiGe 24 – 29.5 GHz 5G beamformer highly integrated RFIC chip. It contains 16 independent transmit (TX) and receive (RX) channels. The RFIC chip provides 6-bit phase shift control and 0.5 dB amplitude step control.

The simulated and measured broadside AR as a function of frequency for the RHCP and LHCP polarization are presented in Fig. 6.25. The simulation and measurement results agree reasonably well, and the AR is below 3 dB in the entire desired 5G band between 27.5 – 28.35 GHz. The simulated total antenna efficiency of the 8 × 12 staggered Butterfly phased array is between 56% - 60% in the desired frequency bandwidth. The total antenna efficiency includes the effect of mismatch loss, conductor and dielectric losses, feed lines losses, and connector losses.

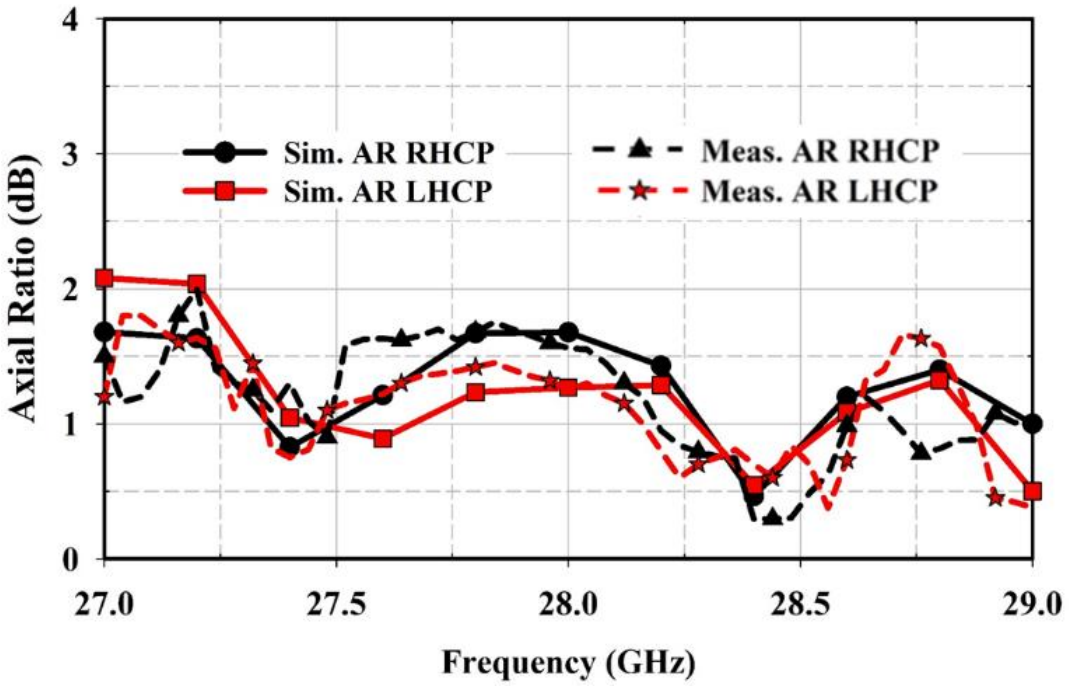

Figure 6.25 Simulated and measured AR for different CP polarizations and simulated total antenna efficiency vs. frequency.

The full-polarization reconfiguration is experimentally verified with the beamforming board integrated with the 8 × 12 staggered phased array antenna. The simulated and measured normalized broadside radiation patterns for the four polarization reconfigurable states, namely, RHCP, LHCP, Linear-X, and Linear-Y, are shown in Figs. 6.26(a) – 6.26(d), respectively, at 28 GHz. The simulated 3 dB gain-beamwidth in the ϕ = 0° plane is 16°, 15.6°, 16.2°, and 15.7° and the 3 dB gain-beamwidth in the ϕ = 90° plane is 4.7°, 4.8°, 4.4°, and 4.2° for the RHCP, LHCP, Linear-X, and Linear-Y polarization, respectively. The corresponding measured 3 dB gain-beamwidth in the ϕ = 0° plane is 17°, 16.1°, 16°, and 15.7° and the 3 dB gain-beamwidth in the ϕ = 90° plane is 5°, 4.9°, 4.5°, and 4.4° for the RHCP, LHCP, Linear-X, and Linear-Y polarization, respectively. The measured cross-polarization isolation for all the polarization is below 18 dB.

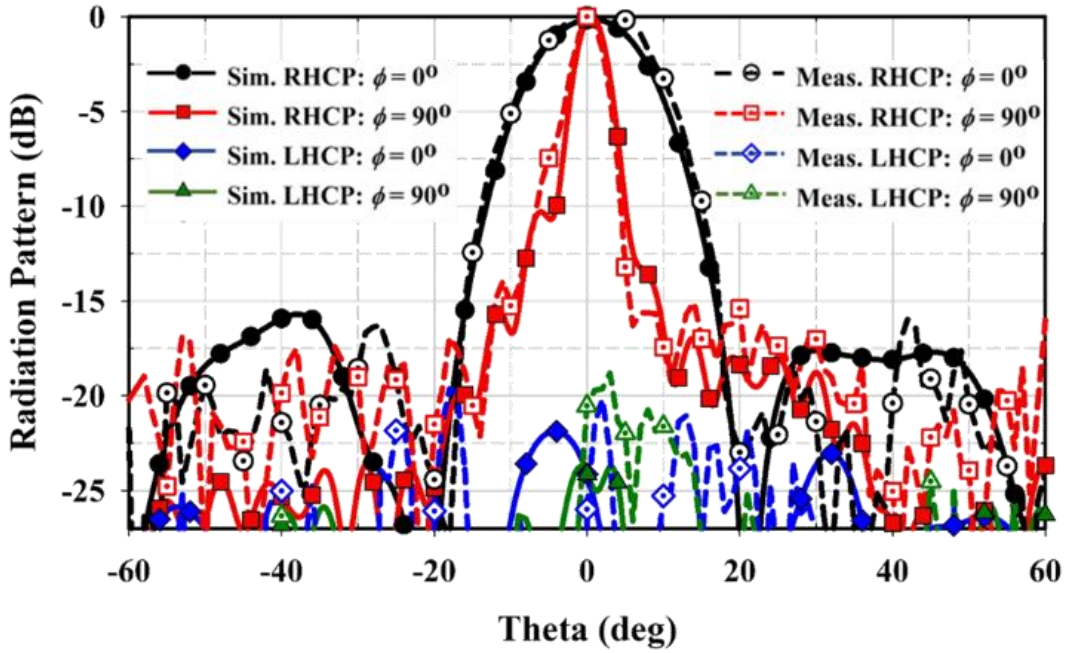
Radiation Pattern (dB)
0
-5
-10
-15
-20
-25
-60
-40
-20
0
20
40
60
Theta (deg)
Sim. RHCP: $\phi = 0^o$
Sim. RHCP: $\phi = 90^o$
Sim. LHCP: $\phi = 0^o$
Sim. LHCP: $\phi = 90^o$
Meas. RHCP: $\phi = 0^o$
Meas. RHCP: $\phi = 90^o$
Meas. LHCP: $\phi = 0^o$
Meas. LHCP: $\phi = 90^o$

(a)

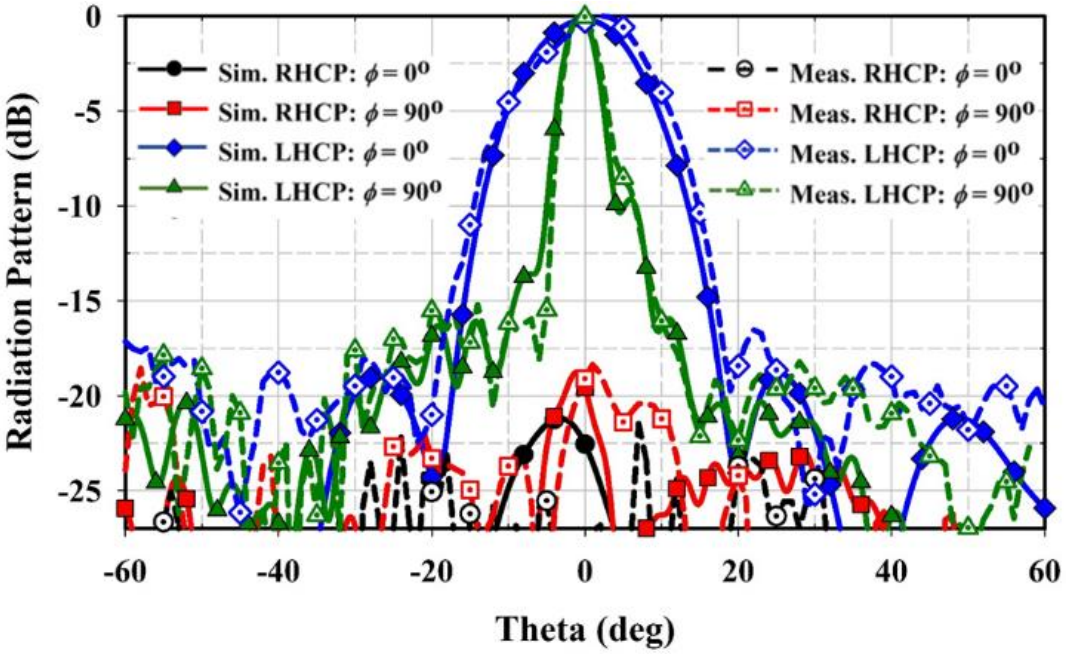
Radiation Pattern (dB)
0
-5
-10
-15
-20
-25
-60
-40
-20
0
20
40
60
Theta (deg)
Sim. RHCP: $\phi = 0^o$
Sim. RHCP: $\phi = 90^o$
Sim. LHCP: $\phi = 0^o$
Sim. LHCP: $\phi = 90^o$
Meas. RHCP: $\phi = 0^o$
Meas. RHCP: $\phi = 90^o$
Meas. LHCP: $\phi = 0^o$
Meas. LHCP: $\phi = 90^o$

(b)

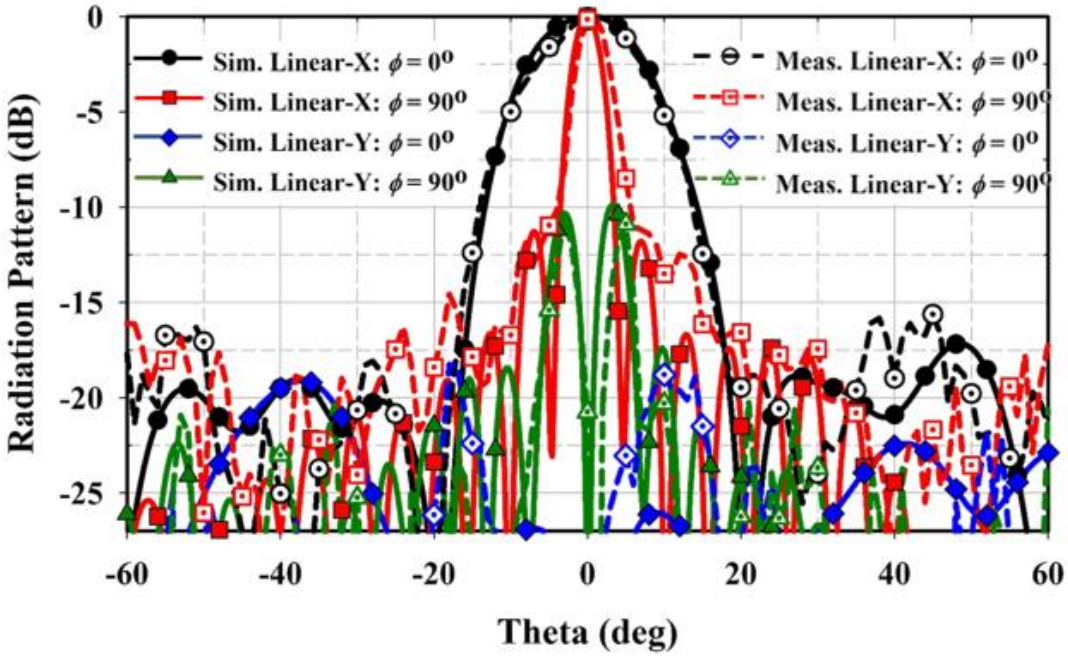

(c)

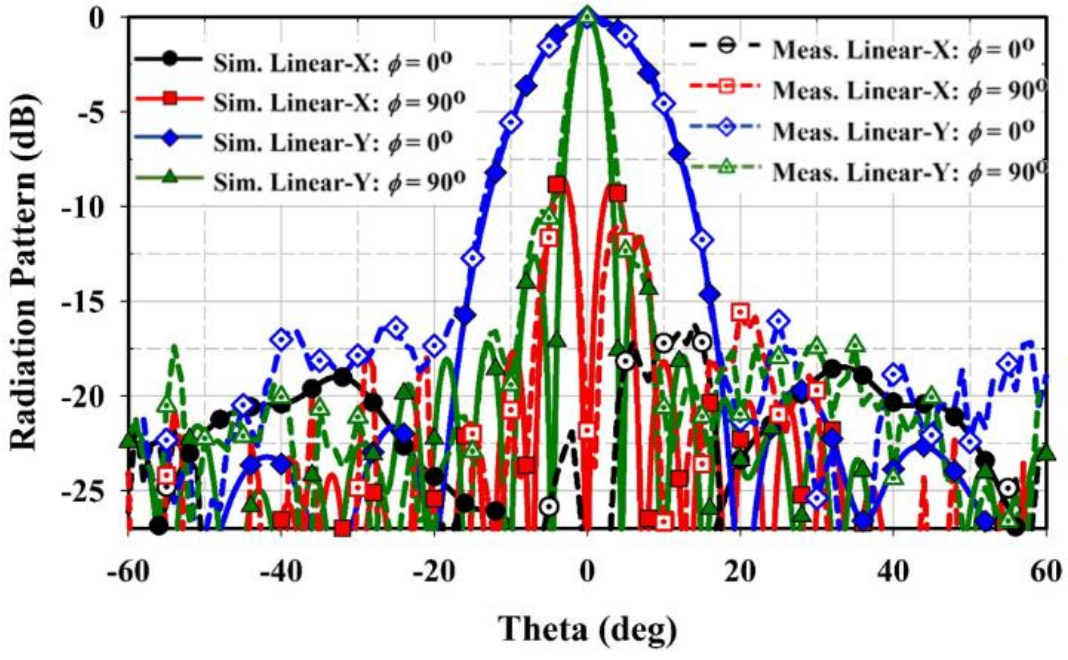

(d)

Figure 6.26 Simulated and measured polarization reconfigurable normalized radiation pattern of the 8 × 12 Butterfly planar array antenna at 28 GHz (a) RHCP (b) LHCP (c) Linear-X, and (d) Linear-Y polarization.

The measured flexible radiation patterns with selective excitation of branches are also verified, as shown in Fig. 6.27. The measured 3 dB gain-beamwidth varies from 17° when all the 8 linear-array branches are excited to 96° when only one linear-array branch is excited. The simulated and measured broadside RHCP and Linear-X realized gain as a function of frequency is plotted in Fig. 6.28. The broadside gain drops by around 3.5 dB for both the simulation and measurement in the squint bandwidth from 27.5 – 28.35 GHz. The simulated broadside realized gain at 28 GHz is 21.6 dBic and 21.8 dBi for RHCP and Linear-X polarization, respectively. The corresponding measured realized gain at 28 GHz is 21.2 dBic and 21.3 dBi for RHCP and Linear-X polarization, respectively.

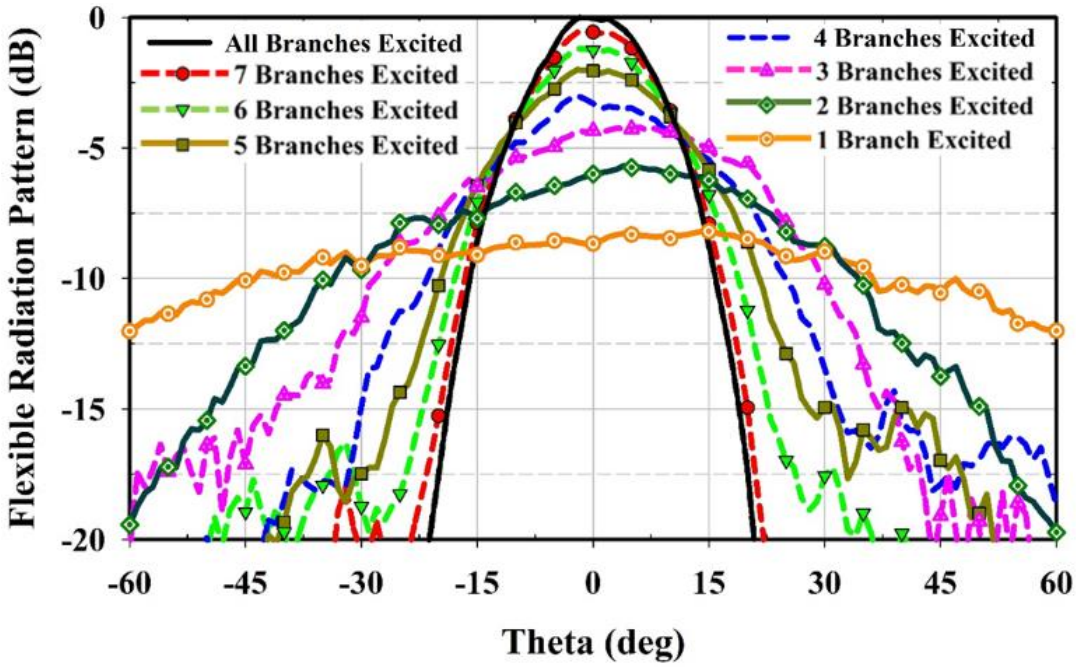

Figure 6.27 Measured flexible realized gain radiation pattern along ϕ = 0° plane for the 8 × 12 staggered Butterfly planar array antenna at 28 GHz.

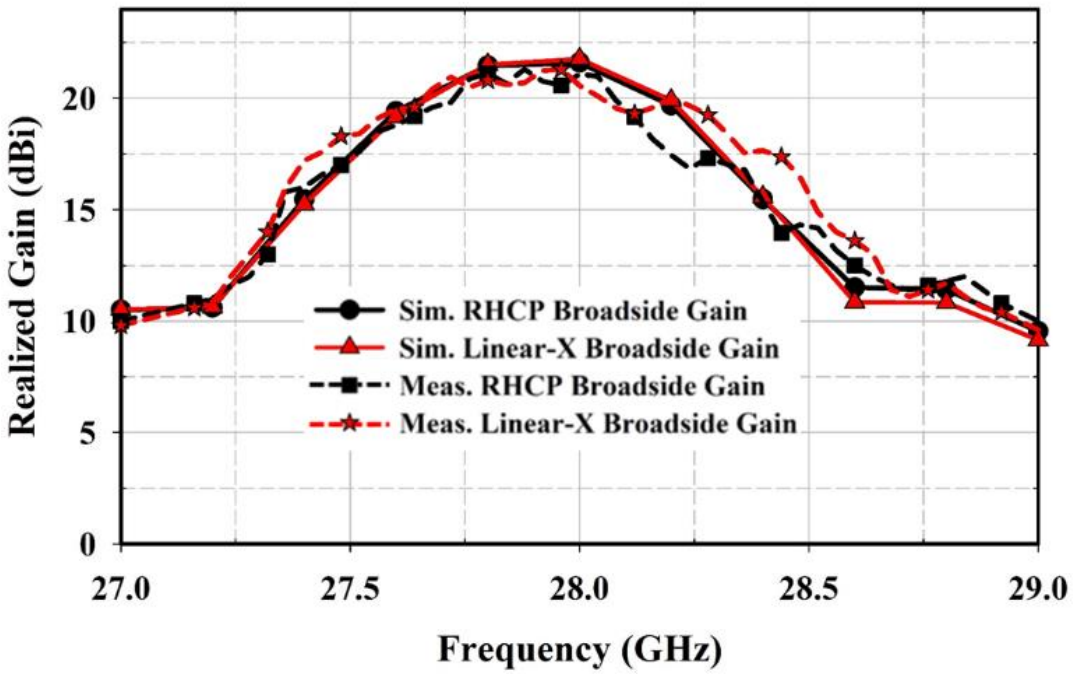

Figure 6.28 Simulated and measured broadside RHCP and Linear-X polarization realized gain of the 8 × 12 Butterfly Antenna.

The experimental verification of the beam steering with the integrated beamforming board is not performed at this stage as the interface could not be configured properly for the correct excitation phase shifts.

6.6 Conclusion

A novel multi-functional Butterfly element based full-polarization reconfigurable staggered phased array antenna was proposed with wide-angle 1D-beam steering and flexible radiation patterns at *Ka*-band (28 GHz). The proposed staggered array was shown to provide wide 1D-beam steering of ±84° without any grating lobes and at least ±45° for 3 dB reduction in the gain. The Analog devices ADMV4821 5G beamformer was integrated with the 8 × 12 staggered Butterfly array to provide full-polarization reconfigurable patterns, and the measurement results

were in excellent correlation with the simulation. Also, flexible radiation patterns were achieved with varying 3 dB gain-beamwidth between 16° to 90° with selective excitation of different channels. The aforementioned properties of the proposed array can be useful in 5G communications in addition to providing flexible cellular coverage.

The next chapter is an investigation into the 3D metal printed dual-CP horn antenna designed at *Ka*-band. It further expands to beam switching application where five proposed dual-CP feed-horn antennas will be placed along the focal arc of the spherical reflector to achieve high gain wide-angle beam switching.

Chapter 7

3D Metal Printed Dual Circular Polarized Feed Horn Antenna Feeding a Spherical Reflector for High Gain Multiple Beam Switching Application

7.1 Introduction

A dual CP horn antenna with high inter-port isolation is highly desired for increasing the system capacity of the wireless communication. In the *Ka*-band due to higher path loss, high gain antennas are required. In addition, multiple beams are desired to accommodate different users positioned in different directions. In this regard, a reflector with multiple dual-CP feed horn antenna can be an ideal candidate.

The metal 3D printing technique can be advantageous because of its lower cost, lighter weight, and faster prototyping. Another critical factor is that the 3D printing process can produce the proposed antenna in a single piece, which can reduce the assembly error. In [14], [15] 3D metal printed CP horn antenna at *Ka*-band and *V*-band are reported. In [14], the inbuilt polarizer consists of radially opposite grooves inside a circular waveguide and excited using a coaxial probe. In [15], the inbuilt polarizer consists of a mono-groove inside the circular waveguide and excited using waveguide ports.

In this research, we investigate a 3D metal printed dual CP feed horn antenna, which is used as a feed source to a spherical reflector to provide high gain. In addition, multiple horns placed along the focal arc of the spherical reflector can provide multiple-switched beams to cater to different users at various locations. The proposed feed horn polarizer is an extension to the polarizer in [9], which was designed by our research group at San Diego State University.

7.2 3D Metal Printing Process

3D metal printing is the process of manufacturing geometries using 3D printing technology. This process enables geometries that are unable to be produced by traditional manufacturing methods. The geometries can be topologically optimized to maximize their performance while minimizing their weight and contain the physical properties of metal superalloys.

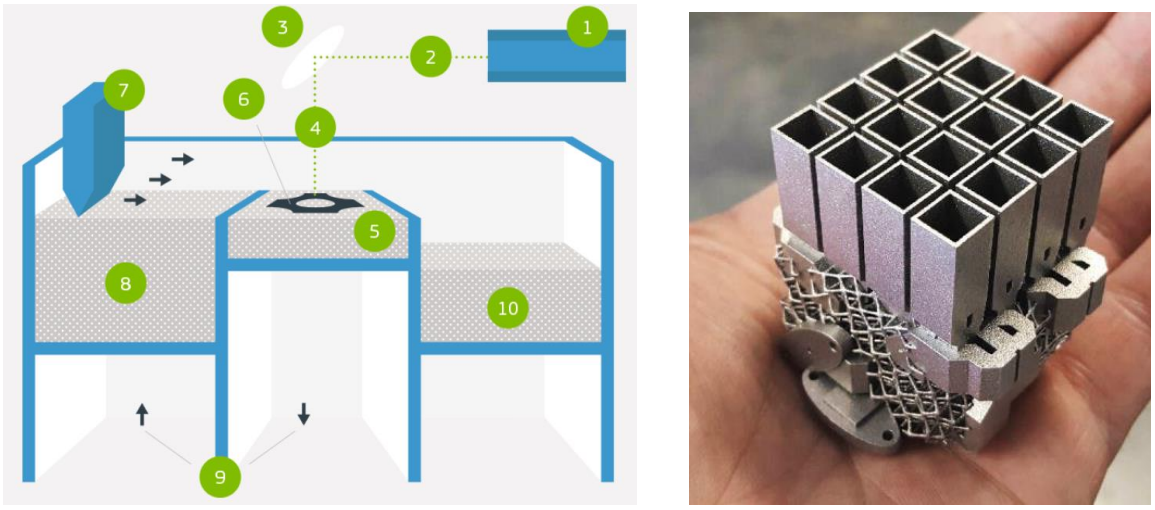

(a) (b)

Figure 7.1 DMLS 3D printing process (a) Components, and (b) Example of 3D metal printed satellite antenna [129].

Selective Laser Melting (SLM) and Direct Metal Laser Sintering (DMLS) are two metal additive manufacturing processes that belong to the powder bed fusion 3D printing family [129]. The two technologies use a laser to scan and selectively fuse the metal powder particles, bonding them together and building a part layer-by-layer. The SLM uses metal powders with a single melting temperature and fully melts the particles. In contrast, in DMLS, the powder is composed of materials with variable melting points that fuse on a molecular level at elevated temperatures.

SLM produces parts from a single metal, while DMLS produces parts from metal alloys. SLM and DMLS can produce geometries from a range of metals and metal alloys, including aluminum, stainless steel, titanium, and cobalt chrome.

The components of the DMLS 3D printer are shown in Fig. 7.1(a) and includes: 1. laser unit, 2. laser beam, 3. mirror/galvo motor system, 4. focused & directed beam, 5. build chamber, 6. manufactured part, 7. recoater blade, 8. powder supply container, 9. pistons, and 10. powder collection container [129]. An example of 3D metal printed antenna is shown in Fig. 7.1(b) [129].

7.3 Feed Horn and Reflector Specifications

The spherical reflector can provide wide-angle beam switching without degrading the beam shape, as opposed to a conventional parabolic reflector. The illustration of the spherical reflector antenna fed by five beam switched dual-CP antenna is shown in Fig. 7.2. The spherical reflector is in offset configuration and has an elliptical rim of size 25 cm × 35 cm. The feed source is the ideal fundamental mode CP horn antenna, analyzed in TICRA GRASP. Five of these feeds are placed along the focal arc of the spherical reflector. The design is proposed at *Ka*-band that supports axial ratio bandwidth (AR < 3 dB) of at least 26.5 – 29.5 GHz. The *f*/*D* ratio of the reflector is chosen as 0.6, which results in the feed tilt angle of 53.13° at the center of the reflector. The detailed feed horn and reflector specifications for the *Ka*-band beam switching application are presented in Table 7.1 and Table 7.2, respectively.

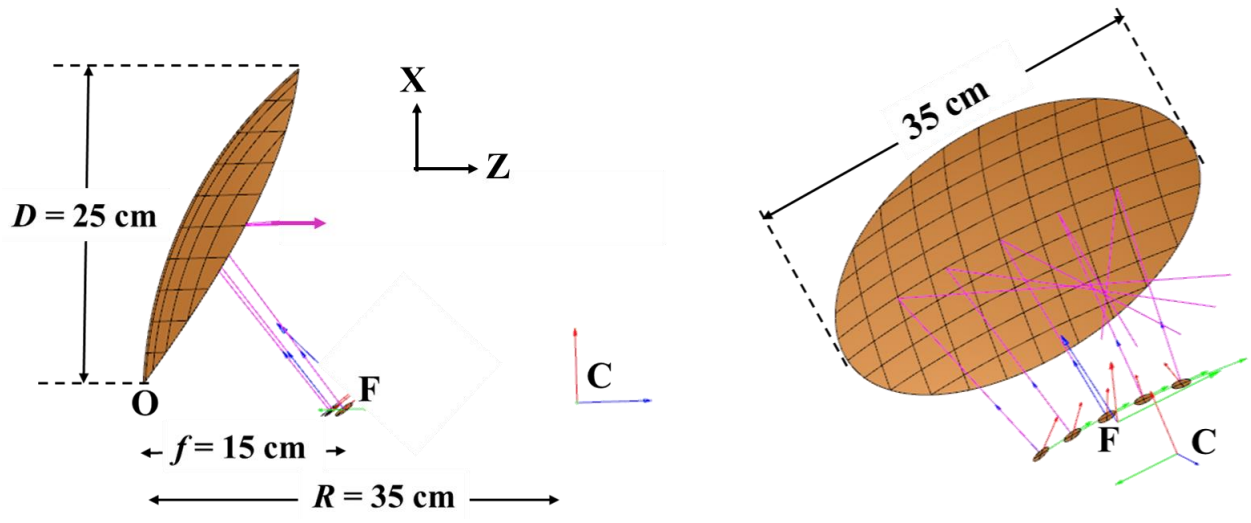

(a) (b)

Figure 7.2 Spherical reflector geometry with five dual CP feed sources along the focal arc modeled in TICRA GRASP (a) Side view, and (b) Isometric view.

Table 7.1 Feed horn antenna specifications for the *Ka*-band beam switching application.

Feed Horn Antenna Specifications	
12 dB half-beamwidth	40°
Polarization	Dual CP: RHCP and LHCP
Frequency of Operation (AR < 3 dB)	26.5 – 29.5 GHz
Inter-Port Isolation	> 20 dB
Impedance Matching $\lvert S_{ii} \rvert$	< -15 dB

Table 7.2 Spherical reflector specification for the beam switching application.

Spherical Reflector Specifications	
Configuration	Offset
Number of dual CP Feeds	5
Elliptical Rim size	25 cm × 35 cm
Reflector Diameter *D*	25 cm
f/*D*	0.6
Radius of Sphere *R*	35 cm
Feed tilt at center of reflector	53.13°

7.4 Ideal Feed-Reflector patterns

The feed used in the initial analysis in TICRA GRASP is a fundamental mode circular waveguide CP source. The radiation pattern of the fundamental mode CP pattern at 28 GHz, as used in TICRA GRASP, is shown in Fig. 7.3. The feed has a 12 dB half beamwidth of 40° and a peak directivity of around 13.5 dBic.

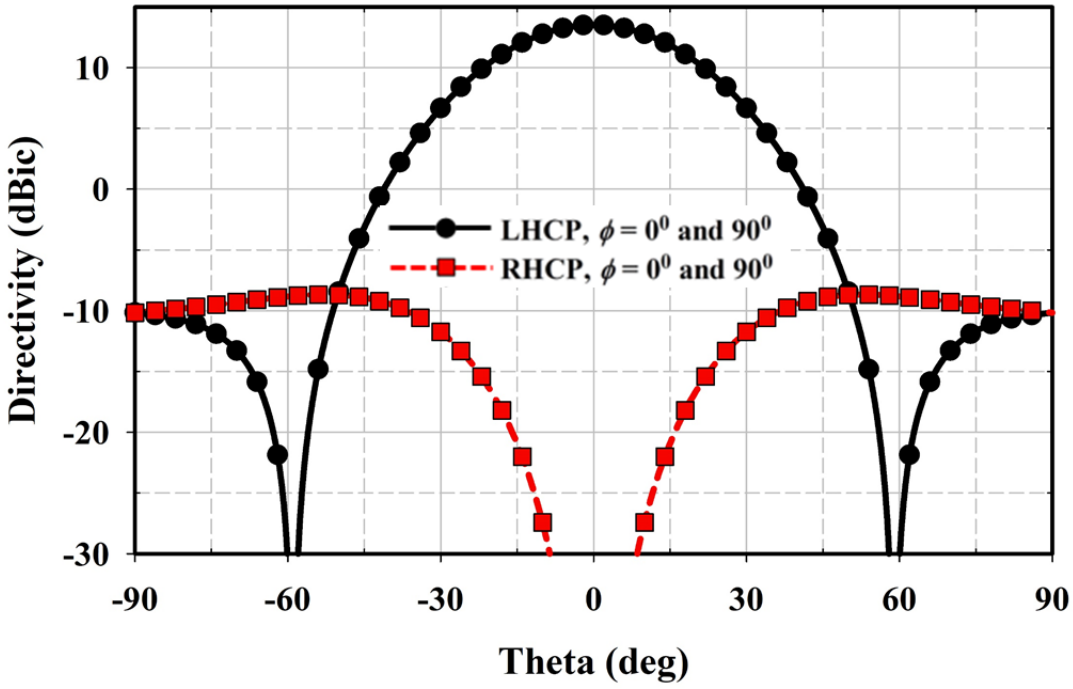

Figure 7.3 Ideal fundamental circular waveguide mode CP radiation pattern source in TICRA GRASP at 28 GHz.

Five ideal fundamental mode CP feed sources are placed along the focal arc of the spherical reflector, and the beam switching characteristics are investigated using TICRA GRASP. The co-polarization and cross-polarization five beams spherical reflector patterns are shown in Fig. 7.4(a) and Fig. 7.4(b), respectively. The peak co-pol CP directivity is 32.3 dBic, and the 3 dB beamwidth is 2.4°. The feeds are placed along the focal arc such that the beam scans at ±10° and ±20°. The cross-polarization isolation of the reflector is around 22 dB with the ideal fundamental feed source.

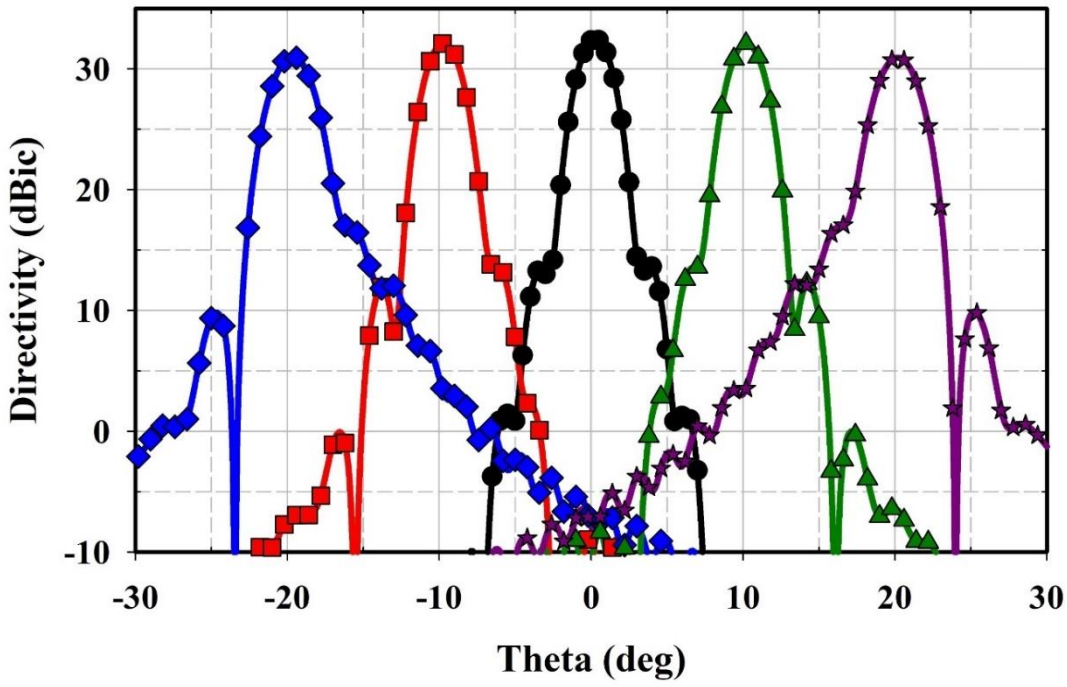

(a)

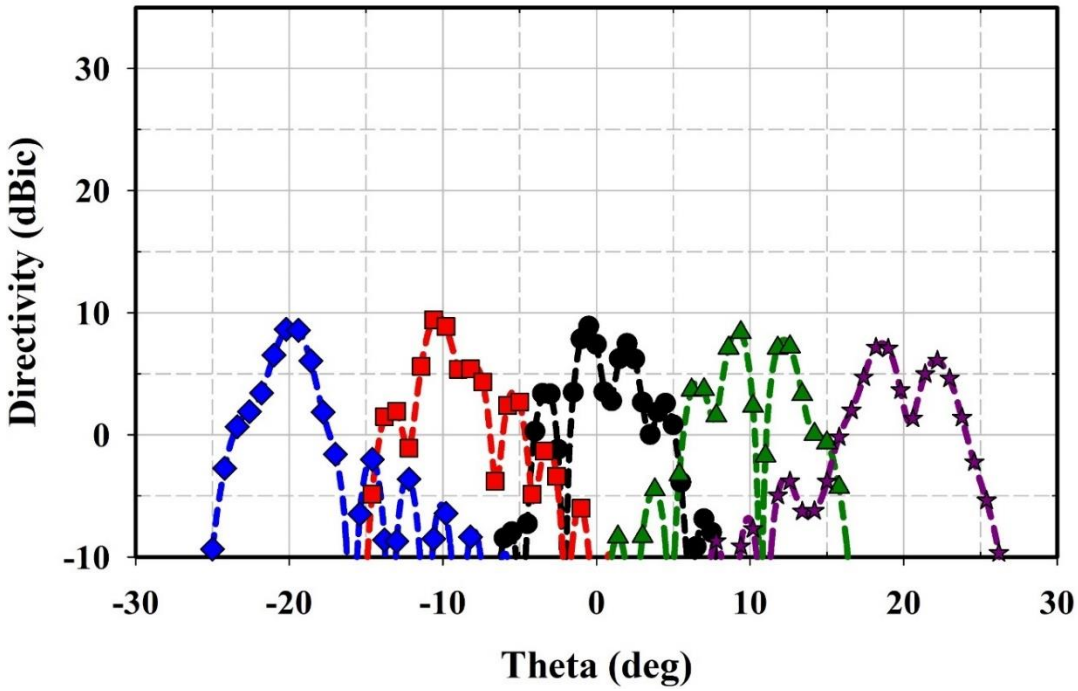

(b)

Figure 7.4 Multiple beam switching spherical reflector directivity patterns at 28 GHz (a) Co-pol patterns; (b) Cross-polarization patterns.

This study will help in the verification and comparison of the spherical reflector performance when fed with the actual proposed dual-CP feed horn antenna.

7.5 Initial Dual-CP Polarizer Geometry and its Characteristics

The initial dual-CP feed polarizer is the structure from [14], as shown in Fig. 7.5. The inbuilt polarizer contains radially opposite rectangular groove pairs inside a circular waveguide section. The groove is placed at 45° with respect to the input excitation. It results in the electric field to split into two different components, one along the groove direction and the other orthogonal to it. The field along the groove experiences an additional time-phase delay of 90°, thus generating

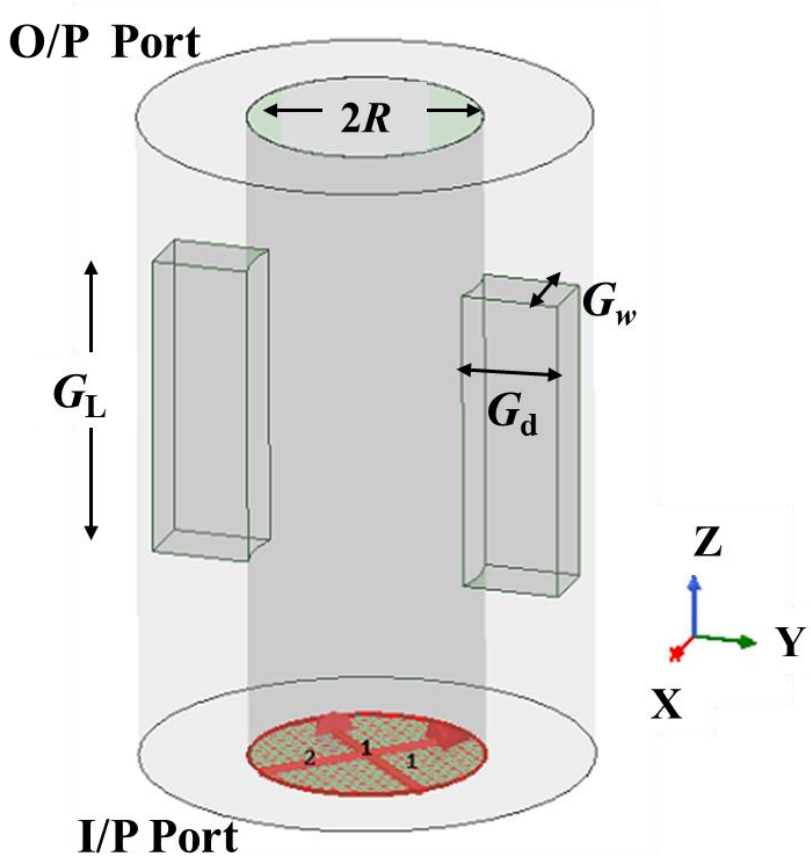

Figure 7.5 Initial dual-CP polarizer geometry.

CP at the output port. The design parameters of the inbuilt dual-CP polarizer are groove length G_L = 9 mm, groove depth G_d = 2.6 mm, groove width G_w = 2 mm, and the circular waveguide of radius R = 3.5 mm. Aluminum metal thickness of at least 0.5 mm is used to model the polarizer.

The polarizer can be represented as a 4-port device as there are two input port modes and two output port modes. The corresponding 4 × 4 scattering matrix of the polarizer is given as (7.1). It shows that when input port 1 is excited RHCP field is generated at the output port, and when input port 2 is excited, then LHCP field is generated at the output port.

$$S = \frac{1}{2}\begin{bmatrix} 0 & 0 & \sqrt{2}\cdot e^{-j\beta_1 L} & -j\sqrt{2}\cdot e^{-j\beta_2 L} \\ 0 & 0 & -\sqrt{2}\cdot e^{-j\beta_1 L} & -j\sqrt{2}\cdot e^{-j\beta_2 L} \\ \sqrt{2}\cdot e^{-j\beta_1 L} & -\sqrt{2}\cdot e^{-j\beta_2 L} & 0 & 0 \\ -j\sqrt{2}\cdot e^{-j\beta_1 L} & -j\sqrt{2}\cdot e^{-j\beta_2 L} & 0 & 0 \end{bmatrix} \tag{7.1}$$

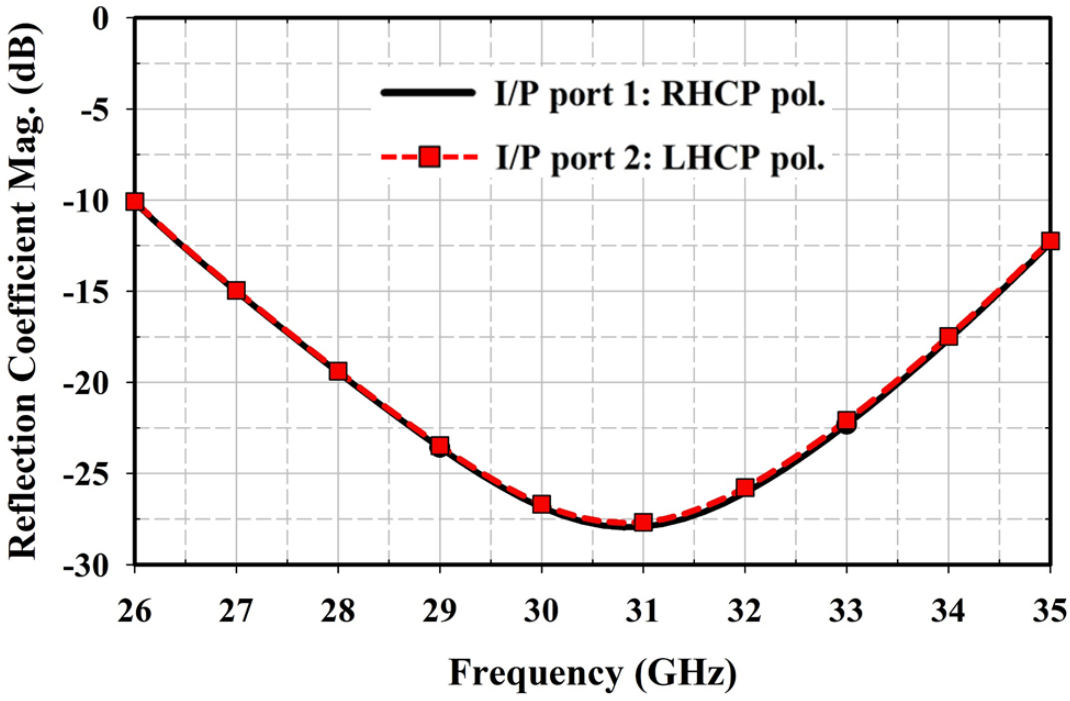

Figure 7.6 Simulated reflection coefficient magnitude of the initial polarizer for the two input modes.

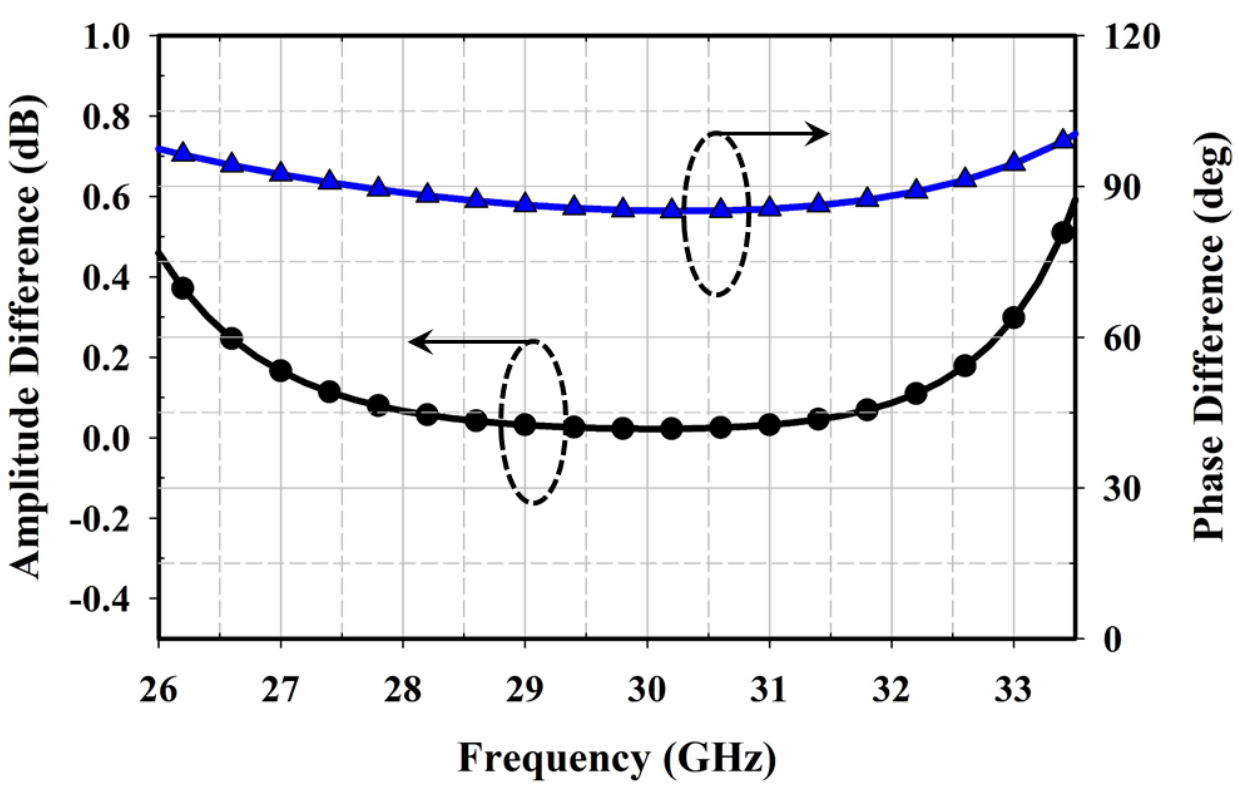

Figure 7.7 Simulated amplitude and phase imbalance between the two output port modes of the initial dual-CP polarizer.

This initial polarizer geometry is simulated using Ansys HFSS, and the reflection coefficient magnitude of the polarizer is presented in Fig. 7.6. The impedance matching $|S_{ii}| < -15$ dB is from 27 – 34 GHz.

The amplitude and phase imbalance of the two output port modes are shown in Fig. 7.7. The amplitude imbalance is less than 0.15 dB and the phase difference between the two output pot modes is less than 10° between 27 – 32 GHz. The simulated AR as a function of frequency for the dual-CP initial polarizer is shown in Fig. 7.8. The broadside AR is less than 1 dB within the desired frequency of 27 – 32 GHz bandwidth. The AR beamwidth for different phi cut-planes at 27 GHz, 30 GHz, and 33 GHz are presented in Figs. 7.9(a), 7.9(b), and 7.9(c), respectively. It is worth

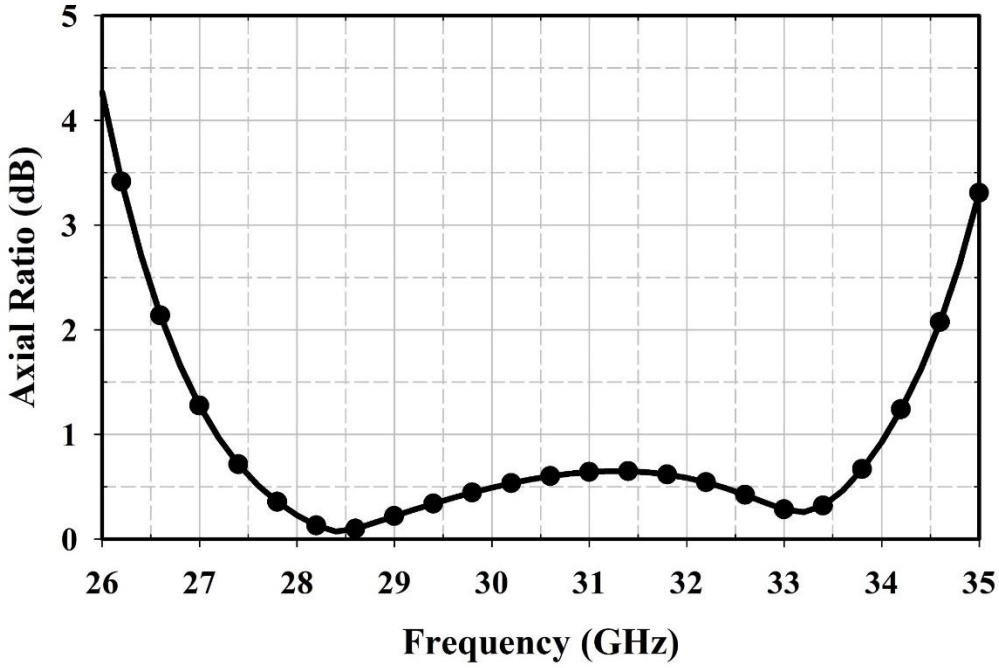

Figure 7.8 Simulated axial ratio vs. frequency of the initial polarizer geometry.

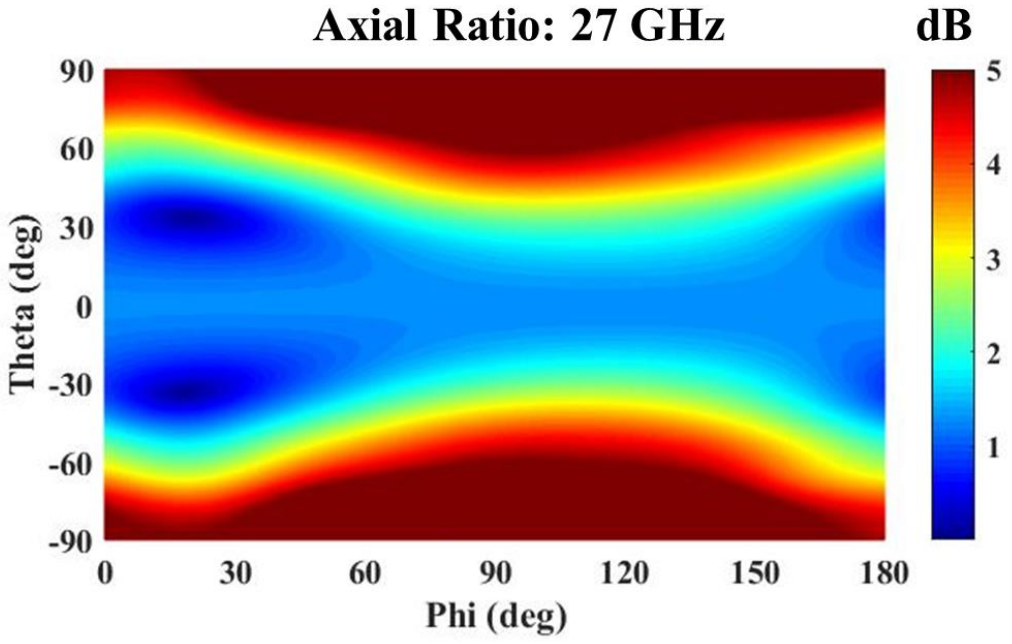

(a)

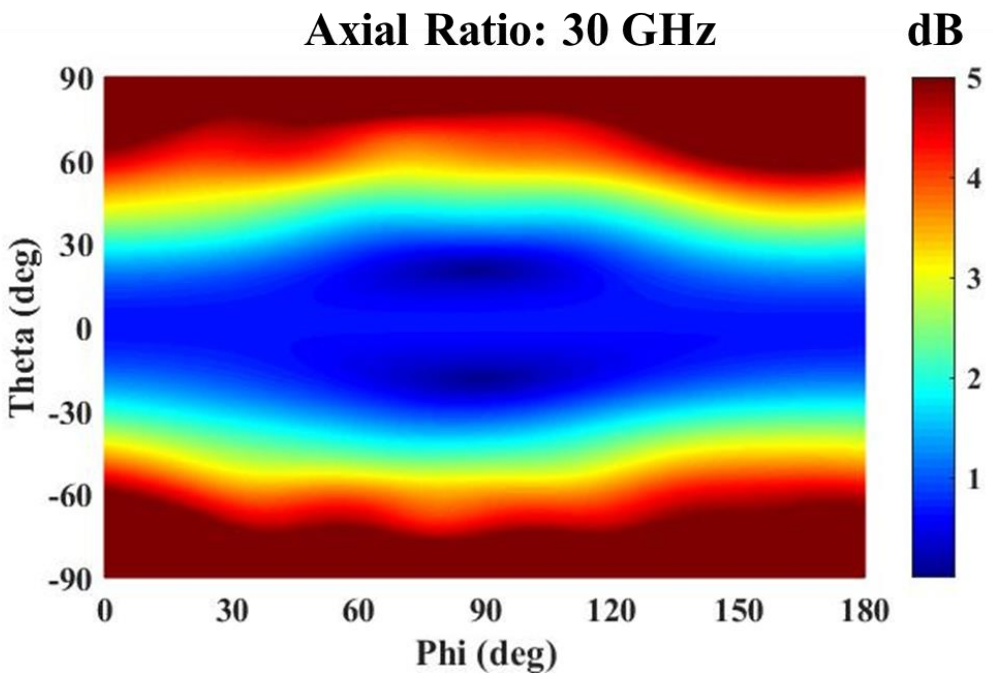

(b)

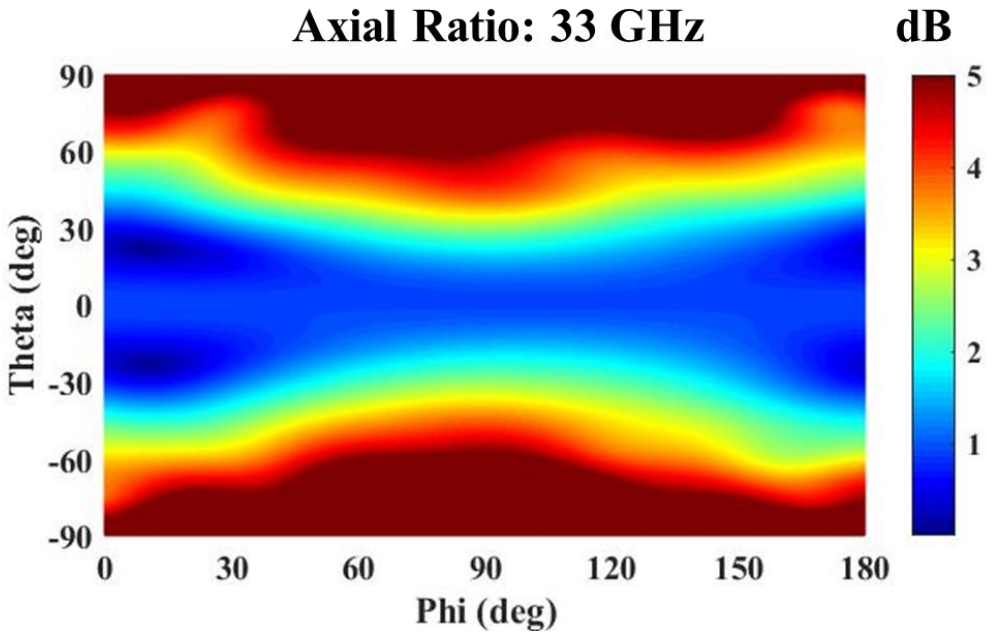

(c)

Figure 7.9 Simulated intensity plot of the AR of the initial polarizer geometry at (a) 27 GHz, (b) 30 GHz, and (c) 33 GHz.

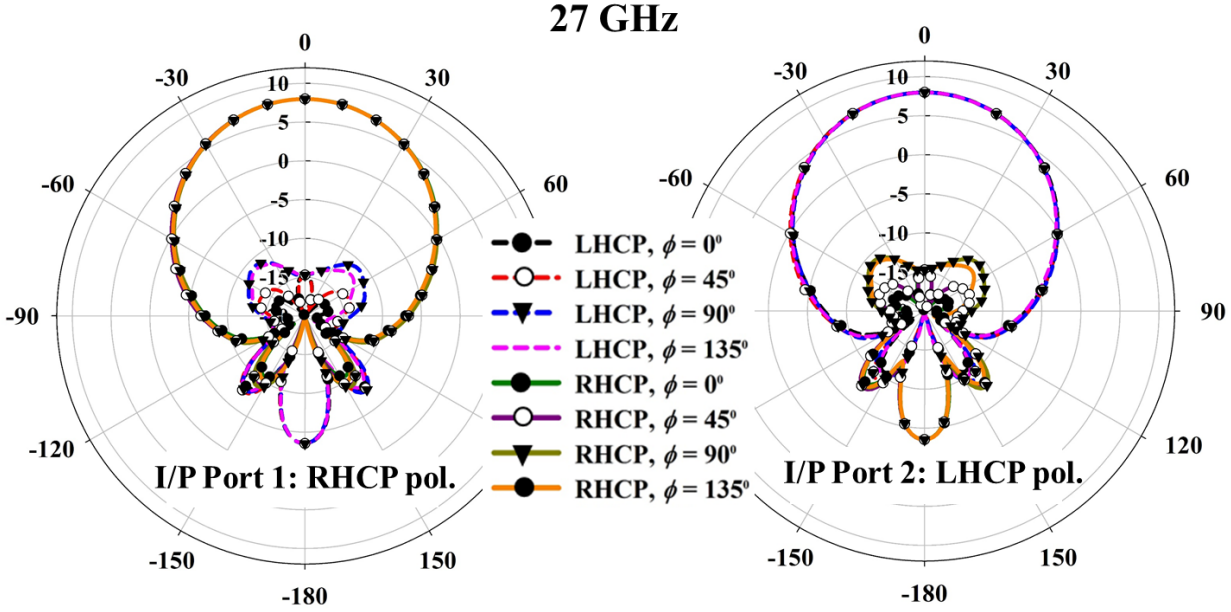
27 GHz
I/P Port 1: RHCP pol.
I/P Port 2: LHCP pol.
LHCP, ϕ = 0°
LHCP, ϕ = 45°
LHCP, ϕ = 90°
LHCP, ϕ = 135°
RHCP, ϕ = 0°
RHCP, ϕ = 45°
RHCP, ϕ = 90°
RHCP, ϕ = 135°

(a)

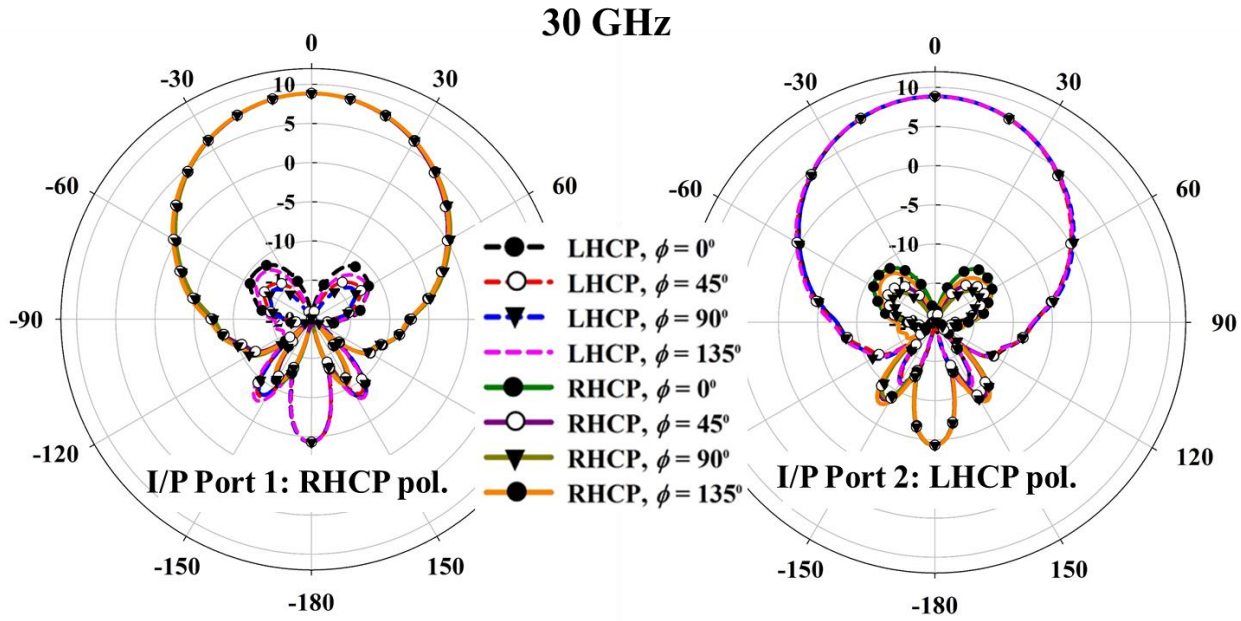
30 GHz
I/P Port 1: RHCP pol.
I/P Port 2: LHCP pol.
LHCP, ϕ = 0°
LHCP, ϕ = 45°
LHCP, ϕ = 90°
LHCP, ϕ = 135°
RHCP, ϕ = 0°
RHCP, ϕ = 45°
RHCP, ϕ = 90°
RHCP, ϕ = 135°

(b)

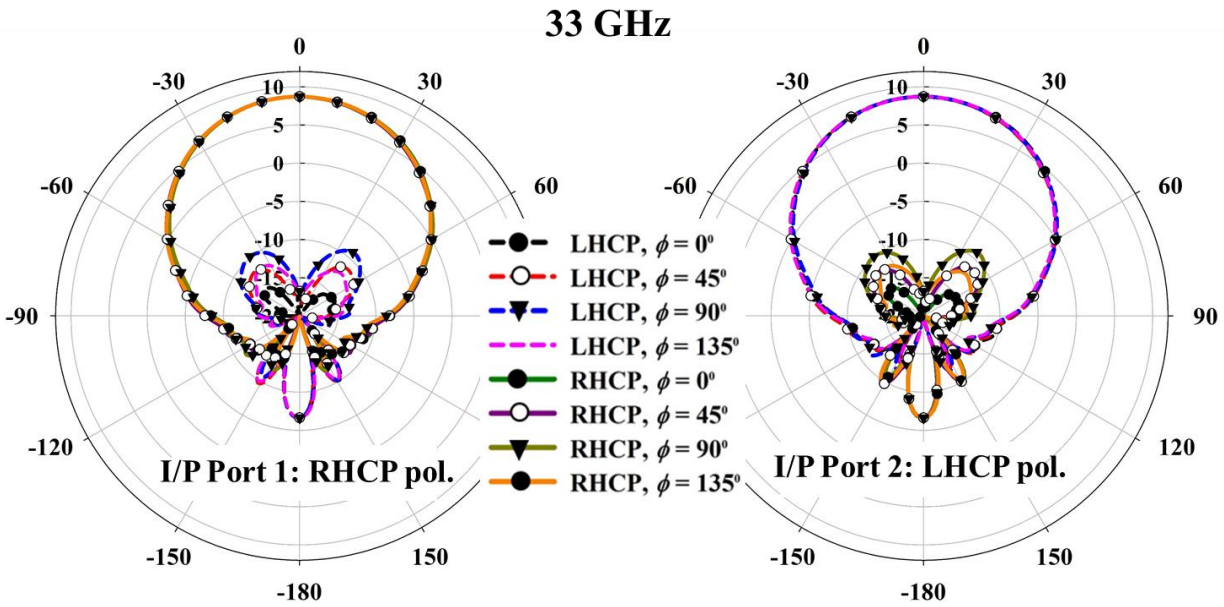

(c)

Figure 7.10 Simulated 2D realized gain radiation patterns of the initial polarizer geometry at (a) 27 GHz, (b) 30 GHz, and (c) 33 GHz.

noting that the average 3 dB AR beamwidth for the initial polarizer geometry is around 90° across different phi cut planes. The corresponding RHCP and LHCP polarization realized gain radiation patterns at 27 GHz, 30 GHz, and 33 GHz are shown in Figs. 7.10(a), 7.10(b), and 7.10(c), respectively. The average 10 dB half-angle beamwidth is 64° for the initial polarizer.

7.6 Modified Dual-CP Polarizer Geometry and its Characteristics

The initial polarizer design provides a wide AR < 3 dB bandwidth, but the average 3 dB AR beamwidth is limited to only 90°. Accordingly, the initial polarizer aperture is modified to include corrugated teeth, as shown in Fig. 7.11. The corrugated teeth at the aperture modify the output *E*-field to be more uniform, thus providing wide AR beamwidth. The teeth design parameters are teeth depth T_d = 2 mm, and teeth height is T_h = 1.3 mm.

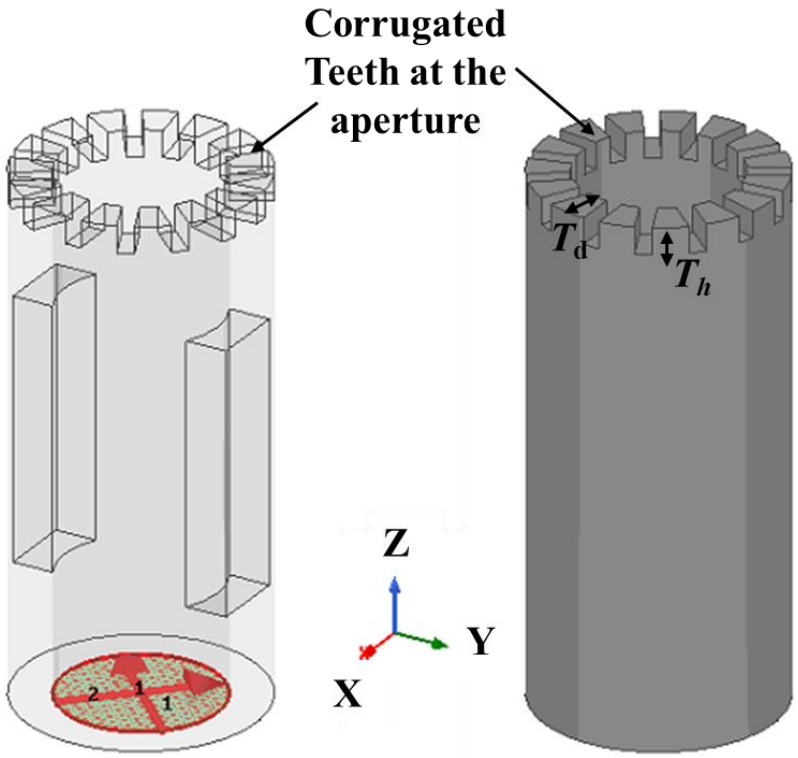

Figure 7.11 Proposed modified dual-CP polarizer geometry with corrugated teeth at the aperture for wide AR beamwidth.

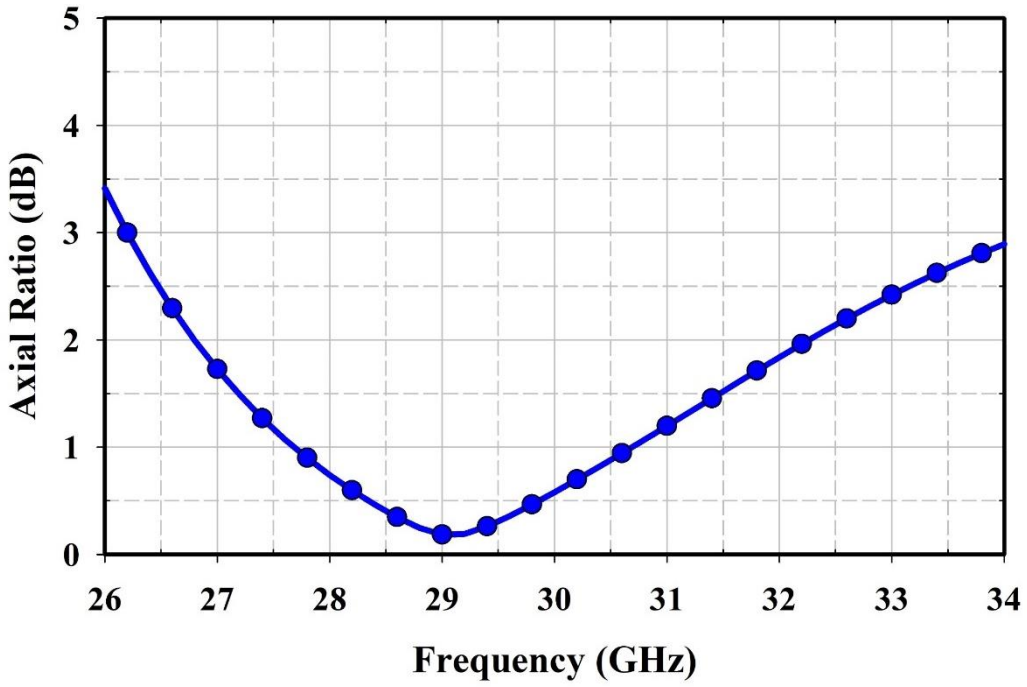

Figure 7.12 Simulated axial ratio vs. frequency of the modified polarizer geometry.

The AR as a function of the frequency of this modified polarizer is shown in Fig. 7.12. The broadside AR < 2 dB is between 27 – 32 GHz. However, the advantage of this design is in achieving wide AR beamwidth, as presented in the AR intensity plots of Fig. 7.13. As observed, the AR beamwidth is less than 3 dB for almost the entire hemisphere across 27 – 32 GHz.

The 2D realized gain RHCP and LHCP dual-CP radiation patterns of the modified polarizer design at 28 GHz, 30 GHz, and 32 GHz are shown in Figs. 7.14(a), 7.14(b), and 7.14(c), respectively. Consistent and stable radiation pattern is achieved across the entire frequency range, and the patterns are symmetric in all the planes, which is a desired characteristic of a feed source for the reflector. The peak realized gain is around 9.3 dBic for both the polarization and the average 10 dB half-angle beamwidth for the modified polarizer is 60°. The desired 10 dB half-angle beamwidth of about 40° can be achieved by flaring the aperture or placing chokes at the aperture, as presented in the next section.

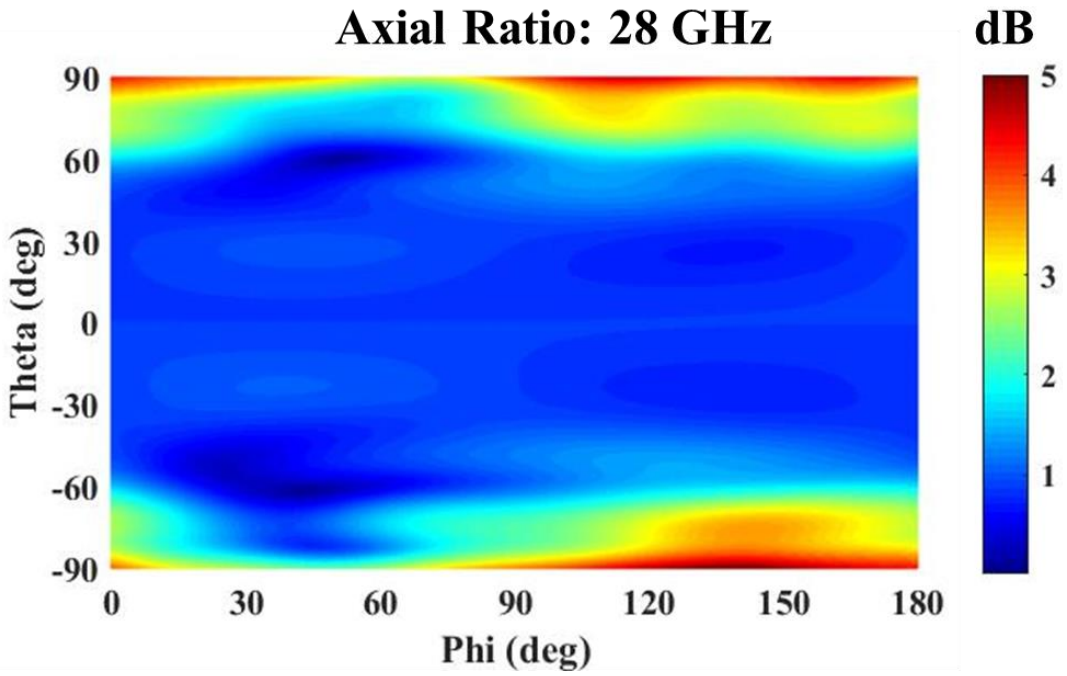

(a)

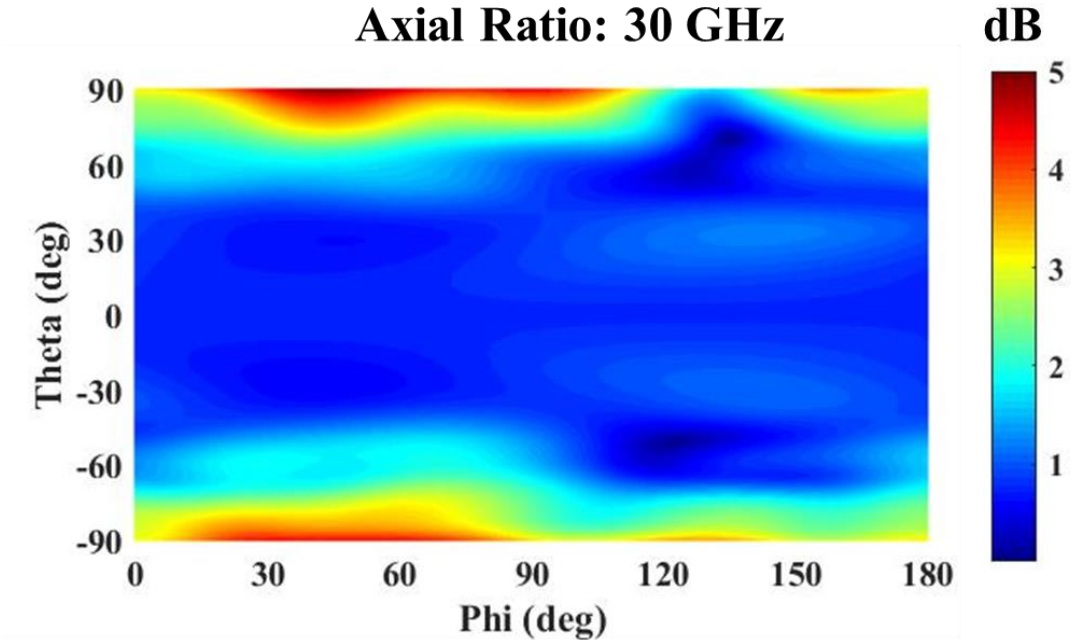

(b)

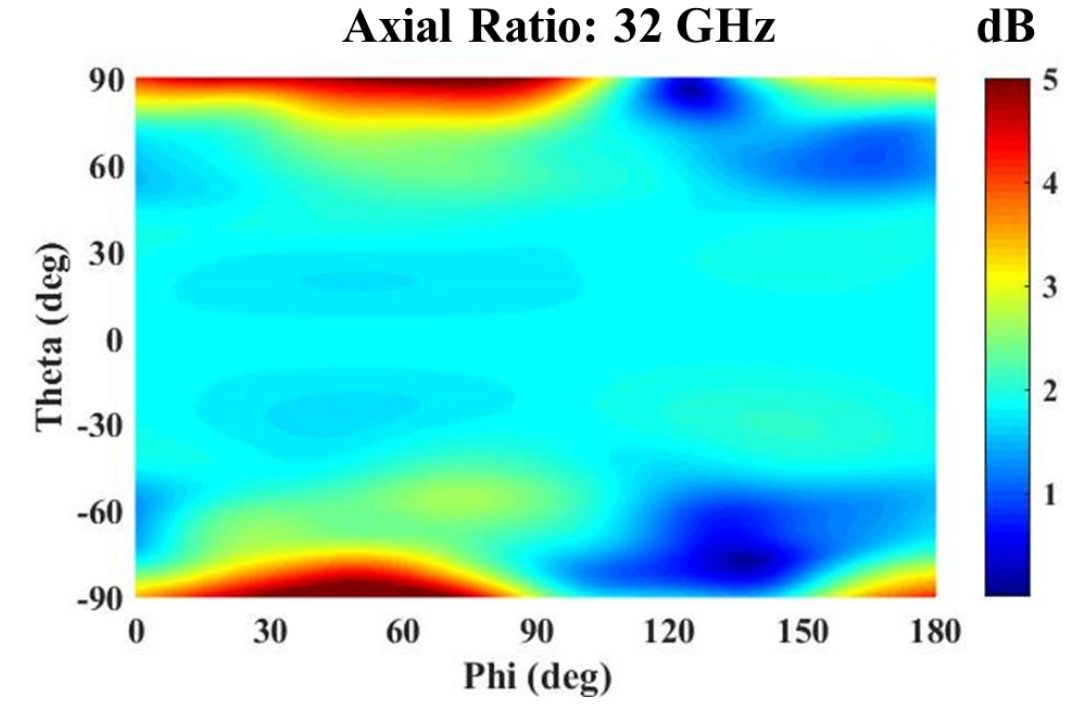

(c)

Figure 7.13 Simulated intensity plot of the AR of the modified polarizer geometry at (a) 28 GHz, (b) 30 GHz, and (c) 32 GHz.

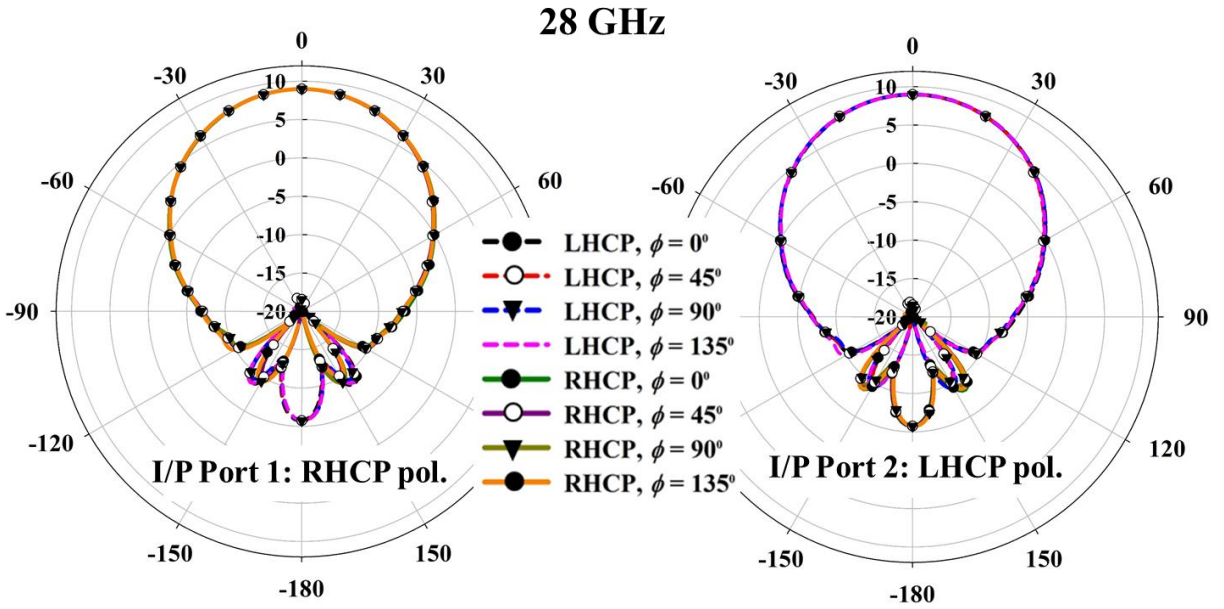
28 GHz
LHCP, $\phi = 0^0$
LHCP, $\phi = 45^0$
LHCP, $\phi = 90^0$
LHCP, $\phi = 135^0$
RHCP, $\phi = 0^0$
RHCP, $\phi = 45^0$
RHCP, $\phi = 90^0$
RHCP, $\phi = 135^0$
I/P Port 1: RHCP pol.
I/P Port 2: LHCP pol.

(a)

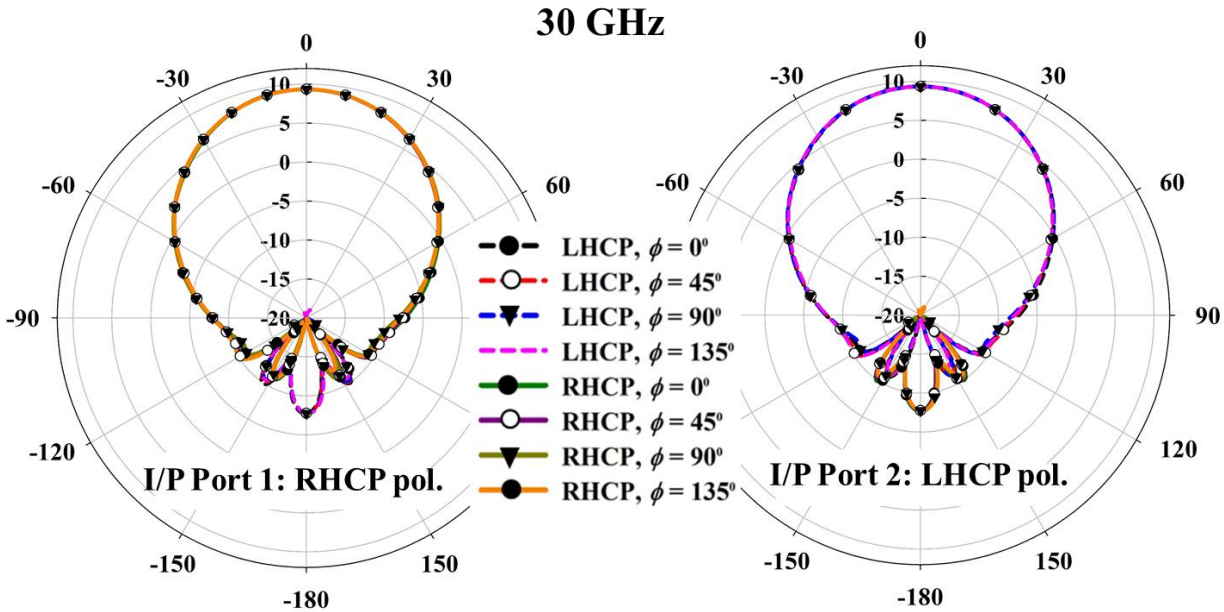
30 GHz
LHCP, $\phi = 0^0$
LHCP, $\phi = 45^0$
LHCP, $\phi = 90^0$
LHCP, $\phi = 135^0$
RHCP, $\phi = 0^0$
RHCP, $\phi = 45^0$
RHCP, $\phi = 90^0$
RHCP, $\phi = 135^0$
I/P Port 1: RHCP pol.
I/P Port 2: LHCP pol.

(b)

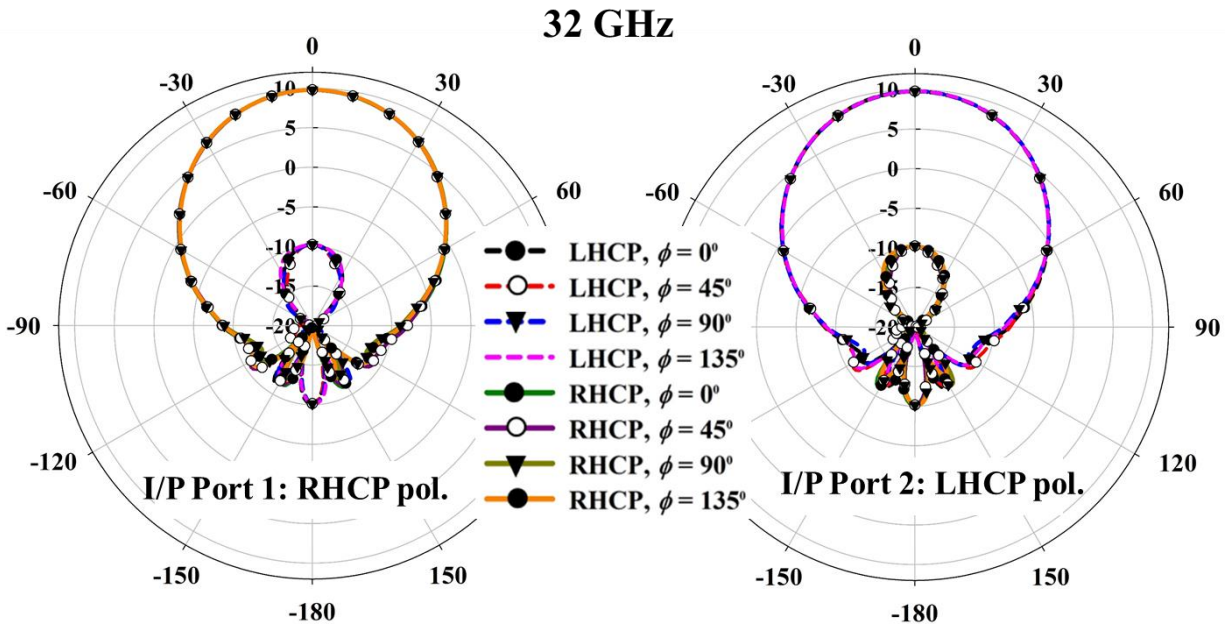

(c)

Figure 7.14 Simulated 2D realized gain radiation patterns of the modified polarizer geometry at (a) 28 GHz, (b) 30 GHz, and (c) 32 GHz.

7.7 Proposed Feed Horn Design

The target 12 dB half-angle beamwidth of the required CP feed source is around 40°, and it can be achieved by appropriate flaring or placement of chokes at the aperture of the proposed modified polarizer structure. One such solution is shown in Fig. 7.15 using a choke at the aperture of the polarizer. Other than increasing the directivity of the feed source, this also offers an additional advantage of further improving the front-to-back (F/B) ratio. A high F/B ratio is desired for the reflector feed as little radiation leaks to the RF circuitry behind the feed source. The added choke design parameters are choke height C_h = 10 mm, and choke radius C_r = 9.5 mm.

The S-parameters of the proposed feed horn antenna is shown in Fig. 7.16. The reflection coefficient magnitude is less than -15 dB for the entire frequency range and the inter-port isolation

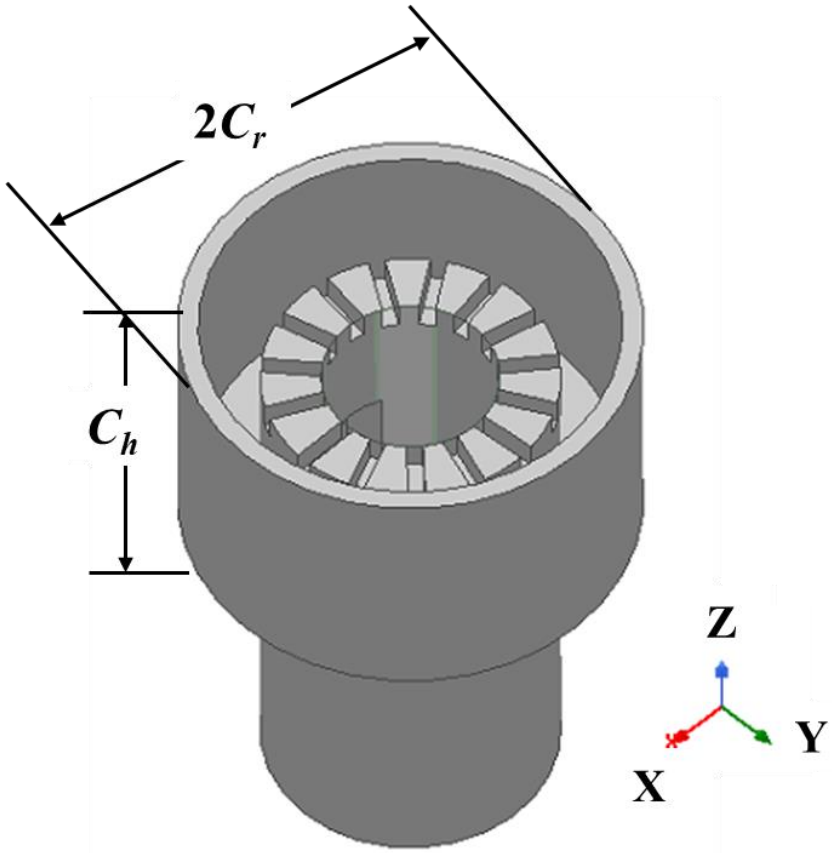

Figure 7.15 Proposed feed horn design with the modified polarizer geometry of Fig. 7.11 with a choke at the aperture for narrower 12 dB half beamwidth and reduced front-to-back ratio.

is better than 20 dB within 26.5 – 29.5 GHz. The AR as a function of frequency for the modified polarizer geometry with a choke is shown in Fig. 7.17. The simulated AR of the proposed feed horn antenna is less than 2 dB between 26.5 – 29.5 GHz. The 2D realized gain radiation patterns at 27 GHz, 28 GHz, and 29 GHz are shown in Figs. 7.18(a), 7.18(b), and 7.18(c), respectively. The peak realized gain is around 13.5 dBic with cross-polarization isolation better than 20 dB for both the dual-CP polarizations. The average 12 dB half-angle beamwidth is about 41° across the frequency range.

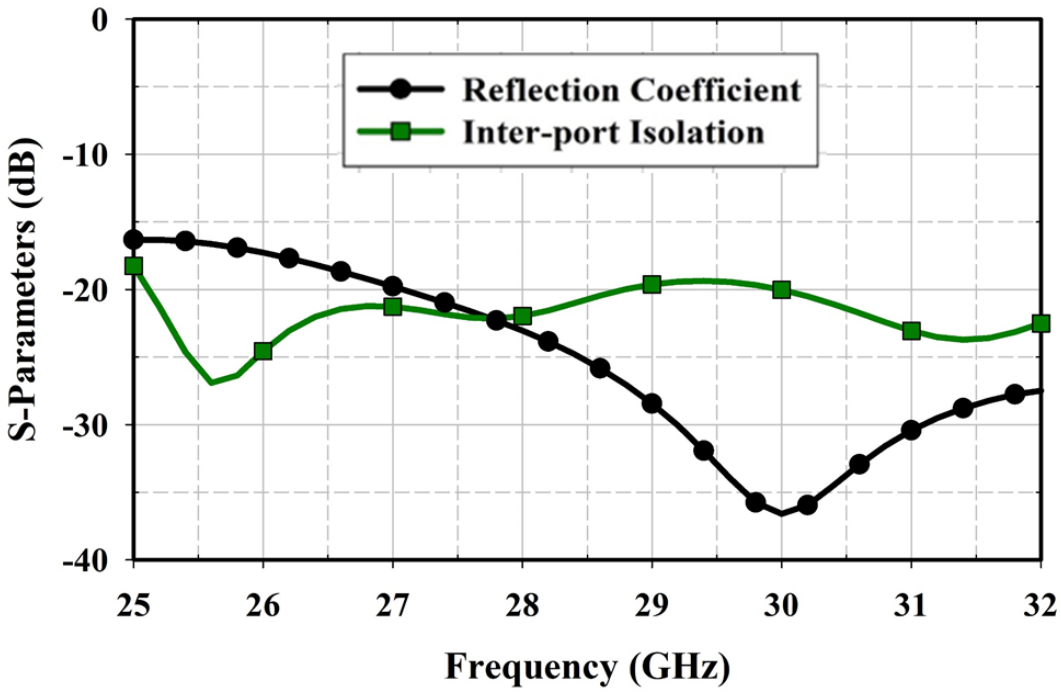

Figure 7.16 Simulated S-parameters of the feed horn antenna consisting of modified polarizer geometry with the choke.

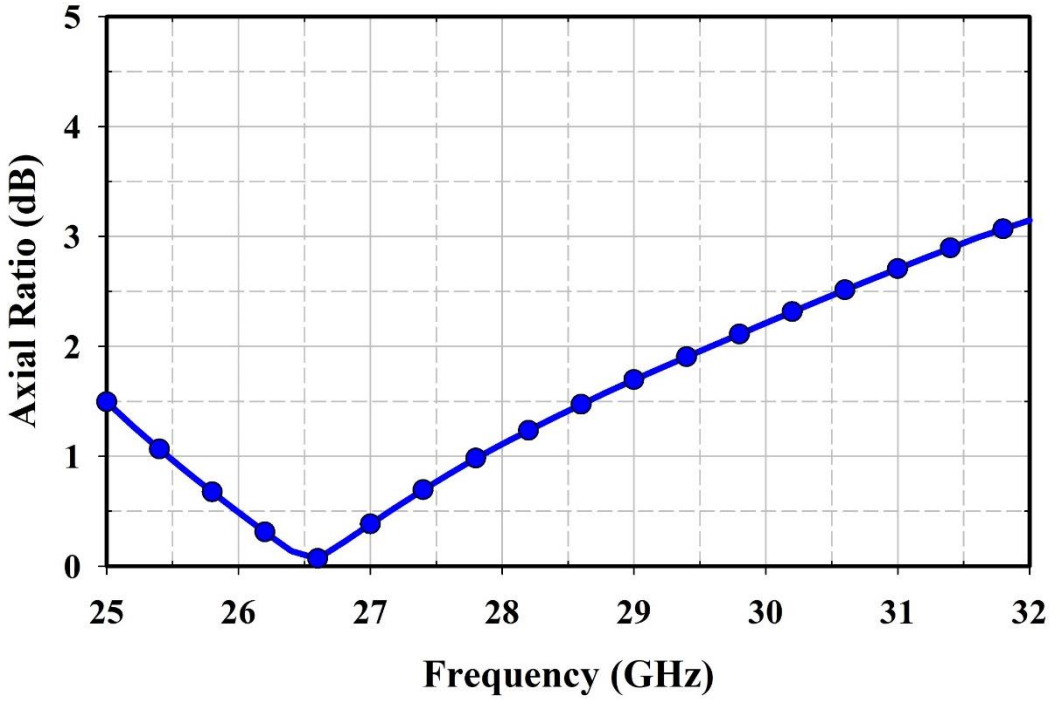

Figure 7.17 Simulated axial ratio vs. frequency of the feed horn antenna consisting of modified polarizer geometry with the choke.

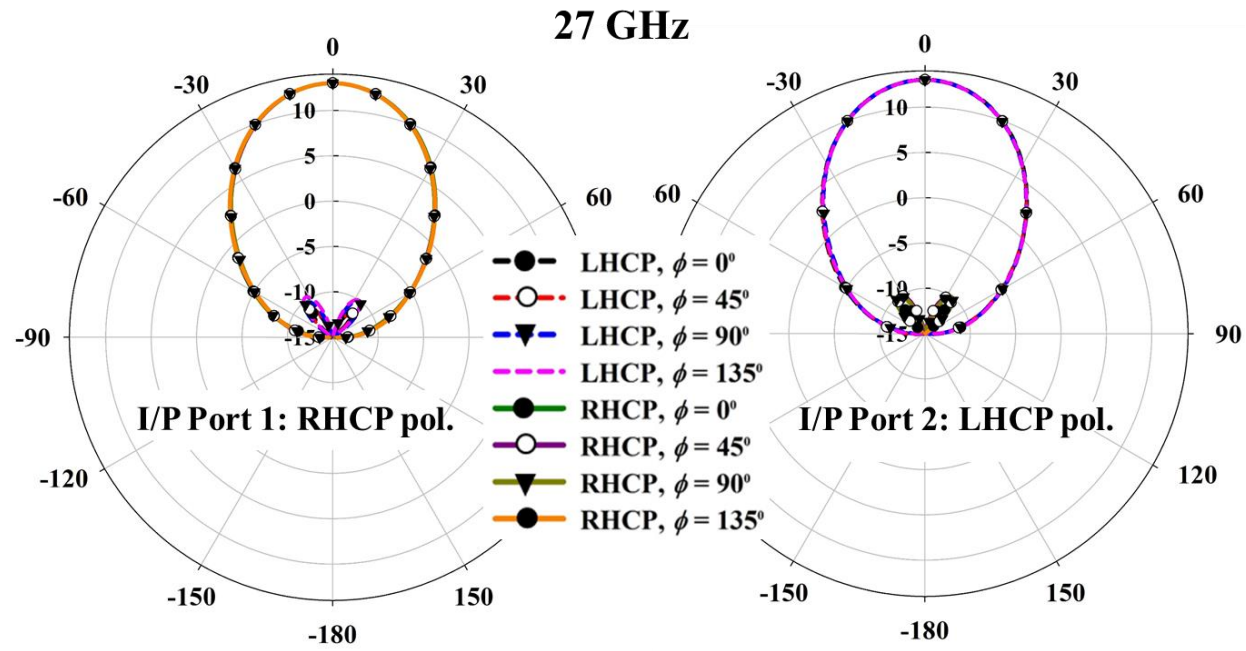
27 GHz
I/P Port 1: RHCP pol.
I/P Port 2: LHCP pol.
LHCP, ϕ = 0°
LHCP, ϕ = 45°
LHCP, ϕ = 90°
LHCP, ϕ = 135°
RHCP, ϕ = 0°
RHCP, ϕ = 45°
RHCP, ϕ = 90°
RHCP, ϕ = 135°

(a)

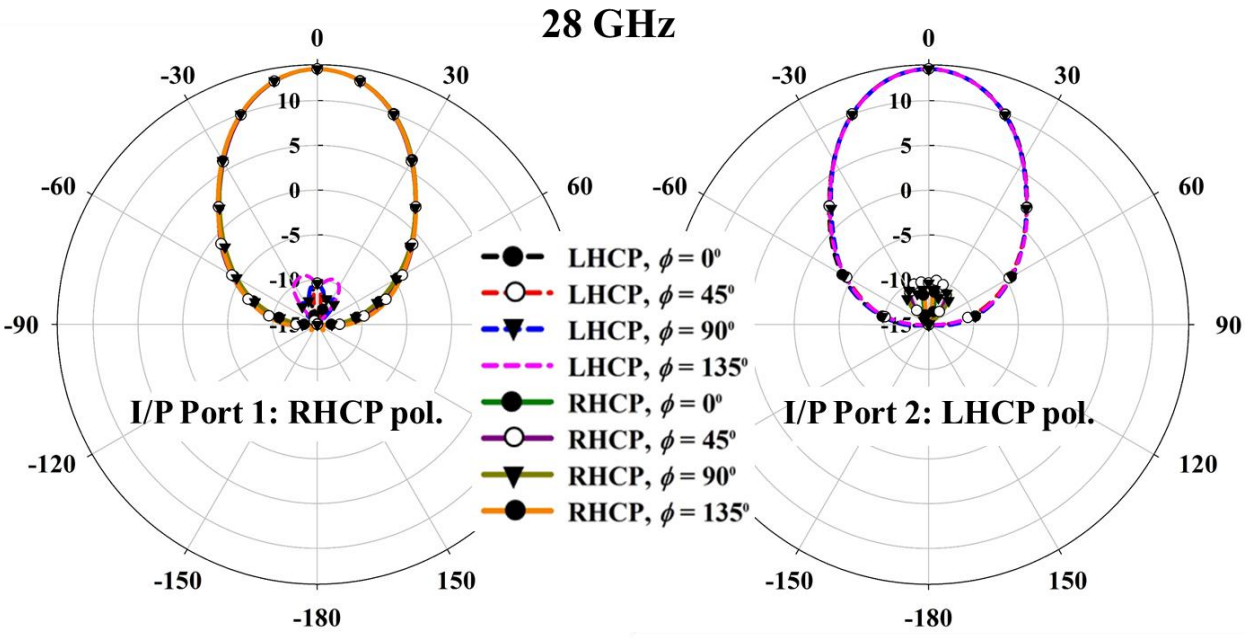
28 GHz
I/P Port 1: RHCP pol.
I/P Port 2: LHCP pol.
LHCP, ϕ = 0°
LHCP, ϕ = 45°
LHCP, ϕ = 90°
LHCP, ϕ = 135°
RHCP, ϕ = 0°
RHCP, ϕ = 45°
RHCP, ϕ = 90°
RHCP, ϕ = 135°

(b)

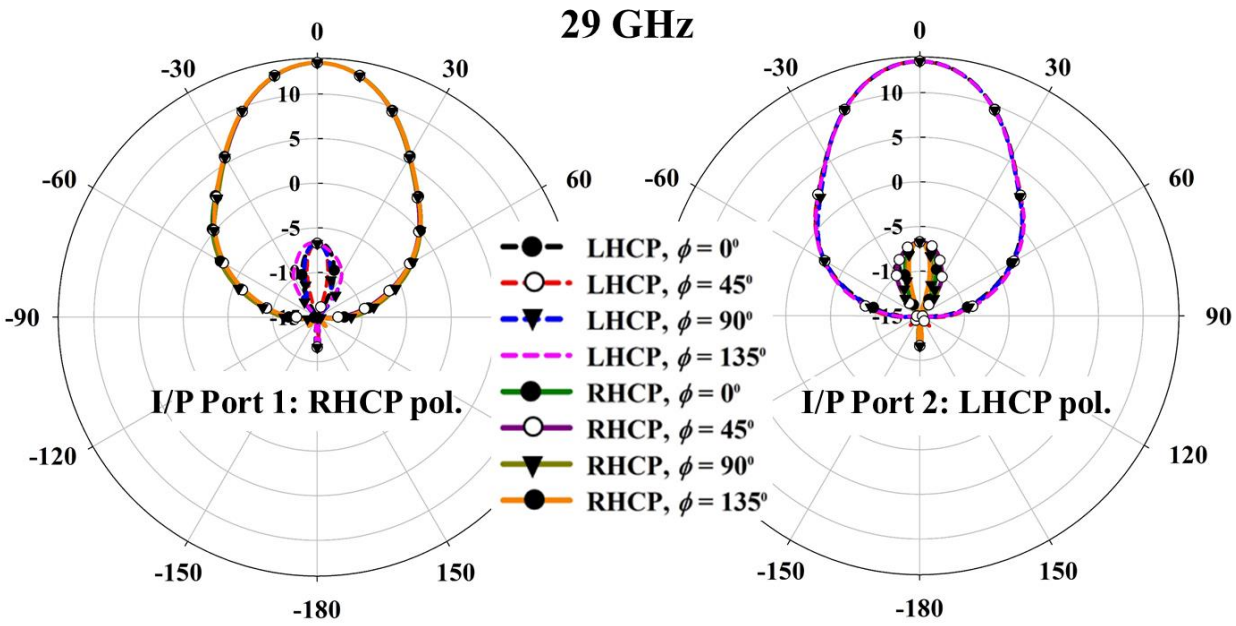

(c)

Figure 7.18 Simulated 2D realized gain radiation patterns of the feed horn antenna consisting of the modified polarizer with the choke at (a) 27 GHz, (b) 28 GHz, and (c) 29 GHz.

The comparison of the target specifications for the feed source and that achieved using the proposed feed horn antenna is shown in Table 7.3. The desired goals of 12 dB half-angle beamwidth, dual-CP polarization, and frequency bandwidth are achieved with the proposed feed horn antenna.

Table 7.3 The target vs. achieved feed horn specification for the spherical reflector feed source.

Feed Horn Antenna Specifications (Target vs. Achieved)		
Parameters	**Target Specs**	**Achieved Specs from Proposed Feed Horn Antenna**
12 dB half-beamwidth	40°	41°
Polarization	Dual CP: RHCP and LHCP	Dual CP: RHCP and LHCP
Frequency of Operation	26.5 – 29.5 GHz	26.5 – 29.5 GHz
Inter-Port Isolation	> 20 dB	> 20 dB
Impedance Matching $\lvert S_{ii} \rvert$	< -15 dB	< -15 dB

7.8 Continued Work

This research is carried out as part of an investigation study for multiple beam switching with a spherical reflector antenna. The following are the future steps for accomplishing this goal.

1. Design and optimize waveguide excitation input ports for the proposed polarizer feed source with inter-port isolation better than 30 dB across 26.5 – 29.5 GHz bandwidth.
2. Analyze the proposed dual-CP feed horn with the spherical reflector using HFSS to achieve multiple-beam switching.
3. 3D metal print the feed horn and reflector and characterize the antenna performances.

The next chapter summarizes the important findings of the dissertation and discusses the possible future studies based on the research performed as part of the dissertation.

Chapter 8

Conclusions and Future Studies

Wireless technology plays a crucial role in today's communications and emerging technologies, including self-driving vehicles, robots, drones, and new medical devices. In this dissertation, we have presented five significant research contributions for innovative high gain, cost-effective, and energy-efficient antenna solutions for satellite and wireless applications. A plethora of computational methods is used for the theoretical analysis, numerical simulations, optimizations, and beam synthesis algorithms. All the concepts introduced in the research are novel and have massive potential for practical implementation. The innovative antenna designs proposed in the research have been prototyped and experimentally characterized to verify the mathematical and computational analysis.

The first research discussed a novel circular polarized feed horn high gain antenna solution that eliminates the need for an external OMT or a complex septum to generate circularly polarized (CP) waves at *W*-band frequency for satellite communication. The detailed parametric analysis was used to determine the optimum dimension of the proposed feed horn antenna. A combination of physical optics (PO) and physical theory of diffraction (PTD) as part of the TICRA GRASP solver was used in the analysis of the reflector. The effect of CubeSat chassis on the radiation performance was also investigated using the multilevel fast multipole method (MLFMM) along with the method of moments (MoM).

Next, a novel series-fed antenna called Butterfly antenna was proposed. A Butterfly traveling wave antenna is a novel high gain, compact, and cost-efficient solution for millimeter-wave (*W*-band) satellite applications. The compact sequentially-rotated series-fed linear array antenna facilitated low cross-polarization radiation and wide axial ratio beamwidth. Furthermore,

periodic leaky-wave antenna LWA analysis was conducted to provide insights into the radiation characteristics of the proposed linear array. Monte-Carlo statistical analysis was carried to quantify the changes in the beam steering array due to random variation in the phase shifters and random element failures.

A hybrid reflector-phased array system at *Ku*-band was the third cost-effective and energy-efficient high gain beam-steering solution for the enhanced data rate wireless communication. The parabolic-cylindrical reflector fed with a phased array antenna was shown to have wide-angle beam steering performance with a high gain at a significantly reduced cost and power consumption compared to a stand-alone phased array antenna. The physical optics approximation was used to analyze the radiation characteristics of the parabolic-cylindrical reflector. Also, the analytically computed results of the reflector were compared with the MoM solver in TICRA GRASP.

A novel multi-functional Butterfly element based full-polarization reconfigurable staggered phased array antenna solution was researched to improve the system capacity and cellular coverage with lower power requirements and installation costs for 5G wireless communication at 28 GHz. The 16-channel Analog Devices ADMV4821 RFIC *Ka*-band beamformer was integrated with the array to provide full-polarization reconfigurable patterns, flexible radiation patterns, and wide-angle 1D beam steering performance. An analytical study using a periodic leaky-wave antenna (LWA) theory was included to provide insights into the radiation characteristics of the Butterfly series-fed linear array antenna.

A cost-effective 3D metal printed dual-CP feed horn antenna was proposed as a feed source to a spherical reflector to provide high gain for *Ka*-band applications. Multiple dual-CP horns placed along the focal arc of the spherical reflector can provide high gain multiple-switched beams to increase the system capacity. The feed horn is analyzed using the finite element method FEM

based HFSS numerical analysis solver, and the spherical reflector is analyzed using PO and PTD solver in TICRA GRASP.

8.1 Future Studies

The feedhorn polarizer presented in chapter 3 is designed for left-hand circular polarization (LHCP) and used as a feed source for an $f/D = 0.25$ offset parabolic reflector. As part of the future work, a dual-CP with both LHCP and right-hand circular polarization (RHCP) can be designed for frequency reuse and increasing the system capacity. Also, the feed can be flared at the aperture to increase the directivity of the horn to be used for a higher f/D reflector, which will increase the cross-polarization isolation.

As part of the Butterfly planar 1D-beam steering array antenna introduced in chapter 4, the characterization for the beam steering could not happen due to the mirroring of the layout in the fabrication process. Accordingly, one of the future work on that could be to re-fabricate the Butterfly planar array with the integrated beamforming network and characterize it for beam steering performance.

In chapter 5, wide-angle 1D beam steering is achieved along the cylindrical axis of the parabolic-cylindrical reflector fed by the phased array antenna. Possible future work on this research could be to use the spherical reflector antenna fed by the phased array antenna to achieve wide-angle beam steering in any plane.

A multi-functional Butterfly staggered planar array antenna is presented in chapter 6, and beamforming was achieved using an external beamforming board ADMV4821 from Analog Devices. In future work, a complete integrated Butterfly array antenna with the beamforming board can be designed and characterized.

In chapter 7, a 3D metal printed dual-CP feed source is introduced for multiple-beam switching applications using a spherical reflector. However, no switching network is studied in this research. As part of the future work, a switching network can be designed to control the excitation of each feed horn antenna and to provide additional beamforming capabilities.

Bibliography

[1] Daniel Selva, and David Krejci, “A survey and assessment of the capabilities of Cubesats for Earth observation”, *Acta Astronautica*, Volume 74, 2012, Pages 50-68.

[2] Everythingrf, “What is the impact of the atmosphere on RF signal propagation?” Aug. 17, 2017. [Online] Available: https://www.everythingrf.com/community/what-is-the-impact-of-the-earths-atmosphere-on-rf-signal-propagation. Accessed: May 02, 2020.

[3] L. Shafai, S. K. Sharma and S. Rao, *Handbook of Reflector Antennas and Feed Systems: Feed Systems*, vol. II. Norwood, MA, USA: Artech House, 2013.

[4] S. K. Sharma, L. Shafai and S. Rao, *Handbook of Reflector Antennas and Feed Systems: Theory and Design of Reflectors*, vol. I. Norwood, MA, USA: Artech House, 2013.

[5] S. K. Sharma, L. Shafai and M. Barakat, "Ka-band dual circularly polarized feed horn polarizer for reflector antennas for satellite communications," *11th International Symposium on Antenna Technology and Applied Electromagnetics [ANTEM 2005]*, St. Malo, 2005, pp. 1-4.

[6] S. Bhardwaj and J. L. Volakis, "Hexagonal Waveguide Based Circularly Polarized Horn Antennas for Sub-mm-Wave/Terahertz Band," in *IEEE Trans. on Antennas and Propagation*, vol. 66, no. 7, pp. 3366-3374, July 2018.

[7] S. B. Sharma, D. Pujara, S. B. Chakrabarty, R. Dey and V. K. Singh, "Design and development of a conjugate matched feed for an offset parabolic reflector antenna," in *IET Microwaves, Antennas & Propagation*, vol. 4, no. 11, pp. 1782-1788, November 2010.

[8] Y. Rahmat-Samii, et. al., “Advanced precipitation Radar antenna: array-fed offset membrane cylindrical reflector antenna,” in *IEEE Transactions on Antennas and Propagation*, vol. 53, no. 8, pp. 2503-2515, Aug. 2005.

[9] Z. Hussein. and J. Hilland, “Cylindrical antenna with partly adaptive phase-array feed,” California Inst. Of Tech., Pasadena, CA, USA, NASA Tech Brief, Rep. NPO-30251, Dec. 2003.

[10] P. S. Kildal, “Radiation characteristics of the EISCAT VHF parabolic cylindrical reflector antenna,” in *IEEE Transactions on Antennas and Propagation*, vol. 32, no. 6, pp. 541-552, June 1984.

[11] B. Babakhani and S. K. Sharma, "Wideband Frequency Tunable Concentric Circular Microstrip Patch Antenna with Simultaneous Polarization Reconfiguration," in *IEEE Antennas and Propagation Magazine*, vol. 57, no. 2, pp. 203-216, April 2015.

[12] B. Babakhani, S. K. Sharma and N. R. Labadie, "A Frequency Agile Microstrip Patch Phased Array Antenna With Polarization Reconfiguration," in *IEEE Transactions on Antennas and Propagation*, vol. 64, no. 10, pp. 4316-4327, Oct. 2016.

[13] S. Krishna, G. Mishra and S. K. Sharma, "A series fed planar microstrip patch array antenna with 1D beam steering for 5G spectrum massive MIMO applications," *2018 IEEE Radio and Wireless Symposium (RWS)*, Anaheim, CA, 2018, pp. 209-212.

[14] I. Agnihotri and S. K. Sharma, "Design of a Compact 3-D Metal Printed Ka-band Waveguide Polarizer," in *IEEE Antennas and Wireless Propagation Letters*, vol. 18, no. 12, pp. 2726-2730, Dec. 2019.

[15] N. Luo, G. Mishra, S. K. Sharma and X. Yu, "Experimental Verification of 3D Metal Printed Dual Circular-Polarized Horn Antenna at V-Band," *2019 Antenna Measurement Techniques Association Symposium (AMTA)*, San Diego, CA, USA, 2019, pp. 1-6.

[16] W. P. Craig, C. M. Rappaport and J. S. Mason, "A high aperture efficiency, wide-angle scanning offset reflector antenna," in *IEEE Transactions on Antennas and Propagation*, vol. 41, no. 11, pp. 1481-1490, Nov. 1993.

[17] J. L. Volakis, A. Chatterjee and L. C. Kempel. *Finite element method for electromagnetics: antennas, microwave circuits, and scattering applications*. The IEEE/OUP Series on Electromagnetic Wave Theory (Formerly IEEE Only), Series Editor Series. IEEE Press, 1998.

[18] Ansys, "HFSS" [Online] Available: https://www.ansys.com/products /electronics/ansys-hfss. Accessed: Nov. 20, 2018.

[19] R. Glazebrook. *Physical Optics*. Text-books of science. Appleton and Company, 1883.

[20] R. E. Collin, *Antennas and Radio wave propagation*, McGraw-Hill Higher Education, Feb 1, 1985.

[21] TICRA, "ESTEAM" [Online] Available: www.ticra.com/esteam. Accessed: May 02, 2020.

[22] Nocedal, J. and Wright, S., *Numerical Optimization*, 2nd. ed., Ch. 18. Springer, 2006.

[23] T. A. Milligan, *Modern Antenna Design*, Hoboken, NJ, USA: Wiley, 2005, p. 580.

[24] K. M. Luk and Yonglun Luo, "Radiation analysis of parabolic cylindrical reflector antenna with a rectangular microstrip patch array as feed," *Proceedings of IEEE Antennas and Propagation Society International Symposium and URSI National Radio Science Meeting*, Seattle, WA, USA, 1994, pp. 974-977 vol.2.

[25] T. Li, "A study of spherical reflectors as wide-angle scanning antennas," IEEE Trans. Antennas Propag., vol. AP-7, no. 3, pp. 223–226, Jul. 1959.

[26] K. Bahadori and Y. Rahmat-Samii, "An array-compensated spherical reflector antenna for a very large number of scanned beams," in *IEEE Transactions on Antennas and Propagation*, vol. 53, no. 11, pp. 3547-3555, Nov. 2005.

[27] S. A. Schelkunoff, “A Mathematical Theory of Linear Arrays,” *Bell Syst. Techn. J.*, vol. 22, pp. 80–107, 1943.

[28] A. C. Schell, “Survey of Ground Based Phased Array Antennas,” *in Phased Array Antennas*, A. A. Oliner and G. H. Knittel, Eds. Artech House, Inc., Dedham, 1972, ch. 2, pp. 9–14.

[29] A. K. Kamal, “Airport Surveillance Radar Design for Increased Air Traffic,” *Int. Conf. Radar 92*, pp. 151–154, 1992.

[30] W. H. Kummer, “Phased Array Antennas for Applications on Spacecraft,” *in Phased Array Antennas*, A. A. Oliner and G. H. Knittel, Eds. Artech House, Inc., Dedham, 1972, ch. 2, pp. 30–42.

[31] D. G. Fang, *Antenna Theory and Microstrip Antennas*. New York, NY, USA: CRC Press, 2009.

[32] C. A. Balanis, *Antenna Theory: Analysis and Design*, 3rd ed. Hoboken, NJ, USA: John Wiley & Sons, 2005.

[33] Microwaves101, “Phased Array Antennas” [Online] Available: https://www.microwaves101.com/encyclopedias/phased-array-antennas. Accessed: May 02, 2020.

[34] D. M. Pozar, *Microwave Engineering*, 4th Edition, Wiley, 2016.

[35] C. S. Lee, S. W. Lee and S. L. Chuang, "Plot of Modal Field Distribution in Rectangular and Circular Waveguides," in *IEEE Transactions on Microwave Theory and Techniques*, vol. 33, no. 3, pp. 271-274, Mar. 1985.

[36] A. A. Oliner and D. R. Jackson, “Leaky-Wave Antennas,” in *Antenna Engineering Handbook*, J. L. Volakis, Ed., 4th ed., New York: McGraw-Hill, 2007, ch. 11.

[37] A. Sutinjo, M. Okoniewski and R H. Johnston, “Radiation from fast and slow traveling waves,” in *IEEE Antennas and Propagation Magazine*, vol. 50, no. 4, pp. 175-181, Aug. 2008.

[38] M. Guglielmi and D. R. Jackson, "Broadside radiation from periodic leaky-wave antennas," in *IEEE Transactions on Antennas and Propagation*, vol. 41, no. 1, pp. 31-37, Jan. 1993.

[39] S.-L. Chen, D. K. Karmokar, Z. Li, P.-Y. Qin, R. W. Ziolkowski, and Y. J. Guo, “Circular-polarized substrate-integrated-waveguide leaky-wave antenna with wide-angle and consistent-gain continuous beam scanning,” *IEEE Transactions on Antennas and Propagation*, vol. 67, no. 7, pp. 4418–4428, 2019.

[40] R. E. Collin, *Foundations for Microwave Engineering*, 2nd ed. New York: McGraw-Hill, 1992.

[41] A. M. Boifot, E. Lier and T. Schaug-Pettersen, "Simple and broadband orthomode transducer (antenna feed)," in *IEE Proceedings H - Microwaves, Antennas and Propagation*, vol. 137, no. 6, pp. 396-400, Dec 1990.

[42] J. A. Ruiz-Cruz, J. R. Montejo-Garai, C. A. Leal-Sevillano and J. M. Rebollar, "Orthomode Transducers With Folded Double-Symmetry Junctions for Broadband and Compact Antenna Feeds," in *IEEE Transactions on Antennas and Propagation*, vol. 66, no. 3, pp. 1160-1168, March 2018.

[43] J. A. Ruiz-Cruz, J. R. Montejo-Garai, J. M. Rebollar and J. M. Montero, "C-band orthomode transducer for compact and broadband antenna feeders," in *Electronics Letters*, vol. 45, no. 16, pp. 813-814, July 30 2009.

[44] M. Esquius-Morote, M. Mattes and J. R. Mosig, "Orthomode Transducer and Dual-Polarized Horn Antenna in Substrate Integrated Technology," in *IEEE Transactions on Antennas and Propagation*, vol. 62, no. 10, pp. 4935-4944, Oct. 2014.

[45] R. Garcia, F. Mayol, J. M. Montero and A. Culebras, "Circular polarization feed with dual-frequency OMT-based turnstile junction," in *IEEE Antennas and Propagation Magazine*, vol. 53, no. 1, pp. 226-236, Feb. 2011.

[46] A. A. Sakr, W. Dyab and K. Wu, "Design Methodologies of Compact Orthomode Transducers Based on Mechanism of Polarization Selectivity," in *IEEE Transactions on Microwave Theory and Techniques*, vol. 66, no. 3, pp. 1279-1290, March 2018.

[47] G. M. Coutts, "Wideband Diagonal Quadruple-Ridge Orthomode Transducer for Circular Polarization Detection," in *IEEE Transactions on Antennas and Propagation*, vol. 59, no. 6, pp. 1902-1909, June 2011.

[48] G. Virone, O. A. Peverini, M. Lumia, M. Z. Farooqui, G. Addamo and R. Tascone, "W-Band Orthomode Transducer for Dense Focal-Plane Clusters," in *IEEE Microwave and Wireless Components Letters*, vol. 25, no. 2, pp. 85-87, Feb. 2015.

[49] G. M. Coutts, "Octave Bandwidth Orthomode Transducers for the Expanded Very Large Array," in *IEEE Transactions on Antennas and Propagation*, vol. 59, no. 6, pp. 1910-1917, June 2011.

[50] W. Hongjian, Y. Min, L. Guang and C. Xue, "Potter Horn and Compact Orthomode Transducer at 150 GHz," in *IEEE Transactions on Antennas and Propagation*, vol. 62, no. 10, pp. 5403-5405, Oct. 2014.

[51] M. J. Franco, "A High-Performance Dual-Mode Feed Horn for Parabolic Reflectors with a Stepped-Septum Polarizer in a Circular Waveguide [Antenna Designer's Notebook]," in *IEEE Antennas and Propagation Magazine*, vol. 53, no. 3, pp. 142-146, June 2011.

[52] C. A. Leal-Sevillano, K. B. Cooper, J. A. Ruiz-Cruz, J. R. Montejo-Garai and J. M. Rebollar, "A 225 GHz Circular Polarization Waveguide Duplexer Based on a Septum

Orthomode Transducer Polarizer," in *IEEE Transactions on Terahertz Science and Technology*, vol. 3, no. 5, pp. 574-583, Sept. 2013.

[53] N. C. Albertsen and P. Skov-Madsen, "A Compact Septum Polarizer," in *IEEE Transactions on Microwave Theory and Techniques*, vol. 31, no. 8, pp. 654-660, Aug. 1983.

[54] I. Kim, J. M. Kovitz and Y. Rahmat-Samii, "Enhancing the Power Capabilities of the Stepped Septum Using an Optimized Smooth Sigmoid Profile," in *IEEE Antennas and Propagation Magazine*, vol. 56, no. 5, pp. 16-42, Oct. 2014.

[55] Ming Hui Chen, "*Waveguide polarizer and antenna assembly*" US Patent # 6118412 granted Sep. 12, 2000.

[56] J. Bornemann and V. A. Labay, "Ridge waveguide polarizer with finite and stepped-thickness septum," in *IEEE Transactions on Microwave Theory and Techniques*, vol. 43, no. 8, pp. 1782-1787, Aug 1995.

[57] R. Nair, A. Kamal and S. Gupta, "A high gain dielectric loaded biconical horn for circular polarization," in *IEEE Transactions on Antennas and Propagation*, vol. 27, no. 6, pp. 860-861, November 1979.

[58] Shih-Wei Wang, Chih-Hung Chien, Chun-Long Wang and Ruey-Beei Wu, "A circular polarizer designed with a dielectric septum loading," in *IEEE Transactions on Microwave Theory and Techniques*, vol. 52, no. 7, pp. 1719-1723, July 2004.

[59] H. Jin, Y. M. Huang, H. Jin and K. Wu, "E-band Substrate Integrated Waveguide Orthomode Transducer Integrated with Dual-Polarized Horn Antenna," in *IEEE Transactions on Antennas and Propagation*, vol. PP, no. 99, pp. 1-1.

[60] M. Narasimhan and M. Sheshadri, "Propagation and radiation characteristics of dielectric loaded corrugated dual-frequency circular waveguide horn feeds," in *IEEE Transactions on Antennas and Propagation*, vol. 27, no. 6, pp. 858-860, November 1979.

[61] G. G. Gentili, P. Bolli, R. Nesti, G. Pelosi and L. Toso, "High-Order FEM Mode Matching Analysis of Circular Horns With Rotationally Symmetric Dielectrics," in *IEEE Transactions on Antennas and Propagation*, vol. 55, no. 10, pp. 2915-2918, Oct. 2007.

[62] A. G. Martin, "Radiation from dielectric sphere loaded horns," in *Electronics Letters*, vol. 14, no. 1, pp. 17-18, January 5 1978.

[63] R. Nevels, "An analysis of a two-dimensional dielectric covered corrugated antenna feed horn," in *IEEE Transactions on Antennas and Propagation*, vol. 32, no. 8, pp. 877-880, August 1984.

[64] J. Chatterjee and W. Croswell, "Waveguide excited dielectric spheres as feeds," in *IEEE Transactions on Antennas and Propagation*, vol. 20, no. 2, pp. 206-208, Mar 1972.

[65] N. Chahat, R. E. Hodges, J. Sauder, M. Thomson, E. Peral and Y. Rahmat-Samii, "CubeSat Deployable Ka-Band Mesh Reflector Antenna Development for Earth Science Missions," in *IEEE Transactions on Antennas and Propagation*, vol. 64, no. 6, pp. 2083-2093, June 2016.

[66] N. Chahat, R. E. Hodges, J. Sauder, M. Thomson and Y. Rahmat-Samii, "The Deep-Space Network Telecommunication CubeSat Antenna: Using the deployable Ka-band mesh reflector antenna.," in *IEEE Antennas and Propagation Magazine*, vol. 59, no. 2, pp. 31-38, April 2017.

[67] N. E. Chahat, "A mighty antenna from a tiny CubeSat grows," in *IEEE Spectrum*, vol. 55, no. 2, pp. 32-37, February 2018.

[68] S. Gao, Y. Rahmat-Samii, R. E. Hodges and X. X. Yang, "Advanced Antennas for Small Satellites," in *Proceedings of the IEEE*, vol. 106, no. 3, pp. 391-403, March 2018.

[69] R. E. Hodges, N. Chahat, D. J. Hoppe and J. D. Vacchione, "A Deployable High-Gain Antenna Bound for Mars: Developing a new folded-panel reflectarray for the first CubeSat mission to Mars.," in *IEEE Antennas and Propagation Magazine*, vol. 59, no. 2, pp. 39-49, April 2017.

[70] I. A. Osaretin, M. W. Shields, J. A. M. Lorenzo and W. J. Blackwell, "A Compact 118-GHz Radiometer Antenna for the Micro-Sized Microwave Atmospheric Satellite," in *IEEE Antennas and Wireless Propagation Letters*, vol. 13, pp. 1533-1536, 2014.

[71] N. A. Adatia and A. W. Rudge, "Beam squint in circularly polarised offset-reflector antennas," in *Electronics Letters*, vol. 11, no. 21, pp. 513-515, 16 October 1975.

[72] S. Gao, Q. Luo, and F. Zhu, *Circularly Polarized Antennas*. Hoboken, NJ, USA: Wiley, 2013.

[73] K. Carver and J. Mink, "Microstrip antenna technology," in *IEEE Transactions on Antennas and Propagation*, vol. 29, no. 1, pp. 2-24, January 1981.

[74] R. Mailloux, J. McIlvenna and N. Kernweis, "Microstrip array technology," in *IEEE Transactions on Antennas and Propagation*, vol. 29, no. 1, pp. 25-37, January 1981.

[75] D. M. Pozar and D. H. Schaubert, *Microstrip Antennas: The Analysis and Design of Microstrip Antennas and Arrays*. New York, NY, USA: Wiley-IEEE Press, 1995.

[76] C. Min and C. E. Free, "Analysis of Traveling-Wave-Fed Patch Arrays," in *IEEE Transactions on Antennas and Propagation*, vol. 57, no. 3, pp. 664-670, March 2009.

[77] J. Huang, “A technique for an array to generate circular polarization with linearly polarized elements,” *IEEE Trans. Antennas Propag.*, vol.AP-34, no. 9, pp. 1113–1123, Sep. 1986.

[78] S. D. Targonski and D. M. Pozar, “Design of wideband circularly polarized aperture-coupled microstrip antennas,” *IEEE Trans. Antennas Propag*., vol. 41, no. 2, pp. 214–220, Feb. 1993.

[79] E. Aloni and R. Kastner, “Analysis of a dual circularly polarized microstrip antenna fed by crossed slots,” *IEEE Trans. Antennas Propag.*, vol. 42, no. 8, pp. 1053–1058, Aug. 1994.

[80] H. Kim, B. M. Lee, and Y. J. Yoon, “A single-feeding circularly polarized microstrip antenna with the effect of hybrid feeding,” *IEEE Antennas Wireless Propag. Lett.*, vol. 2, pp. 74–77, 2003.

[81] K.-H. Lu and T.-N. Chang, “Circularly polarized array antenna with corporate-feed network and series-feed elements,” *IEEE Trans. Antennas Propag*., vol. 53, no. 10, pp. 3288–3292, Oct. 2005.

[82] H. Evans, P. Gale, B. Aljibouri, E. G. Lim, E. Korolkeiwiez, and A. Sambell, “Application of simulated annealing to design of serial feed sequentially rotated 2 × 2 antenna array,” *Electron. Lett.*, vol. 36, no.24, pp. 1987–1988, Nov. 2000.

[83] J. R. James, P. S. Hall, and C. Wood, *Microstrip Antenna Theory and Design*. Stevenage, U.K.: Peregrinus, 1981, ch. 5.

[84] S. Sengupta, D. R. Jackson and S. A. Long, "A Method for Analyzing a Linear Series-Fed Rectangular Microstrip Antenna Array," in *IEEE Transactions on Antennas and Propagation*, vol. 63, no. 8, pp. 3731-3736, Aug. 2015.

[85] R. E. Collin and F. Zucker, *Antenna Theory*, vol. 2. New York, NY, USA: McGraw-Hill, 1969, pp. 151-295.

[86] D. R. Jackson and A. A. Oliner, “Leaky-wave antennas,” in *Modern Antenna Handbook*, C. A. Balanis, Ed., Hoboken, NJ, USA: Wiley, vol. 1. 2008, pp. 325-368.

[87] D. K. Larmokar and K. P. Esselle, “Periodic U-slot-loaded dual-band half-width microstrip leaky-wave antennas for forward and backward beam scanning,” *IEEE Transactions on Antennas and Propagation*, vol. 63, no. 12, pp. 5372–5381, 2015.

[88] M. H. Rahmani and D. Deslandes, “Backward to forward scanning periodic leaky-wave antenna with wide scanning range,” *IEEE Transactions on Antennas and Propagation*, vol. 65, no. 7, pp. 3326–3335, 2017.

[89] D. Ye, Y. Li, Z. Liang, J. Liu, S. Zheng, and Y. Long, “Periodic triangle-truncated DSPSL-based antenna with backfire to endfire beam-scanning capacity,” *IEEE Transactions on Antennas and Propagation*, vol. 65, no. 2, pp. 845–849, 2017.

[90] H. Zhang, Y.-C. Jiao, G. Zhao, and C. Zhang, “Half-mode substrate integrated waveguide-based leaky-wave antenna loaded with meandered lines,” *Electronics Letters*, vol. 53, no. 17, pp. 1172–1174, 2017.

[91] T. R. Cameron, A. T. Sutinjo and M. Okoniewski, "A Circularly Polarized Broadside Radiating “Herringbone” Array Design with the Leaky-Wave Approach," *IEEE Antennas and Wireless Propagation Letters,* vol. 9, pp. 826-829, 2010.

[92] C. Caloz, T. Itoh, and A. Rennings, “CRLH metamaterial leaky-wave and resonant antennas,” *IEEE Antennas and Propagation Magazine,* vol. 50, no. 5, pp. 25–39, 2008.

[93] S. Paulotto, P. Baccarelli, F. Frezza, and D. R. Jackson, “A novel technique for open-stopband suppression in 1-D periodic printed leaky-wave antennas,” *IEEE Transactions on Antennas and Propagation,* vol. 57, no. 7, pp. 1894–1906, 2009.

[94] J. T. Williams, P. Baccarelli, S. Paulotto, and D. R. Jackson, “1-D combline leaky-wave antenna with the open-stopband suppressed: design considerations and comparisons with measurements,” *IEEE Transactions on Antennas and Propagation*, vol. 61, no. 9, pp. 4484–4492, 2013.

[95] S. J. Chen, W. Withayachumnankul, Y. Monnai and C. Fumeaux, "Linear Series-Fed Patch Array with Dual Circular Polarization or Arbitrary Linear Polarization," *2019 International Conference on Electromagnetics in Advanced Applications (ICEAA)*, Granada, Spain, 2019, pp. 0365-0369.

[96] K. Ito, K. Itoh and H. Kogo, "Improved design of series-fed circularly polarised printed linear arrays," in *IEE Proceedings H - Microwaves, Antennas and Propagation*, vol. 133, no. 6, pp. 462-466, December 1986.

[97] S. Otto, Z. Chen, A. Al-Bassam, A. Rennings, K. Solbach and C. Caloz, "Circular Polarization of Periodic Leaky-Wave Antennas with Axial Asymmetry: Theoretical Proof and Experimental Demonstration," in *IEEE Transactions on Antennas and Propagation*, vol. 62, no. 4, pp. 1817-1829, April 2014.

[98] M. M. Sabahi, A. A. Heidari and M. Movahhedi, "A Compact CRLH Circularly Polarized Leaky-Wave Antenna Based on Substrate-Integrated Waveguide," in *IEEE Transactions on Antennas and Propagation*, vol. 66, no. 9, pp. 4407-4414, Sept. 2018.

[99] X. Huo, J. Wang, Z. Li, Y. Li, M. Chen and Z. Zhang, "Periodic Leaky-Wave Antenna with Circular Polarization and Low-SLL Properties," in *IEEE Antennas and Wireless Propagation Letters*, vol. 17, no. 7, pp. 1195-1198, July 2018.

[100] S. Mao, S. Chen, J. Yeh and T. Lin, "Series-fed circularly polarized microstrip antennas with broad bandwidth," in *Radio Science*, vol. 42, no. 04, pp. 1-9, Aug. 2007.

[101] P. Hallbjorner, I. Skarin, K. From and A. Rydberg, "Circularly Polarized Traveling-Wave Array Antenna with Novel Microstrip Patch Element," in *IEEE Antennas and Wireless Propagation Letters*, vol. 6, pp. 572-574, 2007.

[102] J.C.S Chieh, A.V. Nguyen, J. Rowland, and S. K. Sharma, “E-Band 4-Bit Phase Shifter using SP4T Flip Chip Switches,” *International Symposium on Microelectronics*, 2017(1), pp. 595-598.

[103] A. Mrstik and P. Smith, "Scanning capabilities of large parabolic cylinder reflector antennas with phased-array feeds," in *IEEE Transactions on Antennas and Propagation*, vol. 29, no. 3, pp. 455-462, May 1981

[104] G. Borgiotti, "An antenna for limited scan in one plane: Design criteria and numerical simulation," in *IEEE Transactions on Antennas and Propagation*, vol. 25, no. 2, pp. 232-243, March 1977.

[105] M. Burrows and L. Ricardi, "Aperture feed for a spherical reflector," in *IEEE Transactions on Antennas and Propagation*, vol. 15, no. 2, pp. 227-230, March 1967.

[106] N. Amitay and H. Zucker, "Compensation of spherical reflector aberrations by planar array feeds," in *IEEE Transactions on Antennas and Propagation*, vol. 20, no. 1, pp. 49-56, January 1972.

[107] K. Kibaroglu, M. Sayginer, T. Phelps and G. M. Rebeiz, "A 64-Element 28-GHz Phased-Array Transceiver with 52-dBm EIRP and 8–12-Gb/s 5G Link at 300 Meters Without Any Calibration," in *IEEE Transactions on Microwave Theory and Techniques*, vol. 66, no. 12, pp. 5796-5811, Dec. 2018.

[108] J. S. Chieh, E. Yeo, M. Kerber and R. Olsen, "Ku-Band Dual Polarized Phased Array utilizing Silicon Beamforming Chipsets," *2019 IEEE Topical Workshop on Internet of Space (TWIOS)*, Orlando, FL, USA, 2019, pp. 1-3.

[109] E. Alfonso and P. Kildal, "Parabolic cylindrical reflector antenna at 60 GHz with line feed in gap waveguide technology," *2013 7th European Conference on Antennas and Propagation (EuCAP)*, Gothenburg, 2013, pp. 319-323.

[110] P. -. Kildal, "Diffraction corrections to the cylindrical wave radiated by a linear array feed of a cylindrical reflector antenna," in *IEEE Transactions on Antennas and Propagation*, vol. 32, no. 10, pp. 1111-1116, October 1984.

[111] Zhi-Hui Chen, Guo-Dong Liu and Qing-Xin Chu, "A New Method for Analyzing Large Size Parabolic Cylindrical Reflector Antenna," *2006 IEEE Antennas and Propagation Society International Symposium*, Albuquerque, NM, 2006, pp. 4421-4424.

[112] E. Holzman, "Equations for the first-order design of phased array fed reflector antennas," *2016 IEEE International Symposium on Phased Array Systems and Technology (PAST)*, Waltham, MA, 2016, pp. 1-4.

[113] Rudge, A. W.; Withers, M. J.: 'New technique for beam steering with fixed parabolic reflectors', Proceedings of the *Institution of Electrical Engineers*, 1971, 118, (7), p. 857-863.

[114] M. Cooley, "Phased Array Fed Reflector (PAFR) antenna architectures for space-based sensors," *2015 IEEE Aerospace Conference*, Big Sky, MT, 2015, pp. 1-11.

[115] Y. Rahmat-Samii and S. Sinton, “Offset parabolic cylindrical antennas: effects of random surface errors on gain and sidelobes,” *IEEE Antennas and Propagation Society International Symposium. 2001 Digest. Held in conjunction with USNC/URSI National Radio Science Meeting (Cat. No.01CH37229)*, Boston, MA, USA, 2001, pp. 542-545 vol.1.

[116] Fa-Long Luo and Charlie Zhang, Signal Processing for 5G: Algorithms and Implementations. New Jersey: John Wiley and Sons, 2016.

[117] N. Zhu, X. Yang, T. Lou, Q. Cao and S. Gao, "Broadband Polarization-Reconfigurable Slot Antenna and Array with Compact Feed Network," in *IEEE Antennas and Wireless Propagation Letters*, vol. 18, no. 6, pp. 1293-1297, June 2019.

[118] Z. Hao, K. Fan and H. Wang, "A Planar Polarization-Reconfigurable Antenna," in *IEEE Transactions on Antennas and Propagation*, vol. 65, no. 4, pp. 1624-1632, April 2017.

[119] N. Nguyen-Trong L. Hall and C. Fumeaux "A frequency- and polarization-reconfigurable stub-loaded microstrip patch antenna" *IEEE Trans. Antennas Propag.* vol. 63 no. 11 pp. 5235-5240 Nov. 2015.

[120] P.-Y. Qin Y. J. Guo Y. Cai E. Dutkiewicz and C.-H. Liang "A reconfigurable antenna with frequency and polarization agility" *IEEE Antennas Wireless Propag. Lett.* vol. 10 pp. 1373-1376 2011.

[121] C. Gu, et al. "Compact smart antenna with electronic beam-switching and reconfigurable polarizations" *IEEE Trans. Antennas Propag.* vol. 63 no. 12 pp. 5325-5333 Dec. 2015.

[122] M. K. Fries M. Grani and R. Vahldieck "A reconfigurable slot antenna with switchable polarization" *IEEE Microw. Wireless Compon. Lett.* vol. 13 no. 11 pp. 490-492 Nov. 2003.

[123] K. Klionovski, A. Shamim and M. S. Sharawi, "5G antenna array with wide-angle beam steering and dual linear polarizations," *2017 IEEE International Symposium on Antennas and Propagation & USNC/URSI National Radio Science Meeting*, San Diego, CA, 2017, pp. 1469-1470.

[124] S. K. Sharma, and S. Krishna, “A Massive MIMO Panel Array at Ka-Band with Flexible Patterns and Beam Steering Performance”, Book: Ad Hoc Networks, Chapter No: 33, ADHOCNETS 2016, Lecture Notes in Computer Science, LNICST 184, DOI:10.1007/978-3-319-51204-4_33

[125] S. Krishna, and S. K. Sharma, “A Dual Polarization Massive MIMO Panel Array Antenna at Ka-Band With Beamforming Capability" 2017 *USNC-URSI National Radio Science Meeting (NRSM)*, Boulder, CO, USA, Jan. 4-7, 2017.

[126] G. Mishra, S. K. Sharma and J-C. S. Chieh, “A High Gain Series-fed Circularly Polarized Traveling-Wave Antenna at *W*-band using a New Butterfly Radiating Element,” in *IEEE Transactions on Antennas and Propagation*.

[127] G. Mishra, S. K. Sharma and J-C. S. Chieh, " A *W*-Band Butterfly Shaped Series-Fed Circular Polarized Phased Array Antenna for CubeSats," presented at the *IEEE International Symposium on Phased Array Systems and Technology (PAST)*, Waltham, MA, Oct. 15-18, 2019.

[128] G. Mishra, S. K. Sharma and J-C. S. Chieh, "A New Butterfly Radiating Element for Circular Polarized Series Fed Phased Array with Wide Axial Ratio Beamwidth at Millimeter Wave Band," *2018 IEEE International Symposium on Antennas and Propagation & USNC/URSI National Radio Science Meeting*, Boston, MA, 2018, pp. 1909-1910.

[129] Protolabs, “DMLS” [Online] Available: https://www.protolabs.com/services/3d-printing/direct-metal-laser-sintering/. Accessed: May 02, 2020.

Appendix A

MATLAB Code

This appendix includes the matlab code for analyzing an offset fed parabolic reflector antenna using Ray optics method or Aperture distribution method, as discussed in section 2.1.3 of chapter 2.

A.1 Aperture Field Distribution Profile

```
clc;close all;clear all;
% Defining the parameters
psi=26.6*pi/180;        % Tilt Angle
f=0.4877;               % Focal Length
freq= 12e9;             % Operating Frequency
velocity=3e8;
k=2*pi*freq/velocity;   % Wave Number
a=0.6;                  % Radius of the projected Aperture
as=0.016;               %Radius of the feed source
c=0.230574748;          % Center of the projected aperture
lambda=velocity/freq;
r=1000;
deg= 180/pi;

% Feed Profile
```

```
theta_0=-pi/2:0.01:pi/2;
e_theta_0= (1+ (0.81.*cos(theta_0))).*besselj(1,pi.*sin(theta_0))./(sin(theta_0));
figure;
plot(theta_0*180/pi,e_theta_0/max(e_theta_0),'linewidth',2.5);
grid on;
title('Feed Distribution Profile','fontsize',12,'fontname','cambria');
xlabel('\theta, degrees','fontsize',12,'fontname','cambria');
ylabel('Relative Field','fontsize',12,'fontname','cambria');

% Calculating the aperture field Eax and Eay
x1= linspace(-a,a,30);
y1=linspace(-c-a,-c+a,30);
 [x,y]= meshgrid(x1,y1);

rho = sqrt(x.^2 + y.^2);
theta_0= acos(((4*(f^2)- (rho.^2)).*cos(psi) - (4*f.*y.*sin(psi))./((4*(f^2)+(rho.^2))));
e_theta_0= (1+ (0.81.*cos(theta_0))).*besselj(1,pi.*sin(theta_0))./(sin(theta_0));
Den= (4*(f^2)+(rho.^2)).*((4*(f^2)+(rho.^2))-(4*f.*y.*sin(psi)) + (4*(f^2)- (rho.^2)).*cos(psi));
 Num1= 4*f*exp(-j*2*k*f).*e_theta_0;
Num2= (2.*x.*y.*(1-cos(psi)) - (4*f.*x.*sin(psi)));
Num3= ((4*(f^2)+(rho.^2)- (2.*(x.^2)))+ (4*(f^2)-(rho.^2)+ (2.*(x.^2))).*cos(psi) –

(4.*f.*y.*sin(psi)));
E_ax = Num1.*Num2./Den;                    % Ex aperture field
E_ay= (Num1).*(Num3)./(Den);                % Ey aperture field
```

```
figure;
circles(0,-c,a,'facecolor','none','edgecolor','b','linewidth',1.5);    % Plotting the projected aperture
axis equal;


hx=E_ax;
hy=E_ay;
    hx(x > (sqrt(a^2- (y+c).^2))) = 0;
    hx(x < (-sqrt(a^2- (y+c).^2))) = 0;
    hy(x > (sqrt(a^2- (y+c).^2))) = 0;
    hy(x < (-sqrt(a^2- (y+c).^2))) = 0;
hold on;
h2=quiver(x,y,real(hx),real(hy),'linewidth',1.3);    % Plot of the Aperture Field
 xlim([-0.65 0.65]);
 ylim([-0.85 0.45]);
title('Aperture Field Distribution Profile','fontsize',12,'fontname','cambria');
```

A.2 Gain and Efficiency Ignoring the Effect of Feed Blockage

```
dx = 1e-3;
dy = 1e-3;
X = -a:dx:a;
Y = -c-a:dy:-c+a;
[x,y] = meshgrid(X,Y);
rho = sqrt(x.^2+y.^2);
```

```
theta_0= acos(((4*(f^2)- (rho.^2)).*cos(psi) - (4*f.*y.*sin(psi))./((4*(f^2)+(rho.^2))));
e_theta_0= (1+ (0.81.*cos(theta_0))).*besselj(1,pi.*sin(theta_0))./(sin(theta_0));
Den= (4*(f^2)+(rho.^2)).*((4*(f^2)+(rho.^2))-(4*f.*y.*sin(psi)) + (4*(f^2)- (rho.^2)).*cos(psi));
Num1= 4*f*exp(-1i*2*k*f).*e_theta_0;

Num2= (2.*x.*y.*(1-cos(psi)) - (4*f.*x.*sin(psi)));
Num3= ((4*(f^2)+(rho.^2)- (2.*(x.^2)))+ (4*(f^2)-(rho.^2)+ (2.*(x.^2))).*cos(psi) -
(4.*f.*y.*sin(psi)));
E_ax = Num1.*Num2./Den;

E_ay= (Num1).*(Num3)./(Den);
h= abs(E_ay).^2*dx*dy;
h(x > (sqrt(a^2- (y+c).^2))) = 0;
h(x < (-sqrt(a^2- (y+c).^2))) = 0;
 hy= sum(sum(h));
 fun= @(theta_0) (abs((1+
(0.81.*cos(theta_0))).*besselj(1,pi.*sin(theta_0))./(sin(theta_0))).^2.*(2*pi.*sin(theta_0)));
deng= integral(fun,0,pi);
gain= (4*pi/(lambda^2))*hy/deng;
Gain_dB= 10*log10(abs(gain));
sprintf('\b Gain of the offset feed parabolic dish without feed blockage = %.3f dB', Gain_dB)
totaleff= gain*lambda^2/(4*(pi^2)*(a^2))*100;

sprintf('\b Total Efficiency of the offset feed parabolic dish without feed blockage = %.3f %%',
totaleff);
```

ans =

Gain of the offset feed parabolic dish = 42.414 dB

ans =

Total Efficiency of the offset feed parabolic dish = 76.666 %

A.3 H-Plane Radiation pattern and Maximum relative Cross Pol Level

```
dTheta = pi/3000;
theta0 = 0;
thetaEnd = 15*pi/180;
dx = 1e-3;
dy = 1e-3;
theta = theta0:dTheta:thetaEnd;
X = -a:dx:a;
Y = -c-a:dy:-c+a;
[x,y] = meshgrid(X,Y);
rho = sqrt(x.^2+y.^2);
theta_0= acos(((4*(f^2)- (rho.^2)).*cos(psi) - (4*f.*y.*sin(psi))./((4*(f^2)+(rho.^2))));
e_theta_0= (1+ (0.81.*cos(theta_0))).*besselj(1,pi.*sin(theta_0))./(sin(theta_0));
Den= (4*(f^2)+(rho.^2)).*((4*(f^2)+(rho.^2))-(4*f.*y.*sin(psi)) + (4*(f^2)- (rho.^2)).*cos(psi));
Num1= 4*f*exp(-1i*2*k*f).*e_theta_0;
Num2= (2.*x.*y.*(1-cos(psi)) - (4*f.*x.*sin(psi)));
```

```
Num3= ((4*(f^2)+(rho.^2)- (2.*(x.^2)))+ (4*(f^2)-(rho.^2)+ (2.*(x.^2))).*cos(psi) -
(4.*f.*y.*sin(psi)));
E_ax = Num1.*Num2./Den;
E_ay= (Num1).*(Num3)./(Den);
E_co = zeros(size(theta));
for ii = 1:length(theta)
    fy = (E_ay).*exp(1i*k.*sin(theta(ii)).*x)*dx*dy;
    fy(x > (sqrt(a^2- (y+c).^2))) = 0;
    fy(x < (-sqrt(a^2- (y+c).^2))) = 0;
    hy= sum(sum(fy));
    E_co(ii) = (1i*k*exp(-1i*k*r)/(2*pi*r)).*hy.*cos(theta(ii));
    fx = (E_ax).*exp(1i*k.*sin(theta(ii)).*x)*dx*dy;
    fx(x > (sqrt(a^2- (y+c).^2))) = 0;
    fx(x < (-sqrt(a^2- (y+c).^2))) = 0;
    hx= sum(sum(fx));
    E_cross(ii) = (1i*k*exp(-1i*k*r)/(2*pi*r)).*hx;
end
maximumy = max(20*log10(abs(E_co)));
figure;
ax = axes;
hold(ax,'on');
plot(deg*(theta0: dTheta: thetaEnd), 20*log10(abs(E_co))-maximumy,'linewidth',2.5);
grid on;
```

```
plot(deg*(theta0: dTheta: thetaEnd), 20*log10(abs(E_cross))-maximumy,'r','linewidth',2.5);
legend('co-polarized','cross-polarized');
ylabel('Relative Power, dB','fontsize',12,'fontname','cambria');
xlabel('\theta, degrees','fontsize',12,'fontname','cambria');
[maxx,indexx]= max(20*log10(abs(E_cross))-maximumy);
sprintf('\b The maximum relative cross pol level is= %.3f dB occuring at an angle of %.1f deg',
maxx,theta(indexx)*180/pi)
```

```
ans =
```

The maximum relative cross pol level is= -22.127 dB occuring at an angle of 1.0 deg